2017

HALO- AND SOLVATO-FLUOROCHROMIC POLYMER NANOASSEMBLIES FOR CANCER THERANOSTICS

Derek Alexander Reichel
University of Kentucky, derek.a.reichel@gmail.com
Digital Object Identifier: https://doi.org/10.13023/ETD.2017.273

STUDENT AGREEMENT:

I represent that my thesis or dissertation and abstract are my original work. Proper attribution has been given to all outside sources. I understand that I am solely responsible for obtaining any needed copyright permissions. I have obtained needed written permission statement(s) from the owner(s) of each third-party copyrighted matter to be included in my work, allowing electronic distribution (if such use is not permitted by the fair use doctrine) which will be submitted to UKnowledge as Additional File.

I hereby grant to The University of Kentucky and its agents the irrevocable, non-exclusive, and royalty-free license to archive and make accessible my work in whole or in part in all forms of media, now or hereafter known. I agree that the document mentioned above may be made available immediately for worldwide access unless an embargo applies.

I retain all other ownership rights to the copyright of my work. I also retain the right to use in future works (such as articles or books) all or part of my work. I understand that I am free to register the copyright to my work.

REVIEW, APPROVAL AND ACCEPTANCE

The document mentioned above has been reviewed and accepted by the student's advisor, on behalf of the advisory committee, and by the Director of Graduate Studies (DGS), on behalf of the program; we verify that this is the final, approved version of the student's thesis including all changes required by the advisory committee. The undersigned agree to abide by the statements above.

Derek Alexander Reichel, Student

Dr. Younsoo Bae, Major Professor

Dr. David Feola, Director of Graduate Studies

HALO- AND SOLVATO-FLUOROCHROMIC POLYMER NANOASSEMBLIES FOR CANCER THERANOSTICS

DISSERTATION

A dissertation submitted in partial fulfillment of the
requirements for the degree of Doctor of Philosophy in the
College of Pharmacy
at the University of Kentucky

By
Derek Alexander Reichel

Lexington, Kentucky

Director: Dr. Younsoo Bae, Associate Professor of Pharmaceutical Sciences

Lexington, Kentucky

2017

ABSTRACT OF DISSERTATION

HALO- AND SOLVATO-FLUOROCHROMIC POLYMER NANOASSEMBLIES FOR CANCER THERANOSTICS

Theranostics is an emerging treatment approach that combines diagnostics with therapy in order to personalize treatment regimens for individual patients and decrease cancer mortality. Previously, nanoparticles entrapping conventional fluorescent dyes were developed for cancer theranostics, but fluorescent nanoparticles did not allow clinicians to significantly improve cancer treatments.

The use of fluorescent dyes that are sensitive to solvent acidity (halo-fluorochromism) and polarity (solvato-fluorochromism) may overcome the limitations of fluorescent nanoparticles and improve cancer therapy by enabling researchers to detect chemical properties within the nanoparticle core environment. The model halo- and solvato-fluorochromic dye Nile blue was attached to the core of nanoscale drug delivery systems called polymer nanoassemblies (PNAs), which were created by tethering hydrophilic polymers and hydrophobic groups to a cationic polymer scaffold. The fluorescence of empty PNAs increased by 100% at pH 5.0 compared to pH 7.4, and the fluorescence of drug-loaded PNAs increased up to 300% compared to empty PNAs. A comparison of the fluorochromic properties between PNAs with various core properties indicated that both hydrophobic pendant groups and scaffold amines contributed to the fluorochromism of PNAs.

The halo-fluorochromism of PNAs allowed investigators to minimize the detection of fluorescence signals in healthy organs such as the liver. Fluorescence imaging of halo-fluorochromic PNAs diffused into tissue mimics indicated that fluorescence of PNAs in tissues increased by 100% at pH 7.0 compared to pH 7.4. In addition, halo-fluorochromic PNAs identified the acidic perimeter surrounding metastatic tumors in orthotopic metastatic tumor models. Computational simulations of metastatic lesions verified that some halo-fluorochromic PNAs accumulate in the hypoxic/acidic regions of metastatic tumors following intravenous administration. These simulations also indicated that the accumulation of PNAs in the hypoxic regions of tumors doubles at 12 hours post-treatment compared to 1.8 hours post-treatment.

The solvato-fluorochromism of PNAs enabled the fluorescence-based measurement of drug release from the nanoassembly core during dialysis-based drug release measurements. Solvato-fluorochromic methods indicated faster drug release rates than HPLC-based methods. Mechanistic modeling of drug release indicated that solvato-fluorochromic methods were unaffected by released drugs that interfered with HPLC-based methods. However, mechanistic modeling also indicated that drug rebinding and diffusion did not account for all of the differences between drug release rates determined by solvato-fluorochromic- and HPLC-based methods. Based on this evidence, it was hypothesized that solvato-fluorochromic drug release methods measure drug diffusion from near the scaffold of PNAs in a small region of the nanoassembly core, and that this process contributes to overall drug release but does not indicate apparent drug release rates for PNAs.

In order to develop PNAs for potential clinical applications, ionizable amines were removed from the polymer scaffold to increase drug loading and sustain the release of model drugs carfilzomib and docetaxel. The removal of primary amines decreased drug diffusivity in the core of PNAs (D from $3.9*10^{-18}$ cm^2/s to $0.1*10^{-19}$ cm^2/s) and increased the drug release half-life ($t_{1/2}$ from 4 to 26 hours). The controlled release of carfilzomib from PNAs reduced drug metabolism by 60% for up to one hour and sustained proteasome inhibition in cancer cells at 72 h post-treatment compared to free drug.

Overall, this work provides insight into the design of theranostic nanoparticles with beneficial properties for improving cancer treatment.

KEYWORDS: Polymer Nanoassemblies, Fluorochromism, Cancer Theranostics, Nanoparticle Core Environment, Tumor Metastasis

Derek Reichel

6/13/17

HALO- AND SOLVATO-FLUOROCHROMIC POLYMER NANOASSEMBLIES FOR CANCER THERANOSTICS

By

Derek Alexander Reichel

Dr. Younsoo Bae
Director of Dissertation

Dr. David Feola
Director of Graduate Studies

6/13/17

ACKNOWLEDGEMENTS

First, I would like to thank my advisor, Dr. Younsoo Bae, for the opportunity to work together for the past five years. His guidance and support were critical to help me grow as an independent scientist. In addition, I would like to thank my committee members, Dr. Brad Anderson, Dr. Eric Grulke, Dr. Mark Leggas and Dr. Robert Yokel, for their valuable guidance and insight into the directions and goals of my research. Their feedback and advice were critical to help me complete my dissertation.

I also want to thank the collaborators who helped me perform experiments that were beyond my areas of expertise. First, I want to thank Dr. Piotr Rychahou for his assistance with animal experiments, tissue collection and fluorescence imaging of tissue samples. Second, I want to thank Maria Piroli for assisting me with solvato-fluorochromic drug release experiments during her time as an undergraduate researcher in our lab. Finally, I want to recognize Min Jae Lee for her assistance with the proteasome activity assays. Without the assistance of these collaborators, I would not have been able to complete these experiments.

Finally, I would like to thank my current and former colleagues for their support and assistance over the past 5 years. As summer researchers, Nhu Bui and George Plasko helped me perform several experiments that I would not have been able to complete on my own. Amber Jerke and Steven Rheiner taught me many experimental methods and techniques that I used throughout my research. Finally, Dr. Pengxiao Cao, Dr. Matt Dickerson and Dr. Andrei Ponta were valuable lab mentors that helped me design experiments and interpret experimental results. Without assistance from all of my current and former colleagues, I could not have completed this work.

TABLE OF CONTENTS

LIST OF TABLES

LIST OF FIGURES

CHAPTER ONE

FLUOROCHROMISM AND NANOTECHNOLOGY FOR IMPROVING CANCER THERANOSTICS

1 FLUOROCHROMISM AND NANOTECHNOLOGY FOR IMPROVING CANCER THERANOSTICS

1.1 Cancer Theranostics: Promise and Limitations

Theranostics is an emerging approach that combines therapy with diagnostics in order to identify effective treatments, improve disease detection and reduce mortality (1). In general, the use of theranostic methods enables clinicians to maximize the efficacy of therapeutic agents by treating a disease with a conventional therapeutic agent while also identifying patients who may respond poorly to that therapeutic regimen. For this subset of patients, clinicians can select more aggressive therapeutic regimens or switch to targeted therapeutic agents in order to improve patient outcomes (2). Theranostic methods can also enable researchers to increase the sensitivity and accuracy of disease detection in early stages (3). The biological and pharmacological indicators of many diseases can be difficult to elucidate from traditional diagnostic methods such as medical imaging (4). By measuring the physiological response of a disease in response to a treatment, theranostic methods can allow clinicians to identify more effective treatment approaches based on the biological properties of a disease state (5). Additionally, theranostics may also enable clinicians to monitor disease progression and adjust treatment over the course of a treatment regimen (6). Theranostics is an especially promising approach for difficult-to-treat diseases with variable biological properties.

Theranostic methods combining medical imaging with drug delivery can enable clinicians to overcome the limitations of biomarker-based theranostic methods by indicating drug delivery to a targeted site (7). Biomarker-based theranostic methods allow clinicians to detect genes or proteins that predict treatment efficacy in a patient (8, 9).

Unfortunately, the identification of biomarkers that predict treatment responses in patients and the development of clinical devices for biomarker detection remain difficult (10, 11). Biomarker-based theranostic methods also fail to indicate the amount of drug reaching solid tumors in patients. In contrast to biomarker-based theranostic methods, medical imaging-guided theranostic methods often use FDA-approved drug delivery systems that are modified with imaging agents. Clinicians can monitor the distribution of these drug delivery systems after systemic administration (12, 13). By combining the *in vivo* distribution and drug release profiles of these drug delivery systems, clinicians can estimate drug delivery to diseased tissues and adjust treatments to maximize their efficacy (14). Theranostic methods are expected to enable clinicians to measure the real-time ADME of anticancer drugs and to provide timely, personalized treatment regimens that maximize anticancer drug accumulation in metastatic tumors (15-17).

Theranostic methods can also enable oncologists to detect small metastatic tumors in patients. Cancer is the second leading cause of death in the United States, and more than 90% of cancer-related deaths are attributed to metastasis (18). Metastasis is a disease state in which cancer cells migrate from primary tumors to adjacent tissues through blood vessels, lymphatic fluid or the peritoneal cavity (19). Cancer cells in metastatic tumors grow in a heterogeneous tissue microenvironment, in which micrometastatic colonies of cancer cells are surrounded by normal cells (20). The micrometastatic colonies within parenchyma are often too small and too dispersed throughout organs for clinicians to detect accurately. Theranostic methods allow clinicians to detect antigens or receptors on metastatic cancer cells, rather than the tissue properties of metastatic tumors, and accurately distinguish micrometastatic colonies from healthy tissues.

Theranostic methods may allow clinicians to treat micrometastatic colonies while they remain susceptible to treatment. Traditional primary tumor treatment methods such as surgery, chemotherapy, radiotherapy, and heat ablation are often ineffective at treating large metastatic tumors that can be detected with traditional methods (21-23). In contrast to large metastatic tumors with an acidic extracellular microenvironment that can ionize some anticancer drugs and prevent their diffusion through cell membranes, small metastatic tumors remain susceptible to chemotherapy due to increased drug accumulation in metastatic cancer cells (24-27). Theranostic methods can allow clinicians to treat small metastatic tumors earlier in their development and to estimate drug concentrations in tumor metastasis.

Although fluorescence imaging is an established diagnostic method with several applications in theranostics, many fluorescent dyes can provide false signals unless they are used carefully (28). The non-selective cellular accumulation of dyes and nanoparticles has limited the applications of previous theranostic methods using fluorescence imaging. Clinicians using fluorescent dyes for theranostics must also consider the signal-to-noise ratios, quantum yields, and photo-bleaching of these dyes (29). Strategies for improving theranostic methods using fluorescence imaging are needed to increase the accuracy of metastatic tumor detection and improve the pharmacokinetic predictions for anticancer drugs.

1.2 Halo- and Solvato-Fluorochromism for Theranostic Imaging

Fluorochromism is an optical property of fluorescent dyes in which fluorescence excitation wavelengths, emission wavelengths and quantum yields change depending on the solvent environment of the dye. The optical properties of fluorochromic dyes often

change based on solvent pH (halo-fluorochromism) and polarity (solvato-fluorochromism) (30). The halo- and solvato- fluorochromic properties of dyes are controlled by the electronic mobility and conformation of dye molecules in the solvent environment (31, 32). The halo-fluorochromism of dyes is also controlled by the protonation state of ionizable groups such as amines or carboxylate anions that alter the electronic mobility and conformation of dyes. Differences between the molecular interactions among solvents and dye molecules such as solvent-induced dye conformation changes, induced dipole interactions and hydrogen bonding contribute to the solvato-fluorochromism of dyes (33). By measuring the halo- or solvato-fluorochromism of dyes in solution, the chemical properties of their surrounding solvent environment can be quantified (34, 35).

The halo- and solvato-fluorochromism of dyes has allowed investigators to identify specific tissue regions in fluorescence images based on their chemical properties. Halo-fluorochromic dyes with increased fluorescence below pH 5.0 allowed for the identification of acidic lysosomes in cell images (36). In addition, solvato-fluorochromic dyes with strong fluorescence in lipids enabled the detection of intracellular lipid droplets in tissue samples (37). Solvato-fluorochromic dyes with increased fluorescence after binding to DNA permitted researchers to identify cell nuclei in microscopic fluorescence images (38). Fluorochromic dyes remaining in tumor tissue could be used by clinicians to monitor the tumor microenvironment and indicate treatment efficacy, but small molecule fluorochromic dyes often have poor retention in tissues. As a result, there is a critical need to increase the accumulation and retention of fluorochromic dyes in tumor tissue in order to investigate the tumor microenvironment.

1.3 Polymer Nanoassemblies (PNAs) Entrapping Fluorochromic Dyes

Nanotechnology has allowed scientists to increase anticancer drug accumulation in solid tumors with biocompatible nanomaterials that accumulate in the interstitial space surrounding leaky tumor blood vessels (39). One type of biocompatible nanomaterial with these properties is PNAs created from self-assembling or cross-linked copolymers, such as polymer micelles, vesicles and polyionic complexes. The physicochemical properties of PNAs, such as size, morphology and surface charge, can be controlled by altering their chemical composition. Controlling the size (< 100 nm in diameter) and surface charge (neutral or slightly anionic) of PNAs can increase their tumor accumulation compared to other drug delivery systems and fine-tune the pharmacokinetic profiles of entrapped drugs (40). PNAs often contain a hydrophobic core surrounded by a hydrophilic shell. The hydrophobic core can entrap water-insoluble drugs and protect drugs from metabolism, while the hydrophilic shell can prevent the non-specific binding of PNAs to plasma proteins and also reduce the uptake of drug-loaded PNAs by the mononuclear phagocyte system (41). The benefits of PNAs for anticancer drug delivery have been validated in several clinical trials (42, 43).

PNAs can function as theranostic tools and allow oncologists to reduce cancer mortality by combining anticancer drug delivery with fluorescence imaging capabilities. Previous studies demonstrated that PNAs with beneficial physicochemical properties allow clinicians to deliver many therapeutic, diagnostic and imaging molecules to tumors separately or in combination (44-47). The chemical conjugation of fluorescent dyes to PNAs prevents dyes from diffusing out of PNAs during imaging and allows researchers to measure quantitative fluorescence signals. PNA-entrapped fluorescent dyes have

reduced renal clearance compared to free dyes, because nanoassemblies cannot pass through renal glomeruli and enter the urine (48). As a result, PNAs can increase the half-life of dyes in tumor tissue and extend the time window for successful fluorescence detection of tumors from less than 5 minutes up to about two hours (49). PNAs can also extend the imaging time window in healthy organs such as the liver and enable the detection of metastatic tumors (50-52).

PNAs with fluorochromism can allow investigators to overcome the limitations of previously developed fluorescent PNAs. Fluorochromic dyes entrapped in PNAs may allow for the detection of the chemical properties within the nanoparticle core environment without interference from the surrounding environment, because fluorochromism occurs due to short-range molecular interactions (<0.1 nm distance) (53). Figure 1.1A describes the synthesis of PNAs with fluorochromism.

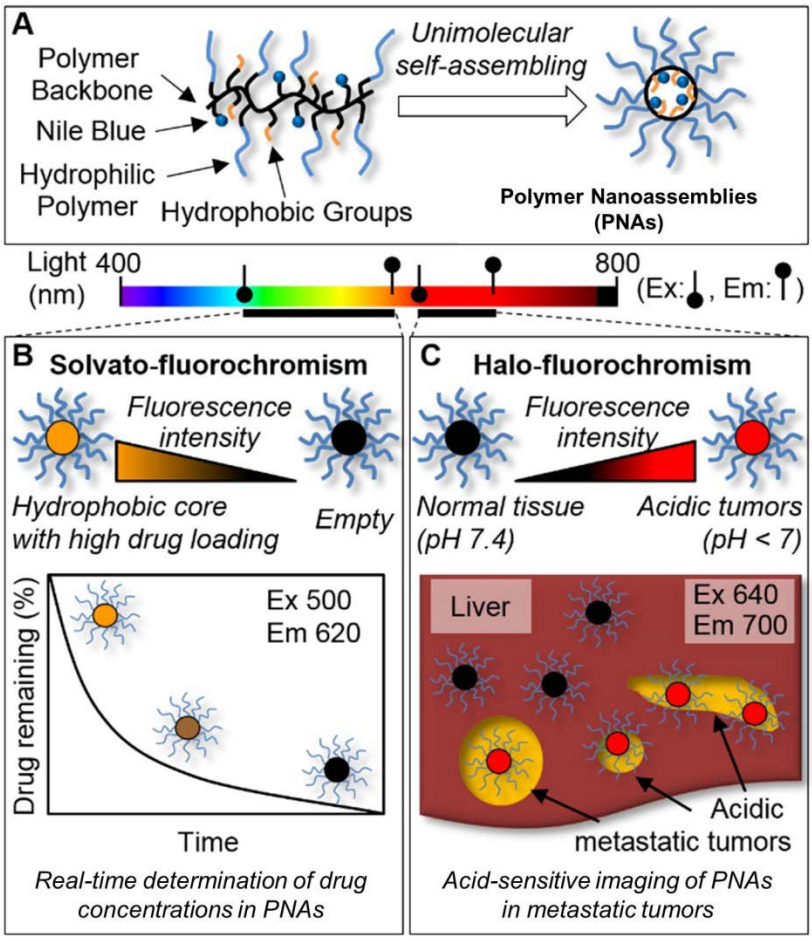

Figure 1.1. Graphical description of PNAs prepared through the unimolecular self-assembling of polymer conjugates (A). Fluorochromic PNAs for the real-time determination of drug concentrations using solvato-fluorochromism (B) and the acid-sensitive imaging of metastatic tumors using halo-fluorochromism (C).

The solvato-fluorochromism of PNAs can allow researchers to measure drug release from the nanoassembly core in real time (Figure 1.1B). The entrapment and release of hydrophobic anticancer drugs from the PNA core may alter the hydrophobicity within the nanoassembly core environment. Solvato-fluorochromism may allow investigators to detect hydrophobicity changes of the PNA core environment in real time indicating drug release. By combining fluorescence measurements of drug release with the biodistribution of PNAs, the ADME of anticancer drugs in patients may be estimated in real time (54).

The halo-fluorochromism of PNAs can allow researchers to improve the sensitivity and accuracy of metastatic tumor detection by increasing the fluorescence signals of PNAs accumulated in the acidic tumor microenvironment (Figure 1.1C). The rapid glucose metabolism of cancer cells in tumors generates acidic by-products, such as lactic acid, that are transported into the extracellular space of tumors (55). The acidification of the extracellular tumor microenvironment, also known as the Warburg effect, has been observed in tumors with various sizes, shapes, locations and biological properties (56, 57). By detecting the acidity of the tumor microenvironment, clinicians can select anticancer drugs that remain effective in the tumor microenvironment conditions of patients (58, 59).

The fluorochromism of PNAs can also allow investigators to identify methods of sustaining drug release and increasing the activity of anticancer drugs in cancer cells. Sustained drug release from PNAs has improved cancer treatment efficacy by maintaining effective drug concentrations in tumors, priming tumors for effective future treatments and preventing cancer cells from developing resistance mechanisms (60-63).

Unfortunately, the relationship between nanoassembly core environment properties and drug release rates is difficult to determine (64). Solvato-fluorochromism may allow researchers to identify specific chemical properties within the nanoassembly core environment that control drug release profiles. By carefully considering the solvato-fluorochromic characterization of the nanoassembly core environment, the therapeutic properties of PNAs may be improved in order to enhance the clinical efficacy of drug-loaded polymer nanoassemblies for cancer treatment.

Therefore, the overall goal of this research is to synthesize fluorochromic PNAs and evaluate their potential for cancer theranostics. First, several fluorochromic PNAs are synthesized and their fluorescence properties are characterized. Measurement conditions for both halo- and solvato-fluorochromism are determined, and the necessary conditions for separating halo- and solvato-fluorochromism in experimental measurements are determined. Next, the diagnostic capabilities of fluorochromic PNAs for metastatic tumor detection and drug release measurement are evaluated. Finally, the therapeutic potential of PNAs to control drug release and sustain drug activity in cancer cells is determined. The results from this work may indicate the potential of fluorochromism as a beneficial approach for cancer theranostics.

**Portions of Chapter 1 were previously published in (65). Reproduced with permission from Future Science Group: Therapeutic Delivery, Volume 6, Issue 10, 2015, Pages 1221-1237, Figure 1 and Introduction. Copyright 2015 is given to the publication in which the material was originally published.

CHAPTER TWO

SYNTHESIS AND CHARACTERIZATION OF POLYMER NANOASSEMBLIES WITH FLUOROCHROMISM

2 SYNTHESIS AND CHARACTERIZATION OF POLYMER NANOASSEMBLIES WITH FLUOROCHROMISM

2.1 Introduction

The development of PNAs with fluorochromism may improve cancer theranostics and decrease patient mortality, but fluorochromic dyes must be selected carefully to maximize their potential for theranostics. The theranostic applications of nanoparticles labelled with traditional fluorescent dyes are often limited by free dye impurities, which increase fluorescence background signals and reduce the fluorescence signals of nanoparticles in fluorescence images (66). Fluorescence signals from fluorochromic dyes should enable researchers to reduce signals from free dye impurities and enhance signals from entrapped dyes. The fluorochromism of dyes should also be detectable by fluorescence imaging systems used in the clinic. The fluorescence properties of these dyes should allow investigators to distinguish between the effects of halo- and solvato-fluorochromism in fluorescence measurements. In order to account for signal fluctuations due to concentration changes of PNAs, fluorochromic dyes should also allow for an internal standard measurement condition (67). The fluorochromic properties of dyes must be carefully considered in order to design PNAs that enable the monitoring of the chemical properties within the nanoassembly core environment.

The chemical composition of the nanoassembly core could affect the fluorochromic properties of the dyes and prevent the sensitive monitoring of the nanoassembly core environment. For example, interactions between fluorochromic dyes and the polymer scaffold in the PNA core could prevent dyes from sensing the surrounding environment. Charged groups could also draw ionized or polar molecules

into the nanoassembly core and decrease the hydrophobicity of the nanoassembly core environment. In addition, hydrophobic groups within the nanoassembly core may also interfere with the ionization of dyes necessary for halo-fluorochromism (68). Hydrophobic groups in the nanoassembly core can also shield dyes from interactions with other hydrophobic molecules in the nanoassembly core. Therefore, polymer nanoassemblies with controlled core environments can allow investigators to elucidate the effects of the nanoassembly core environment on the fluorochromism of dyes.

Nile Blue (NB) is a halo- and solvato-fluorochromic dye that emits strong fluorescence in nonpolar and acidic solvents, but its fluorescence is quenched in water (69). Fluorescence quenching of NB in water can minimize the background fluorescence signals of potential free dye impurities. NB has fluorescence excitation and emission wavelengths in the near-infrared light range, which is a commonly desired optical property for biomedical imaging applications of fluorescent dyes (70). Despite the beneficial optical properties of NB for biomedical imaging, free NB can be quickly removed from the body quickly through renal clearance, which limits its imaging applications (71). Because polymeric nanoparticles are typically larger than the pores on renal glomeruli, NB conjugation to the core of PNAs can prevent the renal clearance of dyes and enhance its capabilities for the theranostics of metastatic tumors.

PNAs with a controlled core environment can be developed by tethering hydrophilic polymers and hydrophobic groups to a modifiable polymer scaffold. By following this approach, simple, unimolecular nanoparticles with a hydrophobic core and a hydrophilic shell can be created to entrap hydrophobic anticancer drugs. In addition, fluorochromic dyes can be tethered to the polymer scaffold in the nanoassembly core.

Stable chemical bonds prevent fluorochromic dyes from diffusing out of the nanoassembly core and reducing the fluorescence signals from PNAs. The unimolecular design of PNAs prevents the nanoassembly core from dissociating at low concentrations and exposing fluorochromic dyes to the surrounding aqueous environment. The chemical conjugation of fluorochromic dyes to the polymer scaffold is expected to maintain an ordered arrangement of dye molecules near the primary amines on the polymer scaffold. The random distribution of functional groups onto the polymer scaffold following conjugation reactions should keep the dyes in contact with pendant groups in the core of the PNAs. Therefore, it is hypothesized that modulating the design parameters of PNAs can control the fluorochromic properties of entrapped dyes.

The purposes of this study are to confirm the feasibility of monitoring the nanoparticle core environment of PNAs with fluorochromism and to determine the effects of PNA core environment properties on halo- and solvato-fluorochromism. Polymer nanoassemblies were synthesized by tethering the hydrophilic polymer poly(ethylene glycol) (PEG) and the hydrophobic pendant palmitate (PAL) group onto a cationic polymer scaffold [poly(ethylene imine) (PEI) or poly(L-lysine) (PLL)] while modifying the core of the nanoassemblies with the fluorochromic dye NB. In addition, the remaining primary amines on PLL-based PNAs were end-capped by reacting the PNAs with acetic anhydride (AA). The simple design of these PNAs allowed the effects of PNA core environment properties on the optical properties of NB-conjugated PNAs to be elucidated. Four types of PNAs were used in this study: PEG-PEI-NB (2PN), PEG-PEI-PAL-NB (3PN), PEG-PLL-PAL-NB (3P'N) and PEG-PLL-PAL-NB-AA (3P'NAA). 2PN has ionizable groups in the core that can attract water and reduce NB fluorescence,

while 3PN has a hydrophobic core to increase the entrapment of hydrophobic anticancer drugs. 3P'N and 3P'NAA had fewer and no remaining amines in the nanoassembly core, respectively. By comparing the fluorochromism of 2PN and 3PN, the effects of hydrophobic groups on fluorochromism can be determined. In addition, by comparing the fluorochromism of 3PN to 3P'N or 3P'NAA, the effects of scaffold amines on fluorochromism can be investigated. The model anticancer drug carfilzomib (CFZ) was selected for this study as a clinically relevant, non-fluorescent, poorly soluble (5-10 μM in water) and lipophilic molecule (logP=4.2). Figure 2.1 contains the chemical structure of CFZ. A further description of the clinical applications of CFZ for cancer treatment is included in chapter 6.

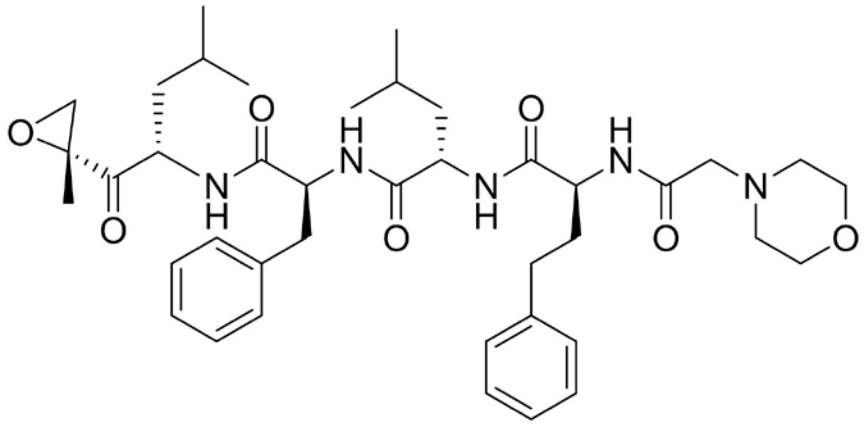

Figure 2.1. Chemical structure of carfilzomib.

2.2 Materials and Methods

2.2.1 Materials

α-Succinimidyloxysuccinyl-ω-methoxy-poly(ethylene glycol) (NHS-activated PEG, 5 kDa) was purchased from NanoCS (New York, NY). Branched PEI, PLL (15-30 kDa), chloroacetyl chloride, palmitoyl chloride and acetic anhydride were purchased from Sigma Aldrich (St. Louis, MO). Acridine orange (AO), NB sulfate, HEPES buffer (pH 8.0, 1 M), phosphate buffered saline (PBS, pH 7.4, 150 mM), acetone, DMF, DMSO, ethanol, isopropanol (IPA), methanol, N-Methyl-2-pyrrolidone (NMP), pyridine, tetrahydrofuran (THF), and dialysis membrane with molecular weight cut-off (MWCO) of 8 and 100 kDa were purchased from Fisher Scientific (Waltham, MA). CFZ was purchased from LC Laboratories (Woburn, MA).

2.2.2 Synthesis of Fluorochromic PNAs

PEI- and PLL-based PNAs were synthesized following the scheme in Figure 2.1. Before the reactions, branched PEI was dialyzed for 24 hours in water using a 100 kDa MWCO membrane in order to remove small impurities (72). PLL was also dialyzed for 24 hours in basic solution using a 6-8 kDa MWCO membrane in order to remove bromide salts. All other reagents were used as provided. PEI (934.6 mg) was reacted with NHS-activated PEG (10.0 g) in a mixed solution of DMSO and HEPES (1:1) at room temperature for 2 days. The reaction product PEG-PEI (2P, 73.2% mass yield) was purified by dialysis in water for 5 days using a 100 kDa MWCO membrane and then collected after freeze drying. A portion of the product PEG-PEI (4.0 g) was reacted with palmitoyl chloride (900 μl) in THF at 40 °C for 2 hours. Pyridine (1.8 ml) was added after 30 minutes to neutralize hydrochloric acid by-products by forming THF-insoluble

pyridinium salts. The reaction product PEG-PEI-PAL (3P, 85.7% mass yield) was purified by ether precipitation and dialysis and then collected after freeze drying. 2PN and 3PN were synthesized following a two-step coupling reaction scheme. First, 2P and 3P (2.0 g each) were reacted with chloroacetyl chloride (300 μl for 2P, and 200 μl for 3P) in THF at 40 °C for 2 hours. Next, NB was dissolved in DMF at 10 mg/ml and added to the reaction solution (685.4 mg for 2P, and 457.0 mg for 3P). The temperature was increased to 60 °C and the reaction continued for 3 additional hours. Pyridine (300 μl for 2P, and 200 μl for 3P) was added 30 minutes after adding NB to neutralize hydrochloric acid by-products. Reaction products 2PN (78.3% mass yield) and 3PN (87.0% mass yield) were purified by dialysis in a mixed solution of methanol and water (9:1) for 3 days, followed by dialysis in pure water for an additional 3 days. The purified reaction products were then collected after freeze drying. The removal of free dyes and other impurities from 2PN and 3PN was confirmed by absence of small molecule peaks on Gel Permeation Chromatography (GPC, Asahipak GF-7M column, 300 mm length, 7.5 mm internal diameter, 7 μm particle size, 40 °C, peaks with >15 minute retention time, 200 nm, PBS at pH 7.4, 0.5 ml/min) and a NB peak on High Performance Liquid Chromatography (HPLC, Agilent Eclipse XDB-C18 column, 150 mm length, 4.6 mm internal diameter, 5 μm particle size, 40 °C, 5.85 min, 600 nm, gradient elution from 10% ACN to 90% ACN, 1.0 ml/min). The chemical compositions of 2PN and 3PN were determined by proton NMR spectroscopy (Varian 400 MHz, DMSO-*d6*) and described in the results section (73). NB conjugation was confirmed by measuring the absorbance and fluorescence of 2PN (Ex 640/Em 680) and 3PN (Ex 600/Em 630) with a microplate reader (SpectraMax M5, Sunnyvale, CA). In addition, NB conjugation was further

confirmed by comparing the molecular weight of PNAs to a calibration curve of PEG standards with known molecular weights (74). By comparing the molecular weights of 2PN and 3PN with intermediates 2P and 3P, respectively, the mass substitution of NB can be determined and the molar substitution of NB can be calculated.

PLL-based PNAs were also synthesized following Figure 2.2. PLL (183.6 mg) was reacted with NHS-activated PEG (2.0 g) in a mixed solution of water, DMSO and pyridine (2:1:1) at room temperature for 2 days. The reaction product PEG-PLL (2P') was purified by dialysis in water for 5 days using a 100 kDa MWCO membrane, and then collected after freeze drying. PEG-PLL (1 g) was reacted with palmitoyl chloride (500 μl) in THF at 40 °C for 2 hours. Pyridine (500 μl) was added after 30 minutes to neutralize hydrochloric acid by-products. The reaction product PEG-PLL-PAL (3P') was purified by ether precipitation and dialysis, and then collected after freeze drying. 3P'N was synthesized following a two-step coupling reaction scheme. First, a portion of 3P' (200 mg) was reacted with chloroacetyl chloride (50 μl) in THF at 40 °C for 2 hours. Next, NB (266.8 mg) was dissolved in DMF at 10 mg/ml and added to the reaction solution. The temperature was increased to 60 °C and the reaction was continued for 3 additional hours. Pyridine (50 μl) was added 30 minutes after adding NB to neutralize hydrochloric acid by-products. The reaction product PEG-PLL-PAL-NB (3P'N) was purified by dialysis in methanol for 14 days, followed by dialysis in pure water for an additional 3 days. Purified 3P'N was collected after freeze drying. Some 3P'N (145 mg) was reacted with acetic anhydride (50 μl) overnight in DMSO. The reaction product PEG-PLL-PAL-NB-AA (3P'NAA) was purified by dialysis in pure water for 2 days and collected after freeze drying. The removal of free dyes and other impurities from 3P'N and 3P'NAA was

confirmed by GPC and HPLC as described for 2PN and 3PN. Chemical compositions of 3P'N and 3P'NAA were also determined by NMR spectroscopy and described in the results section. NB conjugation was further confirmed by absorbance and fluorescence spectroscopy.

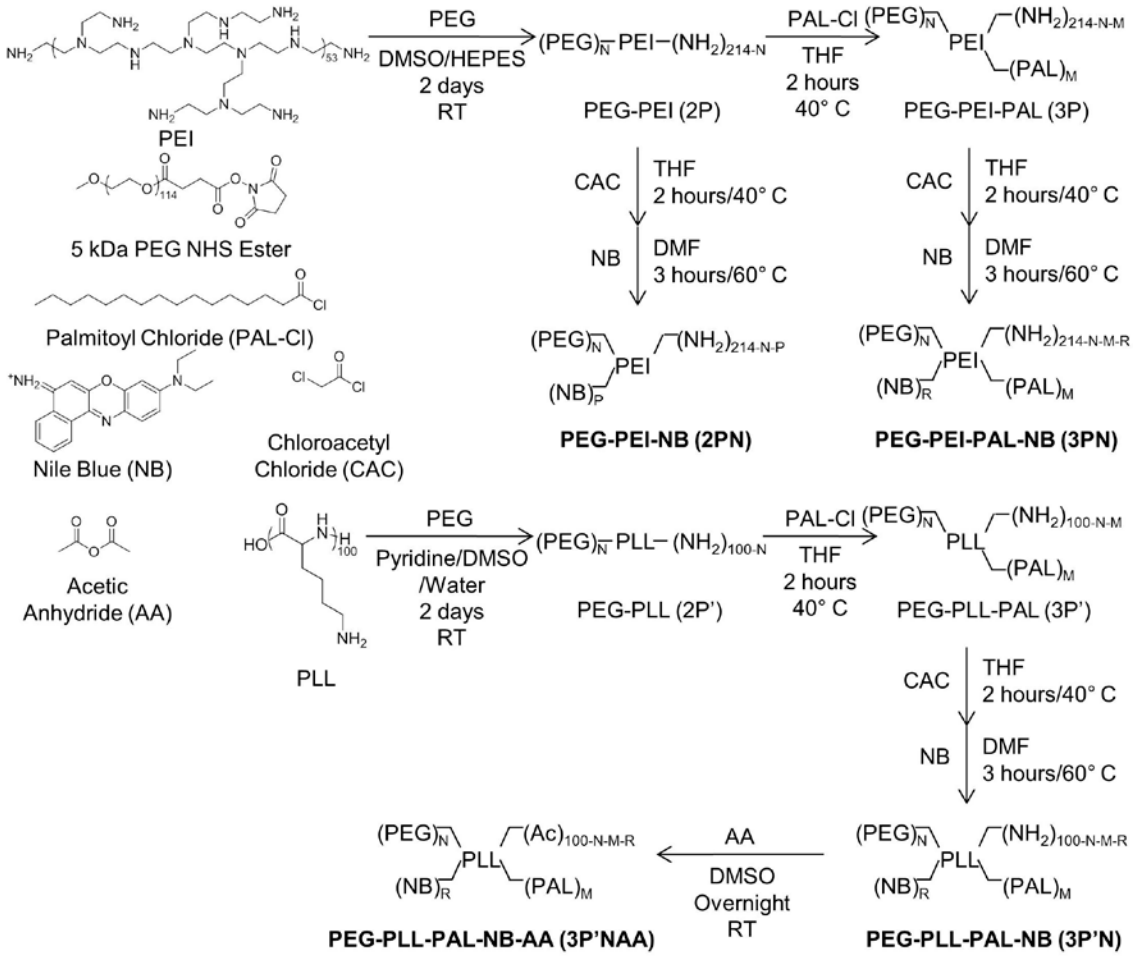

Figure 2.2. Synthesis protocols for PEI-based PNAs with an ionic (2PN) or mostly hydrophobic core (3PN) and PLL-based PNAs with a reduced amine (3P'N) or negligible amine (3P'NAA) content in the nanoassembly core.

2.2.3 Physicochemical Characterization of Fluorochromic PNAs

The diameter and surface charge of PNAs were determined using dynamic light scattering (DLS, Zeta-sizer Nano, Malvern, UK). Hydrodynamic diameters were determined by measuring 173 degree back-scattered light from a He-Ne laser (4 mW, 633 nm), and calculated using the Stokes-Einstein equation. Diameters were determined from number size distribution histograms. Zeta potentials were determined by measuring scattered light while applying voltage (automatic voltage selection), and calculated from light scattering data using the Smoluchowski equation. The molecular weight and uniformity of PNAs were determined by GPC.

2.2.4 Evaluation of the Fluorochromic Properties of Nile Blue

NB was dissolved in various solvents used for biological assays and chemical reactions: deionized water, methanol, ethanol, THF, IPA, DMF, acetone, DMSO, pyridine, and NMP. Changes in light absorbance and fluorescence at various excitation (Ex) and emission (Em) wavelengths were determined for NB in various solvents. NB solutions (200 μl, 100 μg/ml) were added into clear glass vials for optical imaging. To determine the fluorescent properties of NB, NB solutions were serially diluted (250, 125, and 62.5 ng/ml) and imaged over a wide range of excitation and emission wavelengths (500 nm Ex/620 nm Em, 605 nm Ex/660 nm Em, and 640 nm Ex/700 nm Em) using an IVIS Spectrum imaging system (Caliper Life Sciences, Hopkinton, MA).

2.2.5 Quantification of the Fluorochromic Properties of Poly(ethylenimine)-based PNAs

The fluorochromic properties of PNAs were determined in response to both drug loading and solution pH. In order to measure the effects of drug loading on fluorochromism, PNAs were loaded with CFZ by mixing drug and PNA solutions in

organic solvent and evaporating the solvent under reduced pressure. Drug-loaded PNAs were then reconstituted in water and centrifuged to remove free drug and other insoluble impurities. Drug loading of PNAs was verified by HPLC (Agilent Eclipse XDB-C18 column, 55:45 v/v acetonitrile/water with 0.1% formic acid mobile phase, 1 ml/min, 40 °C, 200 nm, 2.01 min retention time). The drug loading efficiency was defined as the weight percent ratio of drug to total formulation.

PNAs (10 mg/ml) with and without CFZ were dispersed in 50 mM buffer solutions at pH 7.4, 7.0, 6.0 and 5.0. Free dyes [NB (2 μg/ml) and AO (1 μg/ml)] were also dissolved in buffer solutions with and without suspended CFZ (1 mg/ml). Each solution (100 μl) was added to a 96 well plate and analyzed using fluorescence emission spectroscopy at multiple excitation wavelengths to determine the optimal fluorescence excitation and emission wavelength pairs. Two pairs were further imaged using a plate reader (500 nm Ex/600 nm Em and 640 nm Ex/680 nm Em) and an IVIS (500 nm Ex/620 nm Em and 640 nm Ex/700 nm Em). Non-fluorescence of CFZ (1 mg/ml, ethanol) was verified by measuring fluorescence emission spectra for several excitation values between 400 and 700 nm.

2.2.6 Evaluation of the Fluorochromic Properties of Poly(L-Lysine)-Based PNAs

PLL-based PNAs (10 mg/ml) with and without CFZ were dispersed in 50 mM buffer solutions at pH 7.4, 7.0, 6.0 and 5.0. Each solution (100 μl) was added to a 96 well plate and analyzed using fluorescence emission spectroscopy at multiple excitation wavelengths to determine optimal fluorescence excitation and emission pairs. These pairs were further imaged using an IVIS (640 nm Ex/680 nm Em and 675 nm Ex/720 nm Em).

2.2.7 Statistics

All values in figures are reported as mean±standard deviation for three measurements unless otherwise reported. Groups of measurements were compared by a one-way ANOVA with Bonferroni's post-test correction, and pairs of measurements were compared by a Student's t test unless otherwise noted. Statistical significance in each figure or table is indicated by * ($p<0.05$), ** ($p<0.01$) or *** ($p<0.001$).

2.3 Results

2.3.1 Synthesis of PNAs with a Hydrophobic, Ionic or Non-Ionic Core Environment

PEI-based PNAs were synthesized as described previously in Figure 2.2. Free NB was difficult to purify from NB-conjugated PNA solutions using traditional dialysis methods, because amphiphilic dye molecules bound to hydrophobic components of the nanoassemblies. However, the complete removal of amphiphilic NB from PNA solutions was achieved by dialysis using a 9:1 mixed solution of methanol and water. The absence of free NB in PNA solutions was further confirmed by performing centrifugal filtration with aliquots of the PNA solutions. The absorbance and fluorescence of each filtrate was measured to detect free NB filtered from the samples. Similar absorbance and fluorescence values between filtrates and deionized water indicated the complete removal of free NB from the PNA solutions.

PLL-based PNAs were synthesized as described in Figure 2.2. The complete removal of free NB from PNA solutions was achieved by dialysis using pure methanol. The absence of free NB in PLL-based PNAs was confirmed by following the method described in the previous paragraph. Because PLL-based PNAs were synthesized to

evaluate the effects of polymer scaffold amine on fluorochromism of PNAs, the physical properties of these PNAs were not analyzed in full detail.

PEG and PAL conjugation were further confirmed by NMR spectroscopy. Due to overlapping DMSO and PEI peaks, the area of peaks on the PEI scaffold with shifts between 2.4 and 2.6 ppm could not be accurately quantified. 2PN and 3PN had NMR peaks corresponding to PEG (3.54 ppm, s, relative area 1.000) and PEI (2.32 ppm, s, relative area 0.017; 2.44 ppm, s; 2.55 ppm, s; 2.60 ppm, s; 2.66 ppm, s, relative area 0.019). In addition, 3PN had NMR peaks corresponding to PAL (0.83 ppm, d, relative area 0.022; 1.20 ppm, s, relative area 0.082). 3P'N and 3P'NAA had NMR peaks corresponding to PEG (3.54 ppm, s, relative area 1.000), PLL (2.23 ppm, m, relative area 0.0013; 2.60 ppm, s, relative area 0.0005; 2.68 ppm, s, relative area 0.0008; 2.97 ppm, s, relative area 0.0009; 3.24 ppm, s, relative area 0.0114; 3.68 ppm, s, relative area 0.027; 4.09 ppm, s, relative area 0.040; 7.78 ppm, s, relative area 0.009), and PAL (0.83 ppm, d, relative area 0.002; 1.23 ppm, s, relative area 0.027; 1.46 ppm, s, relative area 0.009). 3P'NAA also had a peak corresponding to AA (1.78 ppm, s, relative area 0.024).

Based on a comparison of the NMR peak areas of each PNA component to the polymer scaffold, the molar substitution percent of each component to the initial moles of primary amines of the polymer scaffold (defined as the molar substitution) was calculated. Based on the analysis of Qiu *et al.*, a 2.5% coefficient of variation was assumed for each measurement in order to account for error due to NMR accuracy (75). The molar substitution of PEG on 2PN and 3PN was 10.0±0.3%, while the molar substitution of PAL on 3PN was 55.0±1.4%. In addition, the molar substitution of PEG on 3P'N and 3P'NAA was 25.0±0.6%, while the molar substitution of PAL on 3P'N and

3P'NAA was 37.0±0.9%. The molar substitution of AA on 3P'NAA was 17.0±0.4%. In addition, the molar substitution percent of each component relative to the remaining moles of primary amines on the polymer scaffold before the reaction (defined as the molar substitution yield) was calculated for AA. The molar substitution yield of AA on 3P'NAA was greater than 99%, indicating a complete substitution of the remaining primary amines.

2.3.2 Diameters and Surface Charges of PNAs are not Controlled by the Nanoassembly Core Environment

Diameter and zeta potential measurements of 2PN and 3PN confirmed that PNAs were less than 40 nm in diameter and had a neutral surface charge (Table 2.1), which was similar to the physical properties of unlabeled PNAs 2P and 3P, respectively (76). PNAs have a smaller diameter (40 nm) than the pore size of the GPC resin (7 μm). Based on the neutral surface charge of PNAs ($\zeta < \pm 30$ mV), PNAs could due to van der Waals interactions (77). However, histograms from all DLS measurements were unimodal and had narrow size distributions. In addition, 2PN and 3PN maintained consistent diameters and at multiple concentrations, suggesting that PNAs remain unimolecular in solution at the concentrations used in this study likely due to the PEG shell. These results indicate that NB and palmitate substitution do not affect the diameter of PNAs and that the PEG shell efficiently shielded the charge, dyes, and hydrophobic groups within the core. Polydispersity measurements indicate that 3PN has a greater size distribution than 2PN, but GPC measurements (Figure 2.3) suggest that both PNAs have narrow size ranges. This observation suggests that weak interactions between PNAs and the GPC column may limit the accuracy of size distribution measurements from GPC compared to DLS.

Table 2.1. Physicochemical properties of 2PN and 3PN.

PNA	Diameter (nm)	Zeta Potential (mV)	Polydispersity Index (PDI) (unitless)	Drug Loading Efficiency (%)
2PN	26.5±8.8	-0.6±0.4	0.32±0.04**	3.0±0.1**
3PN	34.3±3.5	-1.3±0.3	0.69±0.07**	8.7±0.4**

PNA	PEG (mol/mol primary amine on scaffold) (%)	PAL (mol/mol primary amine on scaffold) (%)	NB (mol/mol primary amine on scaffold) (%)
2PN	10.0±0.3	---	50±1.0***
3PN	10.0±0.3	55.0±1.4	25±0.5***

Diameter, zeta potential, PDI and drug loading efficiency are reported as mean±SD (n=3) for DLS or HPLC. PEG, PAL and NB substitution are reported as measurement±SE from the measurement error for NMR or GPC (n=1). PAL was not detectable on 2PN. Statistical significance is determined with a Student's t test as described in the methods section.

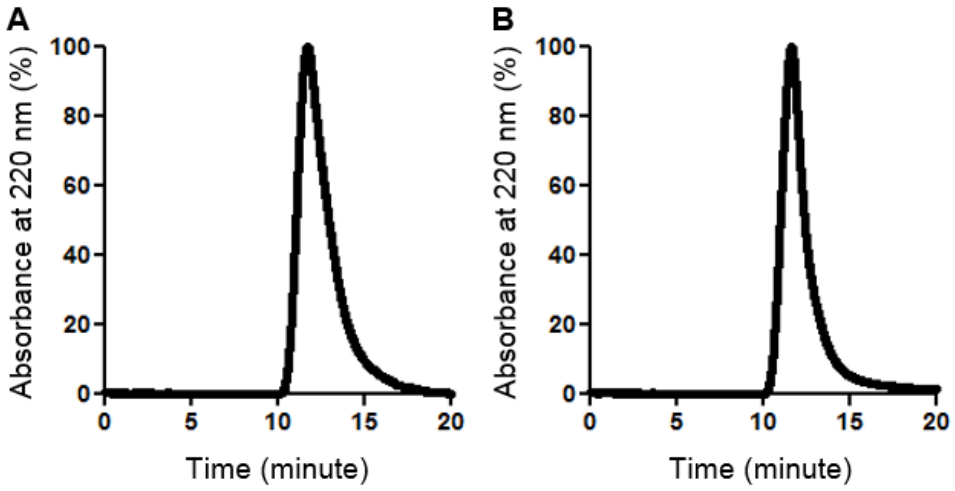

Figure 2.3. Gel permeation chromatographs for 2PN (A) and 3PN (B). Chromatographs were measured by UV-visible absorbance detector at 220 nm.

GPC further indicated that PNAs were larger than their individual components and free of impurities from each component. Based on molecular weight comparisons of PNAs to PEG standards, the molecular weights of 2PN and 3PN were 165 and 176 kDa, respectively. The molecular weights of intermediates 2P and 3P were also determined to be 129 and 159 kDa, respectively. By comparing the molecular weights of each component to the available primary amines on PEI, the substitution yield of each component on PNA could be calculated and compared to the NMR quantification. For 2PN, approximately 10% of the binding sites were substituted with PEG. For 3PN, approximately 10% and 55% of binding sites on PEI were substituted with PEG and PAL, respectively. GPC also allowed the estimation of the molar substitution of NB to 2PN and 3PN. Due to the fluorochromic effects of NB, quantification of NB molar substitution based on spectroscopic comparisons of free NB to NB-conjugated PNAs may introduce measurement error and indicate false substitution values. Based on a comparison of the molecular weights of 2PN and 3PN to 2P and 3P, respectively, 2PN had 50% NB molar substitution while 3PN had 25% NB molar substitution. After normalizing these measurements to the amount of remaining primary amines on 2PN and 3PN, 2PN had a 55% molar substitution yield of NB and 3PN had a 71% molar substitution yield of NB. Although palmitate substitution decreased the available binding sites for NB conjugation, the hydrophobic core environment increased the reaction yield for the remaining binding sites. For 2PN and 3PN, substitution yields calculated by GPC were in agreement with calculated NMR substitution yields.

2.3.3 Solvato-Fluorochromic Properties of Nile Blue are Sensitive to Non-Polar Solvent Environments

Figure 2.4 shows the optical properties of NB in various solvents. NB was blue in water, methanol, ethanol, IPA, and acetone; purple in DMSO; pale pink in THF; and bright pink in DMF, pyridine, and NMP (Figures 2.4A-B). There were no precipitates in any of the samples. Similar to the color properties of NB, the fluorescence of NB changed in a solvent-dependent manner based on excitation wavelength and decreased linearly as dye concentration decreased. At 500 nm Ex, NB fluoresced strongly in DMF, and weakly in acetone, pyridine and NMP (Figure 2.4C). At 605 nm Ex, NB fluoresced strongly in ethanol, methanol and IPA and fluoresced weakly in DMSO (Figure 2.4D). At 640 nm Ex, NB fluoresced strongly in DMSO and weakly in ethanol, methanol and IPA (Figure 2.4E). Importantly, the fluorescence of NB in water remained undetectable under all conditions tested in this study (Figures 2.4C-E). It should be noted that weak fluorescence of NB can be detected in water at high concentrations (>1 μg/ml), but the fluorescence decreases at high concentrations due to dye aggregation. The fluorescence properties of NB in cell media were similar to fluorescence of NB in water, suggesting that interactions with small molecules in cell media do not prevent the fluorescence quenching of NB. Similar to NB in various organic solvents (Figure 2.4A), NB-conjugated PNAs in water had red-shifted fluorescence compared to free NB in water. 3PN with a hydrophobic core had stronger fluorescence than 2PN with a hydrophilic core that can attract water and quench NB fluorescence. 2PN also showed a minor red shift and fluoresced stronger than free NB. These results indicate that the hydrophobicity of the NB solvent environment increases in order of water, 2PN core and 3PN core.

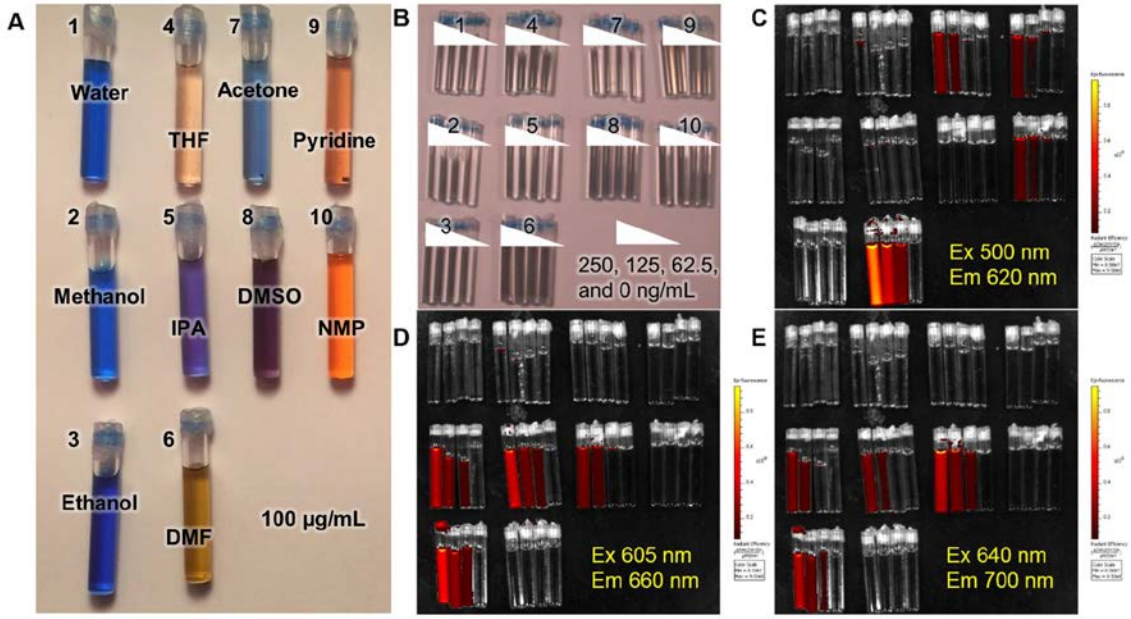

Figure 2.4. Optical properties of Nile Blue in various solvents at high (A) and low concentrations (B). Fluorescence was measured under three detection conditions (C, D, and E) with varying excitation (Ex) and emission (Em) wavelengths at concentrations from part (B).

2.3.4 Halo-Fluorochromic Properties of Nile Blue are Sensitive to Acidic Solvent Environments

Figure 2.5 shows the optical properties of PNAs and free dyes as measured by an IVIS. AO, a common biological indicator for acidic lysosomes, was used as a control for the fluorescence quenching effects of NB in water. At 500 nm excitation (Ex) and 620 nm emission (Em), the fluorescence intensity of AO increased below pH 6.0. At 640 nm Ex/700 nm Em, the fluorescence intensity of NB increased below pH 6.0. The fluorescence of AO and NB was minimally affected by suspended drug. It should be noted that the maximum and minimum fluorescence intensity threshold values are different in fluorescence images with and without drug. As a result, the fluorescence of AO and NB appear to decrease in the presence of drug, but plate reader measurements confirmed that the differences in fluorescence with and without drug were not statistically significant. In contrast to free dyes, fluorochromic PNAs allowed for the simultaneous detection of both pH and core hydrophobicity. These results suggest that the fluorescence properties of NB in the core of PNAs behaved as an environmental sensor, but that interactions with drug molecules did not interfere with the halo-fluorochromism of NB at 640 nm Ex and 700 nm Em. IVIS quantification indicates that pH-dependent differences in the fluorescence of PNAs are significant enough to detect *ex vivo*. In order to quantitatively evaluate the fluorochromism of PNAs, the fluorescence of PNAs was also quantified using a plate reader.

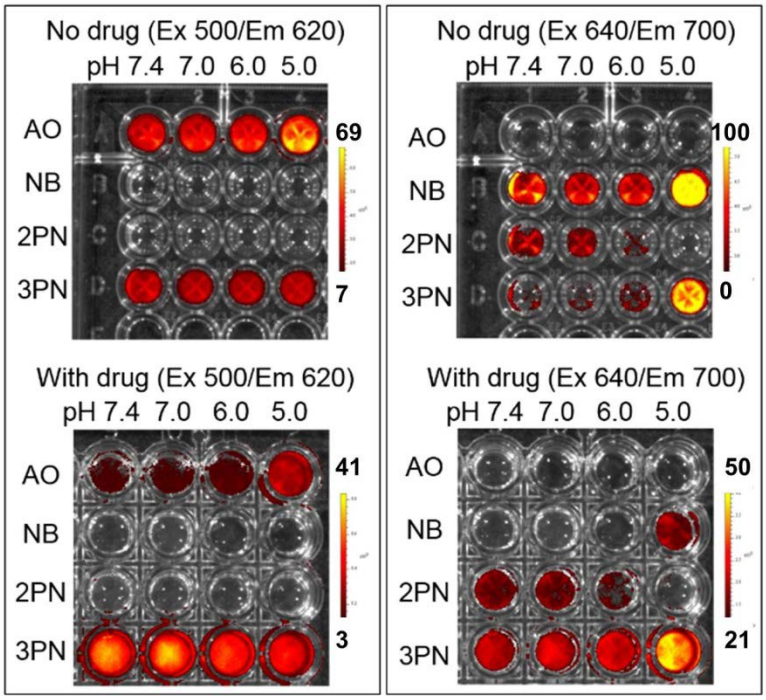

Figure 2.5. Fluorescence excitation (Ex) and emission (Em) wavelength-dependent fluorochromic properties of free dyes (AO and NB) and PNAs with and without the model drug carfilzomib. The relative fluorescence values for each image are on the right.

2.3.5 Entrapment of Nile Blue in the Nanoassembly Core Enables the Fluorochromism of Poly(ethylenimine)-Based PNAs

Figure 2.6 shows pH-dependent changes in the fluorescence of PNAs, as quantified by a plate reader. These quantitative results confirmed the fluorescence behavior of PNAs in Figure 2.5. Empty 2PN and 3PN had pH-insensitive fluorescence properties at 500 nm Ex and 600 nm Em, but demonstrated pH-sensitive fluorescence properties at 640 nm Ex and 680 nm Em. Specifically, empty 2PN demonstrated decreased fluorescence as the pH decreased, but the fluorescence of empty 3PN increased as the pH decreased. Drug-loaded PNAs exhibited increased fluorescence at 500 nm Ex and 600 nm Em compared to empty PNAs. However, the fluorescence of drug-loaded 3PN decreased in acidic conditions, presumably due to changes in the molecular conformation or ionization state of CFZ in the core of PNAs. CFZ ionization may also draw water into the core of PNAs and decrease NB fluorescence. Both empty and drug-loaded 2PN and 3PN showed pH-dependent differences in fluorescence at 640 nm Ex and 680 nm Em. 2PN demonstrated gradually decreased fluorescence as pH decreased, but the fluorescence of 3PN increased as pH decreased. Drug-loaded PNAs had minimal fluorescence changes compared to empty PNAs at 640 nm Ex and 680 nm Em. Based on IVIS observations and plate reader quantification, 3PN was selected for further *ex vivo* imaging studies in chapter 3.

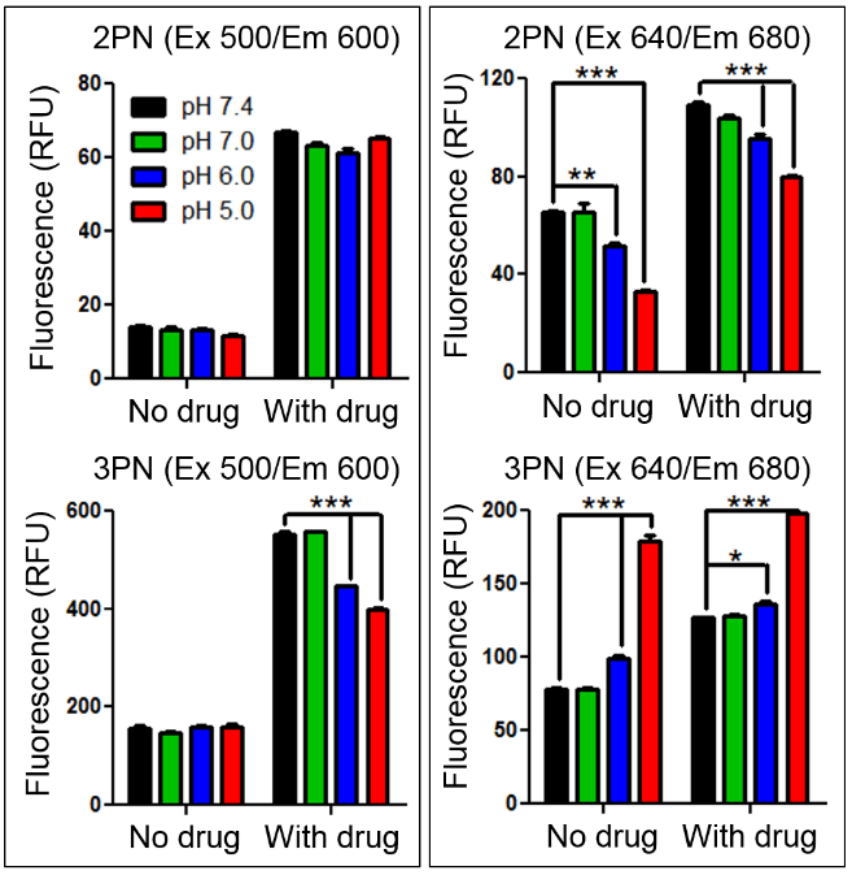

Figure 2.6. Quantification of the fluorochromic properties of 2PN and 3PN (10 mg/ml) by fluorescence spectroscopy. The fluorescence of the PNAs was measured with and without the model drug carfilzomib.

2.3.6 Removal of Ionic Moieties from the Polymer Scaffold Reduces the Fluorochromism of Poly(L-Lysine)-Based PNAs

Figure 2.7 shows the fluorescence properties of PNAs without scaffold amines. Unfortunately, the fluorescence of 3P'N at concentrations up to 10 mg/ml could not be quantified using an IVIS or a plate reader due to weak PNA fluorescence. This observation indicates that the polymer scaffold affects the fluorescence properties of fluorochromic dyes in the core of PNAs. As a result, the fluorochromism of 3P'N was not investigated in detail. In contrast to 3P'N, the fluorescence of 3P'NAA could be detected by an IVIS. However, the fluorescence of 3P'NAA could not be detected by a plate reader due to a weak signal compared to 2PN or 3PN at a similar concentration. In comparison to 2PN and 3PN that changed fluorescence intensities and wavelengths in response to changes in pH and core hydrophobicity, 3P'NAA fluorescence was consistent in response to changes in pH and drug loading. Figure 2.8 shows the quantification of 3P'NAA fluorescence. At 640 nm Ex and 680 nm Em, changes in fluorescence of 3P'NAA in response to drug loading or pH are not statistically significant. In addition, at 675 nm Ex and 725 nm Em, the fluorescence of drug-loaded 3P'NAA decreased at pH 6.0 compared to drug-loaded 3P'NAA at other pH values. There were no overall trends in 3P'NAA fluorescence in response to pH, but drug loading increased the fluorescence of 3P'NAA by 21% at 675 nm Ex and 725 nm Em compared to empty 3P'NAA. Because the halo- and solvato-fluorochromism of 3P'NAA were minimal compared to 2PN and 3PN, the applications of 3P'NAA were not further considered.

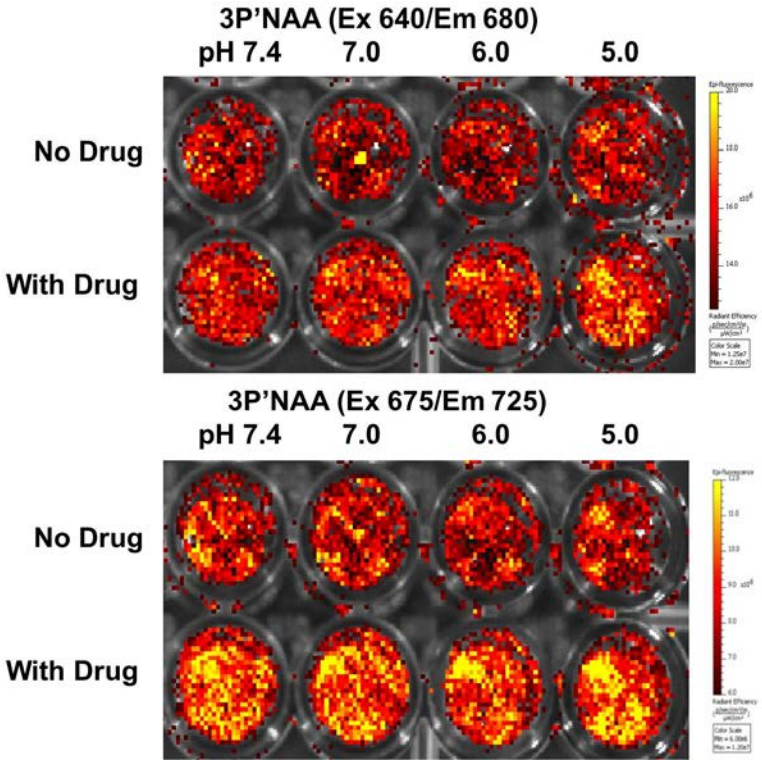

Figure 2.7. Fluorescence excitation (Ex) and emission (Em) wavelength-dependent fluorescence properties of 3P'NAA (10 mg/ml) at various pH values with and without the model drug carfilzomib.

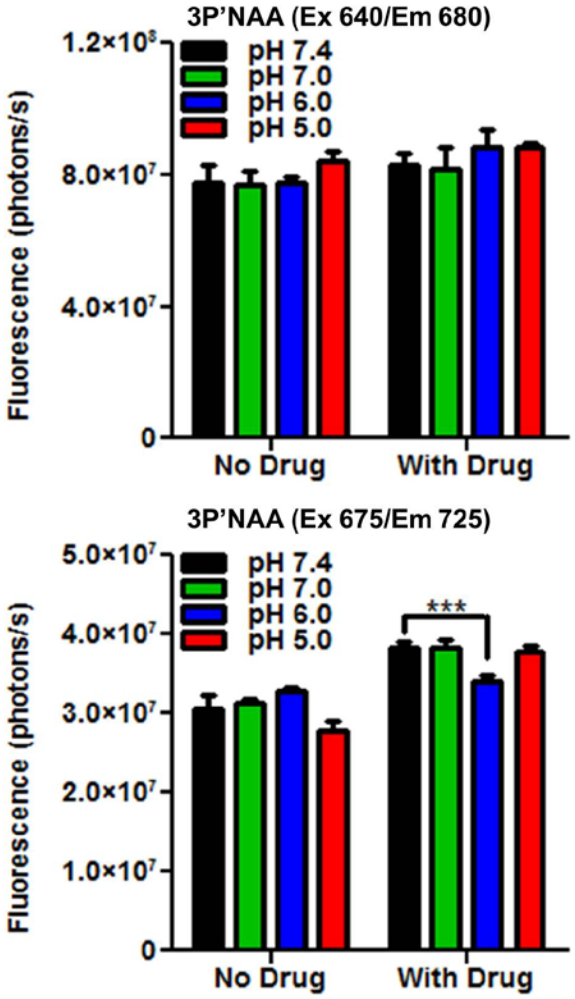

Figure 2.8. Quantification of the non-fluorochromic properties of 3P'NAA using IVIS. 3P'NAA was used at 10 mg/ml for all measurements. The Fluorescence of 3P'NAA was measured with and without the model drug carfilzomib.

2.4 Discussion

2.4.1 PNAs were Synthesized by Bioconjugation Chemistry

PNAs were synthesized by tethering polymers and pendant groups to a polymer scaffold. In all of the studies throughout this dissertation, PNAs were synthesized in a single batch in order to avoid any batch-to-batch variations in the molar substitution of polymers or pendant groups. However, the future applications of PNAs would require the synthesis of additional batches of PNAs with similar properties. In order to tether polymers and pendant groups to the scaffold, NHS ester-activated PEG and acyl-chloride activated palmitate molecules were reacted with primary amines on the polymer scaffolds. The reaction of ester-activated carboxylic acids with primary amines is called transesterification. Transesterification reactions are commonly used in bioconjugation chemistry due to their versatility, reliability and biocompatibility (78). In addition, acid chloride groups are highly reactive with primary amines such as functional groups on the column. Therefore, the reactions used to produce PNAs are expected to be reliable and reproducible for synthesizing additional batches of PNAs.

The synthesis of PNAs for clinical applications requires a significant scale-up of the reaction, which could affect the molar substitution of polymers and pendant groups on the scaffold. In addition, alternative reaction schemes may be needed to replace costly reagents such as NHS-ester activated PEG that are used in this reaction. The scale-up of each reaction in this process should be carefully considered in order to assure that reaction yields are consistent. In addition, the variability in molar substitution of each component must be considered in order to determine if the dispersity of PNAs is acceptable for clinical applications. Although these considerations are beyond the scope

of this work, they are necessary to consider when evaluating the potential clinical applications of PNAs.

2.4.2 Effects of the PNA Core Environment on the Fluorochromism of Nile Blue

Fluorochromism is an optical property of dyes that change their fluorescence spectra in response to environmental factors such as solvent polarity (solvato-fluorochromism) or pH (halo-fluorochromism) (79). NB was selected as a model dye with fluorochromism that can change the fluorescence properties of nanoparticles depending on the amount of entrapped drug as well as the pH of the solvent environment. Other solvato-fluorochromic dyes such as pyrene have been used to detect polarity changes in the core environment of nanoparticles such as polymer micelles (80, 81). The fluorochromic properties of pyrene change slightly when the dye is entrapped in the nanoparticle core compared to water. By measuring the ratio of fluorescence peak intensities of pyrene, polarity changes of the dye environment corresponding to micelle entrapment can be detected. In contrast to the weak fluorochromism of pyrene, NB changes fluorescence significantly in solvents with different polarities. Because of this increased sensitivity, NB was able to detect polarity changes due to both the PNA core environment and hydrophobic drug loading.

The structure and morphology of chemical groups in the core of fluorochromic nanoparticles may contribute to fluorochromism of dyes. It can be assumed that pendant groups are randomly attached to primary amines on the polymer scaffold, and that hydrophilic polymers, hydrophobic groups and fluorochromic dyes are homogenously distributed across the scaffold. The distance between primary amines on the polymer scaffold prevents interactions between dye molecules that could affect fluorescence

spectra. The unimolecular nature of PNAs allows them to attain similar conformations in solution following reconstitution. Hydrophobic groups on PNAs are likely to enter the core environment, while hydrophilic groups remain in the shell. The shell of PNAs is likely composed entirely of PEG interacting with water molecules, because the high molecular weight of PEG compared to other pendant groups (5000 Da vs. ~300 Da) allow it to expand out of the core. The core of PNAs is mainly composed of NB, hydrophobic groups and a polymer scaffold. In addition, the core of the PNAs may contain end portions of PEG molecules that have refolded towards the core (82). By keeping the dye molecules in the core, PNAs reduce NB interactions with water that prevent the detection of NB fluorescence. In the core of 2PN, dye molecules can interact with entrapped drug molecules, PEG or amines on the PEI scaffold. In the core of 3PN, dye molecules can interact with entrapped drug molecules, PEG, palmitate or amines on the PEI scaffold. For PEI-based PNAs, NB remains close to the polymer scaffold. In contrast to NB in PEI-based PNAs, NB in PLL-based PNAs is attached to amines on the lysine side chains. As a result, NB in PLL-based PNAs may be further from the polymer scaffold. Therefore, the distance between dye molecules and the polymer scaffold may contribute to the fluorochromism of dyes.

The hydrophobicity of the nanoassembly core environment controls both the drug loading of PNAs and fluorochromic properties of dyes. The addition of PAL to the polymer scaffold increases the drug loading of PNAs and the fluorescence intensity of both drug-loaded and empty PNAs. In addition, PAL causes the fluorescence of PNAs in acidic conditions to increase rather than decrease. A thorough comparison between 2PN

and 3PN indicates that the design, synthesis and chemical properties of nanoparticles are critical to the successful use of fluorochromic dyes for theranostics.

The removal of amines from the polymer scaffold of PNAs decreased the fluorescence of NB and interfered with its fluorochromism. In comparison to 3PN with strong fluorescence in water, the fluorescence of 3P'N was weak and could not be detected by an IVIS or a plate reader. This result suggests that the PLL scaffold increases the water content of the PNA core compared to PEI and decreases NB fluorescence. In comparison to 3P'N, 3P'NAA had strong fluorescence but lacked fluorochromism. This observation suggests that the interactions between NB and the polymer scaffold in the core of PNAs contribute to fluorochromism. It should be noted that unexpected chemical reactions between AA and tertiary amines on NB in the PNA core could also prevent dye fluorochromism, but previous observations suggests that these reactions are not thermodynamically favorable (83).

Halo-fluorochromic properties of molecules often depend on the ionization of specific chemical moieties resulting in fluorescence spectra shifts (84). The pKa values of these ionization processes can shift greatly depending on the solvent environment of the molecule (85). The addition of hydrophobic groups to the core of PNAs changed the halo-fluorochromic properties of 3PN compared to 2PN. While 2PN had decreased fluorescence intensity in acidic conditions, 3PN had increased fluorescence intensity. The interactions between NB and ionized moieties on PEI may cause this difference by shifting NB fluorescence peak wavelengths. Both drug-loaded and empty PNAs have similar fluorescence trends in response to acidity. This indicates that drug loading in the core of PNAs does not prevent NB from detecting changes in solvent acidity, and

suggests that PNAs have separable solvato- and halo-fluorochromic properties. However, the loading of ionizable drugs could affect the halo-fluorochromic properties of the PNAs. Therefore, the use of these PNAs should be avoided for drugs with pKa values between 6.0 and 7.4.

The ionization of model drugs in the core of PNAs may contribute to the solvato-fluorochromism of PNAs. Although empty 3PN demonstrated no halo-fluorochromism at 500 nm Ex and 620 nm Em, carfilzomib-loaded 3PN had decreased fluorescence at pH 6.0 and 5.0 compared to pH 7.4. The PubChem (NIH) and DrugBank (University of Alberta) databases report that the pKa of carfilzomib is 3.5; however, a literature analysis of the ionization behavior of N-substituted morpholine groups suggests that the pKa of carfilzomib is between 5.0 and 5.2 (86). Additionally, a European Medicines Agency report reports the pKa of carfilzomib to be 5.14 (87). Ionized carfilzomib in the 3PN core could decrease the fluorescence of 3PN and lower excitation wavelengths by decreasing the hydrophobicity within the nanoparticle core compared to unionized carfilzomib. However, additional work is needed to determine an accurate pKa value of carfilzomib in solution and in the nanoassembly core.

Identifying experimental conditions to separate the effects of halo- and solvato-fluorochromism in fluorescence measurements is necessary to evaluate the potential applications of fluorochromism for cancer theranostics. These results show that the fluorescence of 2PN and 3PN at low excitation and emission wavelengths is dependent on drug loading but not solvent acidity. This suggests that specific fluorescence excitation and emission conditions can detect drug loading and ignore solvent acidity. At high excitation and emission wavelengths, the fluorescence of 2PN and 3PN are

dependent on both drug loading and solvent acidity. Therefore, in order to measure the effects of solvent acidity in fluorescence measurements, empty PNAs can be used. It should be noted that the drug loading effects on fluorescence that are solely attributed to solvato-fluorochromism could be partially attributed to halo-fluorochromism if hydrophobic drug molecules alter the protonation behavior of NB. By measuring the activity of the nanoassembly core environment before and after drug loading and comparing activity changes to the halo-fluorochromic properties of PNAs, the specific effects of drug loading on both halo- and solvato-fluorochromism could be determined.

2.4.3 Benefits of Solvato-Fluorochromism for Cancer Theranostics

Solvato-fluorochromism is critical to the design of nanoparticles for the detection of metastatic tumors. Non-fluorochromic dyes entrapped in nanoparticles allowed investigators to detect solid tumors, because the accumulation of dye-containing nanoparticles in solid tumors increased the fluorescence signals from solid tumors and overcame the background signals from free dyes and circulating nanoparticles (88). However, metastatic tumors are not expected to accumulate significant amounts of dye-containing nanoparticles compared to solid tumors, and free dyes or circulating nanoparticles could interfere with fluorescence imaging (89). The results in this study show that NB-conjugated PNAs fluoresce stronger than free NB in water due to solvato-fluorochromism. Because of this result, any potential fluorescence from free NB will not contribute significantly to overall fluorescence signals. Therefore, the development of nanoparticles that can minimize the fluorescence signals from free dyes and circulating nanoparticles, while also enhancing nanoparticle fluorescence in tumor tissue, may allow for the detection of metastatic tumors without interference from free dyes.

Solvato-fluorochromism can overcome the limitations of other fluorescence methods for detecting drug loading in nanoparticles. For example, florescence resonance energy transfer (FRET) has measured hydrophobic drug loading in nanoparticles in real time (90). FRET detection of drug loading requires specific energetic interactions between drugs and dyes in the nanoassembly core, which limits the potential combinations of drugs and dyes that can be used in these systems (91). Because the solvato-fluorochromic properties of dyes do not require hydrophobic drugs to have specific optical properties, fluorochromic PNAs have the potential to measure drug loading and release for various applications (92). However, the use of solvato-fluorochromic dyes to measure drug release has some limitations. First, drugs that absorb and fluoresce light at the same wavelengths as fluorochromic PNAs may interfere with fluorescence measurements. Therefore, the scope of this approach must be narrowed to hydrophobic drugs without absorbance in the visible range of light (400-700 nm). Although this limits the potential applications of fluorochromism, many hydrophobic anticancer drugs do not absorb or fluoresce light in the visible range. Second, hydrophobic anticancer drugs that contain some hydrophilic moieties such as amines or carboxylate anions may draw water into the nanoparticle core and reduce the fluorescence signals of PNAs. Therefore, the chemical properties of hydrophobic drugs should be carefully considered to avoid drawing additional water into the PNA core. Although further feasibility tests are necessary *in vivo*, these results suggest that *in situ* determination of drug concentrations in metastatic tumors or other targeted sites might be possible by using fluorochromic nanoparticles. In combination with measurements of drug metabolism and clearance, this system has the potential to determine the ADME of a

drug in real time. Towards this goal, a method of normalizing fluorochromic signals with respect to drug carrier concentration is needed.

2.4.4 Benefits of Halo-Fluorochromism for Cancer Theranostics

Fluorochromic dyes are often used to identify biological molecules in imaging assays. For example, acridine orange (AO) is a widely used dye to detect nucleic acids, because its Ex and Em maximum wavelengths change upon binding to DNA or RNA (93). In acidic conditions, AO also has a blue shift in excitation wavelength (94). Despite its imaging potential, AO cannot differentiate between metastatic tumors and normal tissue. NB has several advantages over fluorochromic dyes such as AO, such as the potential for dye conjugation to the core of PNAs and the enhanced halo-fluorochromism of NB following conjugation. These unique optical properties of NB allowed NB-conjugated PNAs to provide real-time information on the amount of drugs remaining in the particles and solution acidity.

PNAs entrapping fluorochromic dyes can improve the detection of metastatic tumors compared to traditional biomarker-based methods. Biomarker detection using dye-labelled antibodies or aptamers can be selective for cancer cells, but antibodies or aptamers may have a limited time window for imaging due to dye photobleaching (95). The photostability of NB has been reported in the literature (96), and the photostability of NB during conditions used for fluorescence detection are experimentally confirmed in chapter 4. In contrast to antibodies or aptamers with a limited time windows for imaging, nanoparticles circulating throughout the body for a prolonged period of time can extend the time window for clinicians to observe metastatic tumors (97). Therefore, PNAs may

be a beneficial tool for the sensitive detection of metastatic tumors during surgery or other treatments.

Although the tissue pH of solid tumors has been measured, the detection of metastatic tumor tissue pH remains elusive. One of the obstacles to measuring metastatic tumor tissue pH is the rapid clearance and inconsistent optical properties of reporter molecules within the tumor tissue. In contrast to small molecules, dye-conjugated PNAs can accumulate in tumors and remain in tumor tissue for an extended period of time (98, 99). Although PNAs could detect acidic conditions *in vitro*, further optimization of tissue pH detection conditions such as fluorescence signal normalization at multiple emission wavelengths may be needed to accurately quantify the tissue pH of the acidic tumor microenvironment.

2.5 Conclusions

In this study, polymer nanoassemblies were synthesized by tethering hydrophilic polymer chains (PEG) onto cationic polymer scaffolds (PEI or PLL), followed by conjugation of fluorochromic molecules (NB), lipophilic chains (PAL) and amine end-capping groups (AA) to the core of the nanoassemblies. NB was selected as a model fluorochromic dye because of its increased fluorescence in the PNA core compared to free dyes in solution and its potential for both halo- and solvato-fluorochromism. In comparison to 2PN with a hydrophilic core that quenched NB fluorescence, 3PN with a hydrophobic core showed strong fluorescence in acidic conditions or in the presence of the model hydrophobic anticancer drug (CFZ). In contrast to 3PN, 3P’N had weak fluorescence that could not be quantified, while 3P’NAA had fluorescence but lacked fluorochromism. These results suggest that interactions between dyes, hydrophobic drugs

and the polymer scaffold contribute to the fluorochromism of PNAs. The findings in this study suggest that further experiments with PNAs may validate their potential as diagnostic tools with the capability to deliver chemotherapeutic drugs to tumors.

**Portions of Chapter 2 were previously published in (65). Reproduced with permission from Future Science Group: Therapeutic Delivery, Volume 6, Issue 10, 2015, Pages 1221-1237, Figures 2-6, Methods, Results, Discussion and Conclusion.

CHAPTER THREE

DISTRIBUTION OF HALO-FLUOROCHROMIC POLYMER NANOASSEMBLIES IN NORMAL ORGANS AND SOLID TUMORS FOR THE DETECTION OF METASTATIC CANCER

3 DISTRIBUTION OF HALO-FLUOROCHROMIC POLYMER NANOASSEMBLIES IN NORMAL ORGANS AND SOLID TUMORS FOR THE DETECTION OF METASTATIC CANCER

3.1 Introduction

Colorectal cancer (CRC) is the second most common cause of gender non-specific cancer deaths for adults in the United States, but its treatment is commonly hindered by the lack of effective methods for the early and accurate detection of metastatic CRC (MCRC) (100). Although primary CRC tumors can kill patients by interfering with normal colon functions, metastasis accounts for 90% of CRC-related deaths (101). The primary site of CRC metastasis is the liver; however, liver metastatic CRC has the second shortest median survival time of all metastatic CRC (102). Unfortunately, clinically available detection methods cannot effectively distinguish small MCRC tumors infiltrating into the liver from healthy tissue with high accuracy. In comparison to primary CRC tumors that can be treated with surgery or chemotherapy, MCRC tumors are difficult to treat because they are surrounded by healthy cells (103). In addition, MCRC tumors often become resistant to chemotherapy unless they are treated early in their development because they contain heterogeneous cell sub-populations with high mutation rates (104). As MCRC tumors grow and expand, the delivery of ionizable drugs into MCRC tumors becomes poor due to the dense acidic tissue microenvironment decreasing the diffusion of ionized anticancer drugs through cancer cell membranes (58, 59, 105). Small metastatic tumors may remain susceptible to clinically available micrometastatic tumor treatment methods such as neoadjuvant chemotherapy (106, 107).

Therefore, there is a need to detect small, underdeveloped MCRC tumors accurately before they grow too large to be treated effectively with surgery and chemotherapy.

Medical imaging has been used in the clinic for the non-invasive detection of solid tumors and tumor metastasis, but traditional imaging methods have failed to improve the treatment of MCRC because they cannot detect small metastatic tumors. Traditional medical imaging methods for tumor detection include magnetic resonance imaging (MRI), computerized tomography (CT), and intraoperative fluorescence imaging (108). MRI and CT identify structural abnormalities in normal tissue caused by tumors, but these methods may fail to detect small metastatic tumors that are smaller than the size detection limit. In order to decrease this size detection limit and detect small metastatic tumors, contrast agents have been developed to enhance MRI or CT signals in tumor tissues compared to normal tissue. Unfortunately, many contrast agents still fail to allow clinicians to detect small metastatic tumors that make little to no changes to tissue structure (109). Imaging artifacts also contribute to high false positive rates in MRI and CT. In contrast to MRI and CT, fluorescence imaging holds promise for the high-resolution imaging of tumors (110). Unfortunately, most fluorescent dyes do not selectively accumulate in cancer cells (111). In addition, many fluorescent dyes have poor diagnostic properties such as low signal-to-noise ratios, high background signals, short half-life in tumor tissue, and rapid clearance from the blood (112). Delivery systems that can improve the diagnostic properties of fluorescent dyes hold promise to increase the sensitivity of fluorescence imaging for the detection of primary tumors and tumor metastasis (113).

Nanoparticles entrapping fluorescent dyes may improve the diagnostic properties of fluorescent dyes and allow clinicians to detect CRC, but the effects of nanoparticle distribution on CRC detection are poorly understood. The accumulation of nanoparticles in the fenestrated vasculature surrounding primary tumors enhances fluorescence signals, but significant hepatic vasculature can also increase fluorescence signals in the liver (114). Distinguishing between fluorescence signals from primary tumors and healthy organs complicates tumor detection using fluorescence imaging. In addition, uneven diffusion of nanoparticles throughout tumor tissue due to heterogeneous sub-populations of cells with various cell densities and biological origins may cause clinicians to misidentify the size and shape of tumors (115). Heterogeneous sub-populations of cells create dense collagen meshes near tumor blood vessels with pore sizes of 50-100 nm (116, 117). Fluorescence signals from metastatic tumors may also be obscured by strong background fluorescence from the healthy tissue surrounding tumors. Nanoparticles entrapping halo-fluorochromic dyes can address these imaging limitations and detect small metastatic tumors by combining the indirect detection of abnormal tumor tissue with the direct monitoring of fluorescent dyes within tumors.

Based on this background, it is hypothesized that PNAs accumulate in the extracellular space of solid tumors and in the acidic interstitium between MCRC tumors and healthy cells in liver tissue (Figure 3.1). In order to test this hypothesis, the macroscopic and microscopic distributions of PNAs in tumor tissue were evaluated, and the distributions were compared to computational simulations of PNAs in metastatic tumors. Initially, the diffusion and opsonization of PNAs were evaluated using PNAs entrapping non-halo-fluorochromic dyes (IR820 and Alexa Fluor® 546). In addition,

cellular uptake was evaluated using halo-fluorochromic PNAs with various core environments. Patient-derived xenograft (PDX) models of primary CRC tumors and orthotopic liver MCRC tumor models were selected for this study. PDX tumor models reproduce the heterogeneity and microenvironment of tumors observed in the clinic (118), while orthotopic liver MCRC tumor models mimic metastatic tumors surrounded by healthy tissue in normal organs (119, 120). Orthotopic MCRC tumors also retain heterogeneous sub-populations of cancerous and healthy cells. Liver MCRC tumors were selected for this study because the liver is the primary site of CRC metastasis in patients (121). In addition, collaborators used a computational simulation based on a reaction-diffusion system to model PNA distribution in a metastatic lesion. Modeling results were compared to fluorescence images of PNA accumulation in metastatic tumors. Key simulation parameters such as blood vessel density and tumor cell state (proliferating, hypoxic, necrotic) were calibrated from orthotopic liver MCRC tumor models (122-124). These simulations provide a quantitative method to evaluate the potential of halo-fluorochromic PNAs for the early and accurate detection of metastatic tumors. By comparing the diffusion, cellular uptake, and aggregation of PNAs to the macroscopic and microscopic distribution of PNAs in solid CRC and liver MCRC tumors, the mechanism by which halo-fluorochromic PNAs detect MCRC tumors can be elucidated. Computational simulations can further validate the potential of halo-fluorochromic PNAs for the early and accurate detection of tumor metastasis. Results from this study will aid the development of halo-fluorochromic PNAs and other types of nanoparticles as useful tools for the early and accurate detection of MCRC tumors.

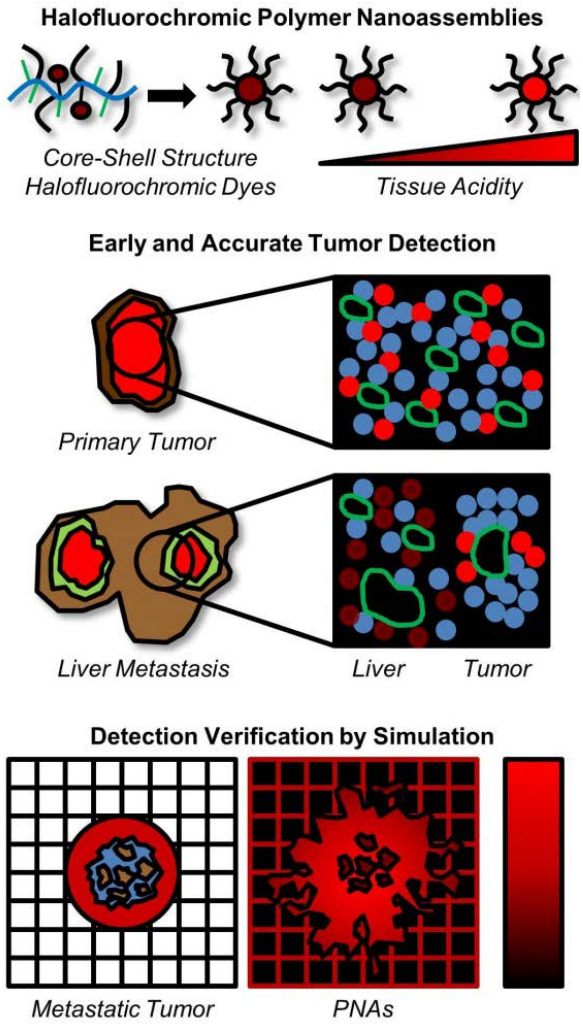

Figure 3.1. Graphical description of the halo-fluorochromic detection of acidic microenvironments (top), macroscopic and microscopic imaging of halo-fluorochromic PNAs in primary tumors or live MCRC tumors (middle), and computational simulations of PNAs in metastatic tumors (bottom). Simulations model a metastatic lesion (bottom left) containing blood vessels (black) and tumor with proliferating (red), hypoxic (blue) or necrotic (brown) regions. The model then predicts PNA distribution (bottom right, red)over time and quantifies PNA accumulation in each region.

3.2 Materials and Methods

3.2.1 Materials and Cells

α-Succinimidyloxysuccinyl-ω-methoxy-poly(ethylene glycol) (5 kDa, NHS-activated PEG) was purchased from NOF America (White Plains, NY). Acetic anhydride, agarose, HEPES sodium salt, IR-820 sodium salt, NHS-activated Alexa Fluor® 546 dye (Alexa 546), palmitoyl chloride, poly(L-lysine hydrobromide) (30-70 kDa, PLL) and sucrose were purchased from Sigma Aldrich (St. Louis, MO). The chemical structure of IR-820 sodium salt is in figure 3.1. Diethyl ether, DMSO, THF, methanol, nuclear staining dye Hoechst 33342, pyridine, chamber slides, dialysis membrane with 3.5 or 100 kDa MWCO, phosphate buffer solutions (50 mM, pH 7.4, 7.0 and 6.0) and preparative size exclusion columns (PD Minitrap, G-25, 3.5 ml) were purchased from Fisher Scientific (Waltham, MA). Aqueous ultramount permanent mounting medium was purchased from Dako (Carpinteria, CA). Optimal cutting temperature compound (OCT) was purchased from Andwin Scientific (Schaumburg, IL). Paraformaldehyde solution (4%) was purchased from Polysciences (Warrington, PA). Mouse EpCAM antibodies were purchased from LSBio (Seattle, WA), while mouse CD31 and donkey anti-mouse NL637-labelled IgG antibodies (secondary antibody) were purchased from R&D Systems (Minneapolis, MN). McCoy's 5A (M5A) media, phosphate buffered saline (PBS) and 0.05% trypsin/EDTA were purchased from GE Healthcare (Logan, UT). Fetal bovine serum (FBS) was purchased from Atlanta Biologicals (Flowery Branch, GA). Human CRC cell-lines (HT29 and HCT116) were purchased from the American Type Culture Collection (ATCC, Manassas, VA). Cells were cultured in M5A supplemented with 10% FBS in a humidified environment with 5% CO_2 at 37 °C.

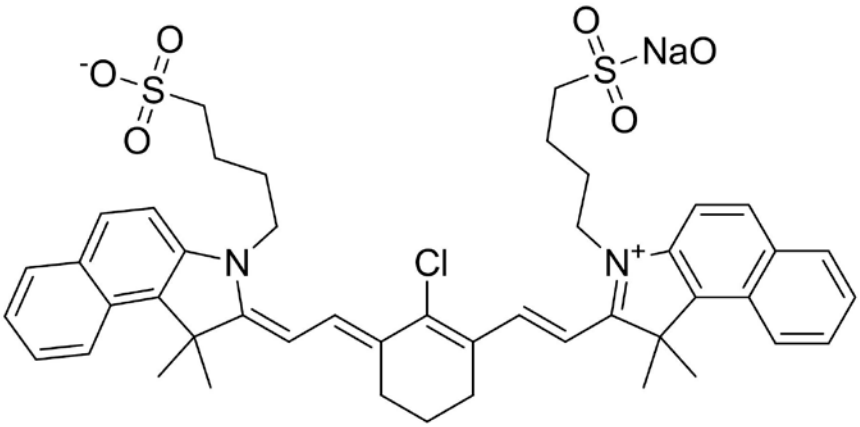

Figure 3.2. Chemical structure of IR-820 sodium salt.

3.2.2 Synthesis of Non-Halo-Fluorochromic PNAs

PNAs were synthesized following Figure 3.3. The synthesis protocol and characterization of halo-fluorochromic PNAs is described in chapter 2. Non-halo-fluorochromic PNAs are denoted as PEG-PLL-PAL-AA-IR-820 (3P'IR820) and PEG-PLL-PAL-Alexa Fluor® 546 (3P'A546). Briefly, PLL (334.4 mg) was reacted with NHS-activated PEG (2.0 g) in 2:1:1 water:DMSO:pyridine at room temperature for 3 days. PEG-PLL was purified by dialysis in water and collected after freeze drying. A portion of the PEG-PLL (1.0 g) was reacted with palmitoyl chloride (299 μl) at 40 °C in THF for 2 h. Pyridine (100 μl) was added to the reaction solution after 15 minutes to scavenge hydrochloric acid by-products. The product PEG-PLL-PAL was purified by ether precipitation and dialysis in water, and then collected after freeze drying. A portion of PEG-PLL-PAL (100.0 mg) was reacted with Alexa 546 (673.0 μg) at room temperature in DMSO overnight. The product 3P'A546 was purified using preparative size exclusion columns and collected after freeze drying. Another portion of the PEG-PLL-PAL (200.0 mg) was reacted with IR-820 (542.4 mg) in methanol at 40 °C overnight. Pyridine (300 μl) was added to the reaction solution after 1 hour to scavenge hydrochloric acid by-products. The product PEG-PLL-PAL-IR-820 was purified by dialysis in water and collected after freeze drying. PEG-PLL-PAL-IR-820 (180.0 mg) was subsequently reacted with acetic anhydride (54.3 μl) at room temperature in DMSO to end-cap remaining primary amines on PLL. The final product 3P'IR820 was purified by dialysis in water and collected after freeze drying.

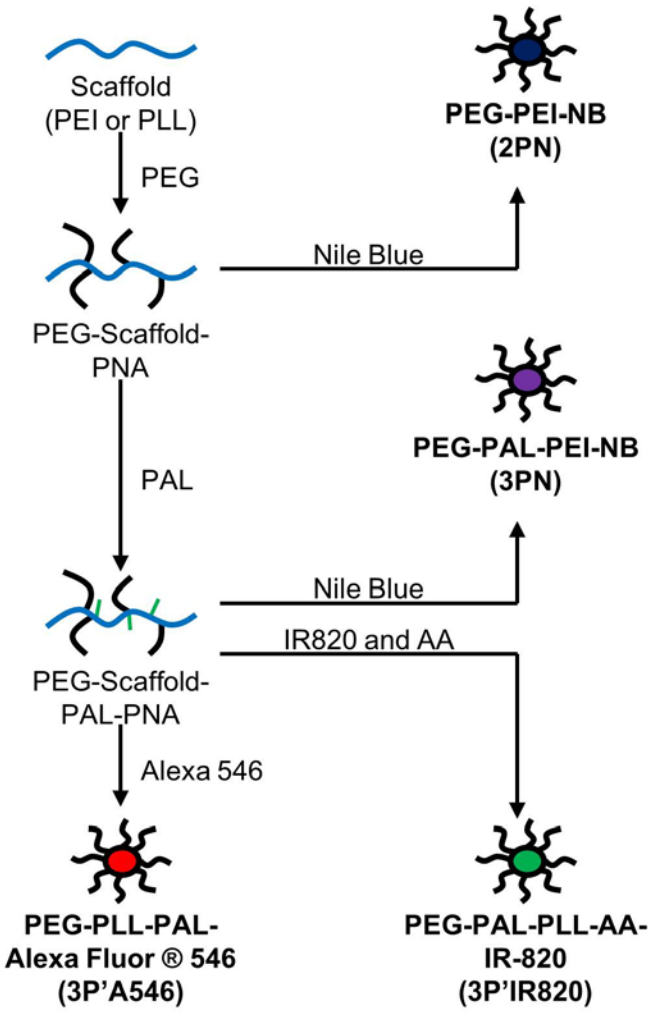

Figure 3.3. Synthesis protocol for halo-fluorochromic and non-halo-fluorochromic PNAs.

3.2.3 Physical and Optical Characterization of Non-Halo-Fluorochromic PNAs

Chemical compositions of non-halo-fluorochromic PNAs were determined by proton NMR spectroscopy (Varian 400 MHz, *d6*-DMSO, referenced to TMS). In order to determine the dye conjugation of PNAs, the absorbance of dye-conjugated PNAs was compared to free dye standards using a plate reader (SpectraMax M5, Sunnyvale, CA). The size distribution and uniformity of PNAs were determined by GPC (Asahipak GF-7M, PBS, 0.5 ml/min, 40 °C, calibrated using PEG standards). The diameter and surface charge of PNAs were determined by DLS (Zetasizer Nano ZS, Malvern, UK). The insensitivity of 3P'IR820 fluorescence to changes in drug loading and solvent pH was confirmed by measuring the fluorescence of PNAs (1 mg/ml) with and without carfilzomib loading at pH 7.4, 7.0, 6.0 and 5.0 using an IVIS (Ex 745 nm/Em 840 nm).

3.2.4 Diffusion and Flux of PNAs in Tissue Mimics

Agarose gels were prepared to mimic the pH and density of healthy and tumor tissues. These gels allowed for the direct measurement of PNA diffusion under controlled conditions (125). Briefly, agarose (0.5% or 1% w/v) was added to buffers (pH 7.4, 7.0 and 6.0) and heated to prepare suspensions. Low gel density (0.5% w/v) creates pores mimicking extracellular space between healthy cells (200 to 500 nm), while high gel density (1.0% w/v) provides pores corresponding to the keratin mesh surrounding tumors (50 to 100 nm) (117). The acidity of gels represents healthy tissue (pH 7.4), tumor periphery (pH 7.0) and the tumor core (pH 6.0) (126). Agarose suspensions were then pipetted into 96 well plates (100 μl per well) and cooled at room temperature to create gels. Stock solutions of 3P'IR820 (1 mg/ml) and 3PN (10 mg/ml) were prepared in water. 3P'IR820 solution (100 μl) was added to wells and allowed to diffuse into gels for 0.1,

0.5, 1, 3, 6 or 24 h at 37 °C. The solutions were removed from the wells and the absorbances of these gels were measured at 820 nm. The background signals of untreated wells were subtracted from the measurements and the corrected signal was normalized to absorbance of 100 μl of 3P'IR820 solution. In an attempt to mimic interarterial pressure forcing PNAs into liver stroma, diffusion experiments were repeated under an additional 16 kPa (120 mm Hg) external pressure. The normalized absorbance changes of gels over time were fit to a linear regression. Flux values were calculated by dividing the slope values from the linear regressions by the well surface area and multiplying by the initial PNA concentration. In order to evaluate the effects of tissue diffusion on halo-fluorochromic imaging, 3PN (100 μl, 10 mg/ml) was added to wells and allowed to diffuse into gels for 24 h at 37 °C. PNA solutions were removed from the wells and gels were imaged using an IVIS (Ex 640 nm/Em 700 nm).

3.2.5 Opsonization and Aggregation of PNAs

PNAs were exposed to anionic, cationic, physiological and serum-containing conditions that were previously reported in the literature to induce nanoparticle aggregation (127-130). Stock solutions of magnesium sulfate (Anionic, 1 M), calcium chloride (Cationic, 30 mM), McCoy's 5A media (Physiological), and McCoy's 5A media containing FBS (Serum-Containing, 50% v/v) were prepared. 3P'IR820 was dispersed in anionic, cationic, physiological and serum-containing solutions at 2 mg/ml and stored at 37 °C for 24 hours. Absorbance changes indicating potential aggregation were measured at 0, 1, 3, 6 and 24 h. Absorbance values above 0.3 (650 nm) indicating 50% turbidity were defined as the aggregation threshold for PNAs. The diameter of PNAs in each

solution was also measured after 24 h using DLS and compared to initial diameter of PNAs in deionized water.

3.2.6 Uptake of PNAs and Small Molecules in Cells

HT29 cells were seeded in chamber slides at 15,000 cells per well. After overnight incubation of the chamber slides, the cells were treated with 2PN, 3PN or Mitotracker Green (MG) (1 mg/ml 2PN and 3PN, 200 nM MG) for 0.5, 1, 3, and 6 h. Cells were then placed on a heated stage maintained at 37 °C and imaged using a fluorescence microscope (Zeiss Axiovert 200M, Thornwood, NY). 2PN and 3PN were imaged using a Texas red filter (Ex 568 nm/Broad Spectum Em), while MG was imaged using a FITC filter (Ex 488 nm/Broad Spectrum Em). The background fluorescence of 2PN, 3PN and MG was equalized in order to normalize the fluorescence signals over time for each treatment. The average intracellular and extracellular fluorescence for 2PN-, 3PN- and MG-treated samples were calculated for each timepoint using ImageJ (NIH, Bethesda, MD). The fluorescence measurements were then converted to relative concentrations using a calibration curve of known concentration standards. The ratio of intracellular to extracellular PNA concentrations was defined as the uptake quotient (Q) in equation 3.1. Q is unitless.

$$Q = \frac{C_{Intracellular}}{C_{Extracellular}} \tag{3.1}$$

To compare cellular uptake between PNAs, the cell experiments were repeated with 2PN and 3PN, but fluorescence images of cells were taken every 10 seconds for 0.5 h following treatment. Kinetic parameters of cellular uptake were determined using a mathematical model based on previous reports (131). Briefly, a chamber with PNA concentration C_1 and volume V_1 was assumed to contain cells with intercellular PNA

concentration C_2, volume V_2 and surface area α_2. In this derivation, the volume of cell media was assumed to be significantly greater than the volume of cytosol, and the surface ratio to volume ratio of cells was assumed to remain constant during measurements.

Mass transfer equations describing PNA movement into (r_{12}) and out of cells (r_{21}) through the cell membrane can be written following equations 3.2 and 3.3, respectively.

$$r_{12} = k_{12}(C_1 - \frac{C_2}{K_{EQ}}) \quad (3.2)$$

$$r_{21} = k_{21}(\frac{C_2}{K_{EQ}} - C_1) \quad (3.3)$$

In equations 3.2 and 3.3, r_{12} and r_{21} have units of moles of PNA per square meter of cell surface area per minute, k_{12} and k_{21} have units of meters per minute, C_1 has units of moles of PNA per cubic meter of cell media and C_2 has units of moles of PNA per cubic meter of cytosol. In addition, K_{EQ} is defined as a unitless cellular partition coefficient (C_1^{eq}/C_2^{eq}) that relates the media PNA concentration to the cytosol PNA concentration at equilibrium.

Equations 3.2 and 3.3 were combined into equation 3.4, which describes the overall kinetic transfer of PNAs into and out of cells.

$$r_A = -K_M\left(\frac{C_2}{K_{EQ}} - C_1\right) \quad (3.4)$$

In equation 3.4, r_A has units of moles of PNA per square meter of cell surface area per minute. K_M is defined as an overall mass transfer coefficient accounting for both physical and biological processes contributing to nanoparticle uptake by cells. Similar to each rate constant, K_M has units of meters per minute.

In addition to a kinetic equation describing uptake of PNAs, a mole balance describing changes in PNA concentrations in cells can be written as described in equation 3.5.

$$\frac{dN_2}{dt} = n_{12} - n_{21} \tag{3.5}$$

In equation 3.5, n_{12}, n_{21}, and dN_2/dt have units of moles of PNA per minute. By assuming that the volume of cell media remains constant and that PNAs accumulate in cells only through mass transfer processes, we can convert equation 3.5 into terms of concentration using equations 3.6 and 3.7.

$$\frac{dN_2}{dt} = V_2 * \frac{dC_2}{dt} \tag{3.6}$$

$$n_{12} - n_{21} = \alpha * r_A \tag{3.7}$$

In equations 3.6 and 3.7, V_2 has units of cubic meters and α has units of square meters. Equations 3.6 and 3.7 were substituted into equation 3.5 to yield equation 3.8.

$$V_2 * \frac{dC_2}{dt} = \alpha * r_A \tag{3.8}$$

Equation 3.4 was substituted into equation 3.8 to yield equation 3.9.

$$V_2 * \frac{dC_2}{dt} = -\alpha * K_M \left(\frac{C_2}{K_{EQ}} - C_1\right) \tag{3.9}$$

If extracellular PNA concentrations remain constant during uptake and M remains constant with respect to PNA concentrations, C_1 is simplified to the initial extracellular PNA concentration C_1^0 and equation 3.9 can be simplified to equation 3.10.

$$V_2 * \frac{dC_2}{dt} = -K_M * \alpha_2 * (\frac{C_2}{K_{EQ}} - C_1^0) \tag{3.10}$$

Equation 3.10 can be rearranged to yield equation 3.11, which was solved for C_2 to yield equation 3.12, using the initial condition of no PNAs in the cytosol or on the cell membrane before treatment.

$$\frac{dC_2}{dt} = \frac{-K_M * \alpha_2}{K_{EQ} * V_2} * (C_2 - K_{EQ} * C_1^0) \quad (3.11)$$

$$\frac{C_2}{C_1^0} = K_{EQ} * (1 - e^{\frac{-K_M * \alpha_2}{K_{EQ} * V_2} * t}) \quad (3.12)$$

As described earlier and repeated below in equation 3.13, K_{EQ} was defined as the cellular partition coefficient. In addition, *k* was defined as the cellular uptake rate constant in equation 3.14. K_{EQ} is unitless, while *k* has units of inverse minutes. In addition, because extracellular PNA concentrations are assumed to remain constant, the left side of equation 3.12 is equal to the uptake quotient. These parameters are substituted into equation 3.12 and simplified to yield equation 3.15. The uptake coefficient-time profiles were fit to equation 3.7 using Prism 5.0 (Graphpad, La Jolla, CA). Because the concentration ratios are determined in equation 3.15 rather than the molar ratios, the phase volumes are not necessary to calculate uptake kinetics.

$$K_{EQ} = \frac{C_1^{EQ}}{C_1^{EQ}} \quad (3.13)$$

$$k = \frac{-K_M * \alpha_2}{K_{EQ} * V_2} \quad (3.14)$$

$$Q = K_{EQ} * (1 - e^{k*t}) \quad (3.15)$$

In order to compare the rate of cellular uptake between different PNAs, t_{95} was defined as the time for the uptake quotient (*Q*) to reach 95 percent of the cellular partition coefficient (K_{EQ}) (equation 3.16). The t_{95} value has units of minutes.

$$t_{95} = \frac{\ln(20)}{k} \quad (3.16)$$

3.2.7 Ex Vivo Imaging of Patient-Derived Xenograft Tumors from Mice using Non-Halo-Fluorochromic PNAs

NOD-scid gamma mice between 6 to 8 weeks old were purchased from the Jackson Laboratory (Bar Harbor, ME). All animal experiments were performed in accordance with the Institutional Animal Care and Use Committee (IACUC) and with approval from the Institutional Review Board of the University of Kentucky. A patient primary CRC tumor sample (F0) was collected, divided and implanted into a mouse flank. When these tumors (F1) grew to 1 cm^3, the tumors were resected and divided into 2 mm^3 sections. The divided tumors were then implanted into mice (F2) for experiments. Mice bearing F2 tumors were dosed with 3P'A546 by tail vein injection (10 mg/kg). As a negative control, mice were also dosed with PBS. Mice were euthanized 1, 4, 8 and 24 hours post-injection and lung, liver, kidney, spleen and PDX tumors were collected. The fluorescence of 3P'A546 in normal organs and tumors were quantified by IVIS. Density maps of PNA fluorescence in tissues were prepared using Living Image 3.1 (Caliper Life Sciences, Hopkinson, MA) and represented as a color gradient centered at the maximum fluorescence intensity. Additionally, tumor tissue samples were fixed in 4% paraformaldehyde containing 10% sucrose at 4°C, embedded in OCT on dry ice, sectioned at 10 μm thickness, and then dried overnight in the dark. Tumor tissue samples were then washed in PBS at room temperature, stained with Hoechst 33342 (500 ng/ml, PBS) and mounted in aqueous permanent mounting medium overnight. Additionally, tumor tissue samples were also treated with either EpCAM or CD31 primary antibodies to identify CRC cells or blood vessels, respectively. Primary antibody-treated samples were then treated with dye-labelled secondary antibodies for fluorescence imaging. Stained tissue slides were imaged by confocal microscopy at 20x magnification (Olympus FV1000, Tokyo, Japan).

3.2.8 Ex Vivo Imaging of Livers from Mice with Liver Metastatic Colorectal Cancer using Non-Halo-Fluorochromic and Halo-Fluorochromic PNAs

Male athymic NCr nude mice between 6 to 8 weeks old were purchased from Taconic (Hudson, NY). Orthotopic liver MCRC tumors were established in these mice. Briefly, mice were injected with HCT 116 cells expressing green fluorescent protein (GFP) into the spleen capsule and allowed to develop MCRC tumors for 6 weeks. The establishment of liver MCRC tumors was confirmed by measuring the fluorescence of GFP corresponding to cancer cells in liver tissue. In order to maximize the fluorescence signals from normal organs without saturating the IVIS fluorescence detector, tumor-free mice were injected with 3P'A546 through the tail vein at varying doses (0, 5, 10 and 20 mg/kg). Twelve hours after injection, mice were euthanized to collect organs for imaging by IVIS (Ex 535 nm/Em 580 nm). Based on the measured fluorescence intensities of livers from tumor-free mice, mice bearing liver MCRC tumors were injected with 3P'A546 (10 mg/kg) through the tail vein and euthanized after 12 h. Mice bearing MCRC tumors were also injected with either 3PN (10 mg/kg) or PBS through the tail vein and euthanized after 6 h. The liver, kidney and lungs were collected from these mice for macroscopic imaging as described above. For microscopic imaging, liver tissue and liver MCRC tumor samples were collected from mice treated with 3P'A546 and fixed as described in the previous section. Tissue samples were stained with Hoechst 33342 (500 ng/ml, PBS) to visualize cell nuclei, and then stained with CD31 primary antibodies to identify blood vessels. Primary antibody-treated tissue samples were then stained with dye-labelled secondary antibodies for fluorescence imaging. Stained tissue slides were

imaged by confocal microscopy at 20x magnification as described in the previous section.

3.2.9 Quantification of Fluorescence Signals in Microscopic Fluorescence Images of Metastatic Tumors

Fluorescence signals corresponding to cell nuclei (DAPI), tumor vasculature (CD31) and PNAs were quantified from microscopic liver MCRC images. First, the fluorescence signals from merged images were split by channel to isolate nuclei, vasculature and PNA signals. To account for differences in fluorescence signal strength between dyes, dye-labelled antibodies and PNAs, the fluorescence signals from each channel were normalized by converting the fluorescence intensities to binary signals using ImageJ. Next, regions of interest (80x80 μm) corresponding to metastatic tumor foci were selected and the total fluorescence per unit area was quantified in these regions. Fluorescence values per unit area were used to estimate cancer cell and vasculature density in metastatic tumors for computational simulations.

3.2.10 Computational Simulations of PNA Distribution in Metastatic Tumors

A computational model was used by Frieboes *et al.* to describe PNA distribution in MCRC tumors as a function of the surrounding tissue vascularization. Frieboes describes the model in detail in previous publications (124, 132-136). Briefly, the model represents viable, hypoxic, and necrotic tissue regions of a tumor in a two dimensional Cartesian coordinate system, and it simulates a small lesion (initial diameter ~50 μm) in the center of a pre-existing vascular capillary grid from healthy tissue. Mass conservation equations describe tissue growth (proliferation as a function of cells cycling) and tissue death via necrosis as a function of hypoxia. Hypoxia induces the release of tumor

angiogenic factors such as Vascular Endothelial Growth Factor (VEGF), which causes neovascularization to supply the tumor with sufficient nutrients for growth. The tumor growth equations are combined with the diffusion of PNAs, oxygen, and cell nutrients to a reaction-diffusion equation. The rate constants for proliferation and death depend on the availability of oxygen, nutrients, and drug, and are thus spatio-temporally heterogeneous.

The tumor growth component of the computational model is based on (137). Briefly, the tumor tissue and its boundary are denoted by Ω and Σ, respectively. The tissue typically has a proliferating region Ω_P (100-200 μm thickness) in which cells have sufficient oxygen and nutrients, a hypoxic region Ω_H in which oxygen and nutrients are sufficient for survival but not for proliferation, and a necrotic region Ω_N in which oxygen and nutrients are insufficient for survival. The non-dimensionalized tumor growth velocity is implemented via a generalized Darcy's law in equation 3.17 (137).

$$\boldsymbol{v}_C = -\mu \nabla P + \chi_E \nabla E \tag{3.17}$$

In equation 3.17, μ is cell-mobility representing the net effects of cell-cell and cell-matrix adhesion, P is oncotic pressure, χ_E is haptotaxis, and E is extra-cellular matrix (ECM) density. Definitions for χ_E and E are in (137). By assuming that the cell density is constant in the proliferating region, the overall tumor growth can be associated with the rate of volume change in equation 3.18.

$$\nabla \cdot \boldsymbol{v}_C = \lambda_P \tag{3.18}$$

In equation 3.18, λ_P is the non-dimensional net proliferation rate as further detailed below.

The angiogenesis component of the model simulates the lesion by (138) and is based on previous work (136, 139). As a tumor grows in the dynamic, vascularized tissue

environment, tumor cells have varying access to molecules diffusing from the vasculature, depending on the tissue pressure and the distance from the nearest blood vessels.

The diffusive transport of oxygen σ through tumor tissue is simulated from the extravasation location of molecules from the tumor blood vessels. Oxygen is supplied from the neo- and pre-existing vessels with extravasation rates $\lambda_{ev}{}^{\sigma} = \lambda_{neo}{}^{\sigma}$ and $\lambda_{ev}{}^{\sigma} = \lambda_{pre}{}^{\sigma}$, respectively, diffuses with a diffusion coefficient D_{σ}, is taken up by both normal cells (with a rate $\lambda_{tissue}{}^{\sigma}$) and tumor cells ($\lambda_{tumor}{}^{\sigma}$ in the proliferating region and q_s in the hypoxic region), and decays (with a rate $\lambda_N{}^{\sigma}$) in the necrotic region. Oxygen is consumed in tumor tissue (with a rate λ_P) depending on the tumor region. Assuming steady-state conditions, the formulation is in equation 3.19 and 3.20, which was derived based on previous reports (133, 135, 137).

$$0 = \nabla \cdot (D_{\sigma} \nabla \sigma) + \lambda_{ev}^{\sigma}(\boldsymbol{x}, t, \mathbf{1}_{vessel}, p_i, \sigma, h) - \lambda^{\sigma}(\sigma)\sigma \tag{3.19}$$

$$\lambda_P = \begin{cases} \lambda_{tissue}^{\sigma} & \text{outside } \Omega \\ \lambda_{tumor}^{\sigma} & \text{in } \Omega_P \\ q_{\sigma}(\sigma) & \text{in } \Omega_H \\ \lambda_N^{\sigma} & \text{in } \Omega_N \end{cases} \tag{3.20}$$

In equation 3.19, $\mathbf{x}$ is position in space, t is time, $\mathbf{1}_{vessel}$ is the characteristic function for the vessels (equals 1 at vessel locations and 0 otherwise), p_i is the interstitial pressure, and h is the hematocrit in the vessel network which is related to oxygen extravasation (following reference (137)). The extravasation of oxygen is modulated by the extravascular interstitial pressure p_i scaled by the effective pressure p_e, with k_{pi} being the weight of the convective transport component of molecules (133). This process is described in equation 3.21.

$$\lambda_{ev}^{\sigma} = \bar{\lambda}_{ev}^{\sigma}\mathbf{1}_{vessel}(\mathbf{x}, \mathrm{t})\left(\frac{h}{\bar{H}_D} - \bar{h}_{min}\right) + \left(1 - k_{p_i}\frac{p_i}{p_e}\right)(1-\sigma) \quad (3.21)$$

In equation 3.21, the constants $\bar{H}_D$ and $\bar{h}_{min}$ represent the normal and minimum blood hematocrit levels required for oxygen extravasation, respectively, and $\bar{\lambda}_{ev}^{\sigma}$ is the constant transfer rate from both pre-existing and tumor-induced blood vessels. The oxygen transport parameters are calibrated so that the growth rate of an avascular spheroid matches the experimentally observed rates (134).

The acidity of the tumor microenvironment is modeled as a first order approximation that is proportional to the release of tumor angiogenic factors (TAF) from hypoxic cells within the tumor. The maximum TAF value represents a pH of 5, and the absence of TAF represents physiological conditions (pH 7.4). TAFs are produced by hypoxic tumor cells at rate $\bar{\lambda}_{prod}$, diffuse into the tissue with a constant diffusion coefficient D_T, are taken up by endothelial cells with a rate $\bar{\lambda}_{binding}^{T}$, and decay exponentially with a rate $\bar{\lambda}_{decay}^{T}$ [33]. This process is described in equation 3.22.

$$0 = \nabla \cdot (D_T \nabla T) + \bar{\lambda}_{prod}^{T}(1-T)\mathbf{1}_{\Omega_H} + \bar{\lambda}_{decay}^{T}T$$
$$-\bar{\lambda}_{binding}^{T}\mathbf{1}_{vessel} \quad (3.22)$$

The transport of PNAs *s* through tumor tissue, like oxygen, is also simulated from the location of extravasation from the vessels. PNAs are simulated to be injected systemically, flowing from the lower left to upper right of the vascularized tumor system. PNAs are taken up both by both normal and tumor cells with a rate $\bar{\lambda}_{uptake}^{s}$. The formulation is described in equation 3.23.

$$0 = \nabla \cdot (D_s \nabla \mathrm{s}) + \lambda_{ev}^{s}(\boldsymbol{x}, t, \mathbf{1}_{vessel}, p_i, s) - \bar{\lambda}_{uptake}^{s} \quad (3.22)$$

Assuming a constant transfer rate $\bar{\lambda}_{ev}^{s}$ from both pre-existing and tumor-induced vessels, the PNA extravasation is described in equation 3.23.

$$\lambda_{ev}^{s} = \bar{\lambda}_{ev}^{s}\mathbf{1}_{vessel}(\mathrm{x,t})(1 - k_{p_i}\frac{p_i}{p_e})(\frac{C_t^s}{\bar{C}^s} - \mathrm{s}) \qquad (3.23)$$

In this equation, the diffusion in tumor tissue is assumed to be modulated by the interstitial pressure (133). The diffusivity is assumed to be similar to previous diffusion measurements for nanoparticles (140).The initial PNA concentration in the vasculature is $\bar{C}^s$, with an extravasation described in equation 3.24.

$$C_t^s = \bar{C}^s e^{-t/\tau} \qquad (3.24)$$

Equation 3.24 assumes first order kinetics, i.e., the extravasation is concentration dependent. The PNA half-life (dependent on τ) is assumed to be proportional to the clearance rate of drug released from them, as previously measured (134).

The model parameters associated with oxygen uptake and transfer rates were determined from the literature (141). In addition, the diffusivity, mass transfer rate and clearance of PNAs were estimated based on previous experiments (123, 142). The tumor proliferation rate, necrosis threshold and hypoxia threshold were calibrated based on growth profiles of liver MCRC tumors.

3.2.11 Statistics

All values in figures are reported as mean±standard deviation for three measurements unless otherwise noted. Groups of multiple measurements were compared by one-way ANOVA with Bonferroni's post-test correction, while pairs of measurements were compared by Student's t test unless described otherwise. Statistical significance in figures and tables is represented with * ($p<0.05$), ** ($p<0.01$) or *** ($p<0.001$).

3.3 Results

3.3.1 Fluorochromism Does Not Affect the Physicochemical Properties of PNAs

The synthesis and characterization of 2PN and 3PN was described in chapter 2. Proton NMR indicated attachment of PEG (3.51 ppm, s, relative area 1.000), PAL (0.83 ppm, d, relative area 0.002; 1.23 ppm, s, relative area 0.027; 1.46 ppm, s, relative area 0.009) and AA (1.78 ppm, s, relative area 0.024) to PLL (2.23 ppm, m, relative area 0.0013; 2.60 ppm, s, relative area 0.0005; 2.68 ppm, s, relative area 0.0008; 2.97 ppm, s, relative area 0.0009; 3.24 ppm, s, relative area 0.0114; 3.68 ppm, s, relative area 0.027; 4.09 ppm, s, relative area 0.040; 7.78 ppm, s, relative area 0.009). The size and chemical purity of 3P'A546 and 3P'IR820 were confirmed by GPC in Figure 3.4. 3P'A546 and 3P'IR820 had 1% molar substitution of Alexa Fluor® 546 and 5% molar substitution of IR820, respectively. Table 3.1 summarizes the diameters, surface charges and chemical properties of non-halo-fluorochromic PNAs. Figure 3.5 shows the fluorescence of 3P'IR820 at various pH values and with and without drug loading in order to confirm non-halo-fluorochromism. Changes in pH did not consistently alter the fluorescence of 3P'IR820, but the fluorescence of drug-loaded 3P'IR820 slightly decreased at pH 7.0 and 6.0 compared to pH 7.4. Drug loading increased the fluorescence of PNAs by about 30% compared to empty PNAs.

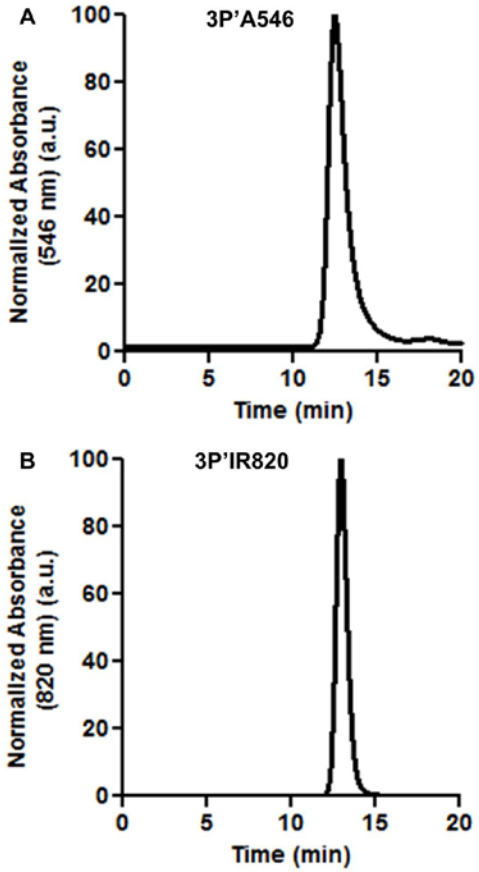

Figure 3.4. Gel permeation chromatographs of 3P'A546 (A) and 3P'IR820 (B). Chromatographs were measured by UV-visible absorbance detector at 546 nm (A) or 820 nm (B).

Table 3.1. Physicochemical properties of 3P'A546 and 3P'IR820. Characterization information for 2PN and 3PN are in Table 2.1 of Chapter 2.

PNA	Diameter (nm)	Zeta potential (mV)	Polydispersity Index (PDI) (unitless)
3P'A546	23.2±1.0**	-0.8±0.4	0.31±0.02
3P'IR820	18.8±0.3**	0.3±0.7	0.29±0.02
PNA	PEG Substitution (mol/mol primary amine on scaffold) (%)	PAL Substitution (mol/mol primary amine on scaffold) (%)	Dye Substitution (mol/mol primary amine on scaffold) (%)
3P'A546	24.0±0.6	37.0±0.9	1.0±0.1***
3P'IR820	24.0±0.6	37.0±0.9	5.0±0.1***

Diameter, zeta potential PDI and dye substitution are reported as mean±SD (n=3). PEG and PAL substitution are reported as measurement±SE for NMR measurement (n=1). Statistical significance is determined with a Student's t test as described in the methods section.

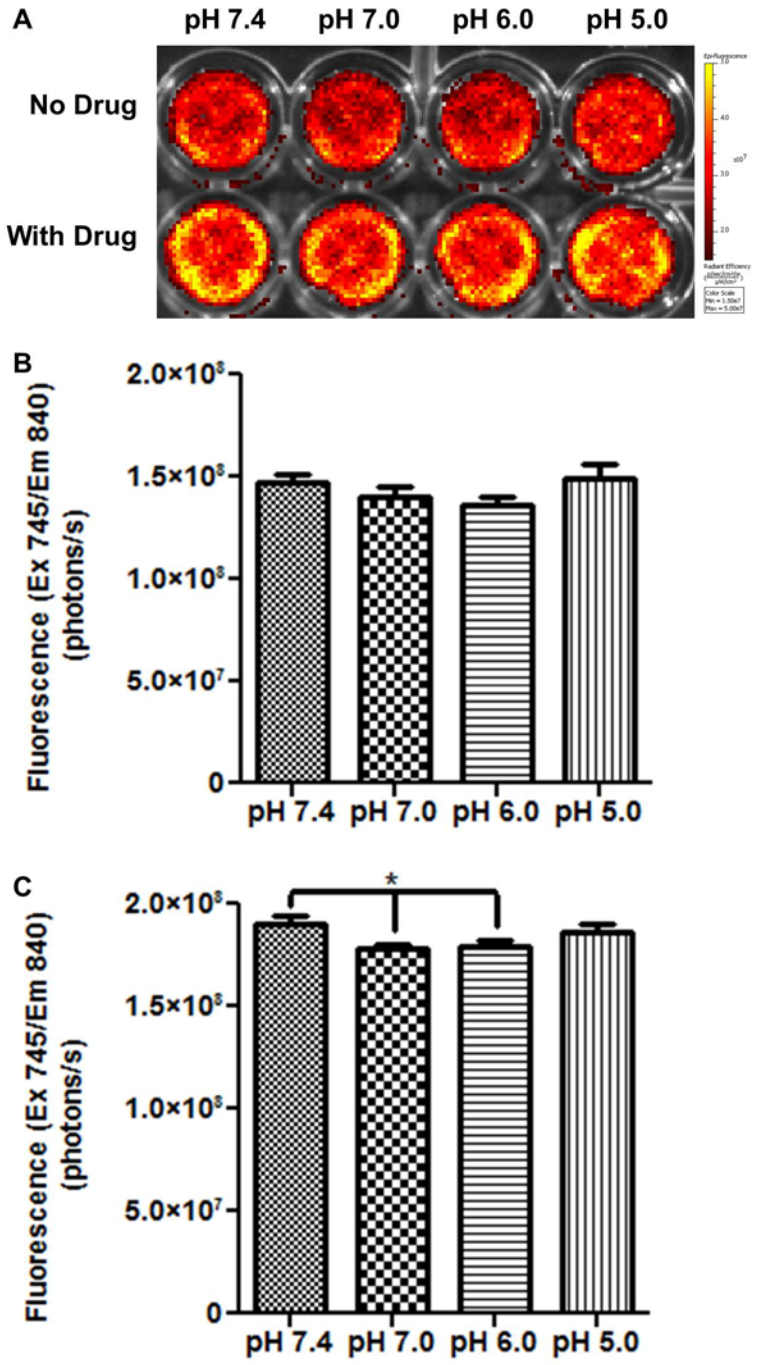

Figure 3.5. Fluorescence properties of 3P'IR820 measured by IVIS (A). The fluorescence of empty (B) and drug-loaded 3P'IR820 (C) were quantified from IVIS images.

3.3.2 PNAs Diffuse into Gels Mimicking Tissue Conditions and Fluoresce in Acidic Environments

Figure 3.6 describes the flux of 3P'IR820 into agarose gel tissue mimics with and without 120 mmHg additional external pressure. The calculated flux for PNAs in each gel density, pH, and pressure condition are located in Table 3.2. The flux of 3P'IR820 decreased by about 40 % in high density gels (1.0%) compared to low density gels (0.5%). Decreases in gel pH did not consistently affect the flux of PNAs, but the flux of PNAs was greater for pressurized 1% gels at pH 7.0 compared to pH 7.4 or 6.0. External pressure decreased the flux of 3P'IR820 slightly, possibly due to the compression of the gel disrupting pores near the top of the gel. To determine the effects of diffusion on the halo-fluorochromic imaging of PNAs, gels were treated with 3PN for 24 h. Figure 3.7 shows the fluorescence of halo-fluorochromic 3PN after diffusion into tissue mimics. Fluorescence images confirm PNA diffusion and distribution in the gel mimics. For each gel density, the fluorescence increased in order of pH 6.0>7.0>7.4. The fluorescence of PNAs in 0.5% gels was slightly greater than the fluorescence in 1.0% gels at varying pH values, except pH 6.0 where 3PN showed greater fluorescence in 1.0% gel than 0.5% gel. The fluorescence of halo-fluorochromic PNAs in 1.0% gel at pH 6.0 is greater than expected, based on fluorescence trends due to changes in pH and gel density. Imperfections on the surfaces of gel surfaces in the pH 6.0 gels with 1.0% gel density, perhaps due to air bubbles at the surface of the gels after solidification, may increase the observed fluorescence signal of PNAs in acidic gels, due to reflections of fluorescence signals during imaging amplifying signals. However, the exact mechanism of increased fluorescence at low pH and high gel density is unknown. Future studies are needed to

elucidate the effects of gel density and acidity on fluorescence signals of dyes diffused into agarose in gels. In addition, the halo-fluorochromism of PNAs appears to be greater in gels than in solution, as measured in chapter 2. Differences in the observed fluorescence behavior of 3PN may be due to the exclusion of the pH 5.0 measurement, which had much greater fluorescence than the other pH values in solution. As a result, the fluorescence of 3PN in gels can more accurately elucidate subtle differences in fluorescence signals due to increased acidity.

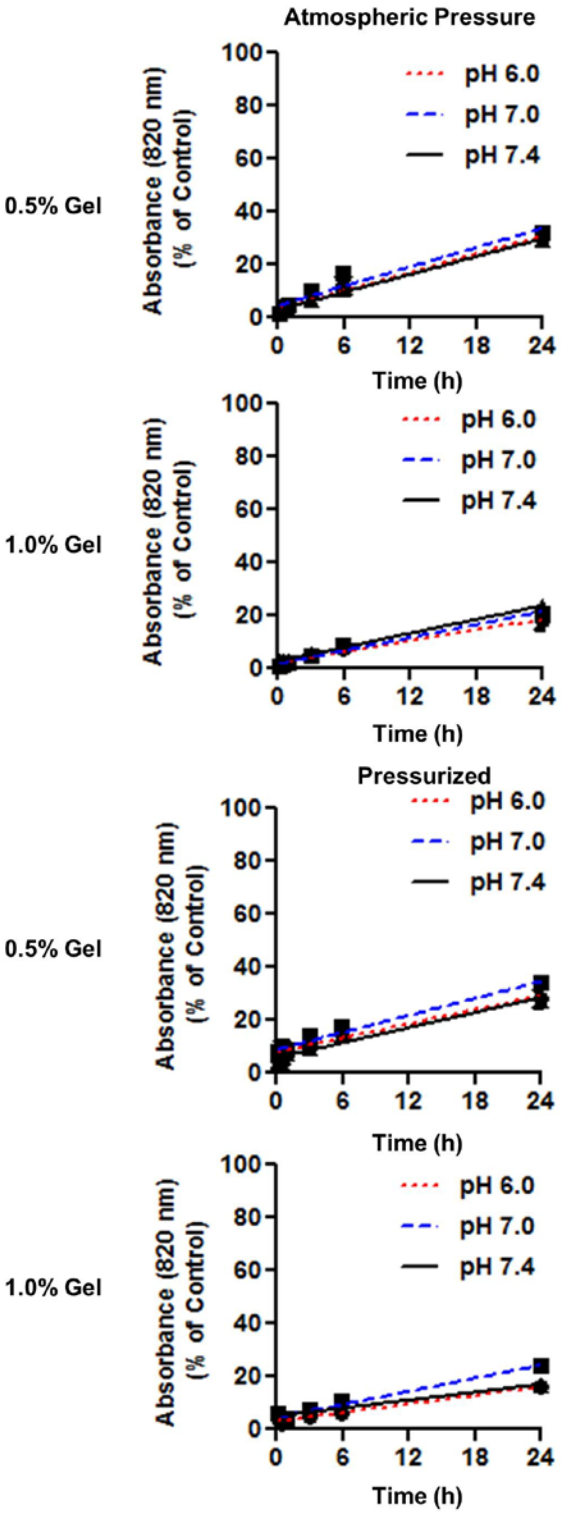

Figure 3.6. Diffusion of PNAs into gels mimicking tissue conditions. The pressurized condition is 120 mm Hg as described in the methods section.

Table 3.2. Calculated flux values for PNAs in gels with and without additional external pressure.

		Flux (kg/(s*cm^2))*10^{10}		
Additional Pressure (mm Hg)	Gel %***	pH 7.4	pH 7.0	pH 6.0
0	0.5	9.76 (9.01-10.47)	10.55 (9.05-12.06)	10.08 (9.01-11.15)
(Atmospheric)	1.0	7.63 (6.95-8.30)	7.12 (6.31-7.94)	5.97 (5.11-6.83)
Additional Pressure (mm Hg)	Gel %***	pH 7.4**	pH 7.0**	pH 6.0**
120	0.5	8.23 (7.05-9.41)	9.31 (8.36-10.25)	7.73 (6.14-9.32)
(Pressurized)	1.0	4.35 (3.45-5.24)	7.18 (6.27-8.09)	4.66 (3.81-5.51)

Flux values are reported as mean with 95% CI in parenthesis. Statistical significance is determined for gel density and pH at each pressure by two-way ANOVA with Bonferroni's post-test correction.

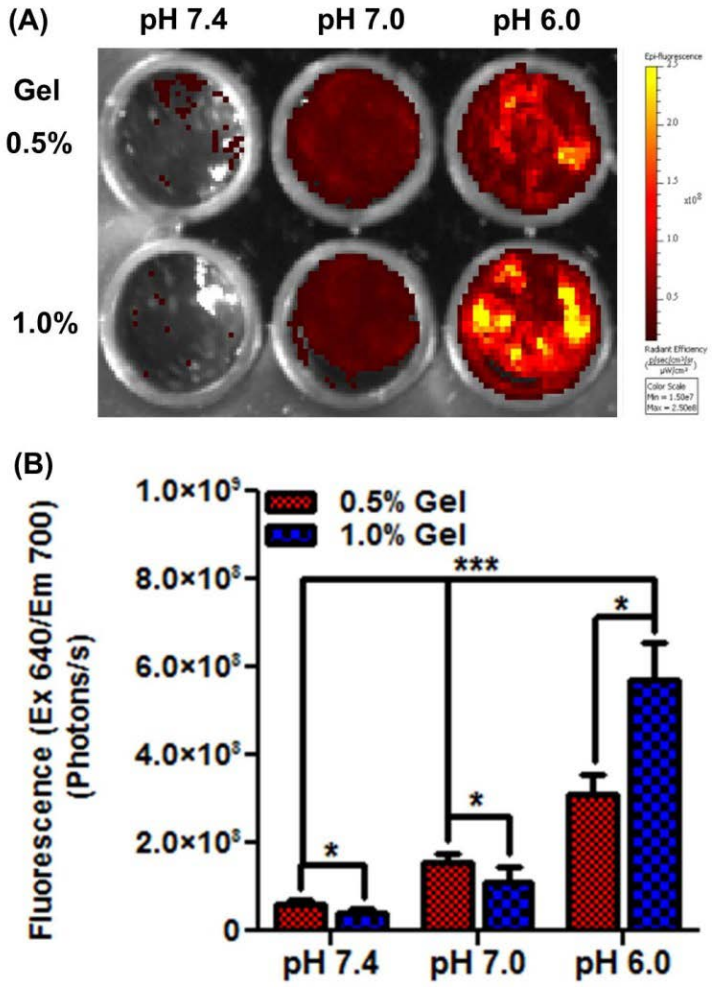

Figure 3.7. Fluorescence of 3PN that has diffused into gels for 24 hours (A). Fluorescence signal was quantified by IVIS (B).

3.3.3 Ionic and Serum-Containing Conditions Do Not Induce the Opsonization or Aggregation of PNAs

Figure 3.8A describes the changes in the absorbance of PNA solutions for up to 24 h in aggregating conditions. The absorbance of PNAs decreased after 1 hour but slightly increased up to 24 h in cationic, physiological and serum-containing conditions. However, the absorbance of PNAs in anionic solutions slightly decreased for 24 h after treatment. No precipitation was observed in the samples over 24 h. Because the absorbance of PNAs in solution was below 0.3 for all time points (black dotted line), PNAs did not aggregate. Figure 3.8B shows the diameters of PNAs in aggregating conditions after 24 h. Changes in PNA diameters are not statistically significant. These results confirm that PNAs do not significantly opsonize for up to 24 h in aggregating conditions.

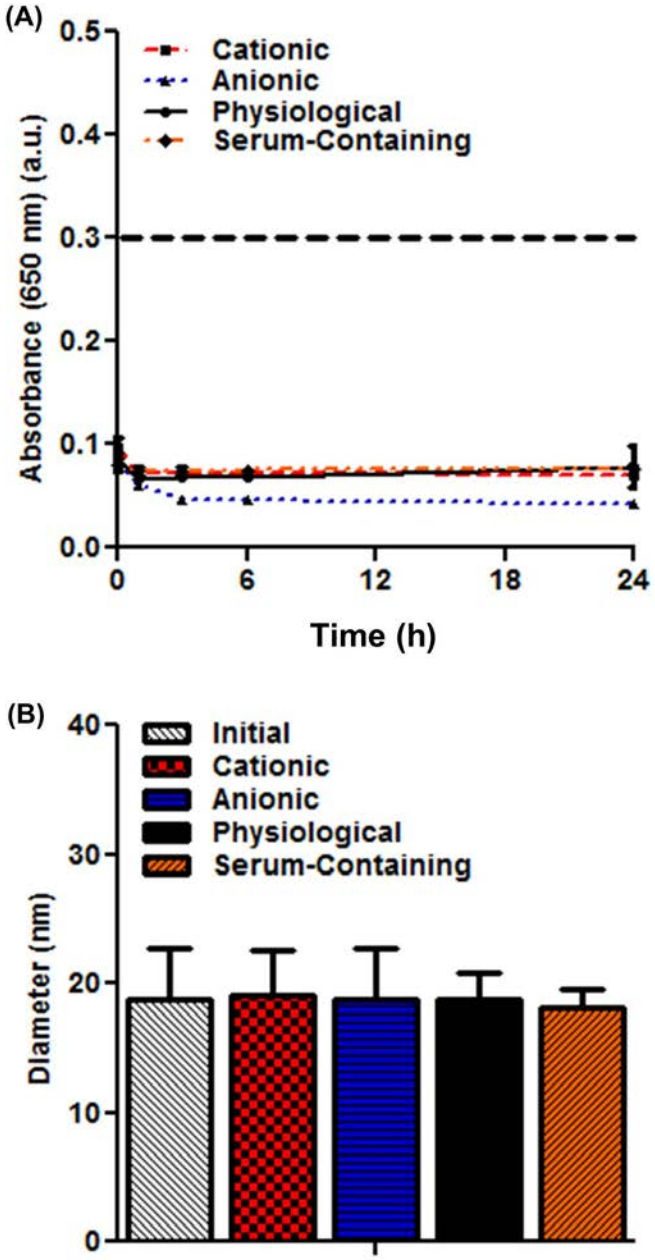

Figure 3.8. Absorbance (A) and diameter (B) changes of PNAs stored in aggregating conditions for 24 hours.

3.3.4 Most Nanoassemblies Remain in the Cell Media During In Vitro Cellular Uptake Measurements

Figures 3.9A-C describe the uptake of 2PN, 3PN and MG in HT29 cells from 0.5-6 h post-treatment. Uptake quotients of 2PN, 3PN and MG were calculated from fluorescence images (Table 3.3). Because uptake quotients (*Q*) are defined as the ratio of intracellular to extracellular PNA concentrations, a low *Q* value (<1) indicates a high concentration of PNAs in the extracellular space relative to cells, while a high *Q* value (>1) indicates a high concentration of PNAs in cells relative to the extracellular space. Low values of *Q* for PNA uptake up to 6 h post-treatment indicate that most PNAs remain in the cell media rather than accumulating inside of cancer cells. In contrast to PNA uptake quotients, MG uptake quotients increased up to 6 h post-treatment. The high values of MG uptake quotients suggest that MG accumulates inside of cancer cells. Figure 3.9D shows the changes in uptake quotient over time for 2PN, 3PN and MG. Time-dependent differences in uptake quotient for 2PN or 3PN were not statistically significant, but time-dependent differences for MG were significant. Treatment-dependent differences between uptake quotients of PNAs and MG are not statistically significant at 0.5 h post-treatment, but they were statistically significant between 1-6 h post-treatment. In addition, Figure 3.9E shows uptake quotients over time of 2PN and 3PN from 0 to 0.5 h post-treatment. Kinetic parameters from a mathematical model of nanoparticle uptake in Figure 3.8E are in Table 3.4. 3PN had a larger cellular partition coefficient (K_{EQ}) and a larger rate constant (*k*) than 2PN; however, both 2PN and 3PN had low cellular uptake quotients (*Q*) compared to small molecules. Cellular partition coefficients of 2PN and 3PN indicate that the intracellular concentrations of 2PN and

3PN are 25% and 40% of their extracellular concentrations, respectively. Small t_{95} values for both 2PN and 3PN suggest that PNAs are taken up in cells by active processes such as endocytosis, but that processes such as exocytosis may remove PNAs from the cytosol and maintain low cellular partition coefficients over time. Rheiner *et al.* previously confirmed that cellular uptake of PNAs was performed by endocytosis (76). All PNAs showed low cellular uptake under *in vitro* conditions based on concentration ratios. Based on estimations of molar ratios of PNA uptake accounting for intracellular volume, extracellular volume and measured cellular partition coefficients (K_{EQ}) of cells in chamber slides, molar ratios of PNA uptake in cells on chamber slides were less than 0.01. A further analysis of PNA uptake in metastatic tumors or solid tumors is in the discussion section.

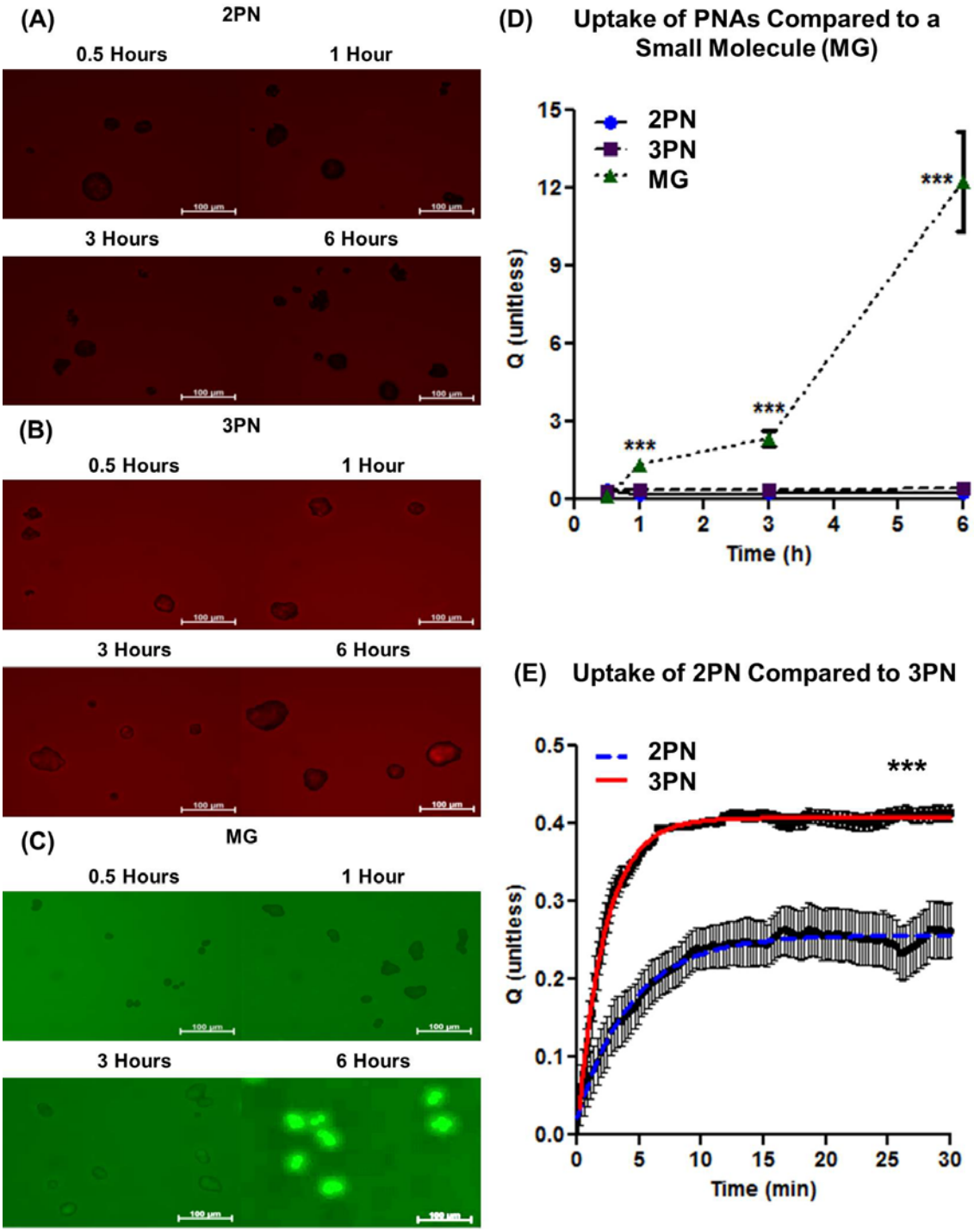

Figure 3.9. Microscopic fluorescence imaging of 2PN (A), 3PN (B) and MG (C) uptake into HT29 cells. Uptake of PNAs and MG were compared up to 6 h of treatment (D). Uptake of 2PN and 3PN was compared up to 0.5 h of treatment (E).

Table 3.3. Uptake quotients of cells treated with 2PN, 3PN and MG.

	Time (h)			
Treatment	0.5	1	3	6
2PN	0.37±0.11	0.22±0.12	0.26±0.10	0.27±0.08
3PN	0.33±0.10	0.39±0.11	0.38±0.11	0.40±0.07
MG	0.11±0.12	1.33±0.14***	2.37±0.31***	12.26±1.92***

Uptake quotients are reported as mean±SD (n=3). Differences in uptake quotients between treatments at each timepoint were compared by a one-way ANOVA with Bonferroni's post-test correction. Statistical significance is reported as described in the methods section.

Table 3.4. Kinetic parameters of PNA uptake from a first order association model.

PNA	K_{EQ} (unitless)	k (min^{-1})	t_{95} (min)
2PN	0.26 (0.25-0.26)***	0.23 (0.20-0.25)***	13.2 (11.8-15.0)***
3PN	0.41 (0.40-0.41)***	0.46 (0.44-0.47)***	6.6 (6.4-6.8)***

Kinetic parameters are reported as mean with 95% CI in parentheses. Differences in kinetic parameters between each model were compared by an extra sum of squares F test. Statistical significance is reported as described in the methods section.

3.3.5 PNAs Accumulate Throughout Cancer Cells in Solid Tumors

Figure 3.10 shows fluorescence imaging of tumors, livers, spleens, kidneys and lungs from mice bearing PDX tumors. Weak fluorescence signals can be observed in PDX tumors at 1 hour post-injection, but the signal increases up to 24 hours post-injection. In contrast to PDX tumors, the fluorescence signals in normal organs are minimal. Figure 3.11A shows microscopic fluorescence imaging of PDX tumors from mice treated with 3P'A546. Weak fluorescence can be observed at 4 hours post-injection, but the fluorescence signal increases up to 24 hours post-injection. The fluorescence of PNAs is near the fluorescence of nuclei in all images, suggesting that PNAs accumulate in PDX tumor cells. Differences between the measured cellular uptake in Figures 3.9 and 3.11A may be due to biological differences between cancer cells and patient-derived tumor cells, extracellular PNA concentrations, exposure times or removal of extracellular PNA signal due to sample preparation. Figure 3.11B shows microscopic fluorescence imaging of PNAs and EpCAM antibodies, which indicates the colocalization of PNAs with cancer cells. The fluorescence of PNAs remains near the fluorescence of EpCAM, suggesting that PNAs accumulate in EpCAM-expressing CRC cells rather than other tumor-associated cells such as macrophages. Figure 3.11C show microscopic fluorescence imaging of PNAs and CD31 antibodies, which indicates the colocalization of PNAs and blood vessels in tumors. Fluorescence of PNAs does not colocalize with CD31 fluorescence, suggesting that PNAs diffuse out of blood vessels and enter the interstitium of tumors. Figure 3.12 shows digitally zoomed versions of the microscopic fluorescence images in Figure 3.11.

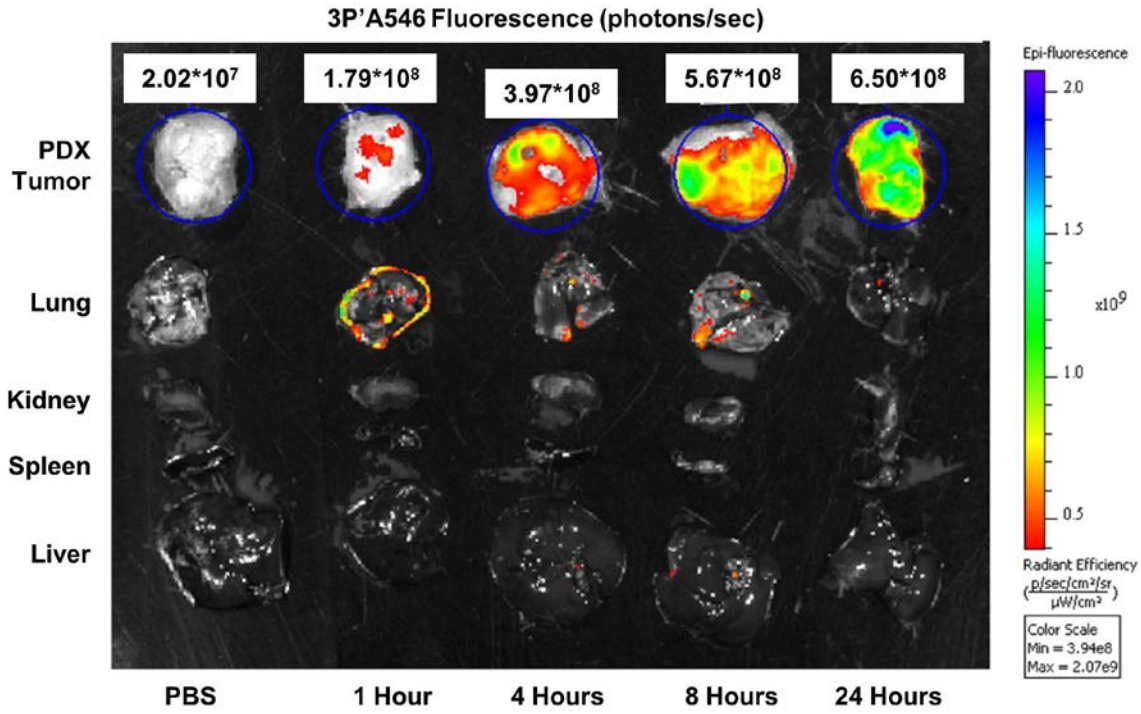

Figure 3.10. Macroscopic fluorescence imaging of PDX tumors and organs from mice treated with 3P'A546 (10 mg/kg).

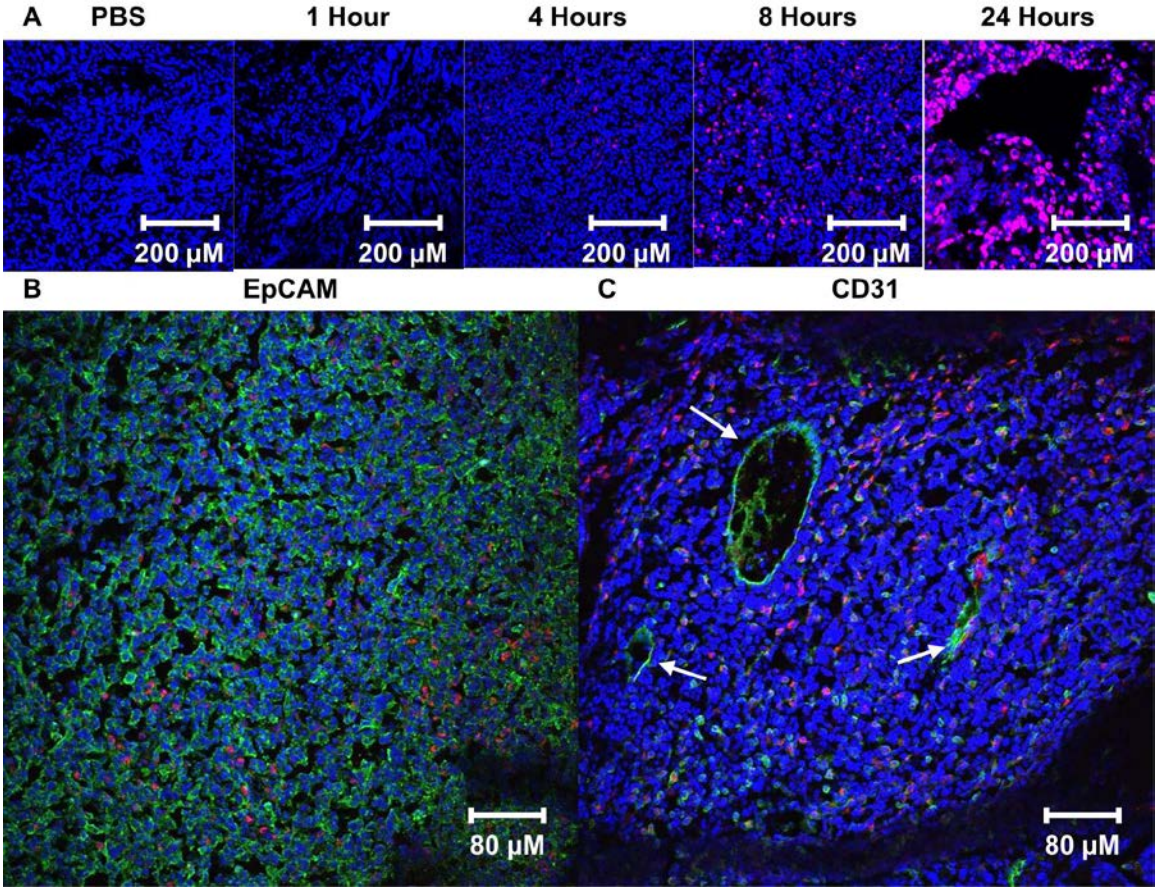

Figure 3.11. Microscopic fluorescence imaging (20x) of PNA uptake in PDX tumors over 24 hours (A). Fluorescence images at 8 hours were also taken with EpCAM (B) or CD31 (C) staining. In all images, blue is the cell nucleus, red is PNAs and green is EpCAM or CD31. The arrows in (C) indicate blood vessels.

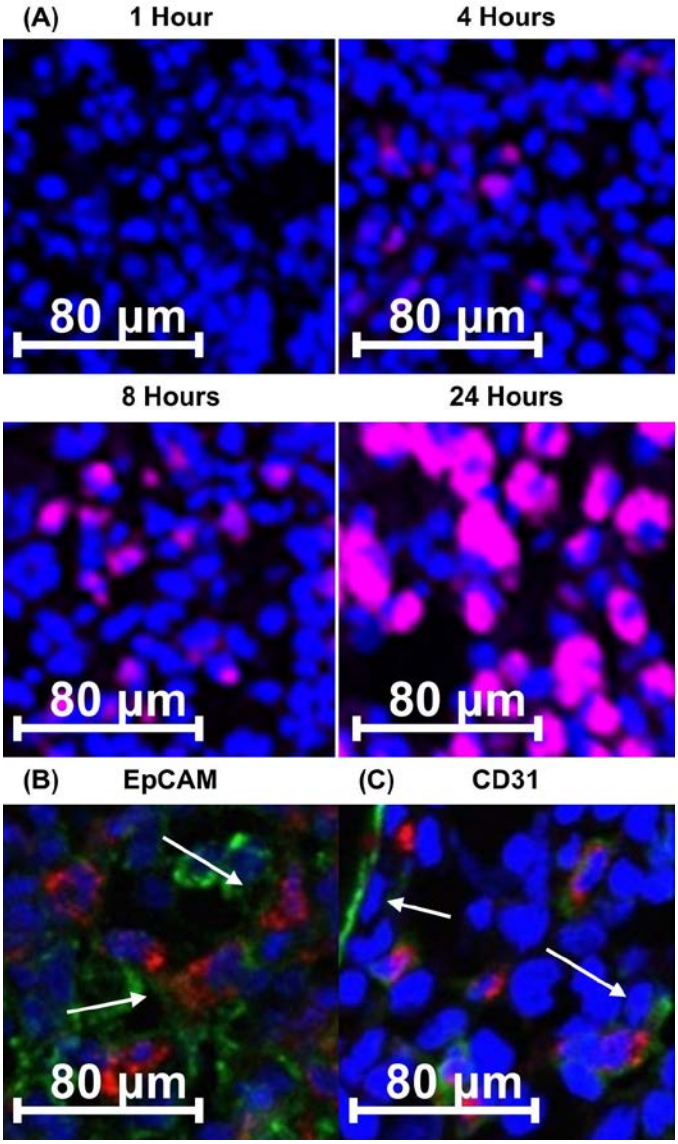

Figure 3.12. Digitally zoomed microscopic fluorescence imaging (80x) of PDX tumors. In all images, blue is the cell nucleus, red is PNAs and green is either EpCAM or CD31. The arrows in (B) and (C) indicate cancer cells and blood vessels, respectively.

3.3.6 Halo-Fluorochromic PNAs Enable the Detection of Liver Metastasis and the Reduction of Background Signals from Healthy Tissue

Figure 3.13 shows a fluorescence signal optimization of 3P'A546 in liver. The fluorescence of the liver increased with increasing doses of PNAs, but the fluorescence signal was not evenly distributed throughout the liver receiving the 20 mg/kg dose. Based on these measurements, a dose of 10 mg/kg was selected to maintain a consistent PNA concentration throughout liver tissue. Figure 3.14A shows the fluorescence of liver, kidney and lungs from mice bearing liver MCRC tumors that were treated with 3P'A546. The presence and location of metastatic tumors in the livers of these mice was confirmed by brightfield and GFP imaging of the liver. PNAs fluoresce throughout the liver, kidney and lungs. In addition, fluorescence is observed in both healthy tissue and MCRC tumors in the liver. Figure 3.14B shows the fluorescence of liver from either healthy mice or mice with liver MCRC tumors that were treated with halo-fluorochromic 3PN. The GFP signal in liver confirms that MCRC tumors were successfully established in mice. No fluorescence signal is observed in healthy mice treated with 3PN, suggesting that halo-fluorochromism of PNAs reduces fluorescence signals from PNAs in in healthy tissue. In mice bearing liver MCRC tumors, the halo-fluorochromic signal from 3PN colocalizes with GFP, but there are differences between the shapes of each signal. Figure 3.15 shows microscopic fluorescence images of the boundary between the healthy liver and metastatic tumors from mice treated with either PBS or 3P'A546. The fluorescence of 3P'A546 is stronger in liver tissue than in metastatic tumors. Figure 3.16 shows microscopic imaging of healthy liver and MCRC tumor tissues from mice treated with either PBS or 3P'A546. Hoechst staining indicates that nuclei are less dense in healthy

liver tissue compared to MCRC tumors. In addition, the nuclei in liver tissue are larger than the nuclei in metastatic tumors. CD31 staining indicates that the number of blood vessels per unit area is greater in liver tissue than in MCRC tumors, and that the distribution of blood vessels in the healthy liver is more homogeneous than in metastatic tumors. Differences in blood vessel density suggest that MCRC tumors are less perfused with blood than healthy liver tissue. Weak fluorescence signal corresponding to 3P'A546 throughout liver tissue suggests that PNAs accumulate throughout liver tissue. Figure 3.17 shows digitally zoomed microscopic imaging of PNAs in healthy liver and liver MCRC tumors. Although most PNAs are evenly distributed throughout tissue samples, some PNAs fluoresce in small circles near outside edges of CD31 fluorescence. The exact cause of these spots is unknown. It should be noted that these small circles are difficult to observe in large microscopic images and do not significantly contribute to overall fluorescence signals in liver tissue. In addition, weak fluorescence of 3P'A546 is observed in the space near blood vessels surrounding colonies of cancer cells in metastatic tumors, but the fluorescence signal decreases near center of metastatic cancer cell colonies. The fluorescence signal of 3P'A546 in microscopic images is weaker than the fluorescence signal from macroscopic images, suggesting that the fixing and staining methods used to prepare tissue samples may extract extracellular PNAs from tissue samples and decrease fluorescence signals.

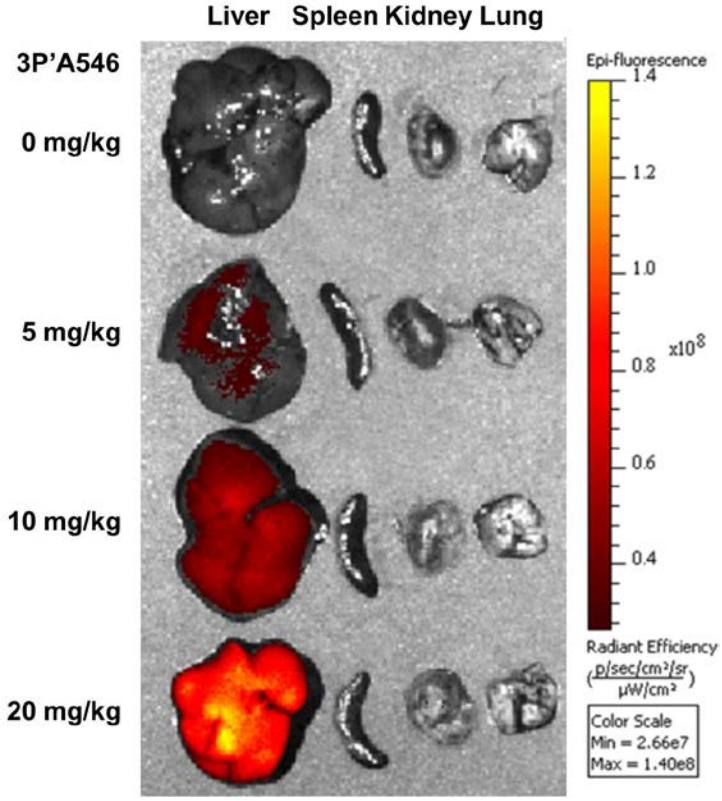

Figure 3.13. Macroscopic fluorescence imaging of liver, spleen, kidney and lung from mice treated with 3P'A546 at various doses.

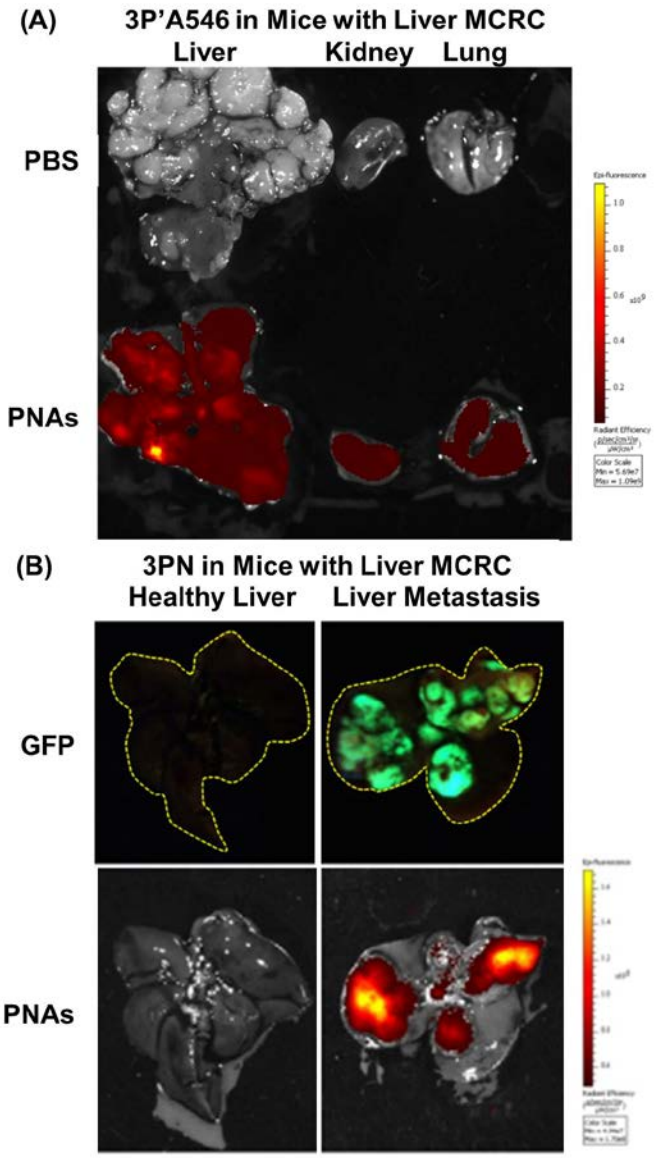

Figure 3.14. Macroscopic fluorescence imaging of non-halo-fluorochromic and halo-fluorochromic PNAs (10 mg/kg for each) in healthy liver and liver metastatic tumors. Fluorescence images of liver, kidney and lung tissue from mice bearing orthotopic liver MCRC tumors treated with 3P'A546 (A). Fluorescence imaging of liver from healthy mice or mice bearing orthotopic liver MCRC tumors treated with 3PN (B).

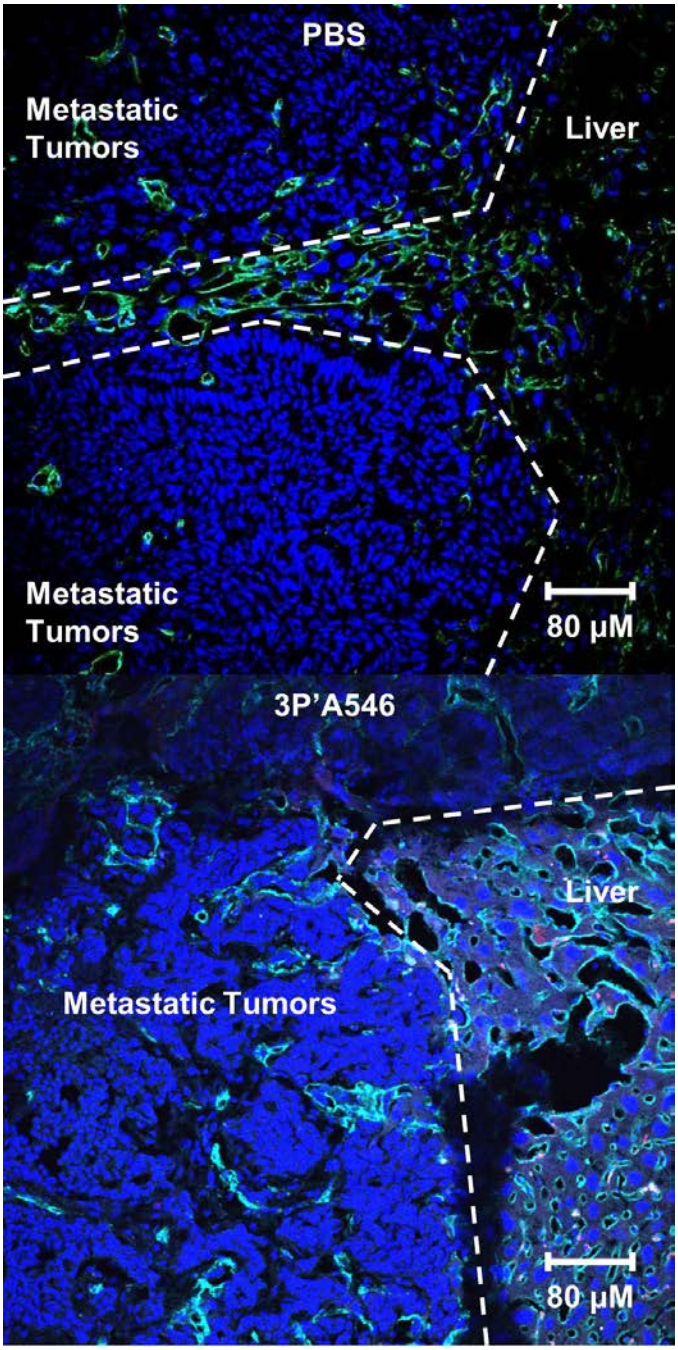

Figure 3.15. Microscopic fluorescence imaging (20x) of 3P'A546 at the boundary of healthy liver and metastatic tumors (10 mg/kg). In all images, blue is the cell nucleus, red is PNAs and green is CD31.

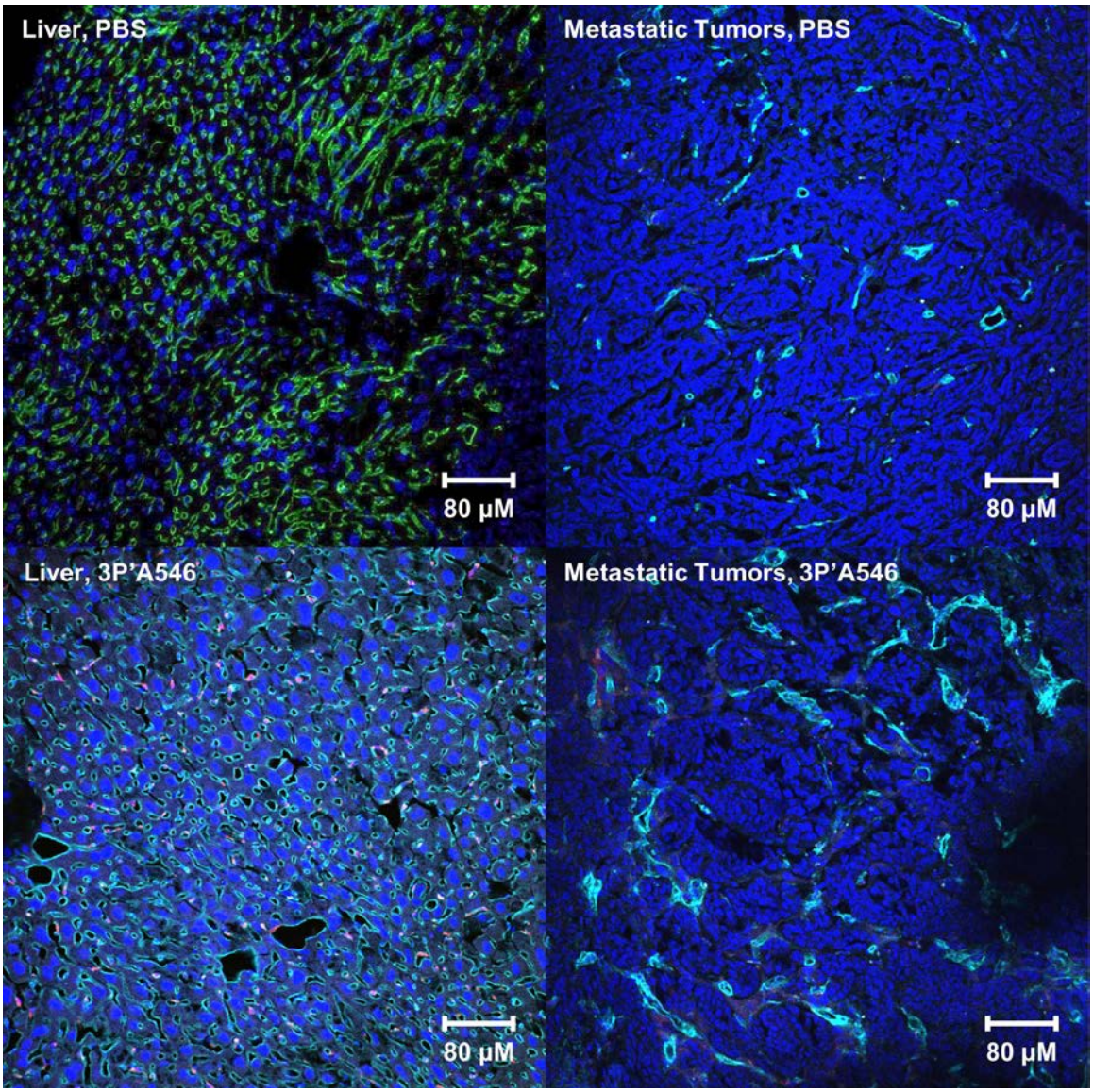

Figure 3.16. Microscopic fluorescence imaging (20x) of 3P'A546 in healthy liver or metastatic tumors (10 mg/kg). In all images, blue is the cell nucleus, red is PNAs and green is CD31.

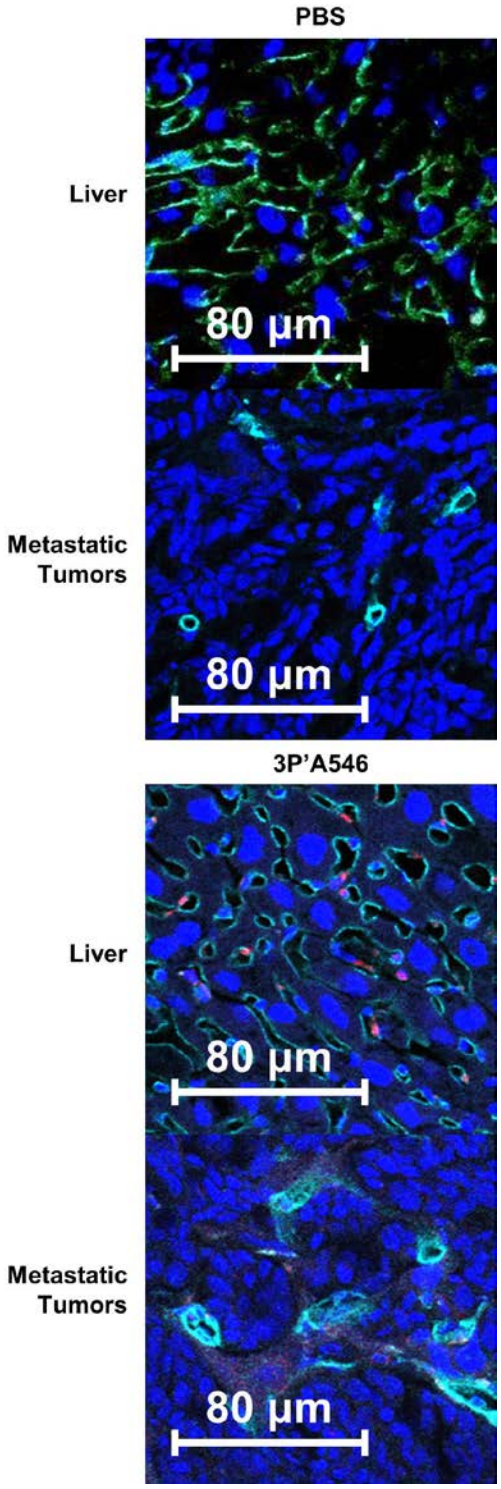

Figure 3.17. Digitally zoomed microscopic fluorescence imaging of healthy liver and metastatic tumors. Blue corresponds to nucleus, green corresponds to CD31 and red corresponds to 3P'A546.

3.3.7 Computational Simulations of PNA Accumulation in Metastatic Tumors

Figure 3.18 shows the distribution and accumulation of PNAs in metastatic CRC tumors after systemic, intravenous bolus injection simulated by Frieboes *et al.* for low, medium and high tissue vascularization densities. Physical parameters for PNAs and biological parameters for tumors are in Table 3.5. The computational model is based on previous results (122), and it builds on computational modeling of a reaction-diffusion-controlled reactor simulating a metastatic tumor (123, 124, 132). PNA concentrations in the blood, indicated by the tumor blood vessels, decrease over time as PNAs are cleared from the plasma. Most PNAs remain in the extracellular matrix surrounding the lesion and the tumor tissue adjacent to it. As the vascular density increases, the PNAs accumulate at higher concentrations in the periphery of the metastatic tumors. The figure also indicates that PNA accumulation near the metastatic tumors is projected to decline to about half of its initial value 12 h post-treatment. In order to quantify PNA accumulation in various regions of the metastatic lesion, the uptake profiles of PNAs were also simulated.

Table 3.5. Parameters for the computational model of PNA distribution in metastatic tumors.

Parameter	Value	Reference
CRC Tumor proliferation rate	1 day^{-1}	Measured (134)
CRC in liver tumor necrosis threshold	0.515	Calibrated
CRC in liver tumor hypoxic threshold	0.575	Calibrated
Oxygen diffusivity	1 (*)	(136)
Oxygen transfer rate from vasculature	5 (*)	(136)
Oxygen uptake rate by proliferating tumor cells	1.5 (*)	(136)
Oxygen uptake rate by hypoxic tumor cells	1.3 (*)	(136)
Oxygen uptake rate by tumor microenvironment	0.12 (*)	(136)
Oxygen decay rate	0.35 (*)	(136)
PNA diffusivity	0.3 (*)	Estimated (140)
PNA transfer rate from vasculature	5 (*)	Estimated (140)
PNA uptake rate by tumor cells	1.5 (*)	Estimated (140)
PNA plasma clearance half life	14.4 h	Estimated (142)

The parameters denoted with (*) were rescaled by the characteristic length (1 cm), the characteristic time (1 s) or oxygen diffusivity ($1*10^{-5}$ cm^2/s) as described in previous work (143).

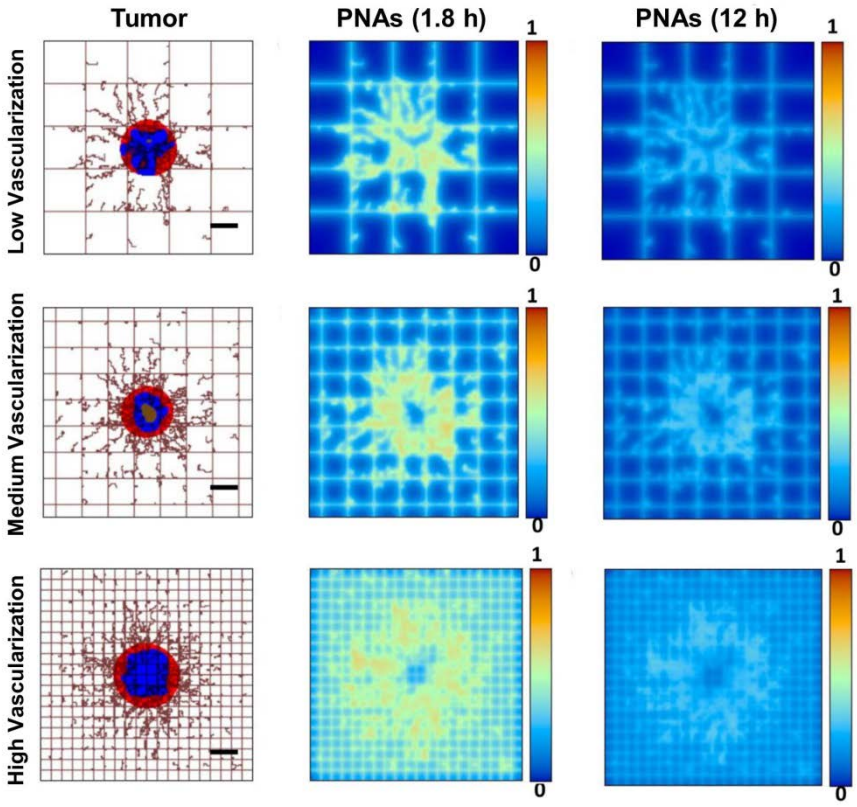

Figure 3.18. Computational simulations of PNA distribution in metastatic tumors. Images on the left represent metastatic tumors with tumor vessels (brown), proliferating (red), hypoxic (blue) and necrotic region (brown). Images in center and right represent PNA distribution in the tumors on the left of each row.

Figure 3.19 describes PNA accumulation based on vasculature surface area (μm^2, based on vessel length x circumference) for up to 60 h following treatment. One day (24 h) after treatment, the total PNA concentration has decreased by 75%, 80%, and 90% for the low, medium and high vascularization cases compared to the initial total PNA concentration, which reflects increasing PNA washout with a higher number of blood vessels. The total PNA concentration has the largest peak for the case of medium vascularization (0.20), while the peak concentration is reached in the hypoxic tissue for the high vascularization case (0.057). Figure 3.20 quantifies the simulated PNA accumulation per vasculature surface area at 1.8 and 12 h post-treatment as a function of the degree of vascularization and the tumor region (proliferating, hypoxic, necrotic, and blood vessels). At 1.8 h post-treatment, the PNA concentration is 10x, 7.8x, and 7.5x higher in the proliferating regions than in the hypoxic regions for the low, medium, and high vascularization conditions, respectively. By 12 h, these concentrations become more comparable (1.8x, 2x, and 1.2x, respectively), with PNA accumulation decreasing by 75% in the proliferating regions, by 50% in the tumor blood vessels, while also increasing by 100% in the hypoxic tissue regardless of vascular density. In all cases, the accumulation of PNAs in the necrotic regions of tumors is negligible. These computational modeling results suggest that although a higher number of PNAs is projected to be initially taken up by the proliferating regions, accumulation in the hypoxic (and more acidic) tissue of the lesion is expected to increase and remain steady for several hours. Further, this accumulation is projected to be mostly independent of the degree of vascularization of the tissue surrounding the lesion.

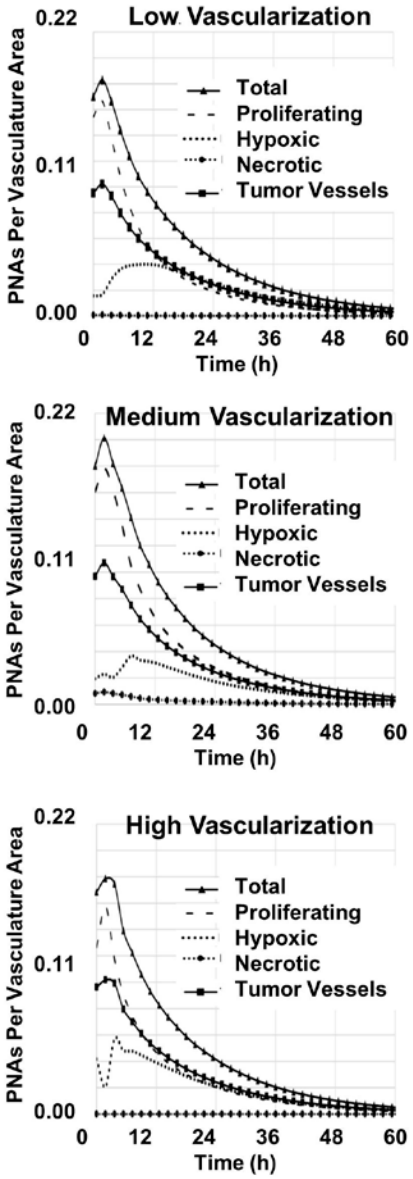

Figure 3.19. Distribution-time profiles of PNAs in simulated metastatic tumors with low, medium and high vascularization.

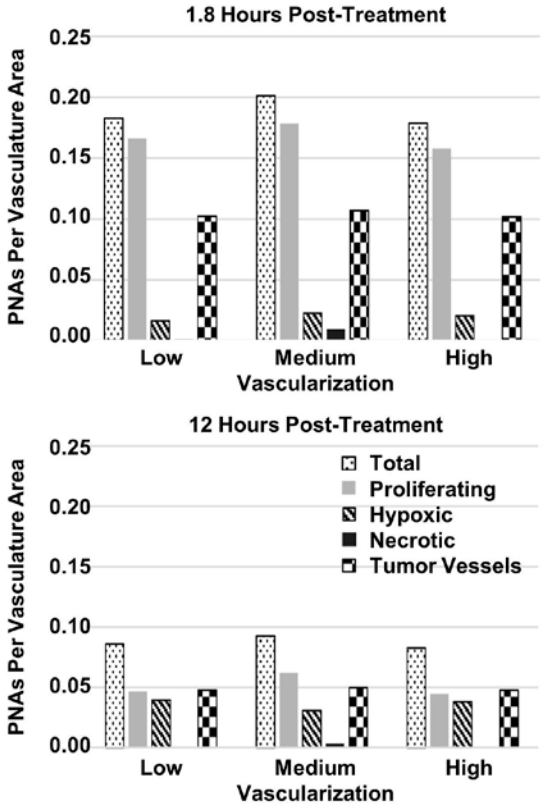

Figure 3.20. Distribution Profiles of PNAs in simulated metastatic tumors at 1.8 and 12 hours post-treatment.

3.4 Discussion

3.4.1 PNAs Sustain Fluorescent Dye Concentrations in Tumors

The successful treatment of CRC depends on the effective detection of small MCRC tumors. Traditional CRC detection methods cannot identify small MCRC tumors that rarely affect the structure and morphology of the surrounding tissues (144). As a result, MCRC tumors cannot be easily detected until they become too large to effectively treat with chemotherapy due to acquired drug resistance (145). Fluorescent dyes are often used to identify small tumors by visualizing cancer cells, but their clinical applications have been limited by low signal-to-noise ratios and short half-lives *in vivo* (146). In order to overcome these limitations, small molecule fluorescent dyes are often entrapped in nanoparticles. In previous studies, nanoparticles entrapping fluorescent dyes increased the strength and duration of fluorescence signals from solid tumors, which allowed for the fluorescence imaging-guided detection of tumors (46).

Despite their benefits for fluorescence imaging, fluorescent nanoparticles can hinder the detection of metastatic tumors by increasing background signals in healthy organs, such as the liver, lung, spleen, or kidney (147, 148). In order to reduce background fluorescence signals and identify MCRC tumors more accurately and earlier in their development, PNAs entrapping halo-fluorochromic dyes were developed. Although halo-fluorochromic PNAs detected liver MCRC tumors in preliminary studies, their fluorescence signals did not perfectly correspond to liver MCRC tumors. Halo-fluorochromic PNAs could emit fluorescence only in some sections of acidic tumor tissue, due to the altered distribution patterns of PNAs in MCRC tumors compared to the liver (149). Therefore, it was hypothesized that halo-fluorochromic PNAs accumulate in

the acidic interstitium between MCRC tumors and healthy liver tissue. To test this hypothesis, the effects of physical and biological factors related to MCRC tumor detection, such as tissue diffusion, cell interactions, and opsonization, were elucidated. The effects of these factors were observed in fluorescence images of PNA distribution in solid tumors, healthy liver tissue and liver MCRC tumors. In addition, fluorescence images were compared to computational simulations of PNAs in metastatic lesions.

3.4.2 Physicochemical Properties of PNAs Predict Their In Vivo Distribution Profiles

Although PNAs accumulated throughout liver tissue with MCRC tumors, the diffusion rate of PNAs into tissue was difficult to measure accurately due to fluctuations in tissue density, interstitial space volume, and tissue pH. To accurately measure tissue diffusion rates for PNAs, agarose gel tissue mimics with controllable mass transport properties such as density and pH were prepared. As described in the methods section, the gel densities in this study mimic the extracellular space between healthy cells (0.5% w/v) and the keratin mesh surrounding tumors (1.0% w/v). In addition, the pH of gels was selected to mimic healthy tissue (pH 7.4) and acidic tumor tissue (pH 7.0 and 6.0). These gels simulate a variety of conditions representative of healthy and tumor tissues. Mass transport properties of agarose gels have been well studied for physical separation methods such as electrophoresis and gel blotting. Unlike ionizable molecules that alter their diffusion rates into agarose gels as a function of pH, PNAs lacking surface charge had consistent flux into agarose gels between pH 7.4 and 6. Although there were small pH-dependent variations in flux, these variations did not represent an overall trend. High gel density reduced PNA flux by about 40% compared to low gel density. Although the pores in both gels are large enough (50 to 500 nm) for 30 nm PNAs to enter, smaller

pores may increase the interactions between pore walls and PNAs and slow long-range diffusion. Therefore, although gel pores should allow PNAs to freely diffuse into tissue mimics, the experimental data demonstrate a clear correlation between tissue density and PNA transport.

Despite these findings, it should be acknowledged that gel mimics have physical and chemical limitations in accurately reproducing tissue conditions. For example, gel mimics lack lipids and proteins that can affect pore structure and PNA interactions during diffusion (150). In addition, tumors have high interstitial tissue pressure due to disrupted lymphatic drainage that can further influence PNA transport into MCRC tumors (151). Previous studies show that high intratumoral pressure limits the diffusion of small molecules and nanoparticles into solid tumors (152, 153). A simple pressurized system was developed to attempt to investigate the effects of pressure on diffusion; however, because the system pressurized gels from all sides, rather than creating a pressure gradient through the gel, the system was unlikely to accurately mimic *in vivo* pressure conditions. In addition, this system did not account for blood flow, which can increase nanoparticle transport out of the blood vessels and into interstitial space surrounding tumors (154, 155). Regardless, pressurized conditions increased short-term entry of PNAs into tissue mimics (<0.5 h) but failed to further enhance PNA diffusion (> 0.5 h). This increase may be due to the deformation of gels near the surface increasing the entry of PNAs into the surface. Future work is needed to develop a robust system that accurately mimics the flow conditions in tumor vasculature and the pressure conditions in solid tumors in order to further investigate nanoparticle transport into gel mimics.

The diffusion of molecules into gel mimics is expected to follow Fick's second law of diffusion. Mathematically, this indicates that the concentration-time data should fit to an unsteady state first order diffusion equation with a constant concentration and a zero concentration boundary condition. The analytical solution of this equation indicates that concentration-distance profiles at each timepoint follow an error function distribution, and total mass-time profiles in gels would follow an exponential function. Preliminary diffusion experiments using the small molecule NB followed this expected behavior; however, mass-time plots from 3P'IR820 yielded linear equations with respect to time. As a result, the flux of PNAs into gels could be determined by the slope of a linear regression of the mass-time profiles. This unexpected result indicates that there are fundamental differences between small molecule and nanoparticle diffusion into gels, and that an unsteady state first order diffusion model may not be appropriate to model nanoparticle diffusion in gel mimics. Small molecules have small hydrodynamic diameters (< 1 nm) compared to PNAs (~30 nm), so small molecules can diffuse unimpeded through gel pores (50-500 nm) compared to small molecules (156). Interactions between PNAs and the walls of pores in tissue mimics may change their diffusion behavior from expected profiles (157). In addition, non-linearity of PNA absorbance due to the heterogeneous distribution of PNAs in gels could increase the absorbance of PNAs diffused into gels at later timepoints and artificially increase measured flux rates. Therefore, the physical properties of PNAs and other nanoparticles related to pore interactions should be carefully considered in addition to their diffusivity in solution in order to increase the *in vivo* diffusion of nanoparticles.

The opsonization and aggregation of nanoparticles can reduce their tumor accumulation, decrease their half-life in blood and increase the interactions between PNAs and immune cells (158, 159). PNAs showed negligible opsonization and aggregation *in vitro*, which indicates that the PEG shell shields dyes from macromolecules in solution and allows dyes to detect the tumor microenvironment. However, fluorescence imaging of halo-fluorochromic PNAs shows that the PEG shell does not prevent the diffusion of small acidic molecules into the PNA core allowing the detection of the acidic environment. Taken together, these results suggest that PNAs with minimal opsonization allow fluorescent dyes to remain in the blood and detect acidic tumors or tumor metastasis.

The accumulation of halo-fluorochromic PNAs in the cytosol or in the endosomes of cancer cells can prevent the detection of the acidic extracellular tumor microenvironment. *In vitro* cellular uptake measurements indicated that only a small fraction of PNAs by mole or mass entered cells, but these conditions had fewer cells and greater extracellular volume than solid tumors. The molar ratio of PNA uptake in cells of tumors at equilibrium is calculated following equation 3.25.

$$\frac{N_{int}^{EQ}}{N_{ext}^{EQ}} = K_{EQ} * \frac{V_{cell} * N_{cell} * \rho_{tumor} * V_{tumor}}{V_{ext} * V_{tumor}} \qquad (3.25)$$

In equation 3.25, K_{EQ} and V_{ext} are unitless, V_{cell} has units of cm^3 per cell, N_{cell} has units of cells per g of tumor tissue, ρ_{tumor} has units of g per cm^3, and V_{tumor} has units of cm^3. If the spatial properties of tumors are assumed to be independent of volume, then the results are independent of V_{tumor}. Experimental measurements by Park *et al.* indicated that solid xenograft tumors have a density (ρ_{tumor}) of 0.79 g/cm^3 (160). Solid tumors are often assumed to contain 10^9 cells per gram of tumor tissue (N_{cell}), but it should be noted that

this value has been challenged for some types of tumors (161). In addition, Vestvik *et al.* estimated the extracellular fluid volume ratio (V_{ext}) of human melanoma xenograft tumors to be between 7.1 to 27.1% based on the cell type (162). Table 3.6 contains calculated molar ratios of 2PN and 3PN uptake for solid tumors with the extracellular fluid volume ratios 7.1, 17.1 and 21.7%. After accounting for the decreased extracellular space and increased cell density in tumors, the estimated *in vivo* molar ratio of PNAs in cells is greater than the *in vitro* measured ratio. In order for this calculation to be valid, it is assumed that the biological factors affecting K_{EQ}, such as a constant surface area-to-volume ratio of cancer cells and the homogeneous distribution of PNAs in the interstitial fluid surrounding cancer cells, remain consistent from *in vitro* conditions to *in vivo* conditions. The decreased surface area-to-volume ratios of cancer cells and the heterogeneous distribution of PNAs in solid tumors may significantly reduce the measured equilibrium constant *in vivo*.

Table 3.6. Calculated molar ratios of PNA uptake using the spatial properties of solid tumors.

	Extracellular Fluid Volume Ratio (%)		
PNA	7.1	17.1	27.1
2PN	5,800 (5,600-6,000)	2,400 (2,300-2,500)	1,500 (1,400-1,600)
3PN	9,100 (8,900-9,300)	3,800 (3,700-3,900)	2,400 (2,300-2,500)

Calculated molar ratios are reported as mean with 95% CI in parentheses. The confidence intervals contain errors that were propagated from the equilibrium constant in equation 3.25. Because these values are calculated estimations and not measured values, they were not compared statistically.

The accumulation of halo-fluorochromic PNAs in acidic endosomes or lysosomes could interfere with the detection of the acidic tumor microenvironment. Fluorescence signals of halo-fluorochromic PNAs were not observed in healthy tissue, suggesting that fluorescence signals from PNAs in endosomes or lysosomes of healthy cells is not sufficient to detect halo-fluorochromic PNAs. Videos of live cell uptake of 3PN showed small circular spots traveling through cells, suggesting that some PNAs were present in endosomes. However, these endosomes quickly disappeared, suggesting that 3PN can escape endosomes and enter the cytosol. Fluorescence imaging of cells stained with lysosome-sensitive dyes indicated that PNAs with a hydrophobic core environment escaped endosomes and entered the cytosol (76). However, it should be noted that some PNAs (~10% of intracellular fluorescence) remained in endosomes, and the fluorescence of PNAs in endosomes or lysosomes may contribute to the overall fluorescence signals of halo-fluorochromic PNAs in tumors.

It is often assumed that nanoparticle uptake by cells depends on interactions between the nanoparticle shell and the surface of the cell membrane. Intracellular uptake of PNAs reached equilibrium within 0.5 h of initial treatment, but small molecules that diffuse through the cell membrane accumulate in cells up to 24 hours post-treatment. Surprisingly, hydrophobic core modifications slightly increased the uptake of PNAs despite the PEG shell, suggesting that the core of PNAs can weakly interact with the cell membrane through hydrophobic interactions and slightly increase cellular uptake.

Differences in cellular uptake mechanisms between samples can contribute to differences in uptake behavior. First, MG and PNAs had distinct cellular uptake profiles up to 6 hours post-treatment. Although PNAs remained outside of cells and quickly

reached equilibrium with the surrounding environment, MG continued to accumulate inside cells up to 6 h post-treatment. MG is a cell membrane-permeable dye that initially accumulates in mitochondria of cells due to mitochondrial membrane potential (163). Due to its lipophilicity at physiological pH, MG can enter cells by diffusion through the cell membrane. Because PNAs are large and contain a hydrophilic shell, they are unlikely to diffuse through the cell membrane. Previous studies indicate that PNAs enter cells through energetic processes such as endocytosis (76). However, differences in equilibrium constants and rate constants were observed between the uptake of 2PN and 3PN, which should contain similar hydrophilic shells due to PEG substitution. Differences between the diameters of 2PN (~25 nm) and 3PN (~35 nm) could slightly increase the uptake of 3PN compared to 2PN. In addition, increased adsorption of 3PN to the cellular membrane could contribute to increased apparent uptake. Simulated illumination methods such as the ApoTome were considered for more sensitive imaging of the cell membrane, but poor spatial resolution of cells imaged by these methods compared to confocal microscopy limited their application for cell membrane imaging (164). In future studies, confocal microscopy of single live cells treated with PNAs could elucidate the differences in spatial distribution between 2PN and 3PN and indicate if differences in cellular uptake are due to extracellular membrane accumulation or intracellular cytosol accumulation.

3.4.3 Computational Simulations of PNA Accumulation in Metastatic Tumors Overcome the Limitations of Microscopic Fluorescence Imaging

Clinicians typically use microscopic fluorescence images of patient tissues from biopsy samples to identify tumors and determine effective treatment regimens.

Macroscopic fluorescence imaging indicated that PNAs accumulate in PDX tumors and liver bearing MCRC tumors, but microscopic fluorescence images had decreased fluorescence compared to macroscopic images. Macroscopic fluorescence images of normal organs and tumors are taken immediately after collection, but microscopic images require significant sample preparation prior to imaging. For example, tissue samples in this study were washed, stained, treated and fixed to microscope slides prior to imaging. Tissue washing may extract water-soluble PNAs from the extracellular space and decrease fluorescence signals, but the cell membrane may prevent the extraction of PNAs from the cytosol (165). Therefore, microscopic fluorescence imaging may underestimate extracellular PNA concentrations in tissues. It should be noted that differences in detection method sensitivity could also contribute to changes in fluorescence signals between macroscopic and microscopic images. Specifically, increased sensitivity of the IVIS compared to the fluorescence microscope could increase fluorescence signals in macroscopic images compared to microscopic images. However, the fluorescence of NB-labelled PNAs was stronger under a fluorescence microscope than under an IVIS, and decreased concentrations of 3PN had to be used in cellular uptake experiments compared to the IVIS characterization experiments in chapter 2. In order to investigate changes in extracellular PNA concentrations following tissue sample preparation, computational simulations of metastatic tumors were used to predict PNA accumulation in these tumors.

Computational simulations of PNA distribution in metastatic tumors were used to quantitatively assess the potential for the early and accurate detection of tumor metastasis. These simulations indicate that PNAs are expected to readily accumulate near the perimeter and within tumor metastases. This accumulation is projected to remain

steady within hypoxic (more acidic) tumor regions. This is consistent with the experimental results showing that PNAs near the perimeter of tumors can increase fluorescence and help identify the acidic environment of metastatic tumors. In the simulation, the uptake rate of PNAs by cancer cells was assumed to be equal to the uptake rate of oxygen. This assumes the highest expected value for the uptake of nanoparticles without receptor-targeting ligands. Decreased uptake parameters of PNAs would increase extracellular concentrations of PNAs and increase the predicted accumulation of PNAs in the hypoxic and necrotic regions of metastatic lesions. In the future, the computational simulations could be improved by calculating uptake parameters for PNAs in proliferating, hypoxic or necrotic regions of metastatic tumors and determining the effects of extracellular pH, oxygen concentrations and angiogenesis on PNA uptake parameters.

3.4.4 Mechanism for the Halo-Fluorochromic Detection of Liver Metastatic Tumors

Determining a mechanism for the halo-fluorochromic detection of liver MCRC holds promise to improve the future detection of small MCRC tumor foci. The results from this study suggest that PNAs diffuse throughout healthy and tumor tissue, and that some PNAs remain outside of cancer cells. Macroscopic imaging implies that halo-fluorochromic PNAs accumulate in acidic MCRC tumor tissue and fluoresce in the interstitial space between liver cells and tumors. However, microscopic imaging showed only small amounts of PNAs accumulating in interstitial space, probably because PNAs outside of cells were extracted during sample preparation for microscopic imaging. Nevertheless, non-halo-fluorochromic PNAs accumulated throughout liver tissue and failed to identify MCRC tumors, while halo-fluorochromic PNAs fluoresce strongly in

acidic microenvironments and identify MCRC tumors. Although some PNAs are taken up by Kupffer cells in the liver, their influence on overall images would be relatively small. Future studies should focus on determining the minimum size of MCRC tumor foci that halo-fluorochromic PNAs can detect effectively.

3.5 Conclusions

Halo-fluorochromic PNAs were developed as a tool for the early and accurate detection of liver MCRC tumors by imaging the periphery of acidic tumor tissues while minimizing signals from liver stroma. PNAs entrapping halo-fluorochromic dyes showed low opsonization, cellular uptake, and tissue diffusion, which allowed PNAs to enter the extracellular space of the liver. Macroscopic and microscopic imaging of PDX tumors showed that PNAs accumulate throughout primary tumors. Non-halo-fluorochromic PNAs diffuse through the healthy liver and hinder the detection of liver MCRC tumors, but halo-fluorochromic PNAs emit fluorescence mainly near acidic tumors and reduce background fluorescence signals from healthy liver. Computational simulations were used to evaluate halo-fluorochromic PNA detection of small metastatic CRC tumors early in development that cannot be detected by traditional imaging methods. These results suggest that halo-fluorochromic PNAs may detect MCRC tumors more effectively than small molecule dyes or nanoparticles modified with traditional dyes.

CHAPTER FOUR

SOLVATO-FLUOROCHROMIC METHODS AS AN APPROACH TO OVERCOME THE LIMITATIONS OF CHROMATOGRAPHY-BASED METHODS FOR DIALYSIS-BASED DRUG RELEASE MEASUREMENTS

4 SOLVATO-FLUOROCHROMIC METHODS AS AN APPROACH TO OVERCOME THE LIMITATIONS OF CHROMATOGRAPHY-BASED METHODS FOR DIALYSIS-BASED DRUG RELEASE MEASUREMENTS

4.1 *Introduction*

PNAs can serve as nanoscale carriers delivering anticancer drugs to solid tumors, and they can increase drug accumulation in tumor cells by fine-tuning drug release rates within the interstitial and intercellular spaces of tumors (134, 142, 166-172). Drug release rates from PNAs have been controlled by modulating their polymer composition, particle stability, and chemical interactions with drug molecules (173-175). The antitumor activity of PNAs was expected to change as a function of their drug release rates (176-183). However, *in vivo* drug release rates from PNAs were difficult to predict from *in vitro* measurements because of complicated interactions between nanoassemblies and released drugs *in vitro* (184, 185).

Dialysis-based methods are often used to determine *in vitro* drug release rates for PNAs and other nanoparticle drug carriers (186-191). Under typical experimental conditions, drug-loaded nanoparticles are added into a dialysis cassette to release drugs over time, and released drugs diffuse through the dialysis membrane into a large volume of buffer solution (dialysis sink). Analytical methods such as HPLC or light spectroscopy are then used to quantify the drug remaining inside the dialysis solution and predict drug release patterns. However, these analytical methods cannot distinguish between released drugs from the nanoparticle carrier and entrapped drugs within the dialysis cassette. To address this issue, investigators have modified traditional dialysis methods for measuring nanoparticle drug release to use tangential flow, ultrafiltration, electrodialysis, surfactants

or organic solvents. These modifications attempt to either facilitate released drug diffusion through the dialysis membrane into the dialysis sink or to sequester released drugs within the dialysis cassette and improve sink conditions (192-198). In addition, computational modeling has corrected for *in vitro* interactions between PNAs and released drugs in the dialysis cassette (199, 200).

Despite these efforts, the accuracy of drug release rates predicted by both traditional and modified dialysis methods remains questionable. Drug release profiles from dialysis-based methods are often fit to simple exponential models, which predict drug release rates based on four main assumptions: 1) all drug in the dialysis cassette is encapsulated in nanoparticles, 2) nanoparticles and dialysis membranes do not interact with released drug, 3) released drug is quickly removed from the dialysis cassette, and 4) released drug in the dialysis cassette does not affect the release rate of drug-loaded nanoparticles. Unfortunately, environmental factors such as molecular interactions and complicated mass transfer effects can invalidate some, if not all, of these assumptions. Drug binding to nanoparticles after release from the hydrophobic core can cause unrealistically slow drug release rates (64). In addition, drug adsorption to dialysis membranes can alter measured drug release rates. The adsorption of released drugs in the dialysis solution to the dialysis membrane can remove released drugs from the dialysis solution and increase the accuracy of chromatography-based drug release measurements, but rapid drug adsorption to the dialysis membranes followed by slow desorption of drug into the dialysis solution could also cause unrealistically slow drug release profiles (177, 184). The slow diffusion of hydrophobic drugs out of the dialysis cassette can also increase the residence time of released drugs inside the cassette. As a result, a measured

in vitro drug release rate is often different from its corresponding *in vivo* release rate. Computational models cannot easily compensate for these modeling errors unless the specific contributions from encapsulated drug, bound drug, and released drug inside a dialysis cassette to the overall drug release rate can be measured. The isolation of these various drug species during drug release measurements from nanoparticle drug carriers remains challenging. Therefore, there is a critical need to develop a novel method to measure drug release profiles of nanoparticles and predict drug release rates in a facile and accurate manner.

Based on this background, this study developed and evaluated a novel method to determine drug release rates from PNAs and potentially other types of nanoparticles with improved convenience and accuracy compared to traditional chromatography-based methods. This method employs solvato-fluorochromism (SFC), which was shown in chapter 2 and in the literature to be useful for analyzing the hydrophobicity of the PNA core and determining drug entrapment (201). Because the fluorescence of NB is quenched in water, potential interactions between free NB and released drug in solution should not interfere with fluorescence measurements. In addition, because SFC occurs over a short distance, NB in the core of PNAs should not interact with released drug. Therefore, in comparison to chromatographic methods that cannot distinguish various drug species in dialysis cassettes, SFC-based methods are expected to elucidate molecular interactions specifically between nanoparticles and drugs entrapped in the nanoparticle core.

In this study, HPLC- and SFC-based methods were compared to determine drug release rates from NB-conjugated PNAs in dialysis cassettes with varying core conditions

that modulate drug entrapment and release (Figure 4.1). NB-conjugated PNAs with an ionic or hydrophobic core were synthesized as described in chapter 2 and reported in the literature (201). Carfilzomib (CFZ) and docetaxel (DOC) were used as clinically relevant model anticancer drugs with well-studied physicochemical and biological properties. To evaluate drug diffusion effects on drug release measurements, hydrophobic excipients (palmitate and deoxycholate) were added to PNAs to force entrapped drugs into the center of the nanoparticle core. Mathematical modeling was also used to elucidate the effects of drug binding and diffusion on each measurement method. Therefore, the goal of this study was to compare HPLC- and SFC-based methods for measuring drug release from dialysis cassettes and to evaluate the potential of the SFC method for the determination of drug release rates from nanoparticles.

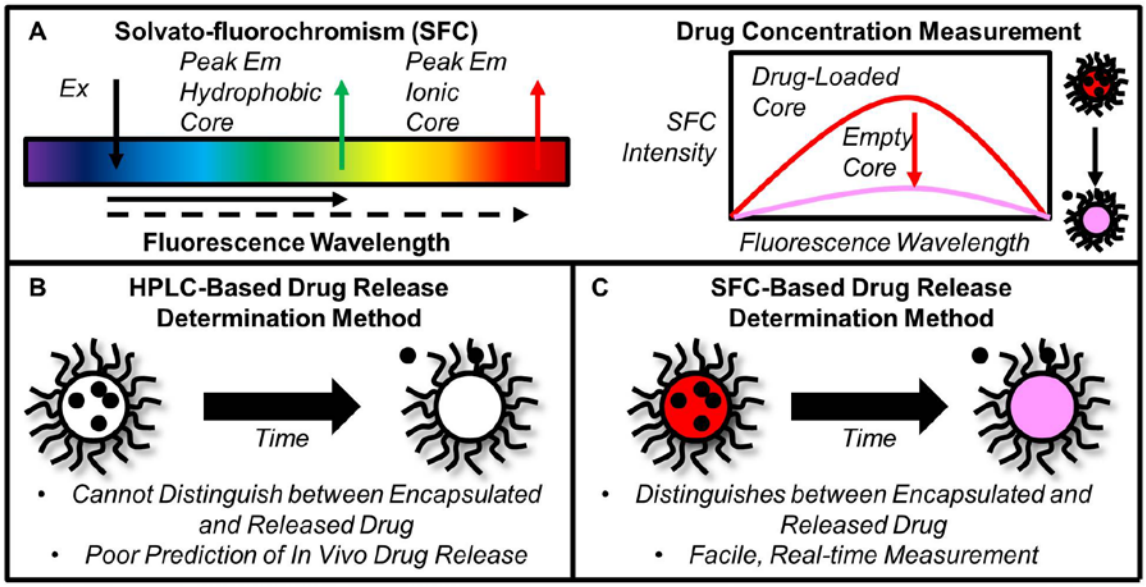

Figure 4.1. Graphical description of solvato-fluorochromism (A) as a fluorescence-based drug release measurement method to overcome the limitations of HPLC-based drug release methods (B) and measure drug release (C).

4.2 Materials and Methods

4.2.1 Materials

2PN and 3PN PNAs were prepared as described in chapter 2. Palmitic acid (PAL) and deoxycholic acid (DOCA) were purchased from Sigma Aldrich (St. Louis, MO). Dimethyl sulfoxide (DMSO), phosphate buffered saline (PBS), McCoy's 5A cell media, ethanol, and dialysis cassettes with a 10 kDa MWCO were purchased from Fisher Scientific (Waltham, MA). CFZ and DOC were purchased from LC Laboratories (Woburn, MA).

4.2.2 Drug Loading of Unstabilized and Excipient-Stabilized PNAs

Stock solutions of PNAs (2PN and 3PN, 100 mg/ml), drugs (CFZ and DOC, 1 mg/ml), and excipients (PAL and DOCA, 100 mg/ml) were prepared in ethanol. PNA (100 μl) and drug solutions (1 ml) were mixed in a round bottom flask and evaporated at reduced pressure to create a thin film. These thin films were reconstituted in water and centrifuged at 1000 RPM for 1 minute to remove free drug, excess excipients, and other insoluble impurities. Drug-loaded PNAs in the supernatant were collected after freeze drying and stored at -20 °C. In addition, excipient-stabilized PNAs were prepared by adding excipient (20 μl), PNA (100 μl) and drug solutions (1 ml) into a round bottom flask and repeating this procedure. Drug concentrations in drug-loaded PNA solutions were determined by HPLC (Agilent Eclipse XDB-C18 column, 40 °C, 1 ml/min mobile phase) for CFZ (55:45 ACN/water with 0.1% formic acid, 200 nm, 2.01 min elution) and DOC (65:35 ACN/water with 0.1% formic acid, 230 nm, 2.65 min elution). Drug peaks in each sample were compared to calibration curves of known concentration drug standards. The drug loading efficiency and encapsulation efficiency were defined as the

weight ratio of drug to drug-loaded PNAs and the weight ratio of drug in PNAs to total drug added, respectively. In addition, the molar drug loading efficiency was calculated as the molar ratio of drug to drug-loaded PNAs.

4.2.3 HPLC-Based and Solvato-Fluorochromic Drug Release Measurements

Drug-loaded PNAs were dispersed at 10 mg/ml in PBS, and the solutions (1 ml) were dialyzed into 1 l of PBS at 37 °C. Aliquots (100 μl) from within the dialysis cassettes were removed after 0, 1, 3, 6, 24 and 48 hours, and drug concentrations were quantified by HPLC as described in the previous section. For the SFC method, drug-loaded PNAs were dispersed at 10 mg/ml in PBS, and the solutions (1 ml) were dialyzed into 1 l of PBS at 37 °C. Aliquots (100 μl) from within the dialysis cassettes were removed after 0, 1, 3, 6, 24 and 48 hours, and drug concentrations were quantified as described below. In order to optimize the SFC method for measuring drug release profiles, fluorescence emission spectra of drug-loaded and empty PNAs were initially measured using several excitation wavelengths. From these spectra, excitation conditions for fluorescence spectra for 2PN (610 nm) and 3PN (580 nm) were selected for measurement using a plate reader (Spectramax M5, Sunnyvale, CA). These fluorescence spectra identified optimal excitation and emission wavelengths for analyzing 2PN (Ex 610 nm/Em 670 nm) and 3PN (Ex 580 nm/Em 630 nm) drug release profiles. Fluorescence measurements were converted to normalized drug concentrations. Briefly, the fluorescence of empty PNAs was subtracted from the fluorescence of each SFC measurement, and the fluorescence was normalized to the initial fluorescence of each drug-loaded PNA. Drug release profiles from dialysis-based and SFC-based methods

were fitted to first order release kinetics models using Prism 5 (Graphpad, La Jolla, CA). Equation 4.1 below describes a first order kinetic model for drug release.

$$\frac{C}{C_0} = 100 * e^{-k*t} \quad (4.1)$$

In equation 4.1, C/C_0 is the percent drug concentration in samples at time t relative to the initial drug concentration, and k is the rate constant. The time t has units of hours, while the rate constant has units of inverse hours. C/C_0 is unitless. The drug release half-life $t_{1/2}$ was defined in equation 4.2 as the time for drug in samples to reach 50% of the initial concentration.

$$t_{1/2} = \frac{\ln(2)}{k} \quad (4.2)$$

The drug release half-life has units of hours.

4.2.4 Free and Spiked Drug Release Measurements using HPLC-based and Solvato-Fluorochromic Methods

The release of free CFZ (1 or 0.5 mg/ml CFZ), free CFZ (1 mg/ml) spiked into 2PN solution (10 or 5 mg/ml) and drug-loaded 2PN (10 or 5 mg/ml) was measured using both the HPLC and the SFC method. Briefly, CFZ was dissolved in DMSO at 100 mg/ml to prepare a stock solution. For free drug release experiments, either 10 or 5 µl of drug solution was added to 990 or 995 µl of PBS, respectively. For spiked drug release experiments, 10 µl of drug solution was added to 990 µl of 2PN solution (5 or 10 mg/ml in PBS). CFZ-loaded 2PN was also dispersed in PBS at 5 or 10 mg/ml for drug-loaded PNA release experiments. Each colloidal solution (1 ml) was dialyzed into 1 l of PBS at 37 °C under sink conditions. Drugs remaining in PNAs were quantified using both the HPLC-based and SFC methods. As a negative control for the effects of organic solvents

on the SFC method, SFC measurements were repeated while adding blank DMSO (10 μl) to 990 μl 2PN solution (5 or 10 mg/ml PBS).

4.2.5 Mechanistic Modeling of Drug Release from PNAs

A mechanistic model of drug release kinetics from PNAs was derived to account for weak drug binding to the shell of PNAs and drug diffusion through the dialysis membrane. The mechanistic model was based on previous studies of drug release kinetics from polymer micelles (184). Mass balances were written for released drug (M_R) and total drug remaining (M_T) in dialysis cassettes in equations 4.3 and 4.4. Encapsulated drug in the core of PNAs was defined as M_E, while drug that is weakly bound to PNAs and released drug in the dialysis solution were defined as $M_{R,P}$ and $M_{R,W}$, respectively.

$$M_R = M_{R,P} + M_{R,W} \tag{4.3}$$

$$M_T = M_E + M_{R,P} + M_{R,W} \tag{4.4}$$

In equations 4.3 and 4.4, all mass values have units of micrograms.

Equation 4.4 was divided by the total volume of the dialysis cassette (V_T) in order to convert total mass to total concentration. Equation 4.5 describes total drug concentration in terms of volume.

$$C_T = \frac{M_{R,W}+M_E+M_{R,P}}{V_T} \tag{4.5}$$

In equation 4.5, V_T has units of milliliters, while C_T has units of micrograms per milliliter in the dialysis cassette. The total volume is assumed to be equal to the volume of the solution (V_W) plus the volume of the PNAs (V_P).

In order to convert equation 4.5 into concentration terms for each species, the mass of each species is converted to the product of its concentration and its species volume in equation 4.6.

$$C_T = \frac{(C_{R,W} * V_W) + (C_E * V_P) + (C_{R,P} * V_P)}{V_T} \quad (4.6)$$

In equation 4.6, all concentration values have units of micrograms per milliliter, and all volumes have units of milliliters of volume per species.

Constants *a* and *b* are defined as unitless volume ratios of solution and PNAs in equations 4.7 and 4.8. These values are substituted into equation 4.6 to yield equation 4.9.

$$a = \frac{V_W}{V_T} \quad (4.7)$$

$$b = \frac{V_P}{V_T} \quad (4.8)$$

$$C_T = aC_{R,W} + bC_E + bC_{R,P} \quad (4.9)$$

Using an estimated 2PN density (1.1 g/ml) and measured dialysis cassette volume, the calculated values of *a* for 2PN at 5 and 10 mg/ml were 0.996 and 0.992, respectively. In addition, the calculated values of *b* for 5 and 10 mg/ml PNA concentrations are 0.004 and 0.008, respectively.

Mass balances were written for encapsulated drug, total released drug and drug in the dialysis sink (M_S) in equations 4.10, 4.11 and 4.12.

$$\frac{dM_E}{dt} = -k_C M_E + k_R M_{R,P} \quad (4.10)$$

$$\frac{dM_R}{dt} = k_C M_E - k_R M_{R,P} - k_D M_{R,W} + k_D M_S \quad (4.11)$$

$$\frac{dM_S}{dt} = k_D M_{R,W} - k_D M_S \quad (4.12)$$

Mass balances were converted to concentration in equations 4.13, 4.14 and 4.15 by assuming that species volumes remain constant over time, and by substituting mass for volume times the concentration.

$$V_P \frac{dC_E}{dt} = -k_C V_P C_E + k_R V_P C_{R,P} \quad (4.13)$$

$$V_T \frac{dC_R}{dt} = k_C V_P C_E - k_R V_P C_{R,P} - k_D V_W C_{R,S} + k_D V_S C_S \quad (4.14)$$

$$V_S \frac{dC_S}{dt} = k_D V_W C_{R,W} - k_D V_S C_S \quad (4.15)$$

In equations 4.14 and 4.15, V_S is the volume of the dialysis sink (1000 ml).

Differential rate equations 4.13, 4.14 and 4.15 were rearranged into equations 4.16, 4.17 and 4.18, respectively. In equation 4.18, 0.001 is calculated volume ratio of the dialysis cassette (1 ml) to the dialysis sink (1 L).

$$\frac{dC_E}{dt} = -k_C C_E + k_R C_{R,P} \quad (4.16)$$

$$\frac{dC_R}{dt} = b(k_C C_E - k_R C_{R,P}) - k_D(aC_{R,W} - C_S) \quad (4.17)$$

$$\frac{dC_S}{dt} = 0.001 * k_D(a * C_{R,W} - C_S) \quad (4.18)$$

The unitless ratio of weakly bound drug to released drug in solution is defined as the PNA-water partition coefficient (K_P) in equation 4.19. Mass balances can be written for released drug in equation 4.20 and converted to concentration in equation 4.21.

$$K_P = \frac{C_{R,P}}{C_{R,W}} \quad (4.19)$$

$$M_R = M_{R,P} + M_{R,W} \quad (4.20)$$

$$V_T C_R = V_P C_{R,P} + V_W C_{R,W} \quad (4.21)$$

By solving equation 4.21 for $C_{R,P}$ or $C_{R,W}$ and substituting in Kp for $C_{R,W}$ or $C_{R,P}$, respectively, the concentration of each species of released drug can be described in terms of total released drug as in equations 4.22 and 4.23.

$$C_{R,W} = \frac{C_R}{a + bK_P} \quad (4.22)$$

$$C_{R,P} = \frac{K_P * C_R}{a + bK_P} \quad (4.23)$$

Equations 4.22 and 4.23 are substituted into equations 4.16, 4.17 and 4.18 to yield equations 4.24, 4.25 and 4.26, respectively. In addition, equations 4.22 and 4.23 were

substituted into equation 4.9, and the equation was rewritten as 4.27. Drug release profiles were simultaneously fitted to equations 4.24, 4.25, 4.26 and 4.27 using a weighting factor of 2 to determine k_C, k_R, K_P and k_D using Scientist 3.0 (Micromath, St. Louis, MO).

$$\frac{dC_E}{dt} = -k_C C_E + k_R \frac{K_P * C_R}{a + bK_P} \quad (4.24)$$

$$\frac{dC_R}{dt} = b\left(k_C C_E - \frac{k_R * K_P * C_R}{a + bK_P}\right) - k_D\left(\frac{a * C_R}{a + bK_P} - C_S\right) \quad (4.25)$$

$$\frac{dC_S}{dt} = 0.001 * k_D \left(\frac{a * C_R}{a + bK_P} - C_S\right) \quad (4.26)$$

$$C_T = C_R + bC_E \quad (4.27)$$

For spiked drug release experiments, all drug in the dialysis cassette is initially assumed to be released. In contrast, all drug in the dialysis cassette is initially assumed to be encapsulated in drug-loaded PNA introduced in release experiments.

4.2.6 Chemical Stability and Photostability of Nile Blue

NB was dissolved at 50 μg/ml in McCoy's 5A cell media and added into a quartz cuvette. The NB-containing cuvette was stored in the dark at 37 °C while gently mixing. The absorbance spectrum of NB in the cuvette was measured from 450 nm to 750 nm at 0, 1, 2 and 5 days post-storage. In addition, NB was dissolved at 100 μg/ml in deionized water and added into a 96 well plate. The fluorescence of NB (Ex 632 nm/Em 680 nm) in the plate was measured 10 times over a period of 10 minutes.

4.2.7 Statistics

All values in figures are reported as mean±standard deviation of three measurements. Groups of measurements are compared by one-way ANOVA with Bonferroni's post-test correction, and pairs of measurements are compared by a Student's

t test unless otherwise noted. Statistical significance in tables and figures is indicated by * ($p<0.05$), ** ($p<0.01$) or *** ($p<0.001$).

4.3 Results

4.3.1 Hydrophobicity of the PNA Core Environment Controls Drug Loading

Drug loading and encapsulation efficiencies of PNAs are described in Table 4.1. Both 2PN and 3PN successfully entrapped CFZ and DOC. 3PN had a higher drug loading efficiency than 2PN for both drugs, possibly due to favorable interactions between the model drugs and PAL in the PNA core. The drug loading and encapsulation efficiency of both DOC-loaded 2PN and 3PN increased in order of no excipient, PAL, and DOCA. Because CFZ-loaded 3PN already had high drug loading and encapsulation efficiencies, hydrophobic excipients were not added to PNAs.

Table 4.1. Drug loading of 2PN and 3PN with and without stabilizing excipients.

PNA	Excipient	Drug	Drug Loading Efficiency (w/w %)	Molar Drug Loading Efficiency (mol Drug/ mol PNA)	Encapsulation Efficiency (w/w %)
2PN	None	CFZ	3.0±0.1***	11.5±0.4	30.5±0.9
3PN	None	CFZ	8.7±0.4***	21.3±1.0	94.7±3.8
PNA***	Excipient***	Drug	Drug Loading Efficiency (w/w %)	Molar Drug Loading Efficiency (mol Drug/ mol PNA)	Encapsulation Efficiency (w/w %)
2PN	None	DOC	1.5±0.1	3.1±0.2	15.1±0.1
2PN	PAL	DOC	2.3±0.1	5.0±0.2	23.0±0.2
2PN	DOCA	DOC	4.6±0.1	10.0±0.2	47.9±0.5
3PN	None	DOC	3.4±0.1	7.4±0.2	34.7±0.4
3PN	PAL	DOC	4.1±0.1	8.9±0.2	42.9±0.1
3PN	DOCA	DOC	6.6±0.1	14.3±0.2	71.0±0.8

Drug loading efficiency, molar drug loading efficiency and encapsulation efficiency are reported as mean±SD (n=3). Statistical significance is determined by either a Student's t-test (CFZ-loaded PNAs) or a two-way ANOVA with Bonferroni's post-test correction (DOC-loaded PNAs) for each group as described in the methods section. For the two-way ANOVA, statistical significance is indicated on each parameter.

4.3.2 HPLC-Based Methods Indicate a Longer Drug Release Half-Life Than Solvato-Fluorochromic Methods

Drug release profiles of DOC and CFZ from 2PN and 3PN were measured using both HPLC-based and SFC methods (Figures 4.2 and 4.3). Because CFZ and DOC were non-fluorescent up to 10 mg/ml, fluorescence of the model drugs did not interfere with the observed SFC spectra of PNAs. Figure 4.2 shows drug release profiles for DOC-loaded 2PN and 3PN, in which HPLC signals from the dialysis method and SFC signals decreased as DOC escaped the dialysis cassettes. CFZ-loaded PNAs showed similar drug release trends (Figure 4.3). Table 4.2 summarizes the kinetic parameters of 2PN and 3PN determined by both HPLC-based and SFC methods. For each drug-loaded PNA, the HPLC-based method indicated a longer drug release half-life than the SFC method. It should be noted that the specific excitation and emission wavelengths used for SFC measurements did not affect the mean values of SFC kinetic parameters, but the weak fluorescence signals from sub-optimal measurement conditions significantly increased measurement variability.

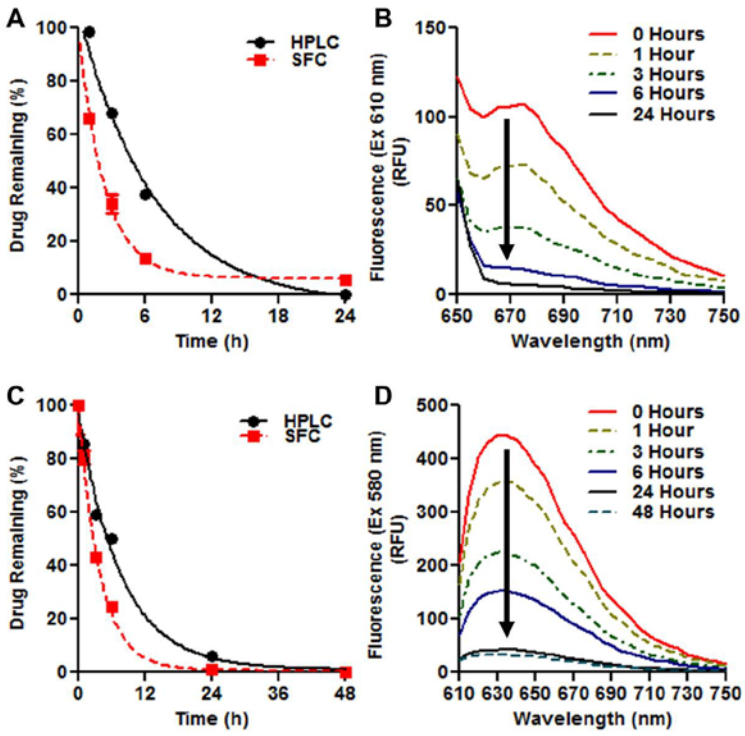

Figure 4.2. Docetaxel release measurements from 2PN (A/B) and 3PN (C/D) using HPLC- and SFC-based methods (A/C). SFC spectra of 2PN (B) and 3PN (D).

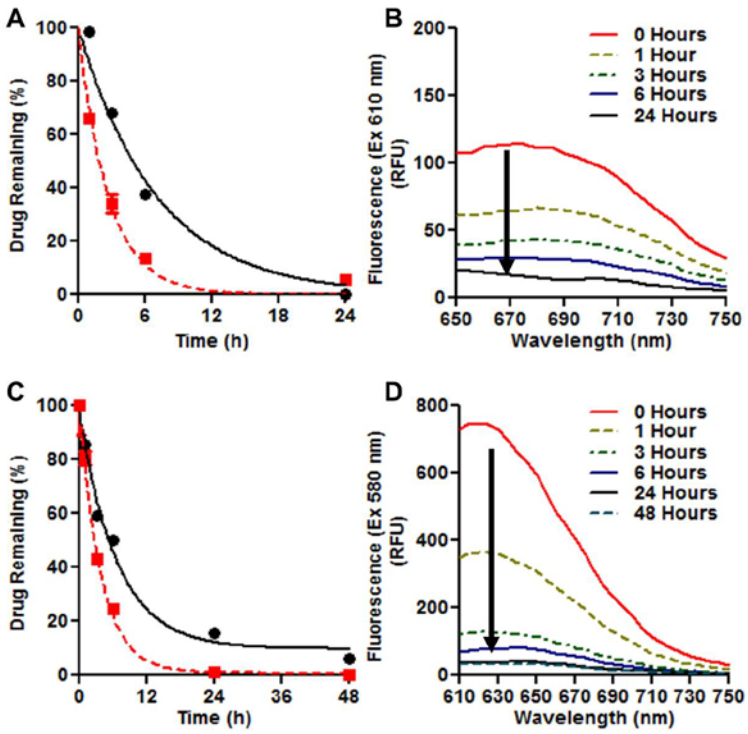

Figure 4.3. Carfilzomib release measurements from 2PN (A/B) and 3PN (C/D) using HPLC- and SFC-based methods (A/C). SFC spectra of 2PN (B) and 3PN (D).

Table 4.2. Parameters from a first order kinetic model of drug release for 2PN and 3PN from HPLC- and SFC-based methods.

PNA	Drug	Method	$t_{1/2}$ (h)	k (h^{-1})	k_{SFC}/k_{HPLC}
2PN	CFZ	HPLC	4.89 (4.22-5.82)	0.14 (0.12-0.16)	2.64 (1.79-3.49)
		SFC	1.89 (1.74-2.07)	0.37 (0.34-0.40)	
3PN	CFZ	HPLC	4.66 (3.91-5.76)	0.15 (0.12-0.18)	1.73 (0.88-2.59)
		SFC	2.68 (2.32-3.18)	0.26 (0.22-0.30)	
2PN	DOC	HPLC	2.25 (2.05-2.49)	0.31 (0.28-0.34)	1.39 (1.02-1.75)
		SFC	1.62 (1.54-1.72)	0.43 (0.40-0.45)	
3PN	DOC	HPLC	5.14 (4.64-5.76)	0.13 (0.12-0.15)	1.92 (1.27-2.58)
		SFC	2.75 (2.49-3.08)	0.25 (0.23-0.28)	

Kinetic parameters are reported as mean with 95% CI in parenthesis. The error for k_{SFC}/k_{HPLC} is propagated from individual rate measurements. The 95% CI of the drug release rate ratio is compared to 1 to evaluate if drug release rates are statistically similar.

4.3.3 Drug Binding to PNAs Reduces the Accuracy of HPLC-Based Measurements but Minimally Affects Solvato-Fluorochromic Measurements

Figure 4.4 shows free CFZ, spiked CFZ, and CFZ-loaded 2PN release profiles. Drug release rates increased in order of drug-loaded 2PN, spiked drug, and free drug for high and low PNA concentrations. The free CFZ release half-life was greater than 10 minutes, suggesting that the diffusion rate of free drug through dialysis membrane could affect the measured drug release rate. Spiked drug release measurements showed a longer drug release half-life than free drug release measurements at high and low concentrations, indicating that the PEG shell of PNAs can bind drug and slow drug release. In addition, drug-loaded 2PN displayed a longer half-life than either spiked or free drug. Figure 4.5 shows SFC measurements of spiked drug and spiked blank DMSO release. Because PNAs are not present in the dialysis cassette for free CFZ release experiments, solvato-fluorochromism could not be used to measure free CFZ release profiles. In contrast to HPLC-based measurements which directly detected spiked drug by HPLC without interference from DMSO, the spiked DMSO interfered with the SFC measurements of drug release. Spiked drug slightly increased the initial PNA fluorescence from DMSO-corrected spiked drug SFC measurements, but the SFC signal was unaffected after 1 hour. Based on these observations, a mathematical model was developed to account for drug binding to PNAs and diffusion through the dialysis membrane during drug release measurements.

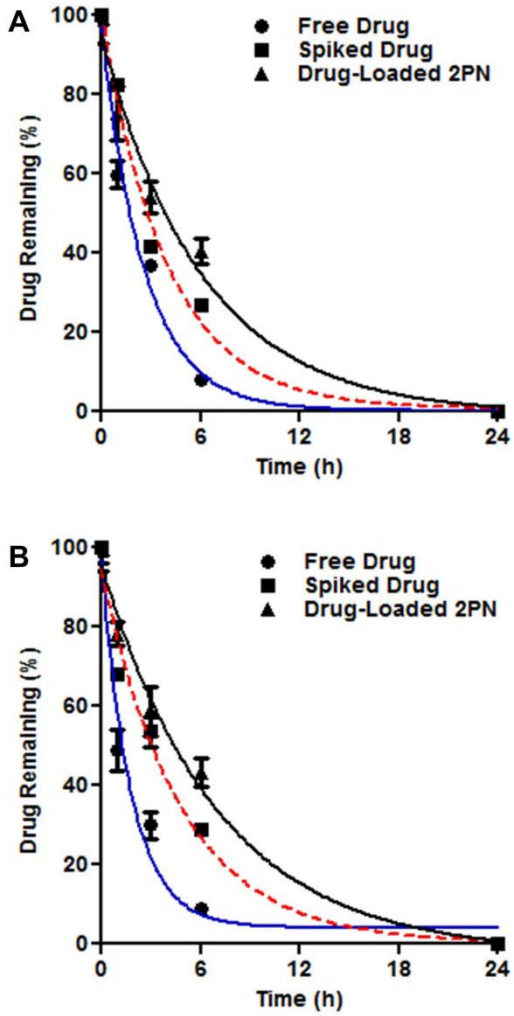

Figure 4.4. HPLC-based measurements for the mechanistic modeling of drug release from PNAs. Measurements were performed at 10 mg/ml (A) and 5 mg/ml (B) 2PN concentration using carfilzomib as a model drug.

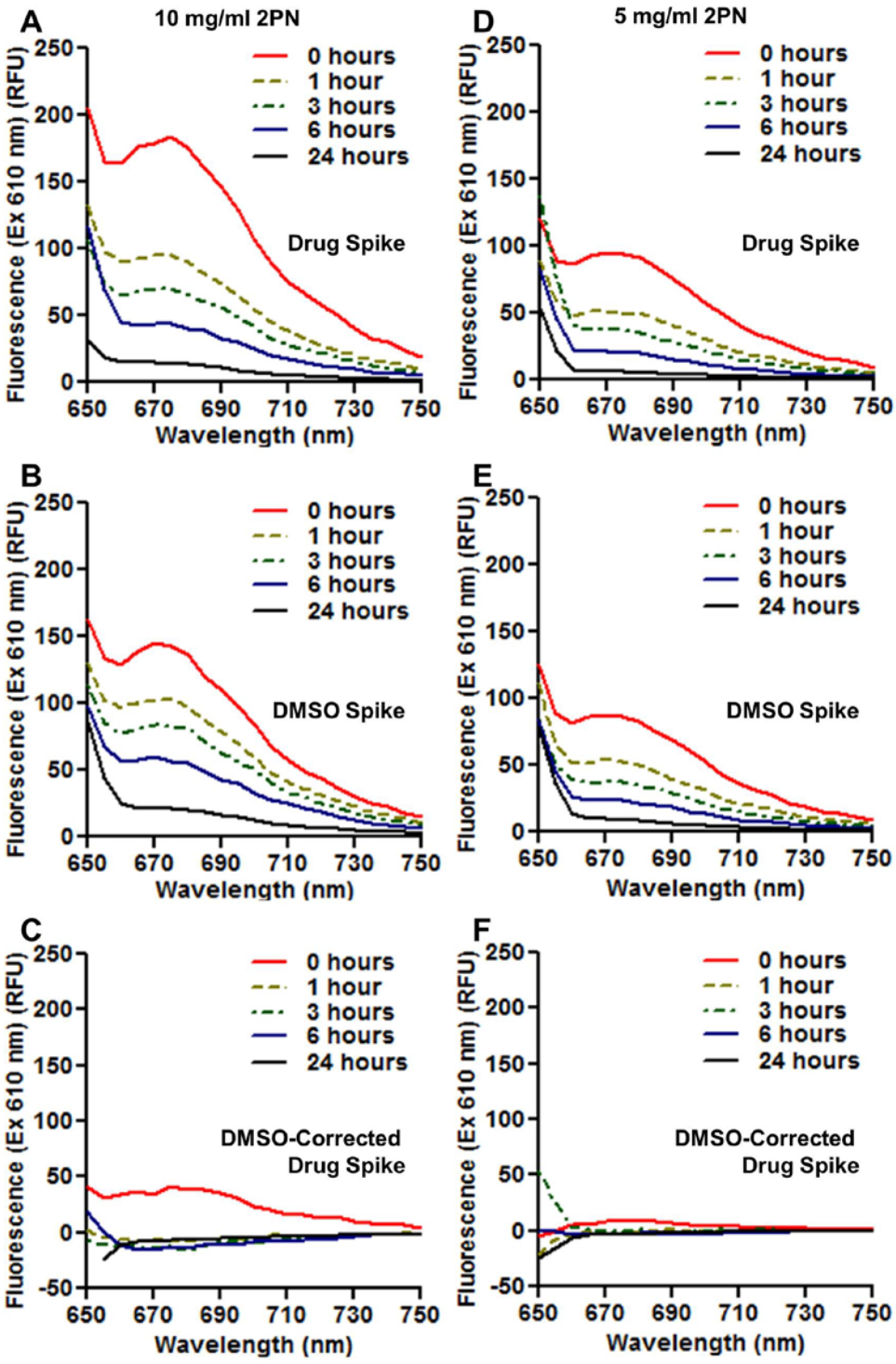

Figure 4.5. SFC-based measurements for the mechanistic modeling of drug release from PNAs. Measurements were performed at high (10 mg/ml) 2PN concentration (A-C) and low (5 mg/ml) 2PN concentration (D-F).Released drug could not be easily detected at high or low PNA concentrations (C,F).

4.3.4 Mechanistic Modeling Indicates that Solvato-Fluorochromic Drug Release Rates Are Insensitive to Free Drug

Figure 4.6 illustrates a mechanistic model of drug release kinetics from PNAs. The released drug diffusion rate through the dialysis membrane (k_D), the rate of encapsulated drug leaving PNA core (k_C), the rate of drug re-entering the PNA core (k_R) and the released drug water-PNA partition coefficient (K_P) are determined by non-linear regression as described in the methods section. It should be noted that a weighting value of 2 reduced the standard error of modeling parameters compared to other weighting values, but the weighting value did not significantly affect the mean values of each parameter. Table 4.3 shows CFZ release kinetic parameters at high and low 2PN concentrations from HPLC-based and SFC methods. The kinetic parameters from HPLC-based measurements were independent of PNA concentration, but it is possible that the selection of a larger PNA concentration range for future experiments could increase the differences between parameters. Since the 95% confidence interval of k_R overlapped zero, the re-entry of drugs into the PNA core was negligible under these experimental conditions. Because the 95% confidence intervals of K_P and k_D were non-zero, weak drug binding and slow diffusion affected HPLC-based drug release measurements. In contrast to HPLC-based methods, k_D and K_P were not detectable by the SFC method. As a result, these observations revealed that released drug would not directly affect SFC measurements in comparison to HPLC-based methods using the experimental conditions described for these drug release measurements.

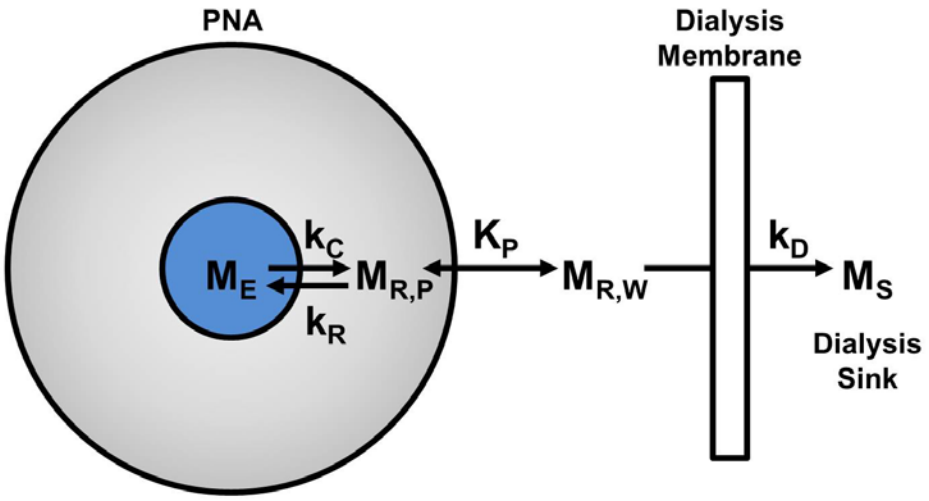

Figure 4.6. Graphical description of the mechanistic model for CFZ release from 2PN during dialysis-based measurements. The model accounts for drug rebinding to PNAs and diffusion through dialysis membrane.

Table 4.3. Kinetic parameters from the mechanistic model of drug release from CFZ-loaded 2PN.

Method	PNA Concentration (mg/ml)	k_C (h^{-1})	k_R*10^5 (h^{-1})
HPLC	10	0.170 (0.090-0.249)	0.3 (-4.3-5.0)
HPLC	5	0.116 (0.049-0.182)	8.1 (-32.2-39.6)
SFC	10	0.37 (0.31-0.43)	---
SFC	5	0.39 (0.35-0.43)	---
Method	PNA Concentration (mg/ml)	K_P (unitless)	k_D (h^{-1})
HPLC	10	121.5 (60.5-182.5)	0.429 (0.361-0.497)
HPLC	5	95.7 (45.4-146.0)	0.421 (0.365-0.478)
SFC	10	---	---
SFC	5	---	---

Kinetic parameters are reported as mean with 95% CI in parentheses. Parameters were compared by a Student's T test. Statistical significance is indicated as described in the methods section.

4.3.5 Hydrophobic Excipients Alter Both the HPLC- and Solvato-Fluorochromic-Based Drug Release Rates of PNAs

Figures 4.7 and 4.8 show HPLC-based and SFC drug release measurements from DOC-loaded 2PN and 3PN that are stabilized by DOCA or PAL. Because the mechanistic model could not be used for SFC measurements as described in the previous section, HPLC- and SFC-based release rates were compared using a first order kinetic model (equation 4.1). DOCA and PAL increased the initial fluorescence of PNAs during SFC measurements, presumably due to increased dye-drug interactions within the core of PNAs. Kinetic parameters of drug release from excipient-stabilized PNAs are summarized in Table 4.4. The addition of hydrophobic excipients to PNAs decreased the difference between drug release rates that were measured by HPLC-based and SFC methods. In addition, both DOCA and PAL slightly decreased the drug release half-life of PNAs that were determined by HPLC-based methods, possibly due to increased drug loading in 2PN and 3PN.

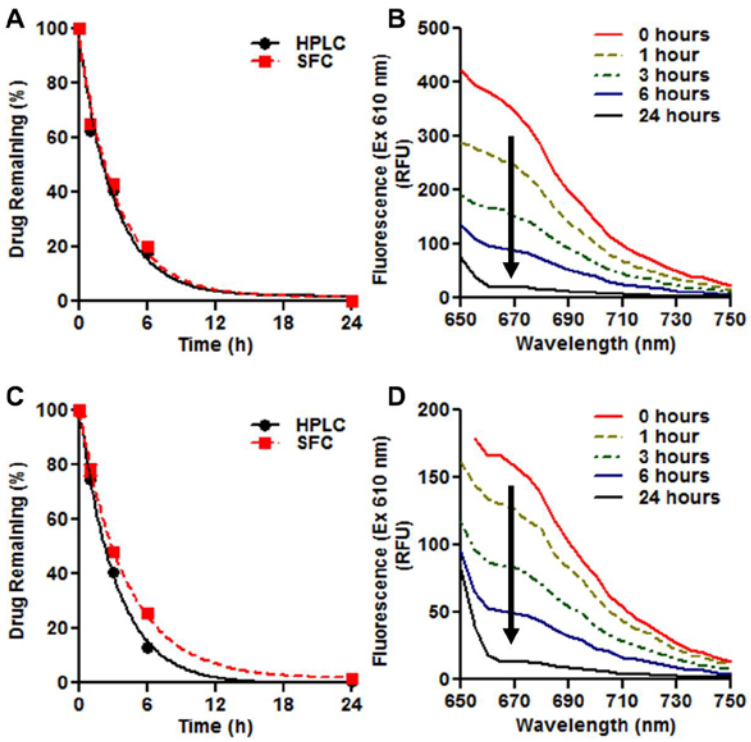

Figure 4.7. Docetaxel release measurements from excipient-stabilized 2PN containing either DOCA (A/B) or PAL (C/D) using HPLC- and SFC-based methods (A/C). SFC spectra of DOCA-stabilized 2PN (B) and PAL-stabilized 2PN (D).

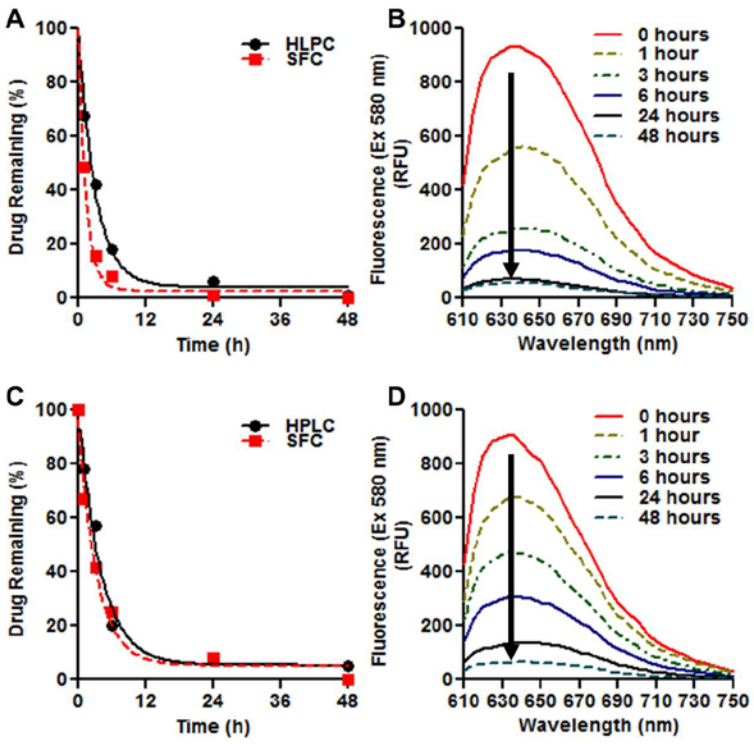

Figure 4.8. Docetaxel release measurements from excipient-stabilized 3PN containing either DOCA (A/B) or PAL (C/D) using HPLC- and SFC-based methods (A/C). SFC spectra of DOCA-stabilized 3PN (B) and PAL-stabilized 3PN (D).

Table 4.4. Parameters from a first order kinetic model for drug release for excipient-stabilized PNAs from HPLC- and SFC-based methods.

PNA	Excipient	Method	$t_{1/2}$ (h)	k (h^{-1})	k_{SFC}/k_{HPLC}
2PN	None	HPLC	2.25 (2.05-2.49)	0.31 (0.28-0.34)	1.39 (1.02-1.75)
		SFC	1.62 (1.54-1.72)	0.43 (0.40-0.45)	
3PN	None	HPLC	5.14 (4.64-5.76)	0.13 (0.12-0.15)	1.92 (1.27-2.58)
		SFC	2.75 (2.49-3.08)	0.25 (0.23-0.28)	
2PN	DOCA	HPLC	2.12 (1.89-2.40)	0.33 (0.29-0.37)	0.91 (0.47-1.34)
		SFC	2.30 (2.07-2.59)	0.30 (0.27-0.34)	
3PN	DOCA	HPLC	2.27 (2.09-2.50)	0.30 (0.28-0.33)	2.20 (1.62-2.78)
		SFC	1.05 (0.96-1.15)	0.66 (0.60-0.72)	
2PN	PAL	HPLC	2.24 (2.16-2.32)	0.31 (0.30-0.32)	0.77 (0.69-0.85)
		SFC	2.93 (2.83-3.03)	0.24 (0.23-0.25)	
3PN	PAL	HPLC	3.07 (2.73-3.51)	0.23 (0.20-0.25)	1.04 (0.61-1.48)
		SFC	2.95 (2.56-3.32)	0.24 (0.20-0.28)	

Data for PNAs without excipients is reproduced from Table 4.2. Kinetic parameters are reported as mean with 95% CI in parenthesis. The error for k_{SFC}/k_{HPLC} is propagated from individual rate measurements. The 95% CI of the drug release rate ratio is compared to 1 to evaluate if drug release rates are statistically similar.

4.3.6 Nile Blue Remains Chemically Stable during Solvato-Fluorochromic Drug Release Measurements

Figure 4.9 shows the chemical stability and photostability of NB under the experimental conditions of the SFC measurements. The absorbance spectra of NB remained consistent up to 5 days post-storage. In addition, changes in the maximum absorbance of NB (632 nm) over time were not statistically significant. In addition, changes in the fluorescence intensity of NB were not statistically significant after 10 measurements of the same sample over 10 minutes.

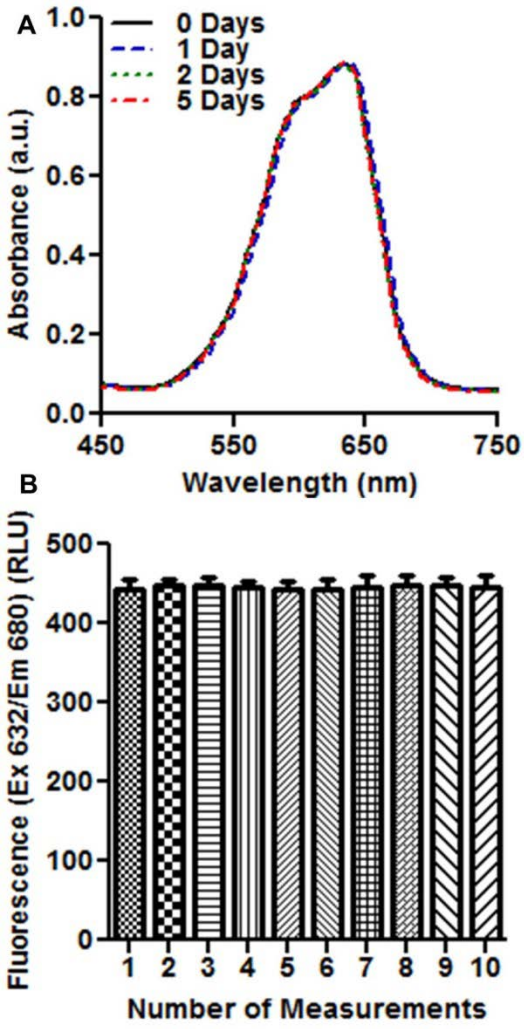

Figure 4.9. Chemical stability (A) and photostability (B) of NB in cell media or deionized water, respectively.

4.4 Discussion

4.4.1 Solvato-Fluorochromism Measures a Step of Drug Release

The measurement of drug release profiles is an important step for developing safe and effective nanoparticle drug carriers for cancer chemotherapy (202, 203). Drug release profiles indicate time-dependent changes in the amount of drugs that nanoparticles release into the blood or the tumor. Nanoparticles are typically designed to minimize drug release in the blood that can increase normal tissue exposure to drugs and cause organ damage or other adverse effects (204). In contrast, drug release into the interstitial space of tumors can facilitate the accumulation of active drugs in cancer cells (205). Nanoparticles that accumulate selectively in tumors and release drugs at slow rates have improved the therapeutic efficacy of anticancer drugs by maximizing drug delivery into tumor cells (204).

Despite their significance to cancer treatment efficacy, *in vivo* drug release profiles for nanoparticle drug carriers are often only estimated from *in vitro* measurements of drug concentrations in nanoparticles, which are often completed using HPLC-based methods that measure remaining drug during dialysis-based experiments. As a result, the real-time determination of drug release in the blood and in tumors is currently unavailable (167, 168, 174). Previous studies reported that HPLC-based methods could inaccurately estimate *in vivo* drug release profiles for PNAs when drugs bind to nanoparticles (206). Drug release profiles from HPLC-based methods may also be inaccurate if drugs are chemically unstable or diffuse slowly through the dialysis membrane (207). As an alternative method to determine drug release from the core of PNAs and potentially other types of nanoparticles, the SFC method was investigated for

the real-time, direct measurement of drug release from PNAs compared to HPLC-based methods for measuring drug remaining in dialysis cassettes.

Differences between *in vivo* and *in vitro* drug release rates from nanoparticles are often attributed to decreased *in vivo* nanoparticle concentrations following treatment compared to *in vitro* measurement conditions. For example, some drug-loaded polymer micelles sustain drug release *in vitro*, but they can release drug rapidly following dilution after intravenous injection (208). Polymer nanoassemblies are made from covalently tethered polymer chains that form unimolecular particles. These unimolecular particles remain intact upon dilution in the blood following intravenous injection as opposed to other multimolecular nanoparticles (209). Therefore, the *in vivo* dilution of PNAs is not expected to alter drug release rates due to dissociation of the hydrophobic core.

Two poorly soluble model drugs, CFZ and DOC (5 μg/ml and 10 μg/ml maximum solubility in water, respectively), were successfully entrapped in PNAs under various conditions. Both CFZ and DOC showed first-order drug release kinetics, although CFZ exhibited weak drug binding to 3PN based on tailing in drug release profiles. However, other drug-loaded PNAs showed complete drug release. Interestingly, 2PN with an ionic core entrapped hydrophobic CFZ, possibly due to favorable interactions between the tetrapeptide backbone of CFZ and cationic PEI backbone or charged amines on NB. In comparison to the HPLC-based method which only provided information about the time-dependent changes of drug concentrations in the dialysis cassette, the SFC method indicated dynamic changes in the PNA core environment during drug release by showing unique SFC spectra and intensities for each PNA formulation.

4.4.2 Mechanistic Modeling Compares HPLC- and Solvato-Fluorochromic-Based Methods for Dialysis-Based Drug Release Measurements

To further investigate the effects of drug binding on HPLC-based and SFC methods, spiked drug release experiments were performed. Drug release rates from the HPLC-based method increased in order of drug-loaded 2PN, spiked drug, and free drug for both high and low concentrations of 2PN. These data indicate that the diffusion of free drug through the dialysis membrane slows apparent drug release rates, which is often overlooked in HPLC-based methods. Unexpectedly, the SFC signals of PNAs increased in the presence of DMSO used to dissolve CFZ during the spiked drug release experiments. Spiked drug release data corrected for DMSO interference revealed that weakly bound drugs and drugs in solution could not be detected. As a result, CFZ that is weakly bound to 2PN or in solution would not affect SFC-based methods compared to HPLC-based methods. These results indicate that the SFC method is less sensitive to drug binding than HPLC-based methods under these experimental conditions, and that the SFC method would provide more accurate information about drugs leaving the core of the nanoparticle drug carriers than HPLC-based methods. However, additional work is needed to verify if this conclusion is valid for PNAs with higher drug loadings or increased substitution of fluorochromic dyes.

The unexpected increase in SFC signals from DMSO raised concerns about potential interactions between PNAs and other hydrophobic molecules in solution. To address these concerns, SFC drug release profiles for 3PN were compared to a physical mixture of 2PN and hydrophobic excipients such as PAL. DOC was selected as a model drug because it showed no tailing in drug release profiles. Drug release profiles revealed

that DOCA and PAL increased drug entrapment in PNAs but also accelerated drug release rates. In addition, hydrophobic excipients were confirmed to induce no change in the SFC spectra of PNAs. PNAs with PAL, either covalently conjugated to the core or physically mixed in the core, should have the same molecular components (i.e., 3PN compared to 2PN and PAL), but they showed distinct SFC spectra. 2PN retained its SFC spectra in the presence of PAL, although a physical mixture of 2PN and PAL exhibited greater SFC intensity than 2PN. Hydrophobic excipients also increased the SFC intensity for 3PN without affecting the shape of its SFC spectra.

It was initially hypothesized that SFC-based drug release rates would by equal to HPLC-based drug release rates that were corrected for drug rebinding and diffusion. However, k_{SFC} values were significantly greater than k_C, indicating that factors other than drug rebinding and diffusion contribute to these differences. Factors other than drug rebinding and diffusion could be decreasing apparent drug release rates measured by HPLC compared to SFC, but the possible nature of these factors is unclear. In contrast, SFC-based methods could be overestimating drug release compared to HPLC-based methods. The fluorescence of NB-conjugated PNAs increased linearly in response to drug loading, suggesting that increased apparent drug release rates from SFC-based methods are not due to detection method limitations. PNAs could contain a heterogeneous core environment, in which only the region of the core environment near the scaffold is sensitive to drug loading. In this region, NB can interact with hydrophobic drug molecules. The core environment closer to the PNA-water interface may not contain NB, because the NB molecule is small and covalently conjugated to the polymer scaffold. In this region, hydrophobic drugs do not interact with NB. In addition, water may enter

the outside of the core, but fail to diffuse evenly throughout the core. If these statements are valid, SFC-based drug release measurements would measure the diffusion of drugs out of the NB-enriched region of the PNA core. Because drug molecules diffuse towards the PNA-water interface, drug in the NB-enriched region of the PNA core could decrease before the concentrations near the interface decrease. In this manner, SFC drug release rates would measure a step of drug release, but not the rate-limiting step indicating overall drug release rates. Unfortunately, experimental measurements of PNA core heterogeneity remain challenging. Future studies may elucidate the relationship between SFC drug release rates, HPLC-based drug release rates and physical processes occurring during drug release.

4.4.3 Mechanistic Modeling Assesses the Thermodynamic Conditions of Dialysis-Based Drug Release Measurements

Dialysis-based drug release measurements depend on a sink condition in the dialysis solution in order to assure that *in vitro* drug release rates are accurate. Researchers often assume that sink conditions are maintained if nanoparticle solutions are dialyzed into a solution with a much greater volume than the nanoparticle solution (210). The dialysis sink is expected to maintain an activity gradient between nanoparticles and the solution that facilitates drug diffusion out of the nanoparticle core. However, a large dialysis sink does not guarantee sink conditions for drug release, because the chemical potential of the drug at the nanoparticle interface relative to the solution is often non-zero (211). It is hypothesized that *in vivo* conditions such as reduced PNA concentrations and blood flow promote the removal of released drugs from PNAs, allowing PNAs to maintain sink conditions *in vivo*. By comparing HPLC-based drug release rates from the

first order kinetic model to HPLC-based drug release rates from the mechanistic model, the presence or absence of a sink condition can be assessed. Differences between these release rates were not statistically significant, suggesting that HPLC-based drug release measurements are occurring under sink conditions. However, due to the size of the 95% confidence intervals, more precise methods of assessing sink conditions during dialysis-based drug release measurements may be needed.

The PNA-water partition coefficient (*Kp*) of carfilzomib allowed investigators to measure the re-binding of hydrophobic drugs in solution to PNAs. For sink conditions to be maintained during drug release, the dilution of hydrophobic drugs after they were released into the dialysis solution would either prevent drugs from re-binding to the surface of PNAs or make the process difficult to observe and quantify experimentally. The mechanistic modeling of CFZ release from 2PN indicated that the PNA-water partition coefficient of CFZ was non-zero. As a result, sink conditions cannot be assumed for these drug release measurements. In order to allow for sink conditions during future drug release studies, the rebinding of drugs to PNAs could be reduced by sequestering released drug in the dialysis solution. For example, carfilzomib has been shown to form cyclodextrin complexes (212). Determining the appropriate experimental conditions for using cyclodextrins to sequester released CFZ is a future area of work.

The mechanistic model of drug release also allowed researchers to account for the potential re-entry of drugs into the PNA core. The re-entry parameter (k_R) allowed the model to account for two potential experimental conditions: 1) a high released drug concentration that causes the chemical potential of released drug and drug at the PNA-water interface to be equal, and 2) a high chemical potential of drug at the PNA-water

interface relative to solution that slows drugs entry into solution but does not necessarily affect drug leaving the core. The 95% confidence interval of the modeled kinetic parameter for drug re-entry (k_R) was not statistically different from zero. This observation suggests that either the released drug is unlikely to interact with the PNA core due to a small surface area of the core compared to the released drug binding area, or that PNAs did not have a high enough initial drug concentration to detect the re-entry of drug into the core of PNAs. Future experiments using a variety of model drugs at several drug loading values may elucidate the necessary properties of both nanoparticles and drugs to observe the re-entry of released drugs into the PNA core.

The addition of hydrophobic excipients to 3PN was expected to alter SFC signals by controlling drug distribution in the core, but it also decreased the DOC release rate measured by HPLC. Carboxylate anions at the interface of excipient-stabilized PNAs could increase the apparent drug release rate by decreasing K_p. This phenomenon would be difficult to measure experimentally, because excipients are not conjugated to the core of PNAs and can diffuse into solution over time. As a result, the K_p value of excipient-stabilized PNAs may change during the release measurement. In order to investigate the effects of excipients on the PNA-water partition coefficient of drugs, investigators could identify excipients that can be conjugated to the core of PNAs while introducing a carboxylate anion to the surface of the PNA core, or they could chemically modify DOCA or PAL so that they can be conjugated to PNAs without affecting the carboxylate anion. Additionally, interactions between released drugs and excipients could decrease k_D. The effects of excipient-drug interactions on drug diffusivity should be investigated in future work.

4.4.4 Excipients Increase Drug Concentrations in the Nanoassembly Core

Hydrophobic excipients were expected to increase DOC encapsulation in order of no excipient, DOCA, and PAL, because PAL (logP=7.2) is more lipophilic than DOCA (logP=3.5) (213, 214). However, DOCA increased DOC loading by 2% more than PAL in both 2PN and 3PN. Although PAL and DOCA increased the DOC release half-life for 2PN from SFC methods, the excipients unexpectedly accelerated DOC release from 3PN from HPLC methods. Based on these results, it is speculated that the excipients mix with PNAs during drug loading and increase core hydrophobicity and drug entrapment, while NB detects the core environment changes and emits a stronger SFC intensity. However, carboxyl groups on PAL and DOCA keep the excipients near the core-shell interface and prevent direct contact between the excipients and NB, allowing PNAs to maintain their distinct fluorescence spectra. Excipients may leave the core of excipient-stabilized PNAs quickly along with drugs and accelerate drug release rates. Figure 4.10 illustrates this potential mechanism.

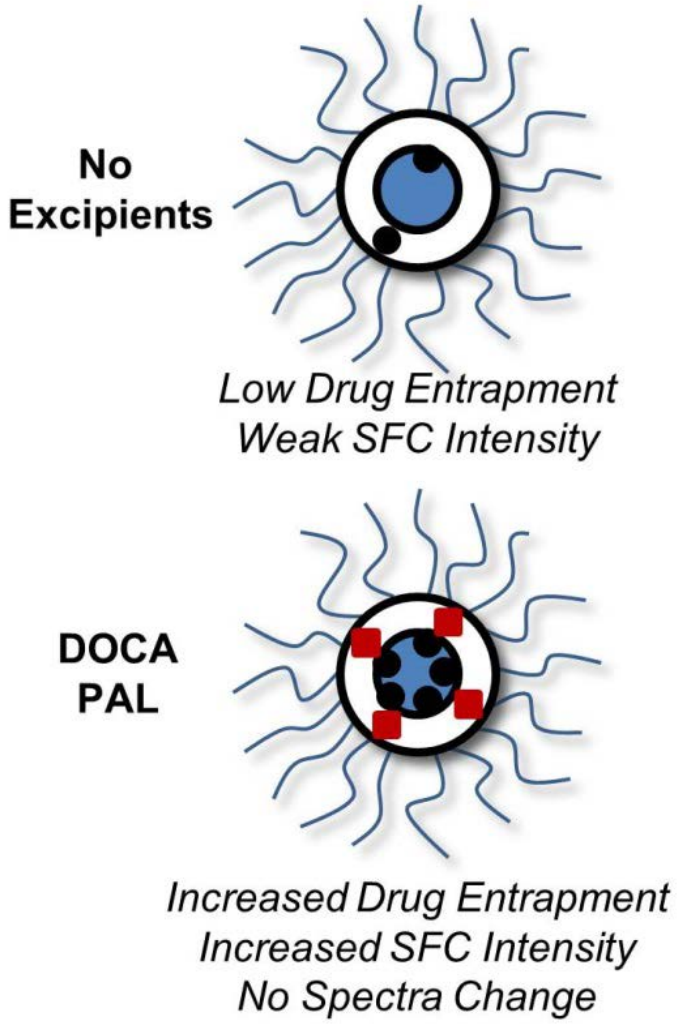

Figure 4.10. Graphical description of the theoretical mechanism for the effects of excipients on solvato-fluorochromism.

4.4.5 Advantages of Solvato-Fluorochromic Drug Release Measurements

This study suggests that the SFC method has the potential to monitor drug release from PNAs with a hydrophobic core. Although 2PN has a higher NB molar substitution than 3PN, drug-loaded 3PN showed greater fluorescence intensity than drug-loaded 2PN, suggesting that PAL kept drugs in the PNA core and forced water out of the core. As a result, hydrophobic drugs could interact with NB more efficiently in the hydrophobic 3PN core than in the hydrophilic 2PN core. Importantly, drug loading did not alter the maximum absorbance wavelengths for both PNAs. When DOCA was added to DOC-loaded 2PN and PAL was added to DOC-loaded 3PN, the HPLC-based and SFC methods showed statistically similar drug release rates. These observations suggest that the excipients could help hydrophobic drug molecules stay in the PNA core and interact with NB during drug release.

It should be noted that the HPLC-based method could not detect changes in the PNA core environment. The HPLC-based method failed to distinguish between DOC release profiles of 3PN and 2PN physically mixed with PAL, but the SFC method detected distinct SFC spectra for each formulation. The SFC method also indicated that hydrophobic excipients increased the initial dye-drug interactions in the core of PNAs, but the drug-dye interactions decreased quicker than in PNAs without excipients. This observation suggests that excipients may diffuse into solution over time, and the diffusion of excipients accelerates drug diffusion out of the nanoassembly core. Therefore, in comparison to HPLC-based methods, the SFC method provides more information regarding changes in the physicochemical properties within the nanoassembly core during drug delivery.

In regard to future clinical applications, SFC-based drug release determination may have two primary advantages over HPLC-based methods. First, SFC methods may enable researchers to perform *in situ* drug release measurements. In this study, SFC measurement timepoints and PNA concentrations were matched to HPLC timepoints and PNA concentrations in order to directly compare the methods, but fluorescence signals could be measured directly from tissues as well as dialysis cassettes without having to sample the solutions for fluorescence measurements (215, 216). Second, the SFC method may provide investigators with real-time drug release profiles that describe drug release more accurately than mathematical models of drug release kinetics using HPLC-based methods. Mathematical models of drug release from HPLC-based methods can oversimplify drug release kinetics by assuming that drug release rates remain constant over time. In addition, many HPLC-based methods sample high initial drug concentrations more than low terminal drug concentrations, which can increase fitting error by overweighting initial or terminal drug concentrations. However, SFC methods can provide real-time information about drugs leaving the nanoparticle core, which may overcome some of the limitations of mathematical modeling associated with HPLC-based method analysis. Therefore, NB-conjugated PNAs are expected to allow clinicians to address some of the limitations of HPLC-based methods and eventually perform *in situ* real-time measurements of drug concentrations in nanoparticles circulating in the bloodstream or accumulating in targeted tissues including tumors.

4.4.6 Limitations of Solvato-Fluorochromic Drug Release Measurements

Despite their previous applications described in chapter 2 and in the literature (217), SFC dyes have several limitations for measuring drug release from various

nanoparticle drug carriers. First, SFC dyes must remain in the nanoparticle core to detect accurate chemical properties within the nanoparticle core environment. Physically entrapped dyes in nanoparticles could diffuse into solution and reduce the SFC signal, which would cause the SFC method to overestimate drug release rates. For this reason, NB was covalently conjugated to PNAs with stable amide and imine bonds that prevent NB from leaving the PNA core during SFC measurements. In addition, SFC dyes must detect the entire nanoassembly core environment in order to accurately measure nanoassembly core properties. Therefore, nanoparticles should be designed to allow chemically conjugated SFC dyes to disperse throughout the entire nanoassembly core. Future experiments should determine if the spatial distribution of SFC dyes in the core of PNAs is homogeneous or heterogeneous.

SFC dyes in the nanoparticle core must remain intact during drug release experiments in order to measure accurate drug release. Chemical degradation of SFC dyes could decrease the fluorescence intensity of dye-loaded nanoparticles and increase SFC drug release rates. Based on the optical characterization of NB, the dye is chemically stable for up to 5 days in cell culture media at 37 °C. Therefore, NB in 2PN and 3PN should be chemically stable under the described experimental conditions. The photostability of NB was also confirmed for up to 10 fluorescence measurements under the described experimental conditions. In addition, solvato-fluorochromism of dyes in the nanoparticle core should be selective for encapsulated drugs in order to avoid interactions with hydrophobic small molecules such as free lipids that could diffuse into the hydrophobic core of nanoparticles and interfere with SFC signals (80, 218, 219). Based on the negligible value of the measured rate of drug re-entry into the PNA core,

hydrophobic small molecules are not expected to enter the PNA core and interact with fluorochromic dyes.

The sensitivity of the SFC method to detect drug in the PNA core indicates the potential of this method to measure accurate drug release rates. By measuring the fluorescence of PNAs, 1.5% and 3% drug loading by weight could be detected in DOC-loaded and CFZ-loaded 2PN. During SFC drug release measurements, 20% of the initial drug loading could be detected in PNAs before reaching minimal fluorescence values. Based on these values, minimum drug loading values of 0.3% DOC and 0.6% CFZ by weight could be detected by measuring the fluorescence of NB-conjugated PNAs. Estimations of the minimum detectable drug loading by solvato-fluorochromism are higher than the minimum detection limit of the HPLC-based method used in study. However, it should be noted that the minimum detectable drug loading was estimated from drug release data, and that a direct measurement of the SFC detection limit could indicate a higher sensitivity of the SFC method to detect drugs entrapped in the nanoassembly core.

It should be noted that 1) the SFC method is intended to only detect drugs leaving the nanoparticle core, 2) the SFC method cannot distinguish free drug in solution from drug that is weakly bound to the surface of the carriers, and 3) the relationship between SFC drug release measurements and the amount of biologically active drug in solution needs to be further elucidated. As a result, SFC measurements may overestimate free drug concentrations in tumor tissue. Mechanistic modeling showed that some released drug binds to the surface of PNAs and slows drug release during HPLC-based measurements, but previous research suggests that drug binding may not significantly

affect drug release rates *in vivo* because of low PNA concentrations in the blood or interstitial space compared to dialysis cassettes (220, 221). Determining the relationship between SFC drug release rates and drug concentrations in tissues is a significant area of future work.

4.5 Conclusions

A novel, SFC-based drug release measurement method was developed to overcome the limitations of HPLC-based methods for dialysis-based drug release measurements, such as unanticipated molecular interactions and complicated mass transfer effects between drugs, PNAs, and dialysis membranes. The SFC method demonstrated a facile and accurate determination of drug release rates compared to HPLC-based methods. A comparisons of both methods revealed that HPLC-based methods may be inaccurate at determining drug release involving interactions among drug, drug carriers, and hydrophobic excipients. Mechanistic modeling confirmed that drug rebinding and slow drug diffusion would influence HPLC-based but not the SFC-based method. These results indicate that the SFC method holds great promise to measure drug release rates for PNAs and potentially other nanoparticle drug carriers with improved convenience and accuracy compared to HPLC-based methods.

**Portions of Chapter 4 were previously published in (222). Reproduced with permission from Springer: Pharmaceutical Research, Volume 34, Issue 2, 2017, Pages 394-407, Figures 1, 4-10, and Text. Copyright 2016 is given to the publication in which the material was originally published.

CHAPTER FIVE

CHEMICAL MODIFICATIONS TO PNAs BASED ON A SOLVATO-FLUOROCHROMIC CHARACTERIZATION OF THE NANOASSEMBLY CORE ENVIRONMENT TO CONTROL DRUG RELEASE AND IMPROVE TEMPORAL DRUG DISTRIBUTION

5 CHEMICAL MODIFICATIONS TO PNAs BASED ON A SOLVATO-FLUOROCHROMIC CHARACTERIZATION OF THE NANOASSEMBLY CORE ENVIRONMENT TO CONTROL DRUG RELEASE AND IMPROVE TEMPORAL DRUG DISTRIBUTION

5.1 Introduction

Drug release rates from nanoparticles are often used to predict the spatial and temporal distribution of drugs in tumors, but modulating drug release rates in order to improve cancer treatment efficacy remains challenging (223). Nanoparticles with small diameters (10-100 nm) often accumulate in the leaky vasculature surrounding tumors at 3-12 hours post-injection and deliver anticancer drugs into the tumor interstitium (224, 225). Optimal drug release rates from nanoparticles can increase the accumulation of anticancer drugs in tumors by maximizing drug release from nanoparticles accumulated in the tumor vasculature (226). Rapid drug release rates can force nanoparticles to release drugs in blood vessels before the nanoparticles can accumulate in tumors (227). Drugs that are released in blood vessels may not reach tumors due to rapid renal clearance or off-target accumulation in healthy organs causing dose-limiting toxicity. In addition, slow drug release rates may decrease treatment efficacy by reducing peak anticancer drug concentrations in cancer cells. Therefore, methods of modulating drug release rates from nanoparticles are needed to increase anticancer drug accumulation in tumors and improve treatment efficacy.

The core environment of drug-loaded nanoparticles controls drug release into tumor tissue, but drug release rates remain difficult to modulate due to complicated thermodynamic and mass transport effects between drugs and polymers in the

nanoparticle core. For polymeric nanoparticles such as PNAs, diffusion out of the PNA core and binding to hydrophobic polymers are two main factors governing drug release (228, 229). Drugs must diffuse through the hydrophobic mesh-like core environment to reach the interface between the core and the hydrophilic shell. Diffusion rates of drugs in the hydrophobic core are influenced by both the chemical properties of the hydrophobic groups in the core and the pore size of the hydrophobic mesh. The hydrophobic core often contains water molecules that can interact with drugs or weakly hydrophobic portions of the core and influence diffusion rates. After drugs diffuse to the core-shell interface, they must cross the shell and partition into the surrounding solution. Environmental factors such as the solution pH and the chemical potential of drug at the interface in relation to the surrounding media can reduce drug release rates by decreasing the amount of drug that can partition into the surrounding solution (230). Researchers often control drug release rates from nanoparticles by altering the core environment hydrophobicity, which can slow diffusion by increasing the affinity of the drug for the core (231). Unfortunately, this approach is often ineffective at controlling drug release rates, because the specific effects of hydrophobic interactions on drug release are difficult to elucidate from drug release profiles. Experimental methods for determining the thermodynamic and mass transport effects contributing to poor drug release rates may identify rational approaches to modify the PNA core environment in order to control drug release rates.

Solvato-fluorochromism was previously identified as a useful method to probe the nanoparticle core environment and monitor its chemical properties during drug delivery. Although PAL was attached to the core of PNAs to create a hydrophobic core

environment capable of entrapping drugs, the quenched fluorescence of NB in the PNA core indicated that some water remained in the core and decreased the nanoassembly core hydrophobicity. The presence of water in the nanoassembly core was attributed to amines on the polymer scaffold that can interact with water molecules entering the PNA core. In addition, charged amine groups in the core can also repel cationic drugs or draw counterions into the PNA core. Chemical modifications to the polymer scaffold in the core of PNAs may remove these ionizable functional groups from the nanoassembly core. For example, primary amines can be end-capped by chemical reactions that form stable, unionizable amide bonds. In addition, secondary and tertiary amines can be removed from the core by synthesizing PNAs with polymer scaffolds that lack ionizable secondary or tertiary amines. Therefore, chemical modifications to PNAs to reduce the water concentration in the hydrophobic core promise to sustain drug release and improve temporal and spatial drug distribution in tumors.

This study addresses the drug delivery limitations of fluorochromic PNAs by rationally modifying the chemical environment of the nanoassembly core based on solvato-fluorochromism. These improved PNAs are synthesized similarly to fluorochromic PNAs (Figure 5.1). However, the remaining ionizable groups on polymer scaffolds were removed by replacing the PEI scaffold with a PLL scaffold, and by end-capping the remaining primary amines with either a chloroacetyl chloride (CAC) or acetic anhydride (AA) reaction. The core environments of these PNAs are fine-tuned to increase drug entrapment, avoid burst drug release and fine-tune drug release half-lives. In order to determine the effects of drug properties such as pKa or functional groups on drug loading and release, the entrapment and release of model drugs carfilzomib (CFZ)

and docetaxel (DOC) were determined. CFZ and DOC were selected as model anticancer drugs with distinct chemical structures (peptide vs. taxane), ionization potential (pKa of 5.1 for the morpholine group of CFZ vs. 11.0 for the carbamate group of DOC) and lipophilicity (logP of 4.2 vs. 2.4), respectively. Drug release kinetics of end-capped PNAs were evaluated using three models: a first order kinetic model, the Korsmeyer-Peppas model and the unsteady state spherical diffusion model. A first order kinetic model allowed the comparison of half-lives to determine the effects of polymer scaffold and end-capping groups on drug release. The Korsmeyer-Peppas model was selected as a semi-empirical model that indicates the mechanism of drug release from PNAs and justifies the selection of mechanistic drug release models. The unsteady state spherical diffusion model was selected as a mechanistic model that can measure the diffusivity of drug molecules in the core of PNAs. By removing ionizable functional groups from the nanoassembly core, this study evaluates the effects of ionizable groups on drug release from PNAs and validates solvato-fluorochromism as a beneficial method for characterizing the core environment of PNAs and potentially other nanoparticle drug carriers.

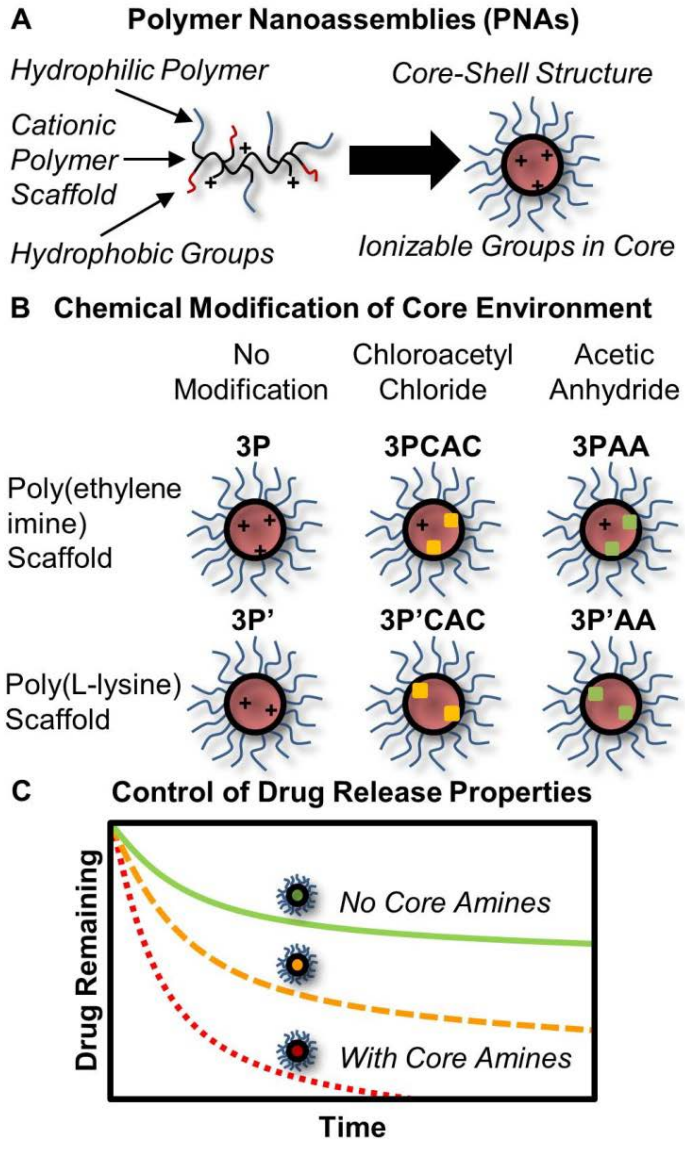

Figure 5.1. Graphical description of the end-capping approach to remove amines from the core of PNAs (A). Six PNAs were synthesized by varying the polymer scaffold and amine end-capping modification (B) to fine-tune drug release properties of PNAs (C).

5.2 Materials and Methods

5.2.1 Materials

α-Succinimidyloxysuccinyl-ω-methoxy-poly(ethylene glycol) (NHS-activated PEG, 5 kDa) was purchased from NOF America (White Plains, NY). Branched poly(ethylene imine) (PEI, 25 kDa), poly(L-lysine) (PLL, 15-30 kDa), acetic anhydride (AA), chloroacetyl chloride (CAC), HEPES sodium salt, palmitoyl chloride (PAL-Cl) and fluorescamine were purchased from Sigma Aldrich (St. Louis, MO). Acetonitrile (ACN), diethyl ether, dimethyl sulfoxide (DMSO), ethanol, pyridine, tetrahydrofuran (THF), water, phosphate buffered saline (PBS), dialysis membranes with molecular weight cut-off (MWCO) of 6-8 or 100 kDa, centrifugal filters (100 kDa MWCO) and dialysis cups (20 kDa MWCO) were purchased from Fisher Scientific (Waltham, MA). Carfilzomib (CFZ) and docetaxel (DOC) were purchased from LC Laboratories (Woburn, MA). To remove low molecular weight impurities from PEI before reactions, PEI was dialyzed in water overnight using a 100 kDa MWCO membrane. All other chemicals were used without further purification.

5.2.2 Synthesis of Unmodified and End-Capped PNAs with Various Polymer Scaffolds

As shown in Figure 5.2, PNAs containing various scaffolds and end-capping groups were synthesized by tethering NHS-activated PEG and PAL-Cl to PEI or PLL to yield 3P (PEG-PEI-PAL) and 3P' (PEG-PLL-PAL). 3P and 3P' were further reacted with either AA or CAC to yield 3PAA (PEG-PEI-PAL-AA), 3P'AA (PEG-PLL-PAL-AA), 3PCAC (PEG-PEI-PAL-CAC) and 3P'CAC (PEG-PLL-PAL-CAC). The synthesis of 3P was described in chapter 2. NHS-activated PEG (1951.8 mg) was reacted with PLL (100.0 mg) in a 4:1 mixed solution of HEPES buffer and DMSO for 3 days. The reaction

yielded PEG-PLL, which was purified by dialysis and collected after freeze drying. A portion of the PEG-PLL (1000.0 mg) was reacted with PAL-Cl (299 μl) at 40 °C for 2 hours in THF. To neutralize hydrochloric acid by-products formed during reactions, pyridine was added to the reaction mixtures in equal volume ratios to the acyl chloride reagents of all acyl chloride reactions 15 minutes after adding the reagent. The product 3P' was purified by ether precipitation and dialysis, and then collected after freeze drying. 3P and 3P' (100.0 mg each) were separately reacted with either AA (19.3 μl for each) at room temperature overnight in DMSO or with CAC (16.7 μl for each) at 40 °C for 2 hours in THF. Each AA or CAC reaction products was purified by dialysis and collected after freeze drying, yielding AA- and CAC-modified 3P and 3P'.

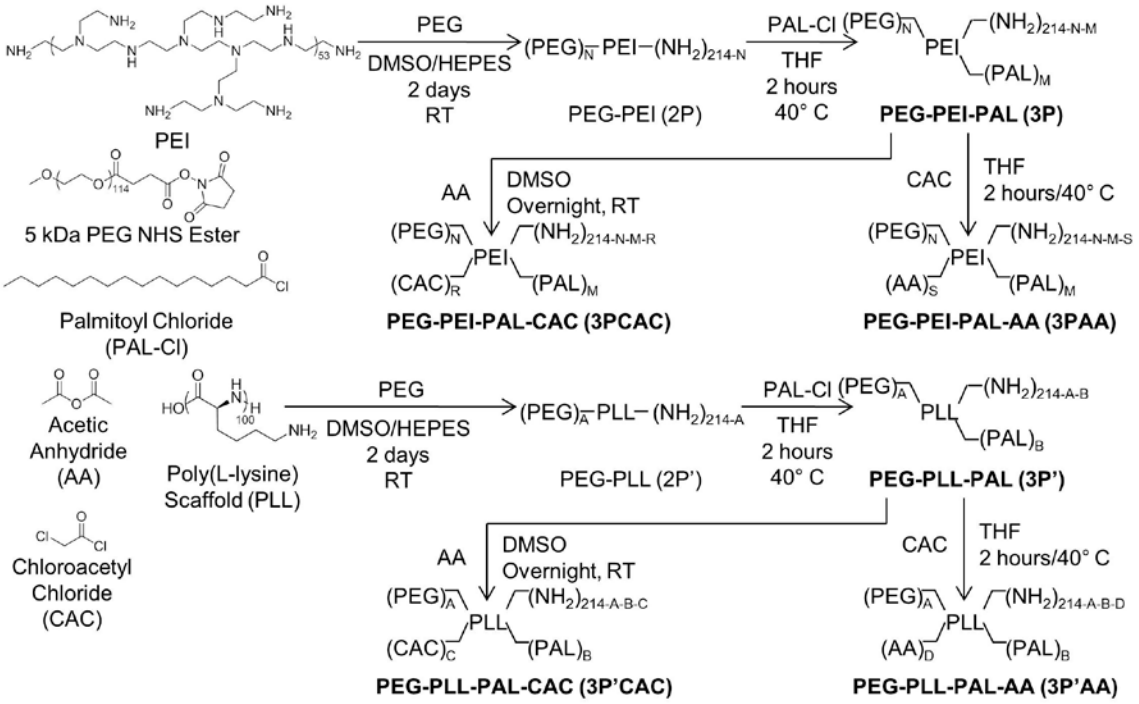

Figure 5.2. Synthesis protocol for unmodified and end-capped PNAs. All PNAs are shown to contain potentially unreacted primary amines.

5.2.3 Physical Characterization of Unmodified and End-Capped PNAs

Primary amines remaining in the core of PNAs were directly quantified using the amine-reactive fluorogenic dye fluorescamine. Because of potential fluorescence interactions between amine-conjugated fluorescamine and NB in the core of PNAs, primary amines in NB-conjugated PNAs were not quantified by fluorescamine in chapter 2. The PNAs 3P, 3PAA, 3PCAC, 3P', 3P'AA and 3P'CAC were separately dispersed in 1:1 DMSO/water solutions at 1 mg/ml, and fluorescamine was dissolved in DMSO at 10 mg/ml. Ten microliters of fluorescamine solution was added to 100 μl of blank solution and each PNA solution. The fluorescence of amine-conjugated fluorescamine (Ex 390 nm/Em 460 nm) in each solution was measured using a plate reader (Spectramax M5, Sunnyvale, CA). The baseline signal was removed from each sample by subtracting the fluorescence of the blank solution from the fluorescence of each sample. The baseline-corrected sample fluorescence was then normalized to the fluorescence of 3P (3PAA and 3PCAC) or 3P' (3P'AA and 3P'CAC). The relative size and dispersity of PNAs was determined by GPC as described in chapter 2 (Asahipak GF-7M, PBS, 0.5 ml/min, 40 °C, calibrated using PEG standards). The chemical compositions of each PNA were determined by proton NMR spectroscopy (Varian 400 MHz, DMSO-*d6*). The diameter and surface charge of each PNA was also determined by DLS (Zetasizer Nano ZS, Malvern, UK).

5.2.4 Hydrophobic Drug Loading of End-Capped PNAs

Stock solutions of PNAs (3P, 3PCAC, 3PAA, 3P', 3P'CAC and 3P'AA; 100 mg/ml) and drugs (CFZ and DOC; 1 mg/ml) were prepared in ethanol. Each PNA solution was mixed with either CFZ or DOC solution in a round-bottom flask, aiming for

10% drug loading. The mixed solutions were evaporated under reduced pressure to prepare thin films, which were rehydrated with deionized water and sonicated for 5 minutes. PNA solutions were then centrifuged for 1 minute at 1000 RPM to remove free drug and other insoluble impurities. The supernatants were then collected and lyophilized for storage. The drug loading efficiency, molar drug loading efficiency and encapsulation efficiency of PNAs was determined from reconstituted samples using HPLC as described in chapter 4.

5.2.5 Drug Release Measurements from Unmodified and End-Capped PNAs

Drug-loaded PNAs were dispersed in PBS (10 mg/ml). Each drug-loaded PNA solution (500 μl) was added to dialysis cups and dialyzed at 37 °C in 1 l of PBS. Aliquots of each sample (50 μl) from within the dialysis cups were collected at 0, 1, 3, 6, 24 and 48 hours. Drug remaining in these aliquots was quantified by HPLC, and the drug release profiles for each drug-PNA combination were fitted to multiple kinetic models of drug release using Prism (GraphPad, La Jolla, CA). Initially, drug release models were fit to first order kinetic models (equation 4.1) as described in chapter 4.

In order to further elucidate the mechanism of drug release from PNAs, drug release profiles were fit to the Korsmeyer-Peppas model of drug release in equation 5.1.

$$\frac{M_t}{M_\infty} = Kt^N \qquad (5.1)$$

In equation 5.1, M_t is the mass of released drug at time t, M_∞ is the mass of released drug after an infinite amount of time, K is a kinetic constant with units of inverse hours and N is a unitless constant determined experimentally. Equation 5.1 was simplified to equation 5.2.

$$\frac{C_t}{C_0} = Kt^N \qquad (5.2)$$

In equation 5.2, C_t/C_0 is the concentration ratio of drug in the dialysis cup at time *t* to the initial concentration as a percent. For drug release modeling, an N value with standard error of mean equal to or below 0.45 was defined as Fickian diffusion-controlled drug release, while N values between 0.45 and 0.85 were defined as non-Fickian transport-based drug release.

An unsteady state spherical diffusion model of mass transfer was developed to determine the diffusivity of drugs in the PNA core. The model was based on detailed derivations by Arifin *et al.* (232). Initially, PNAs were assumed to be spherical and have a constant diameter during drug release. The core-shell interface was also assumed to have zero chemical potential for the drug (sink condition). Equation 5.3 below describes diffusion-controlled drug release from a sphere obeying these assumptions.

$$\frac{M_t}{M_\infty} = 1 - \frac{6}{\pi^2} * \sum_{n=1}^{\infty} \frac{1}{n^2} * e^{\frac{-D*n^2*\pi^2*t}{a^2}} \quad (5.3)$$

In equation 5.3, M_t is the mass of released drug at time *t*, M_∞ is the mass of released drug after an infinite time, *D* is the drug diffusivity with units of m^2/s, and *a* is the radius of the hydrophobic core with units of m (core radius measurement described below). In order to simplify comparison, *D* is reported in units of cm^2/s and *a* is reported in units of nm. Equation 5.3 can be rearranged in terms of concentration in the form of equation 5.4.

$$C = C_0 * \frac{6}{\pi^2} * \sum_{n=1}^{\infty} \frac{1}{n^2} * e^{\frac{-D*n^2*\pi^2*t}{a^2}} \quad (5.4)$$

In equation 5.4, *C* is the concentration of drug in the dialysis cup in micrograms per milliliter. At the initial timepoint, the concentration of drug is equal to the total initial

drug concentration C_0 with units of micrograms per milliliter and the infinite sum is equal to $\pi^2/6$. Therefore, equation 5.4 can be further simplified into equation 5.5.

$$\frac{C_t}{C_0} = \frac{6}{\pi^2} * \sum_{n=1}^{\infty} \frac{1}{n^2} * e^{\frac{-D*n^2*\pi^2*t}{a^2}} \quad (5.5)$$

Drug release profiles were fit to equation 5.5. In order to assure the accurate fitting of drug release profiles, weighting values were adjusted between 0 and 2. Because the higher order terms in the infinite series converged to zero quickly, equation 5.5 was approximated to ten terms in order to prevent overfitting of the data.

The radius of the hydrophobic core (a) of PNAs in equation 5.5 was estimated using equation 5.6, which assumes the hydrodynamic diameter of a PNA is equal to two times the sum of the radii of the hydrophobic core and PEG shell (233).

$$D_{HYD} = 2 * R_{SHELL} + 2 * a \quad (5.6)$$

In equation 5.6, D_{HYD} is the hydrodynamic diameter of nanoparticles measured by DLS, a is the radius of the hydrophobic core and R_{SHELL} is the radius of the PEG shell. All diameters and radii have units of nm. R_{SHELL} is determined using equation 5.7.

$$R_{shell} = 2R_{G,PEG} - 2 * 0.215{M_W}^{0.583} \quad (5.7)$$

In equation 5.7, $R_{G,PEG}$ and M_W are the radius of gyration (nm) and molecular weight of PEG (g/mol), respectively. For the methoxy-terminated 5 kDa PEG in the shell of PNAs, R_{SHELL} was determined to be 6.16 nm.

5.2.6 Statistics

All values are reported as mean±standard deviation of triplicate measurements, while model parameters are described as mean±SEM unless indicated otherwise. Groups of measurements were compared using one-way ANOVA with Bonferroni's post hoc

test, while pairs were compared with a Student's t test. Statistical significance is indicated by * ($p<0.05$), ** ($p<0.01$) or *** ($p<0.001$).

5.3 Results

5.3.1 End-Capping Groups Do Not Affect the Size or Surface Charge of PNAs

Proton NMR confirmed the successful synthesis of 3P [PEG (3.54 ppm, s, relative area 1.000), PEI (2.32 ppm, s, relative area 0.017; 2.44 ppm, s; 2.55 ppm, s; 2.60 ppm, s; 2.66 ppm, s, relative area 0.019), and PAL (0.83 ppm, d, relative area 0.022; 1.20 ppm, s, relative area 0.082)] and 3P' [PEG (3.51 ppm, s, relative area 1.000), PLL (1.24 ppm, s, relative area 0.043; 2.23 ppm, m, relative area 0.102; 2.60 ppm, s, relative area 0.007; 2.68 ppm, s, relative area 0.009; 2.97 ppm, s, relative area 0.009; 3.24 ppm, s, relative area 0.118; 3.42 ppm, s, relative area 0.117; 3.68 ppm, s, relative area 0.012; 4.09 ppm, s, relative area 0.007; 7.78 ppm, s, relative area 0.008), and PAL (0.83 ppm, d, relative area 0.006; 1.23 ppm, s, relative area 0.043; 1.46 ppm, s, relative area 0.021)]. Acetyl peaks on 3PAA (1.90 ppm, s, relative area 0.017) and 3P'AA (1.78 ppm, s, relative area 0.011) confirmed AA end-capping, while acetyl chloride peaks on 3PCAC (4.15 ppm, s, relative area 0.018) and 3P'CAC (4.27 ppm, s, relative area 0.006) confirmed CAC end-capping. The calculated molar substitutions (defined in chapter 2) of PEG, PAL, CAC, and AA on the polymer scaffolds of PNAs are described in Table 5.1. Based on the molar substitution of each component, 52 to 100 percent of primary amines on these PNAs were end-capped. GPC confirmed that 3P, 3PCAC, 3PAA, 3P', 3P'CAC and 3P'AA had uniform molecular weight distribution and were free of small molecule impurities as shown in Figure 5.3.

Table 5.1. Molar substitution of unmodified and end-capped PNAs. PEG, PAL and end-capping group substitution were determined by NMR quantification.

	Molar Substitution (mol/mol primary amine on scaffold) (%)				Remaining Amines (mol/mol primary amine on scaffold) (%)
PNA	PEG	PAL	CAC	AA	NH_2
3P	10.0±0.3	55.0±1.4	---	---	35.0±1.4
3PCAC	10.0±0.3	55.0±1.4	20.0±0.5	---	15.0±1.5
3PAA	10.0±0.3	55.0±1.4	---	23.0±0.6	12.0±1.6
3P’	5.0±0.1	47.0±1.2	---	---	48.0±1.2
3P’CAC	5.0±0.1	47.0±1.2	33.0±0.8	---	15.0±1.4
3P’AA	5.0±0.1	47.0±1.2	---	48.0±1.2	0.0±1.7

PEG, PAL, CAC and AA substitution are reported as measurement±measurement error for NMR (n=1). CAC and AA were not detectable on 3P or 3P’. CAC was not detectable on 3PAA or 3P’AA, while AA was not detectable on 3PCAC or 3P’CAC. Error from PEG, PAL, CAC and AA quantification were propagated into the remaining amine quantification.

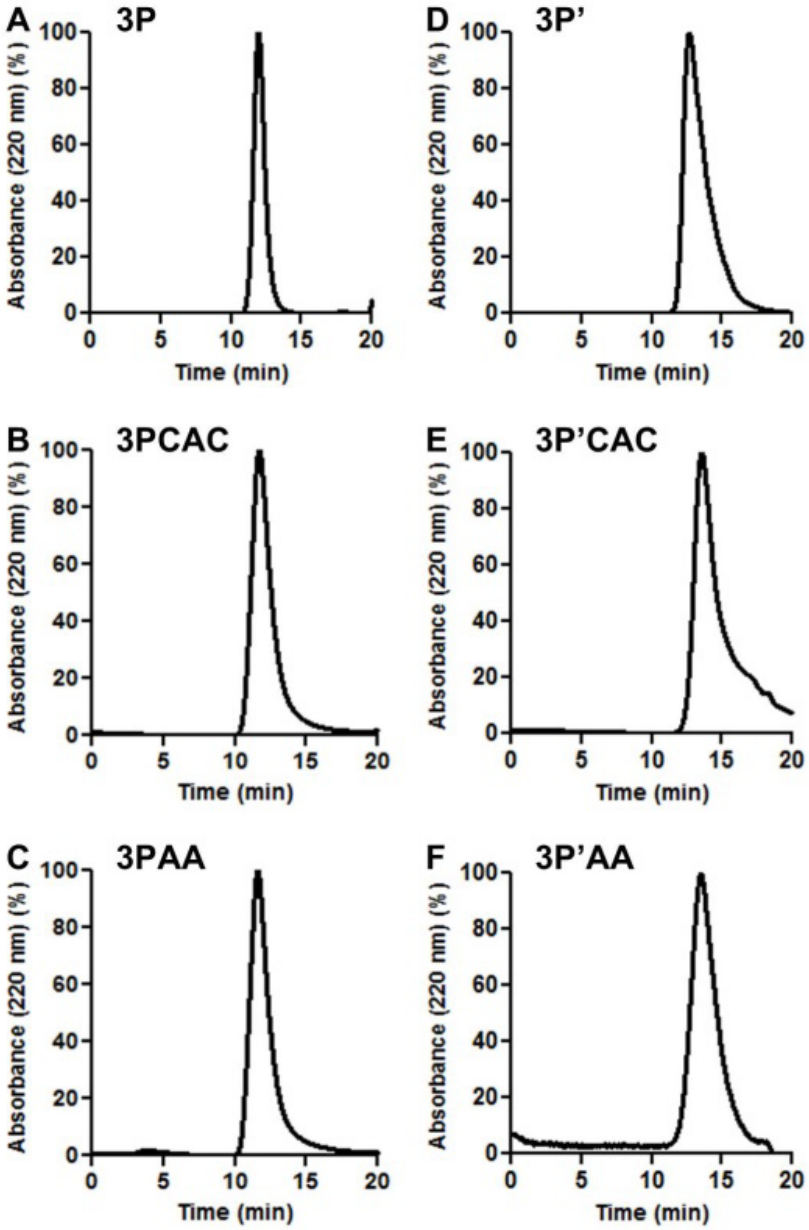

Figure 5.3. Gel permeation chromatographs of unmodified and end-capped PNAs 3P (A), 3PCAC (B), 3PAA (C), 3P' (D), 3P'CAC (E) and 3P'AA (F). Chromatographs were measured by UV-visible absorbance detector at 220 nm.

The diameter and surface charge of the PNAs were measured by DLS. As summarized in Table 5.2, all PNAs were between 15 and 40 nm in diameter. End-capping reactions slightly decreased the diameter of 3P, but the reactions increased the diameter of 3P'. However, the size changes of each PNA following end-capping reactions were not statistically significant. All PEI-based PNAs had zeta potentials between -10 and 10 mV indicating a neutral surface. The PEG in the shell of PEI-based PNAs shields any charged groups remaining in the core and allows the PNAs to have a neutral surface charge. 3P'AA without core amines also had a neutral surface, but 3P' and 3P'CAC with core amines had large positive zeta potentials (>10 mV) indicating a positively charged surface. These results suggest that the PEG in the shell of PLL-based PNAs may not shield charged groups in the core from the surface. The differences in surface charge between PEI-based PNAs are not statistically significant, but the differences in surface charge between 3P'AA and 3P' or 3P'CAC are statistically significant. The diameter and zeta potential of drug-loaded PNAs could not be directly determined by DLS due to the turbidity of the samples which prevented the accurate detection of scattered light. Increased turbidity of PNA colloidal solutions after drug loading could be due to two factors: 1) increased diameter of drug-loaded PNAs increasing light scattering by the Tyndall effect (234), or 2) disruption of the palmitate in the nanoassembly core leading to the formation of a cloudy emusion near the PNA core due to undesired interactions between water and palmitate groups. Further studies are needed to elucidate the causes for cloudiness of drug-loaded PNAs.

Table 5.2. Physicochemical properties of unmodified and end-capped PNAs.

Nanoparticle	Diameter (nm)	Zeta Potential (mV)	PDI (unitless)
3P	35.2±5.5	-5.2±0.8	0.38±0.04
3PCAC	32.6±7.8	-1.3±0.6	0.37±0.01
3PAA	29.5±4.6	-4.1±0.7	0.42±0.08
3P’	16.3±3.0	29.5±1.6	0.56±0.02
3P’CAC	22.4±3.4	26.0±3.5	0.54±0.01
3P’AA	22.4±2.8	-6.0±0.6***	0.62±0.09

Diameter, zeta potential and PDI are reported as mean±SD (n=3). Statistical significance is determined by a one-way ANOVA with Bonferroni’s post-test correction for each group as described in the methods section.

5.3.2 End-Capping Group Bulkiness and Scaffold Amine Steric Hindrance Control End-Capping Reaction Yields

A fluorescamine assay was used to quantify the remaining primary amines in PNAs after end-capping reactions with AA or CAC. Figure 5.4 shows the normalized fluorescence of fluorescamine-modified PEI- and PLL-based PNAs. All PNAs were in the linear range of a fluorescamine calibration curve. The AA reaction decreased the fluorescence of 3PAA by 65% compared to 3P, and the reaction decreased the fluorescence of 3P'AA by greater than 99% compared to 3P'. The decreases in fluorescence correspond to a 65% and greater than 99% molar substitution yield for AA on 3PAA and 3P'AA, respectively. By comparing the changes in fluorescence to the remaining primary amines on 3P or 3P' before the reaction, the molar substitution of AA on PNAs could be determined. These decreases in fluorescence correspond to 23% and 48% AA molar substitution of 3PAA and 3P'AA, respectively, which is in agreement with NMR quantification. In contrast, the CAC modification showed false positive signals during the fluorescamine assay which were not in agreement with NMR quantification. The CAC reaction increased the fluorescence of 3PCAC by 54% compared to 3P, and it increased the fluorescence of 3P'CAC by 68% compared to 3P'. The decreases in fluorescence correspond to a 54% and 68% increase in primary amines on 3PCAC and 3PCAC following the reaction with CAC. These increases correspond to a 19% and 33% increase in primary amines on 3P and 3P', respectively. False positives from the fluorescamine assay may be due to three causes: 1) physical interactions between amine-conjugated fluorescamine and CAC groups in the core of PNAs that alter the electronic environment of the dye, 2) an unexpected reaction between fluorescamine

and CAC that produces a highly fluorescent side product, or 3) fluorescence of CAC groups in the same wavelength range as amine-conjugated fluorescamine. It should be noted that fluorescamine reacts with primary amines by nucleophilic addition of the amine (235), and that chloride groups are unlikely to undergo the same addition. In addition, both 3PCAC and 3P'CAC were non-fluorescent under fluorescamine measurement conditions. Although physical reactions between CAC groups and reacted fluorescamine in the core of PNAs are hypothesized to increase fluorescence signals, further studies are needed to elucidate a detailed mechanism of the increased fluorescence signals. Other amine-reactive fluorogenic dyes such as ninhydrin were considered as an alternative method of directly quantifying the remaining primary amines in the core of CAC-reacted PNAs, but the elevated temperature often required for these reactions may degrade the peptide scaffold of 3P' PNAs and generate primary amines that increase the fluorescence signal following the assay (236, 237). Because NMR quantification was verified as an accurate method to determine the AA end-capping yield of PNAs, the NMR quantification was used exclusively to determine the end-capping reaction yield of CAC-modified PNAs.

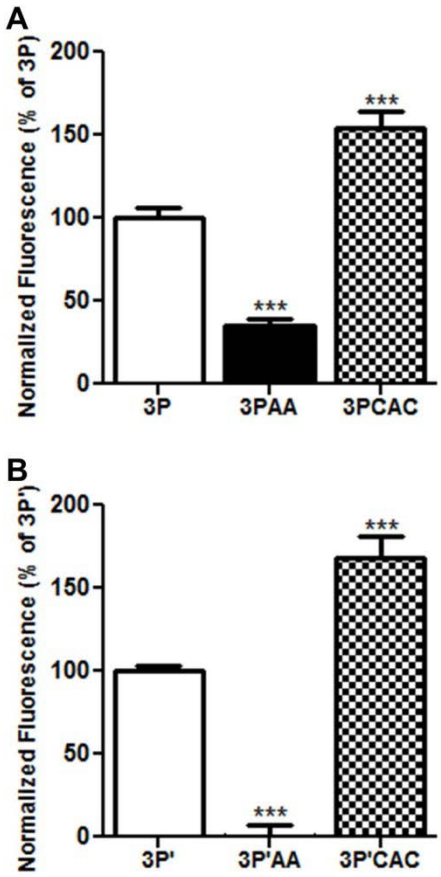

Figure 5.4. Fluorescamine quantification of primary amines in unmodified and end-capped PNAs. Primary amines were quantified in PEI-based (A) and PLL-based (B) PNAs and normalized to unmodified PNAs for each group.

5.3.3 Removal of Amines from the PNA Core Increases Drug Loading and Encapsulation Efficiency

The drug loading and encapsulation efficiencies of PNAs are summarized in Table 5.3. End-capped PNAs increased CFZ loading compared to unmodified PNAs, and end-capping reactions allowed PNAs to stably entrap DOC. In addition, PLL-based PNAs had higher CFZ and DOC loading efficiencies than PEI-based PNAs. These differences in drug loading efficiencies between PNAs are statistically significant. Both 3P and 3P'were unable to stably entrap DOC, and thus DOC-loaded 3P and 3P' were not tested further. For both PEI- and PLL-based PNAs, drug loading and encapsulation efficiency were highest with the AA modification. Statistical trends of the drug loading and encapsulation efficiencies of PNAs are summarized in Figure 5.5.

Table 5.3. Drug loading of unmodified and end-capped PNAs.

Drug	PNAs	Drug Loading Efficiency (w/w %)	Molar Drug Loading Efficiency (mol Drug/mol PNA)	Encapsulation Efficiency (w/w %)
CFZ	3P	4.3±0.2	9.7±0.5	44.5±1.8
	3PCAC	6.7±0.5	15.4±1.1	71.8±5.7
	3PAA	6.8±0.2	15.5±0.5	73.5±2.1
CFZ	3P’	5.3±0.5	4.4±0.4	55.8±5.2
	3P’CAC	8.3±1.0	7.2±0.9	90.1±10.4
	3P’AA	8.8±0.7	7.5±0.6	96.2±7.2
DOC	3P	---	---	---
	3PCAC	3.3±0.1	6.8±0.2	34.2±2.0
	3PAA	4.7±0.1	9.6±0.2	49.3±1.1
DOC	3P’	---	---	---
	3P’CAC	6.2±1.0	4.8±0.8	66.4±10.8
	3P’AA	7.6±0.7	5.8±0.5	81.9±7.9

Drug loading efficiency, molar drug loading efficiency and encapsulation efficiency are reported as mean±SD (n=3). Statistical significance is indicated in Figure 5.5.

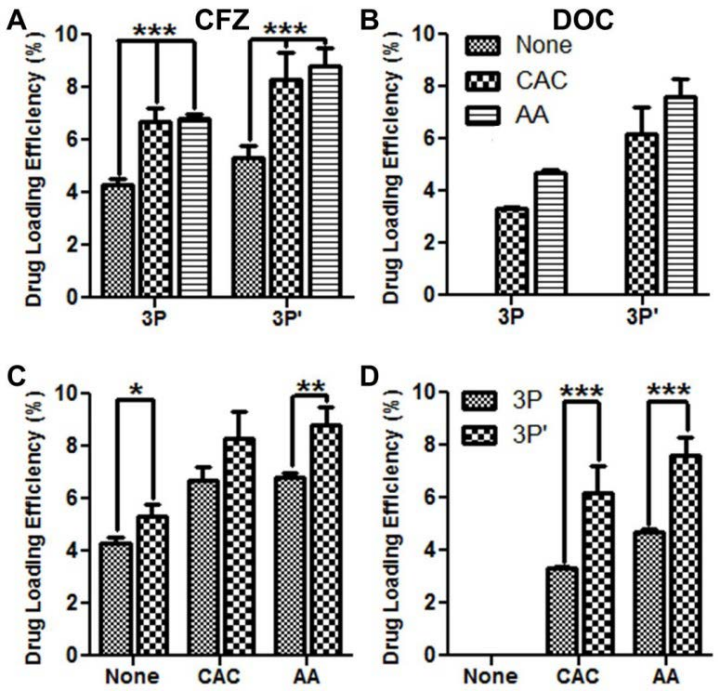

Figure 5.5. Drug loading efficiency of unmodified and end-capped PNAs. Drug loading was determined using the model drugs carfilzomib (A,C) and docetaxel (B,D).

5.3.4 Amine End-Capping Groups Sustain Drug Release from PNAs

Figures 5.6 and 5.7 show drug release profiles from CFZ- and DOC-loaded PNAs, respectively. The first order kinetic model was a good approximation for the release of CFZ and DOC from drug-loaded PNAs. Drug release rates were consistent over 48 hours, and burst release was not observed for the PNAs used in this study. This model failed to provide any mechanistic information about drug release mechanisms from PNAs, but it did provide a facile method of comparing drug release between formulations. End-capping modifications increased the half-life of CFZ release from PNAs in order of no, CAC, and AA modifications for both PEI- and PLL-based PNAs, with the exception of CFZ-loaded 3P'CAC which decreased its drug release half-life (Table 5.4 and Figure 5.8). In addition, the AA modification increased the half-life of DOC release compared to CAC modification for both PEI- and PLL-based PNAs. PLL-based PNAs increased drug release half-life compared to PEI-based PNAs with the exception of CFZ-loaded 3P'CAC. These results suggest that the chemical modification of PNAs to remove charged groups from the core can increase drug release half-life and sustain drug release over time.

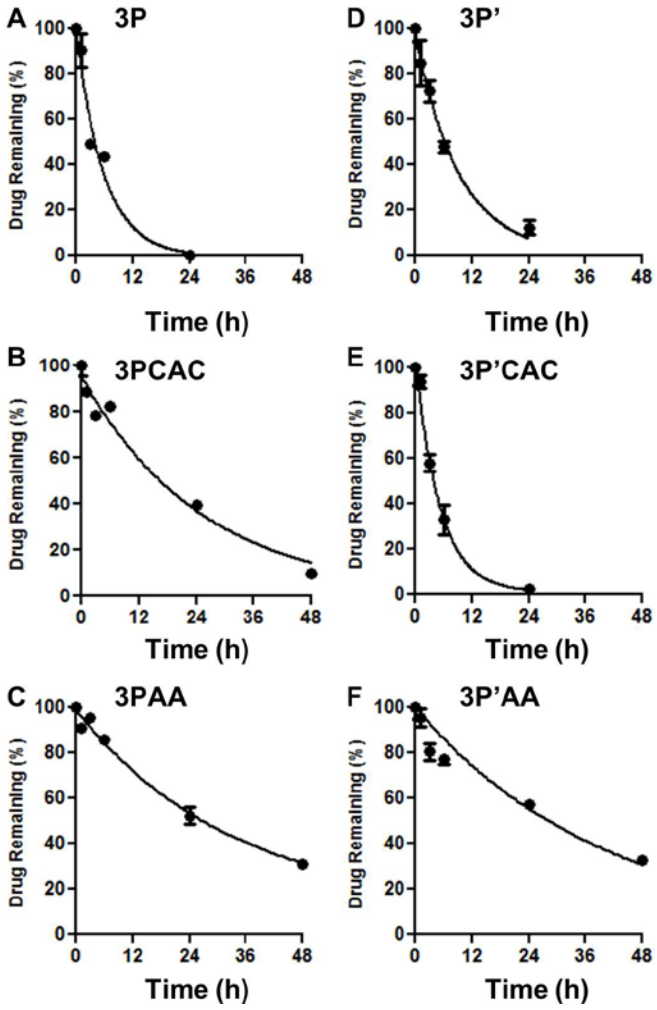

Figure 5.6. Carfilzomib release profiles from unmodified and end-capped PNAs 3P (A), 3PCAC (B), 3PAA (C), 3P' (D), 3P'CAC (E) and 3P'AA (F).

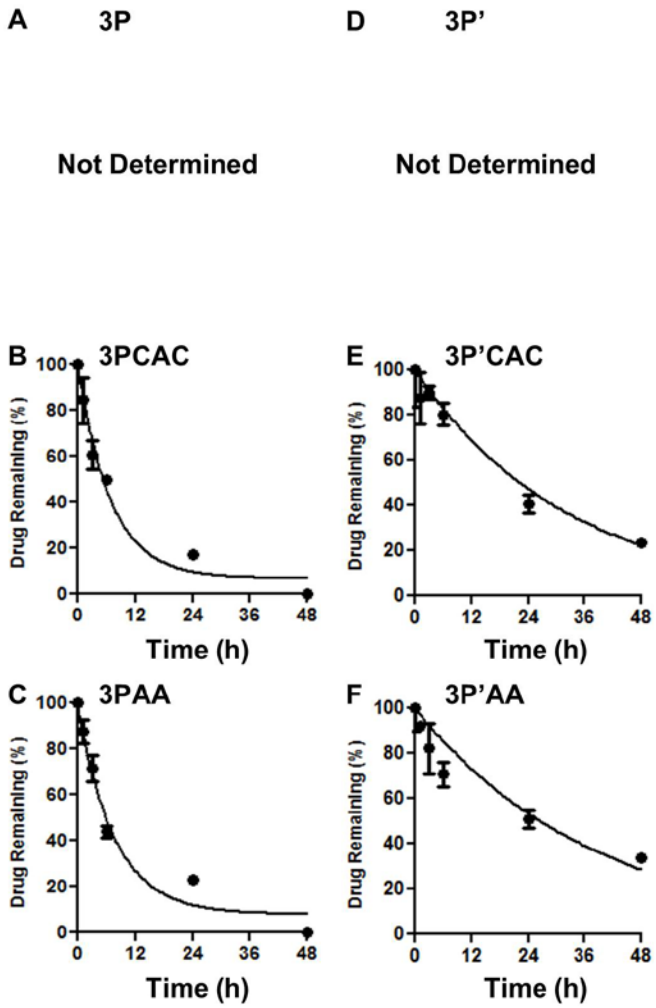

Figure 5.7. Docetaxel release profiles from unmodified and end-capped PNAs 3P (A), 3PCAC (B), 3PAA (C), 3P' (D), 3P'CAC (E) and 3P'AA (F). Due to poor drug loading of 3P (A) and 3P' (D), drug release was not measured from these PNAs.

Table 5.4. Parameters from a first order kinetic model for drug release from unmodified and end-capped PNAs.

Drug	PNAs	$t_{1/2}$ (h)	k (h^{-1})
CFZ	3P	4.1 (3.0-6.6)	0.169 (0.106-0.233)
	3PCAC	17.5 (14.9-21.1)	0.040 (0.033-0.046)
	3PAA	23.1 (17.8-33.2)	0.030 (0.020-0.039)
CFZ	3P’	6.5 (4.9-9.6)	0.107 (0.072-0.142)
	3P’CAC	3.6 (2.7-5.5)	0.190 (0.127-0.253)
	3P’AA	28.2 (24.5-33.1)	0.024 (0.020-0.028)
DOC	3P	---	---
	3PCAC	4.8 (3.6-7.1)	0.146 (0.097-0.194)
	3PAA	5.3 (3.7-9.5)	0.130 (0.072-0.187)
DOC	3P’	---	---
	3P’CAC	22.3 (18.8-27.5)	0.031 (0.025-0.037)
	3P’AA	26.6 (22.3-33.1)	0.026 (0.021-0.031)

Kinetic parameters are reported as mean with 95% CI in parentheses. Differences in kinetic parameters between each model were compared by an extra sum of squares F test. Statistical significance is reported in figure 5.8.

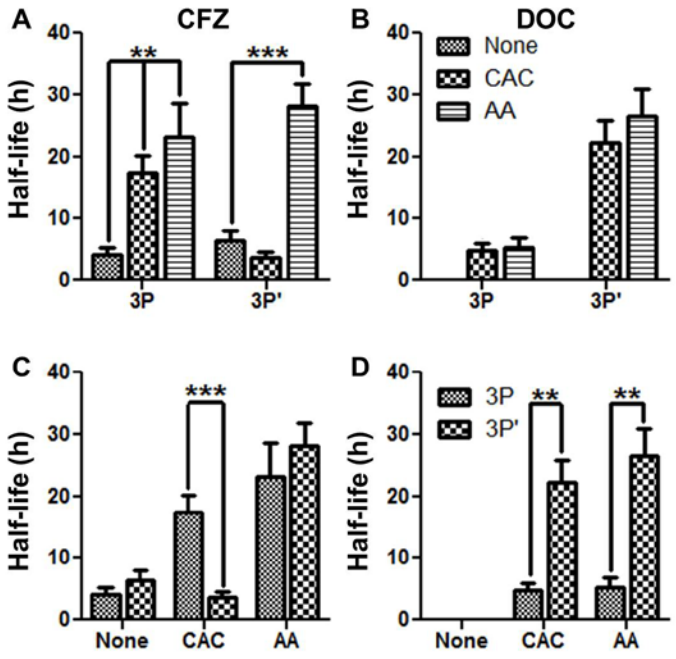

Figure 5.8. Drug release half-lives from unmodified and end-capped PNAs. Drug release half-lives were determined using the model drugs carfilzomib (A,C) and docetaxel (B,D).

5.3.5 Drug Diffusion through the Hydrophobic Core of PNAs Controls Drug Release

Figure 5.9 shows drug release profiles of PNAs that were modeled with the Korsmeyer-Peppas model. The Korsmeyer-Peppas model fit the drug release profiles well for all PNAs except for DOC-loaded 3P'CAC, which underestimated terminal drug release for weighting values of 0, 1 and 2. Table 5.5 shows kinetic parameters from the Korsmeyer-Peppas model. End-capping reactions decreased the kinetic constant *K* compared to unmodified PNAs, which confirms the results from the first-order kinetic models. In all cases, AA-modified PNAs had lower *K* than CAC-modified PNAs. PLL-based PNAs decreased *K* for DOC compared to PEI-based PNAs, but the scaffold had a minimal effect on *K* for CFZ-loaded PNAs. Figure 5.10 compares N values of drug release from end-capped PNAs. The 95% confidence intervals of the N values for most PNAs contained 0.45, indicating that drug release was diffusion-controlled. The 95% confidence intervals of the N values for CFZ-loaded 3PCAC and 3PAA were between 0.45 and 0.65, indicating that other transport processes in addition to diffusion may control drug release. The 95% confidence intervals of the N values for PNAs was not greater than 0.85, suggesting that a receding boundary of the hydrophobic core did not contribute to drug release. Based on these findings, drug release profiles were further modeled using a diffusion-based drug release model.

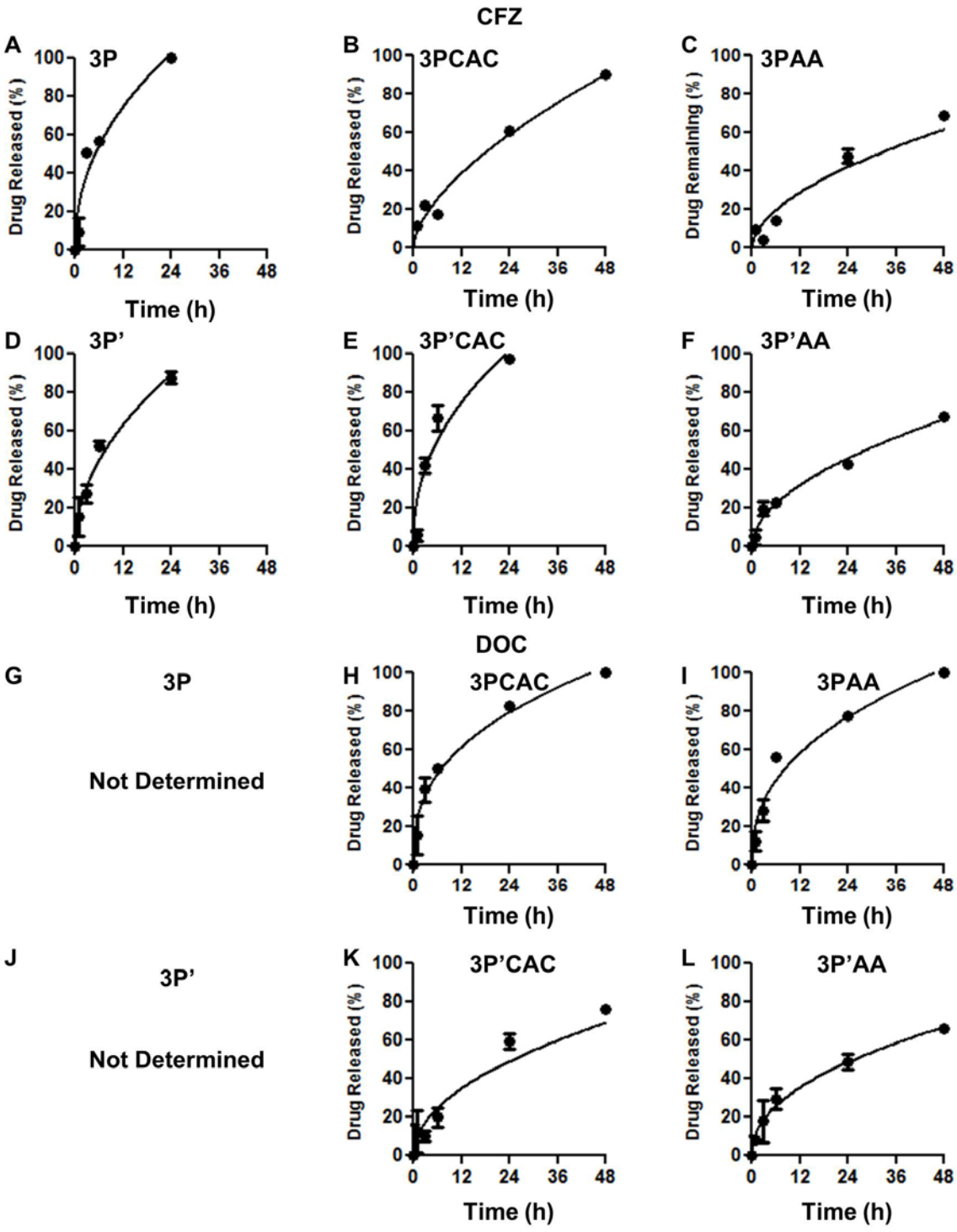

Figure 5.9. Drug release profiles of unmodified and end-capped PNAs using the Korsmeyer-Peppas drug release model. Drug release profiles were measured using model drugs CFZ (A-F) and DOC (G-L). Due to poor DOC loading of 3P (G) and 3P' (J), drug release was not measured from these PNAs.

Table 5.5. Kinetic parameters for drug release from unmodified and end-capped PNAs using the Korsmeyer-Peppas model. N values indicate a Fickian diffusion-controlled (N=0.45), a non-Fickian transport-controlled (0.45<N<0.85), or an anomalous transport-controlled drug release mechanism (N>0.85).

Drug	PNA	K (h^{-1})	N (unitless)	Release Mechanism
CFZ	3P	24.0 (16.5-31.5)	0.46 (0.34-0.57)	Fickian Diffusion
	3PCAC	8.5 (5.9-11.1)	0.61 (0.53-0.70)	Non-Fickian Transport
	3PAA	7.3 (4.3-10.2)	0.55 (0.46-0.65)	Non-Fickian Transport
CFZ	3P’	18.3 (11.5-25.1)	0.50 (0.36-0.63)	Fickian Diffusion
	3P’CAC	25.1 (15.2-35.0)	0.44 (0.30-0.58)	Fickian Diffusion
	3P’AA	8.7 (6.3-11.1)	0.52 (0.45-0.60)	Fickian Diffusion
DOC	3P	-	-	-
	3PCAC	24.1 (17.7-30.5)	0.38 (0.30-0.46)	Fickian Diffusion
	3PAA	21.1 (15.2-27.1)	0.41 (0.32-0.49)	Fickian Diffusion
DOC	3P’	-	-	-
	3P’CAC	10.2 (5.6-14.9)	0.49 (0.40-0.60)	Fickian Diffusion
	3P’AA	11.2 (7.0-15.4)	0.46 (0.37-0.55)	Fickian Diffusion

Kinetic parameters are reported as mean with 95% CI in parentheses. The 95% confidence intervals of N values were compared to 0.45 to determine the drug release mechanism.

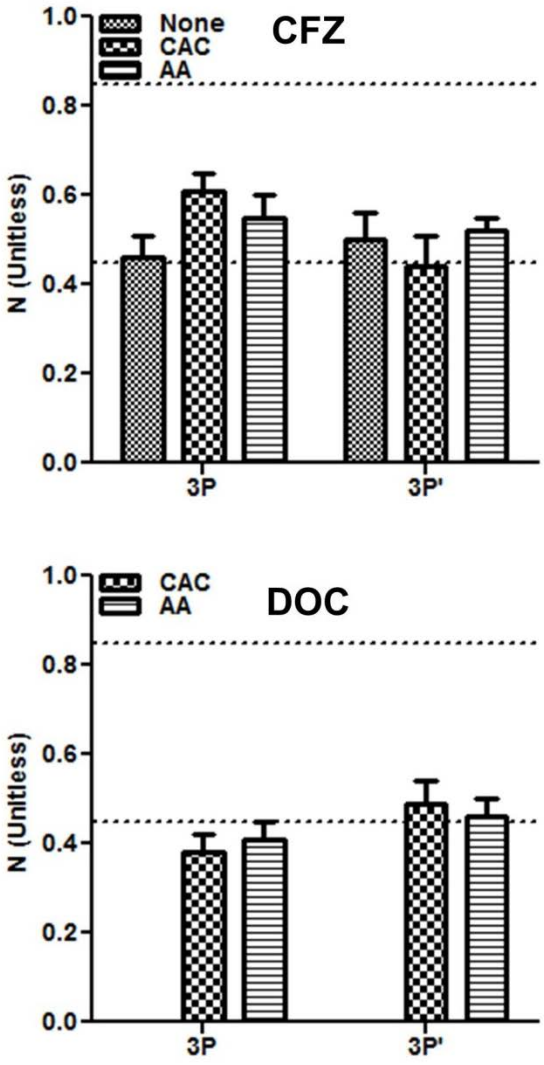

Figure 5.10. N values from the Korsmeyer-Peppas drug release model for unmodified and end-capped PNAs.

5.3.6 Amine End-Capping Groups Decrease Drug Diffusivity in the Core of PNAs

Figure 5.11 shows drug release profiles for CFZ and DOC using an unsteady state spherical diffusion model. Semi-log plots of concentration vs. time were slightly curved, but the model fit the data well up to 90% of drug released. Table 5.6 summarizes the drug diffusivities and hydrophobic core diameters of various PNAs. In comparison to the estimated diffusivity of free CFZ or DOC at 37 °C in water from the Stokes-Einstein equation, PNAs reduced drug diffusivity by 4- to 5-fold, perhaps due to increased density and interactions with the PNA core. Amine end-capping reactions decreased the radius of the hydrophobic core for PEI-based PNAs, but they increased the hydrophobic core radius of PLL-based PNAs. PLL-based PNAs had smaller core radii than PEI-based PNAs for each end-capping modification, possibly due to the compact secondary structure of unmodified PLL compared to PEI. Figure 5.12 compares drug diffusivities in the core of end-capped PNAs. AA modifications decreased the diffusivity of both CFZ and DOC in PNAs, but CAC modifications increased the diffusivity of CFZ in 3P'CAC. These results suggest that end-capping modifications to PNAs can sustain drug release from the core of PEI-based PNAs by decreasing the diffusivity of drugs in the PNA core, but that end-capping modifications of PLL-based PNAs sustain drug release by increasing the diameter of the hydrophobic core.

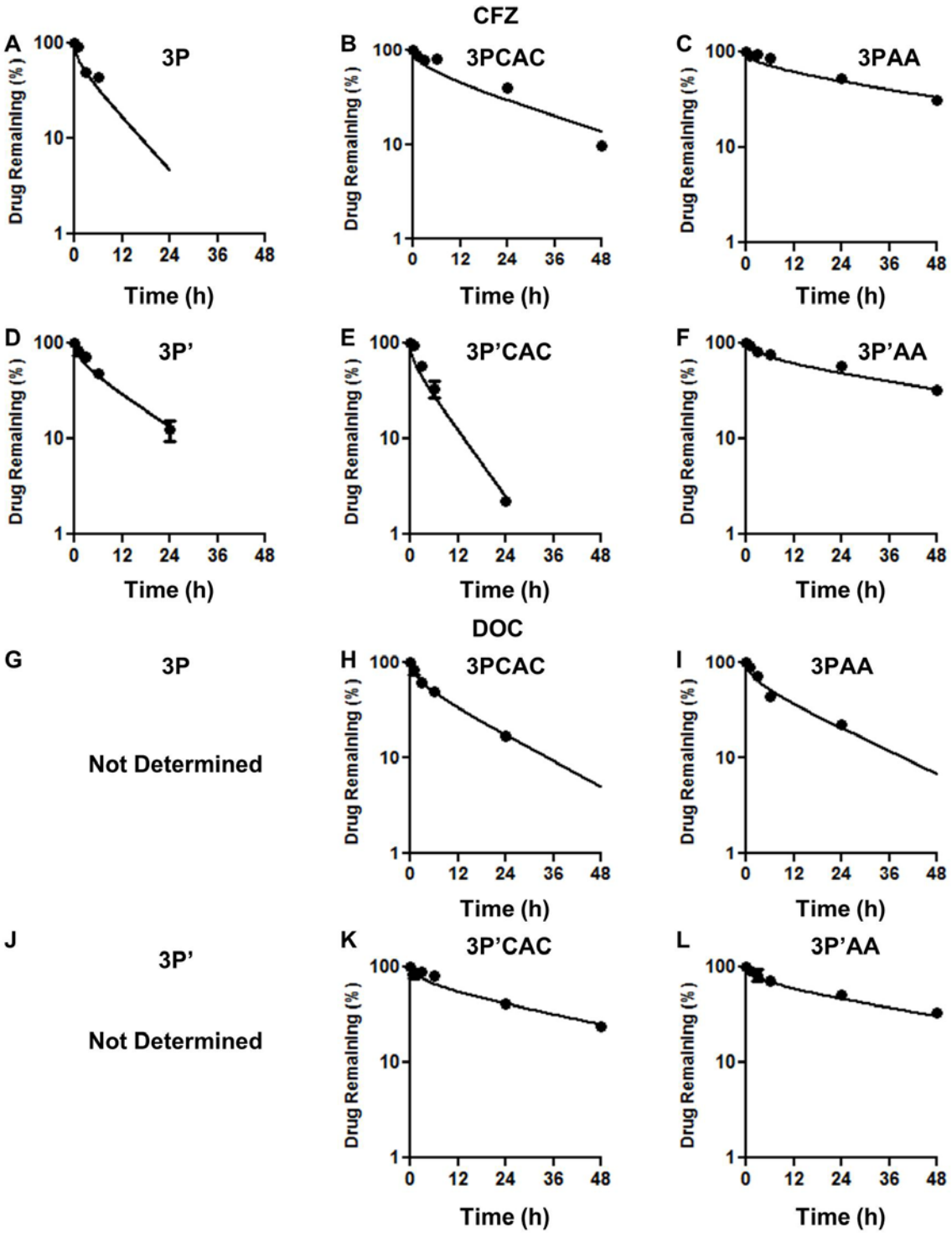

Figure 5.11. Drug release profiles of unmodified and end-capped PNAs using the unsteady state spherical diffusion model. Drug release profiles were measured using the model drugs CFZ (A-F) and DOC (G-L). Due to poor DOC loading of 3P (G) and 3P' (J), drug release was not measured from these PNAs.

Table 5.6. Diffusion parameters for PNA-encapsulated drugs from the unsteady state spherical diffusion model (equation 5.5). Diffusion parameters for free drugs were estimated using the Stokes-Einstein equation and are included for comparison.

Drug	PNA	a (nm)	D (cm^2/s) $*10^{18}$
CFZ	None	---	53,400
CFZ	3P	11.4±2.8	3.90 (2.70-5.10)
	3PCAC	10.1±3.9	0.89 (0.73-1.05)
	3PAA	8.6±2.3	0.27 (0.22-0.33)
CFZ	3P’	2.0±1.5	0.07 (0.06-0.08)
	3P’CAC	5.0±1.7	0.93 (0.81-1.05)
	3P’AA	5.0±1.4	0.10 (0.08-0.11)
DOC	None	---	53,000
DOC	3P	11.4±2.8	---
	3PCAC	10.1±3.9	1.50 (1.08-1.93)
	3PAA	8.6±2.3	0.95 (0.63-1.22)
DOC	3P’	2.0±1.5	---
	3P’CAC	5.0±1.7	0.13 (0.11-0.15)
	3P’AA	5.0±1.4	0.11 (0.08-0.13)

Hydrophobic radius is reported as mean±SD. The error is propagated from equation 5.7 into equation 5.6. The diffusivity is reported as the mean with 95% CI in parentheses. Statistical significance is determined in Figure 5.12.

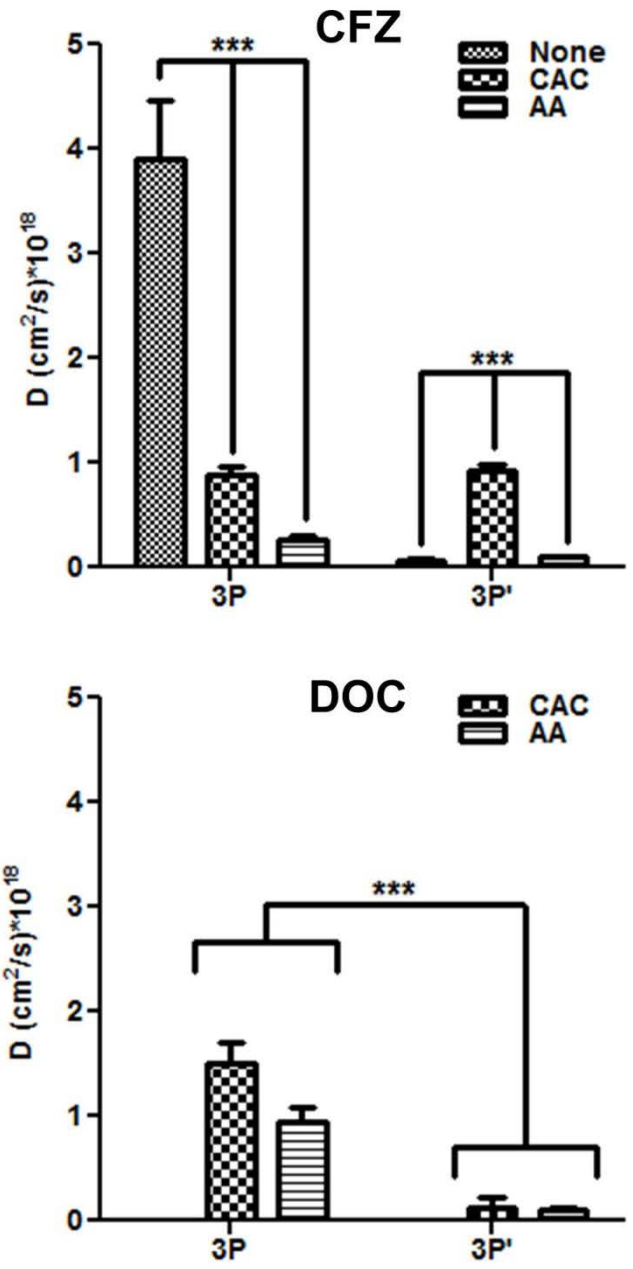

Figure 5.12. Drug diffusivities in the core of unmodified and end-capped PNAs from the unsteady state spherical diffusion model.

5.4 Discussion

5.4.1 PNAs with an Uncharged Core are Effective Carriers for Hydrophobic Drugs

PNAs forming globular, micellar and vesicular structures have drawn attention as multifunctional drug carriers over the past several decades (238-240). Unfortunately, the therapeutic efficacy of PNAs is often disappointing due to particle instability, low drug entrapment, and rapid drug release in the blood (241-243). Polymer micelles are used as FDA-approved drug delivery vehicles (244, 245), but micelles often demonstrate initial burst drug release followed by sustained long-term drug release. This two-step drug release pattern reduces drug accumulation in tumors, which can limit the efficacy of cancer chemotherapy (246). Drugs that are released from drug carriers that are away from the tumor may accumulate in healthy tissues and cause undesired side effects (247). Two-step drug release profiles are often attributed to drugs that remain weakly bound to the polymer shell of nanoassemblies, even after extensive purification (248, 249). Unlike free drugs that often co-exist as impurities along with drug-loaded carriers, weakly bound drugs cannot be easily separated from drug-loaded nanoassemblies without removing entrapped drugs. Therefore, despite the critical need to fine-tune drug release from nanoparticles, preventing burst drug release from PNAs remains difficult.

A simplified form of PNA with a charged scaffold (PEI or PLL), hydrophobic groups (PAL), and amine end-capping pendant groups (CAC and AA) was synthesized. By following this process, a family of polymer nanoassemblies was synthesized for entrapping CFZ and DOC. The data demonstrated that all six PNAs were small enough to maintain sufficient PEG shell density in order to minimize weak binding of drugs or other molecules to the surface of PNAs (250). Amine end-capping modifications to the core of

PNAs did not significantly affect their particle size, suggesting that chemical modifications to the nanoparticle core do not prevent PNAs from permeating throughout small blood vessels in the body. PNAs were also uniform in molecular weight distribution, which maintains the intermolecular consistency of nanoassemblies and minimizes changes in dispersity among the formulations after core modifications.

The fluorescamine characterization and NMR quantification of PNAs showed that NHS-activated PEG and palmitoyl chloride reactions could not remove all remaining primary amines from the core of PNAs, but amine end-capping reagents further removed some of the remaining primary amines. This suggests that the steric hindrance of the remaining primary amines on PNAs increases following PEG and PAL reactions, which limits the molar substitution of larger hydrophilic polymers or hydrophobic groups on polymer scaffolds (251). Both AA and CAC modifications removed more remaining primary amines from 3P' than from 3P, indicating that the primary amines on PLL are less hindered than the primary amines on PEI (252). AA modification of 3P' removed all remaining primary amines in the PNA core, verifying that the use of small pendant groups and less sterically hindered scaffolds allows for the complete removal of remaining primary amines from PNAs. These results also indicate that the selection of polymer scaffolds with less sterically hindered amines or lower amine density may allow for higher substitution yields of PEG and PAL on PNAs.

5.4.2 End-Capping Modifications Modulate Drug Encapsulation and Release

Experimental results show that amine end-capping groups increased the drug loading and encapsulation efficiency of PNAs. Charged amines in the PNA core may prevent drugs from entering nanoassemblies during loading. In addition, these results

demonstrated that PLL, a polymer scaffold with minimal ionic effects resulting in a distinct pKa value, could increase drug loading compared to PEI, a polymer scaffold with significant ionic effects and a broad pKa value (253, 254). Therefore, removing ionic groups to increase the hydrophobicity of the PNA core is an effective approach to increase drug loading and ultimately improve the delivery of anticancer drugs to tumors.

Drug release profiles of CFZ-loaded PNAs demonstrated that this experimental approach helped to prevent the burst release of CFZ from PNAs compared to previously developed CFZ-loaded polymer micelles (255). Drug release studies also indicated that PNAs could fine-tune drug release as a function of scaffold and pendant group modifications to the core. The drug release half-lives of PNAs ranged from 4 to 28 hours as amines were removed from the core by changing scaffold from PEI to PLL and by increasing the end-capping group substitution from no modification to AA modification. Although some primary amines of 3P were reacted during the conjugation of PEG and PAL to the scaffold, the remaining primary, secondary and tertiary amines make the core of 3P charged (256). Because of this core charge, drugs could be weakly bound in the 3P core and release quickly compared to 3P' with only primary amines.

5.4.3 Mechanistic Modeling Elucidates a Mechanism for Controlling Drug Release from PNAs

In order to determine the mechanism for the changes in drug release profiles of PNAs following end-capping reactions, drug release profiles were fit to several mathematical models. Initially, a first order kinetic model was used to determine the effects of end-capping modifications on overall drug release rates. Although this model indicated that end-capping modifications increase the drug release half-lives of PNAs, it

fails to provide detailed information about drug release mechanisms from PNAs (257). It was hypothesized that the rate-determining step of drug release from PNAs was the diffusion of drug out of the PNA core, and that end-capping modifications decreased drug diffusivity in the PNA core. In order to elucidate the rate-determining step for drug release from PNAs, the drug release profiles were then fit to the Korsmeyer-Peppas model of drug release. By comparing the N values from fitted drug release profiles to literature, a rate-determining step could be determined (258). For *N* values equal to 0.45, the drug release is controlled by the Fickian diffusion of drug molecules out of the hydrophobic core. Fickian diffusion indicates that the diffusivity value of drug in the nanoparticle core is independent of both time and drug concentration. The 95% confidence intervals for the *N* values of most drug-PNA combinations overlapped 0.45, indicating that drug release from these PNAs occurred because of Fickian diffusion (259). *N* values between 0.45 and 0.85 indicate that non-Fickian transport processes control drug release. Non-Fickian transport processes refer to a combination of Fickian diffusion and a time- or drug concentration-dependent change in nanoparticle core environment during drug release such as a glass transition for polymers (260). The 95% confidence intervals for the *N* values of CFZ-loaded 3PCAC and 3PAA were between 0.45 and 0.85, indicating that CFZ loading may alter the rigidity of the PNA core or alter diffusion rates in the core of these PNAs (261). *N* values above 0.85 indicate that processes other than diffusion control the release of drug from the nanoparticle core. None of the 95% confidence intervals of the *N* values for PNAs were greater than 0.85.

Because the Korsmeyer-Peppas model indicated that the rate-determining step for drug release was diffusion, an unsteady state spherical diffusion model was used to

measure drug diffusivity in the PNA core. End-capping modifications to 3P decreased CFZ diffusivity, suggesting that end-capping modifications reduce the pore sizes for drug diffusion in the PNA core. In contrast, end-capping modifications increased the hydrophobic core diameter of PLL-based PNAs but had a minimal effect on drug diffusivity, suggesting that end-capping modifications of PLL-based PNAs do not affect the pore sizes in the core of these PNAs.

5.4.4 PNAs with a Positive Core Charge Release Carfilzomib Quickly Compared to Similar PNAs with a Neutral Core

The CFZ release half-life of 3P'CAC was shorter than initially expected. Although drug release rate trends suggest that the CFZ release half-life of 3P'CAC would be 22 hours, the observed CFZ release half-life of 3P'CAC was 4 hours. One explanation for the relatively short CFZ release half-life of 3P'CAC is that the positive core charge of 3P'CAC drew charged molecules into the PNA core. In this highly charged core environment, CFZ may become positively charged and repel from the cationic core environment. In contrast, DOC is not easily ionizable and hydroxyl groups on DOC may favorably interact with charged molecules in the PNA core. Therefore, pendant groups that do not increase core charge of PNAs would achieve stable entrapment and sustained release of hydrophobic anticancer drugs.

5.5 Conclusions

In this study, a novel delivery system was developed for CFZ and DOC by using polymer nanoassemblies (PNAs). Six PNAs were synthesized with various polymer scaffolds and end-capping modifications to determine the effects of ionizable groups in the PNA core on drug delivery. Removing charged groups from the core of PNAs

increased their drug loading and encapsulation efficiency, while also sustaining drug release and increasing their drug release half-life. In addition, mechanistic modeling showed that drug release from PNAs was controlled by decreasing drug diffusivity in the nanoassembly core. In summary, this study has demonstrated a mechanism-based, facile engineering method for the development of PNA drug carriers that can entrap drugs at high yields and enhance their therapeutic efficacy by suppressing initial burst drug release.

**Portions of Chapter 5 were previously published in (262). Reproduced with permission from Future Science Group: Therapeutic Delivery, Volume 7, Issue 10, Pages 665-681, Figures 1-7 and Text. Copyright 2016 is given to the publication in which the material was originally published.

CHAPTER SIX

PNAs WITH CONTROLLED DRUG RELEASE PROFILES IMPROVE CARFILZOMIB EFFICACY BY PREVENTING RAPID DRUG METABOLISM AND SUSTAINING PROTEASOME INHIBITION IN CELLS

6 PNAs WITH CONTROLLED DRUG RELEASE PROFILES IMPROVE CARFILZOMIB EFFICACY BY PREVENTING RAPID DRUG METABOLISM AND SUSTAINING PROTEASOME INHIBITION IN CELLS

6.1 Introduction

The inhibition of novel biological targets such as the proteasome has emerged as a promising approach to improve cancer treatment. The proteasome is a multi-protease enzyme complex that plays an essential role in the regulation of cellular processes by degrading the proteins involved in cell proliferation and signaling (263). Small molecule inhibitors of proteasomes can increase the accumulation of misfolded proteins in cells. The accumulation of misfolded proteins in cancer cells following sustained proteasome inhibition causes cell stress leading to apoptosis. Because of the essential role that the proteasome plays in the survival of all living cells, the selectivity of proteasome inhibitors towards cancer cells was initially questioned (264). However, several studies have validated proteasome inhibition as a selective method for killing rapidly proliferating cancer cells compared to normal cells (265). In particular, cancer cells that are resistant to other conventional and targeted chemotherapies have shown sensitivity to proteasome inhibitors (266, 267). Three proteasome inhibitors (bortezomib, carfilzomib and ixazomib) have received FDA approval for cancer treatment (268-270).

Carfilzomib (CFZ) is a second-generation proteasome inhibitor with the potential to treat solid tumors, but its clinical applications have been limited to blood cancers such as multiple myeloma (271). CFZ showed efficacy at treating a variety of solid cancers in animal models (272, 273). While many clinical studies have proposed the use of CFZ in solid tumors, clinical trials in breast, lung, and colon cancers were unsuccessful (274).

The limited clinical applications of CFZ are often attributed to its poor biopharmaceutical properties such as its rapid clearance that limits the accumulation of active drug in tumors and prevents the sustained inhibition of proteasomes in cancer cells (275). Therefore, there is a need to improve the biopharmaceutical properties of CFZ in order to increase drug accumulation in solid tumors and improve treatment efficacy.

CFZ is clinically available as an intravenous cyclodextrin formulation (Kyprolis®), but this formulation fails to increase the metabolic stability of CFZ (276). Although cyclodextrin complexation increased the solubility of CFZ, the half-life of CFZ in blood after intravenous injection of Kyprolis is less than 30 minutes (277, 278). The poor half-life of CFZ in blood is typically attributed to the rapid extrahepatic metabolism of free drug. As free CFZ is degraded in the blood, the cyclodextrin complex rapidly dissociates to maintain thermodynamic equilibrium between the free CFZ, the unbound cyclodextrin and the CFZ-cyclodextrin complex. As a result, cyclodextrin formulations of CFZ fail to increase the accumulation of CFZ in solid tumors. Therefore, there is a growing need to develop novel formulations of CFZ to expand the therapeutic benefits of proteasome inhibition therapy to a variety of human cancers.

Previously, polymer micelle (PM) carriers for CFZ were developed using FDA-approved materials, but these formulations had poor pharmacokinetic properties that limited their *in vivo* efficacy (160). Several drug-loaded PMs are either used clinically (e.g., Genexol, Nanoxel) or are undergoing clinical trials (e.g., NK012, NK105, SP1049C, NC-6004) for the controlled delivery of anticancer drugs to solid tumors (279-281). These formulations reduced the systemic, cardiac, hepatic, and renal toxicities of anticancer drugs (282). In a previous study, CFZ-loaded PMs protected the drug from

enzymatic degradation in the presence of mouse liver homogenate (255). However, the antitumor efficacy of CFZ-loaded PMs was similar to cyclodextrin-complexed CFZ. This unexpected result was attributed to the poor drug release properties of CFZ-loaded PMs such as burst release and rapid drug release rates (160). In addition, the dilution of PMs after intravenous injection can destabilize the micelles and increase drug release into the blood. Stable PNA formulations of CFZ with improved drug release properties may increase the *in vivo* treatment efficacy of CFZ by protecting the drug from extrahepatic metabolism and sustaining drug release into solid tumors.

In this study, the treatment efficacy of CFZ-loaded PNAs was compared to free CFZ using cell-based assays mimicking *in vivo* drug delivery conditions. 3P'AA was selected as a model PNA with the highest CFZ loading and release half-life of the previously tested formulations in chapter 5. The metabolic stability, cytotoxicity and proteasome inhibition profile of CFZ formulations were identified as three key factors controlling the *in vivo* treatment efficacy of CFZ. HT29 colon cancer cells were used as a model cell line for CRC tumors, while H23 lung cancer cells were selected as a model cell line with well-characterized proteasome activity profiles following treatment with proteasome inhibitors. The results from this study will indicate the potential of nanoparticle drug carriers with sustained CFZ release to improve the treatment of solid tumors and justify further *in vivo* experiments.

6.2 Materials and Methods

6.2.1 Materials and Cells

3P'AA was synthesized and loaded with CFZ as described in chapter 5. Epoxomicin, ethylenediaminetetraacetic acid (EDTA), resazurin sodium salt, sodium

dodecyl sulfate (SDS), and Tris-HCl were purchased from Sigma Aldrich (St. Louis, MO). A fluorogenic peptide substrate Succinate-Leu-Leu-Val-Tyr-(7-amino-4-methylcoumarin) (Suc-LLMY-AMC) was purchased from Biovision (Milpitas, CA). Acetonitrile (ACN), dimethyl sulfoxide (DMSO), phosphate buffered saline (PBS), water and Hanks' balanced salt solution (HBSS) were purchased from Fisher Scientific (Waltham, MA). Passive lysis buffer solution was purchased from Promega (Madison, WI). 20S proteasome assay buffer (20 mM Tris-HCl, 0.5 mM EDTA, 0.035% SDS, pH 8.0) was prepared by dissolving components in water and adjusting the pH with sodium hydroxide. Carfilzomib (CFZ) was purchased from LC Laboratories (Woburn, MA). McCoy's 5A media (M5A), RPMI-1640 media and 0.05% trypsin/EDTA were purchased from GE Healthcare (Logan, UT). Fetal bovine serum (FBS) was purchased from Atlanta Biologicals (Flowery Branch, GA). The human lung cancer cell line H23 and human colon cancer cell line HT29 were purchased from American Type Culture Collection (ATCC, Manassas, VA). H23 cells were cultured in RPMI-1640 media with 10% FBS, while HT29 cells were cultured in M5A with 10% FBS. All ATCC recommendations were followed for both cell lines. Cells were cultured in a humidified environment with 5% CO_2 at 37 °C.

6.2.2 Screening of Carfilzomib Degradation Conditions

A stock solution of CFZ was prepared (DMSO, 10 mg/ml). Ten microliters of CFZ stock solution was added to 990 microliters of acetonitrile, M5A containing 25% inactivated FBS (iFBS), M5A containing 25% active FBS (aFBS) and M5A without FBS. The CFZ-spiked solutions were stored at 37 °C while gently mixing. Aliquots (50 µl) of each solution were removed after 0, 30 and 60 minutes. Each aliquot was diluted in

50 µl of acetonitrile to quench the degradation reactions. The quenched aliquots were then centrifuged at 14,500 RPM for 20 minutes to remove serum proteins and other insoluble impurities. Drug concentrations in each sample were quantified using HPLC as described in chapter 2. Drug concentration measurements were normalized to the initial sample concentration for each condition. To determine if any drug concentration changes in the samples were due to drug precipitation during centrifugation, 10 µl of CFZ stock solution was added to 990 µl of deionized water and the solution was immediately centrifuged at 1000 RPM for 1 minute. Sample aliquots before and after centrifugation were diluted in acetonitrile (1:1 v/v) to prevent any potential further drug precipitation. Changes in drug concentration following centrifugation were measured by HPLC and normalized to the initial sample concentration.

6.2.3 Cytotoxicity of Carfilzomib-Loaded PNAs and Free Carfilzomib With and Without Pre-Incubation in Cell Media

HT29 cells were seeded in 96 well plates at 3,000 cells per well. Cells were treated with either fresh or pre-incubated CFZ. Pre-incubation of CFZ in FBS for 1 hour at 37 °C was selected as an experimental condition to mimic the expected extrahepatic metabolism of CFZ in the blood following intravenous administration. Briefly, serial dilutions of free CFZ and CFZ-loaded PNAs were prepared in DMSO and PBS, respectively, and added to M5A to create 2X stock solutions of free CFZ and CFZ-loaded PNAs. Half of each solution was immediately diluted with M5A containing 20% FBS to yield 1X solutions in M5A containing 10% FBS (fresh), while the other half was stored at 37 °C for 1 hour with mixing before dilution (pre-incubated). Cells were treated with fresh or pre-incubated CFZ (free or PNAs) for 72 hours. Cell viability was measured by

adding 10 µl of 1 mM resazurin solution to each well and measuring the fluorescence of the oxidized product resorufin (Ex 560 nm/Em 590 nm) after 3 hours of incubation. Cell viability was calculated from equation 6.1.

$$CV = \frac{(FLU_S - FLU_M)}{(FLU_V - FLU_M)} * 100\% \quad (6.1)$$

In equation 6.1, *CV* is the percent cell viability, FLU_S is the fluorescence of CFZ-treated samples, FLU_M is the average fluorescence of media-only samples, and FLU_V is the fluorescence of vehicle-treated cells. All fluorescence measurements have units of relative fluorescence units. The half maximal inhibitory concentration (IC_{50}) of each formulation was calculated from a sigmoidal fit of the cell viability vs. the logarithm of drug concentration using Prism 5.0 (Graphpad, La Jolla, Ca). The IC_{50} value has units of nM.

6.2.4 Carfilzomib Treatment of Cells and Proteasome Collection

H23 cells were seeded in 12 well plates at 150,000 cells per well. Cells were treated with 7 nM of either free CFZ or CFZ-loaded PNAs for 0, 6, 24, 48 or 72 hours. The media was removed after treatment and the cells were washed twice with HBSS. Cells were lysed in passive lysis buffer for 15 minutes, and soluble proteins were collected after centrifuging the cell lysate at 14,000 RPM for 20 minutes and collecting the supernatant.

6.2.5 Proteasome Activity Measurement in the Cell Lysates of Carfilzomib-Treated Cells

Total protein concentrations in the supernatants of cell lysates were quantified using a Bradford assay, which was calibrated using protein standards. The supernatants of the cell lysates were diluted in 20S proteasome assay buffer to create a 55.6 µg total

protein/ml stock solution. Ninety microliters of cell lysate stock solution for each sample was added to a 96 well plate and incubated at room temperature for 60 minutes. Ten microliters of 1 mM Suc-LLMY-AMC substrate solution was added to each well. The fluorescence of the wells was measured (Ex 360 nm/Em 460 nm) every minute for 1 hour at 37 °C using a plate reader. To account for non-proteasomal proteolytic activity in cell lysate solutions, cell lysate solutions were treated with the 20S proteasome-inhibitor epoxomicin (10 μM) and the proteasome activity of these solutions was subtracted from the activity of CFZ-treated sample measurements. The proteasome activities of H23 cells treated with either free CFZ or CFZ-loaded PNAs were reported as a percentage of the proteasome activity of untreated H23 cells.

6.2.6 Statistics

All values are reported as mean±standard deviation of three measurements unless described otherwise. Groups of measurements were compared to each other using a one-way analysis of variance (ANOVA) with Bonferroni's post hoc test. Pairs of measurements are compared with Student's t test. Statistical significance is indicated by * ($p<0.05$), ** ($p<0.01$) or *** ($p<0.001$).

6.3 Results

6.3.1 Serum Minimizes Carfilzomib Degradation in Cell Media

Stability profiles of CFZ are shown in Figure 6.1. CFZ concentrations remain consistent in acetonitrile or M5A containing FBS. However, the CFZ concentration decreases by 62% after 1 hour in M5A without FBS. As CFZ peaks on the HPLC decreased, a peak with a shorter retention time (1.6 min vs. 2.0 min) appeared. It should be noted that CFZ degrades rapidly in human blood containing serum proteins, and that

differences between FBS-containing media and whole blood may contribute to this discrepancy. A full discussion of these differences is postponed until the discussion section. Centrifugation did not decrease the measured CFZ concentration in control samples, indicating that any decreases in CFZ concentrations during experiments are not attributed to drug precipitation.

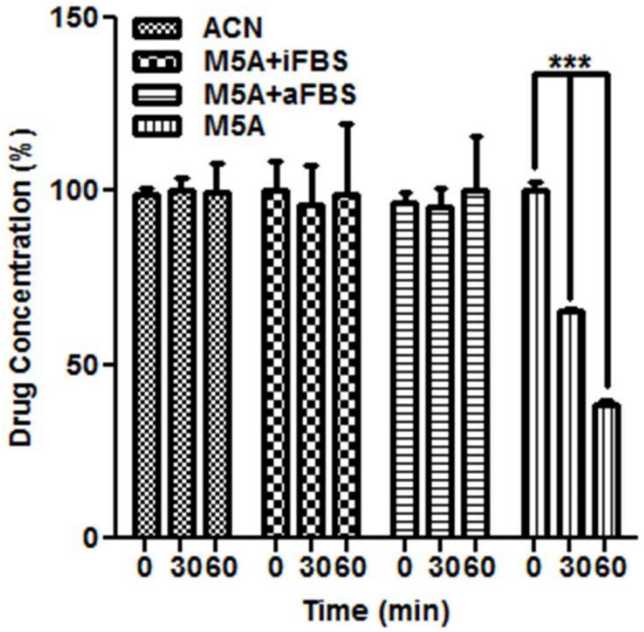

Figure 6.1. Stability of free CFZ at 37 °C in various solvent conditions. CFZ was stored in acetonitrile (ACN), McCoy's 5A with 25% inactive FBS (M5A+iFBS), McCoy's 5A with 25% active FBS (M5A+aFBS) or pure McCoy's 5A (M5A) following 0, 30 or 60 minutes of incubation.

6.3.2 Carfilzomib-Loaded PNAs Maintain Drug Cytotoxicity after Pre-Incubation

The cytotoxicity of fresh and pre-incubated CFZ in HT29 colon cancer cells are shown in Figure 6.2 and Table 6.1. The differences in IC_{50} values between fresh and pre-incubated free CFZ are statistically significant, but the differences between fresh and pre-incubated CFZ-loaded PNAs are not statistically significant. Differences between the IC_{50} ratios of free CFZ and CFZ-loaded PNAs are statistically significant. Figure 6.3 compares the predicted changes in CFZ cytotoxicity based on drug concentrations to the measured cytotoxicity changes in cancer cells. For CFZ-loaded PNAs, released drug was assumed to degrade, while encapsulated drug was assumed to remain stable. Based on changes in drug concentrations from the HPLC quantification of free CFZ following pre-incubation, the free CFZ and CFZ-loaded PNA IC_{50} ratio are predicted to be 2.61 and 1.02, respectively. The differences between predicted and measured treatment efficacy were not statistically significant, but the differences between each formulation were significant. These results suggest that PNAs with sustained drug release can prevent drug degradation and deliver active drug to cancer cells.

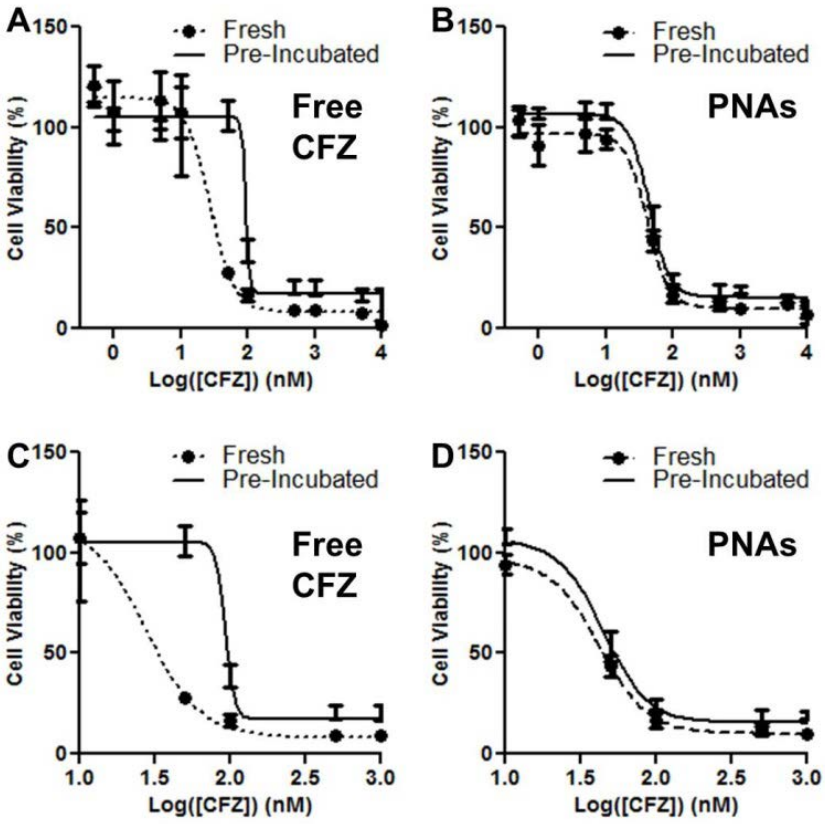

Figure 6.2. Cytotoxicity of fresh and pre-incubated free CFZ (A) and carfilzomib-loaded PNAs (B). Zoomed-in graphs of free CFZ (C) and PNAs (D).

Table 6.1. Cytotoxicity parameters of fresh and pre-incubated free CFZ and CFZ-loaded PNAs.

Formulation	Treatment Condition	IC_{50} (nM)	IC_{50} Ratio
Free CFZ	Fresh	28.6 (23.1-35.3)*	---
Free CFZ	Pre-Incubated	85.5 (76.2-96.1)*	2.99 (2.08-3.89)*
CFZ-Loaded PNAs	Fresh	42.1 (37.4-47.3)	---
CFZ-Loaded PNAs	Pre-Incubated	44.7 (41.6-48.0)	1.06 (0.83-1.29)*

Pharmacological parameters are presented as mean with 95% CI in parentheses. Error in the IC_{50} ratio is propagated from each IC_{50} value. IC_{50} values for each formulation and IC_{50} ratios were compared by a Student's t-test. Statistical significance is indicated as described in the methods section.

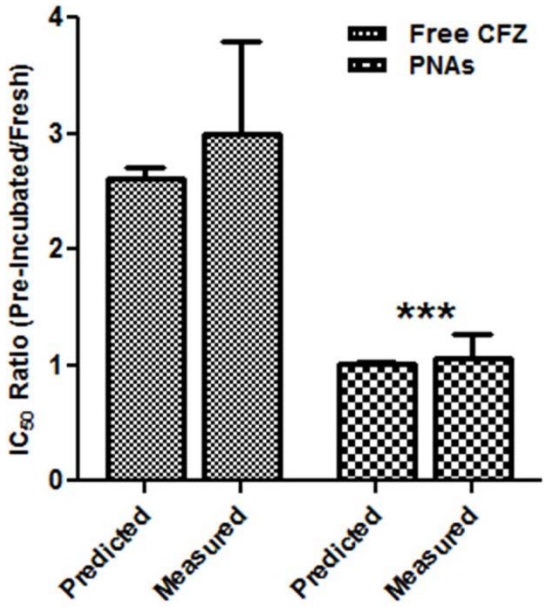

Figure 6.3. Predicted and measured changes in the cytotoxicity of free CFZ and CFZ-loaded PNAs.

6.3.3 Carfilzomib-Loaded PNAs Sustain Long-Term Proteasome Inhibition in Cancer Cells

Proteasome inhibition profiles of H23 lung cancer cells treated with either free CFZ or CFZ-loaded PNAs are shown in Figure 6.4. The proteasome activity of H23 cells decreased at 6 hours compared to untreated samples. Some proteasome activity was recovered up to 48 hours post-treatment for both formulations compared to 6 hours post-treatment. Free CFZ-treated cells continued to recover proteasome activity at 72 hours post-treatment compared to 48 hours, but PNA-treated cells decreased proteasome activity. Free CFZ-treated cells had reduced proteasome activity compared to PNA-treated cells at initial times post-treatment, but PNA-treated cells had reduced proteasome activity compared to free CFZ-treated cells at 72 hours post-treatment.

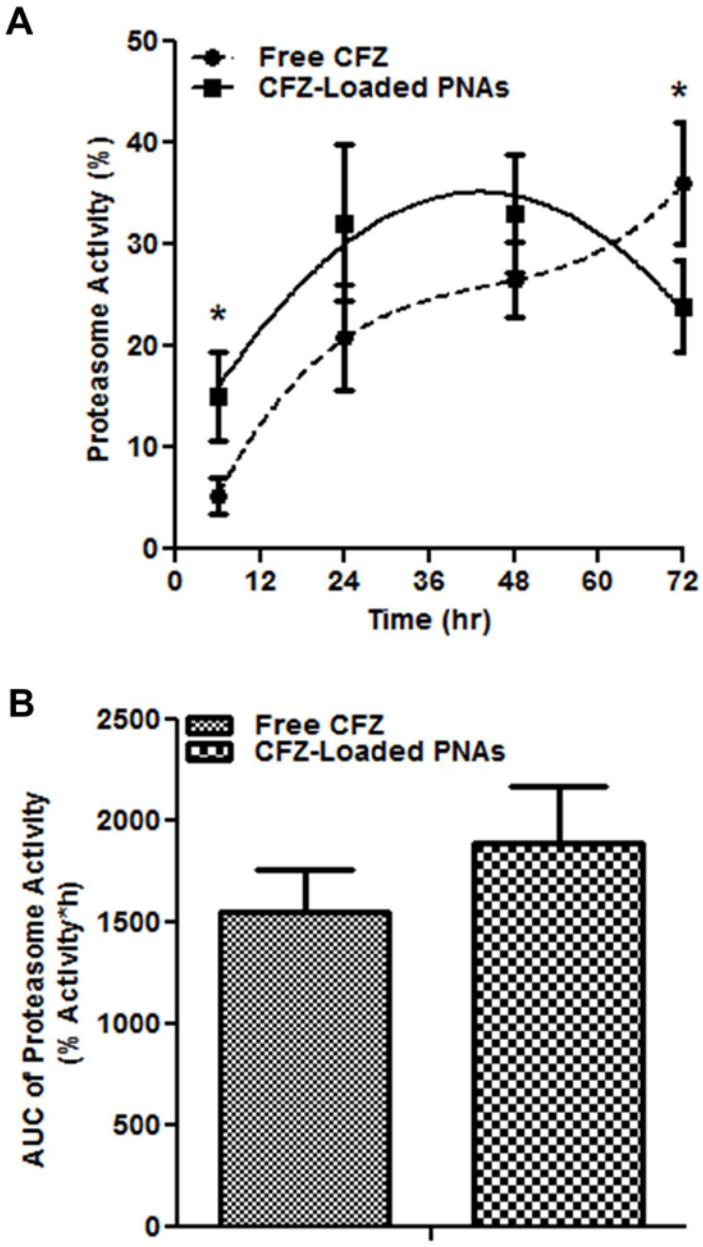

Figure 6.4. Proteasome activity of H23 cancer cells treated with free CFZ or CFZ-loaded PNAs. Proteasome activity was measured at 6, 24, 48 and 72 hours post-treatment and normalized to the activity of proteasomes from untreated cells (A). The AUC of proteasome activity from each sample was also compared (B).

6.4 Discussion

6.4.1 PNAs Reduce the Degradation of Carfilzomib

CFZ is promising for the effective treatment of a variety of human cancers, but it has been ineffective in clinical trials for solid tumors (267). These discouraging results are often attributed to extrahepatic metabolism that prevents the necessary accumulation of active drug in solid tumors. As a result, misfolded proteins fail to accumulate in cancer cells and cause cell stress leading to apoptosis (283). PMs were previously reported as a promising formulation to solubilize hydrophobic anticancer drugs and prevent drug metabolism, but PMs had similar treatment efficacy to clinically available cyclodextrin formulations (160). In contrast to PMs that can dissociate after injection and release CFZ into the blood, unimolecular PNAs may remain stable and sustain drug release. Therefore, this study compares free CFZ to CFZ-loaded PNAs using *in vitro* models to determine the effects of sustained release on proteasome inhibition and cytotoxicity.

Physiologically relevant models of *in vivo* drug metabolism are difficult to develop, because the factors contributing to metabolic stability profiles such as *in vitro* exposure time, enzyme concentrations and buffer conditions must be carefully optimized for each drug (284, 285). One common *in vitro* metabolism model is the liver homogenate model, in which drugs are exposed to proteins collected from liver tissue (286). Changes in drug concentrations over time are correlated to *in vivo* metabolic drug stability, but previous studies suggest that the accuracy of these models at predicting *in vivo* metabolism are limited for drugs undergoing extrahepatic metabolism (287). As an alternative to liver homogenate experiments, a facile method was developed to mimic the extrahepatic metabolism of CFZ and predict the metabolic stability of CFZ. Although

M5A does not contain all of the enzymes present in whole blood, 60% of the free CFZ in M5A was found to degrade within one hour. In contrast, over 95% of CFZ degraded within 5 minutes following exposure to liver homogenate, which significantly overestimates CFZ degradation rates *in vivo* (60). These results suggest that the storage of free CFZ in cell media without FBS may be advantageous compared to compared to liver homogenate studies at predicting extrahepatic metabolism due to drug hydrolysis (288).

Although CFZ can rapidly metabolize in whole blood and other tissue homogenates (60), CFZ remained stable in active FBS-containing media mimicking whole blood. This surprising result suggests that FBS-containing cell media fails to mimic the enzymatic properties of whole human blood, and that the chemical components of M5A contribute to observed CFZ degradation profiles. Two potential factors could contribute to these differences: 1) the manufacturing steps for FBS preparation such as coagulation and centrifugation may not collect the specific proteases from whole blood that cause CFZ degradation, and 2) the peptide bonds in carfilzomib may not be substrates for bovine serum proteases. Further work is needed to determine enzymatic activity of proteases in FBS compared to human serum. CFZ remains relatively stable under neutral and slightly acidic conditions in water, but recent publications suggest that the formation of chloride adducts increases the *in vitro* hydrolysis of the epoxyketone group on CFZ (289, 290). This observation suggests that the high chloride concentrations in M5A (>110 mM) may contribute to epoxyketone ring opening, but that interactions between CFZ and serum proteins protect CFZ from degradation in serum-containing samples. However, significant experimental work is needed to test this hypothesis.

6.4.2 Controlled Release of Carfilzomib from PNAs Sustains Proteasome Inhibition

CFZ-loaded PNAs can increase proteasome inhibition in cancer cells compared to free CFZ at 72 h post-treatment. Sustained proteasome inhibition in cancer cells may increase the efficacy of CFZ in MM or solid tumors by increasing the accumulation of misfolded proteins in cancer cells (291). However, it should be noted that IC_{50} values are lower for free CFZ than for CFZ-loaded PNAs, and that initial proteasome inhibition is greater with free CFZ than with CFZ-loaded 3P'AA. In addition, the area under the curve (AUC) up to 72 hours post-treatment indicating overall proteasome activity is slightly greater for CFZ-loaded PNAs than for free CFZ (1888 vs 1551 normalized activity/h, respectively, $p>0.05$). Taken together, these results suggest that short-term proteasome inhibition controls *in vitro* CFZ cytotoxicity, and that *in vitro* cytotoxicity measurements of proteasome inhibitors may not mimic the long-term proteasome inhibition necessary for solid tumor treatment. Determining the relationship between *in vitro* proteasome inhibition profiles and the *in vivo* effects of sustained proteasome inhibition in solid tumors is an important area of future work.

6.4.3 PNAs May Increase the Accumulation of Active Carfilzomib in Solid Tumors

By extending the drug release half-life of CFZ, PNAs can increase the accumulation of active drug in solid tumors compared to free drugs. Nanoassemblies such as PNAs can passively accumulate in the porous vasculature of solid tumors and increase the concentration of nanoparticles in tumor tissue compared to healthy tissue (282). The maximum accumulation of nanoassemblies in the vasculature surrounding solid tumors typically occurs between 3 to 6 hours after intravenous injection (292, 293). Based on drug release measurements in chapter 5, 3P'AA will release less than 15% of

drug before accumulating in solid tumors, which decreases the amount of free drug released into the blood before PNAs can reach solid tumors. Therefore, PNAs are expected to increase the amount of active anticancer drugs delivered to tumors and potentially enhance anticancer efficacy (294, 295). Future studies will focus on elucidating the benefits of PNA drug delivery in animal models of solid tumors.

6.5 Conclusions

In this study, the treatment efficacies of free CFZ and CFZ-loaded PNAs were compared using *in vitro* drug metabolism, cytotoxicity and proteasome activity models. The sustained release of CFZ from PNAs maintained drug efficacy after pre-incubation compared to free CFZ. Changes in the efficacy of free CFZ following pre-incubation corresponded to predictions based on HPLC quantification of active drug, suggesting that drug activity controls cytotoxicity. In addition, PNAs with a longer drug release half-life sustained proteasome inhibition in model cancer cell lines compared to free drug, suggesting that CFZ delivery using PNAs can modulate proteasome activity in various types of cancer cells. Overall, this study has demonstrated the advantages of PNAs to protect CFZ from metabolic degradation, maintain cytotoxicity and extend proteasome inhibition in cancer cells to potentially improve the efficacy of CFZ in solid tumors.

**Portions of Chapter 6 were previously published in (262). Reproduced with permission from Future Science Group: Therapeutic Delivery, Volume 7, Issue 10, Pages 665-681, Figures 8-10 and Text. Copyright 2016 is given to the publication in which the material was originally published.

CHAPTER SEVEN

CONCLUSIONS AND FUTURE DIRECTIONS

7 CONCLUSIONS AND FUTURE DIRECTIONS

7.1 Conclusions

7.1.1 Dye Entrapment in Polymer Nanoassemblies Enable Fluorochromism for Theranostics

In this work, dyes were entrapped in the core of polymer nanoassemblies in order to create PNAs for cancer theranostics. The conjugation of non-fluorochromic dyes such as IR820 and Alexa Fluor® 546 to the polymer scaffold created PNAs without fluorochromism. Non-fluorochromic PNAs such as 3P'IR820 and 3P'A546 had consistent fluorescence properties in various solvent and core environments. The consistent fluorescence properties of non-fluorochromic PNAs allowed for the accurate quantification of PNAs in agarose gels, organs and sectioned tissue samples. In contrast, the conjugation of the model fluorochromic dye NB to the nanoassembly core yielded PNAs with fluorochromism. While the fluorescence of free NB was quenched in water, NB in the core of the PEI-based PNAs fluoresced strongly. Fluorochromic PNAs detected environmental properties such as acidity and nanoparticle core environment properties such as drug loading. Therefore, the entrapment of fluorochromic dyes in PNAs enabled fluorochromism in comparison to PNAs entrapping traditional fluorescent dyes.

In order to investigate the effects of the PNA core environment on fluorochromism, NB was attached to the polymer scaffold of PNAs with either an ionic or a hydrophobic core environment. PNAs with a hydrophobic core environment (3PN) fluoresced strongly in comparison to PNAs with an ionic core environment (2PN), suggesting that increasing the PNA core hydrophobicity prevents fluorescence quenching

of NB by forcing water out of the PNA core. 3PN fluoresced at lower excitation and emission wavelengths than 2PN, indicating that interactions between hydrophobic groups and dyes increase the energy of their fluorescence emission spectra. 2PN had decreased fluorescence in acidic solution while 3PN had increased fluorescence, suggesting that shifts in fluorescence spectra contribute to the halo-fluorochromic properties of PNAs. Taken together, these results suggest that the core environment of PNAs must be carefully considered to maximize the fluorochromism of entrapped dyes.

The effects of polymer scaffold composition on dye fluorochromism were also evaluated using PNAs with fewer (3P'N) or no amines in core (3P'NAA). Amines were removed from the PNA core by replacing the PEI scaffold with a PLL scaffold (3P'N) lacking secondary and tertiary amines, and by further end-capping and remaining primary amines on the scaffold (3P'NAA). The fluorescence of 3P'N could not be detected, suggesting that the PLL scaffold draws water into the PNA core compared to the PEI scaffold and quenches NB fluorescence. The further removal of remaining primary amines restored the fluorescence of PNAs but interfered with their fluorochromism. Therefore, interactions between amines on the polymer scaffold and fluorochromic dyes in the core of PNAs contribute to the fluorochromism of PNAs entrapping fluorochromic dyes.

7.1.2 Halo- and Solvato-Fluorochromism are Useful Theranostic Properties

The halo-fluorochromism of PNAs allowed for the sensitive and accurate detection of metastatic tumors compared to PNAs without fluorochromism. 3PN diffused into agarose gels and fluoresced strongly in tumor microenvironment conditions ($pH<7.0$) compared to healthy tissue ($pH=7.4$). In addition, PNAs failed to interact with

ions or proteins that could cause false positive fluorescence signals in healthy tissue by altering the acidity of nanoassembly core. Although PNAs without fluorochromism fluoresced throughout healthy organs, healthy liver and metastatic tumors in the liver, 3PN minimized background fluorescence signals in healthy tissues and identified the acidic perimeter of liver metastatic tumors. As a result, halo-fluorochromic PNAs are promising tools for the early and accurate detection of tumor metastasis, which can allow for effective cancer treatment and potentially reduce cancer mortality.

The solvato-fluorochromism of PNAs allowed for the detection of drug release from the PNA core. A fluorescence-based method of measuring drug release from PNAs was developed and compared to HPLC-based methods for measuring drug release during dialysis-based drug release measurements. Although HPLC-based methods measure encapsulated and released drug, solvato-fluorochromism only detected drug release from the PNA core. Solvato-fluorochromism indicated that PNAs released drug very quickly in comparison to HPLC-based methods, but molecular modeling of HPLC-based measurements indicated that drug rebinding and slow diffusion did not cause these differences. Based on this observation, it was hypothesized that PNAs contain a NB-enhanced region by the polymer scaffold in the PNA core, and that solvato-fluorochromism is only sensitive to drug diffusion out of this region and towards the interface. As a result, solvato-fluorochromism may detect one step of drug release, but drug release rates determined by solvato-fluorochromism may not represent the rate-limiting step of *in vivo* drug release. Hydrophobic excipients forced drug into the PNA core and increased the solvato-fluorochromism of PNAs, suggesting that interactions between drugs and dyes control the SFC intensity and spectra of dyes. Based on this

information, solvato-fluorochromism may be a beneficial method for investigating drug release processes in the core of PNAs without interference from drug rebinding or diffusion.

7.1.3 Theranostics Overcomes Some Limitations of Cancer Nanotechnology

PNAs with controlled drug release profiles can increase drug accumulation in tumors and improve treatment efficacy, but many nanoparticles have rapid drug release rates that limit their treatment efficacy. The solvato-fluorochromism of PNAs indicated that the polymer scaffolds draw water into the nanoassembly core and decreases the core hydrophobicity, which weakens the interactions between hydrophobic drugs and PNAs. Based on this observation, ionizable amines were removed from the polymer scaffolds of PNAs in order to increase core hydrophobicity and sustain drug release. The removal of amines increased both the drug encapsulation and drug release half-life of model drugs CFZ and DOC. This result suggests that chemical modifications based on solvato-fluorochromism can improve the drug delivery properties of PNAs for cancer chemotherapy.

Controlled drug release from PNAs can increase the metabolic stability of drugs and increase drug accumulation in solid tumors in comparison to free drugs. Free CFZ remained stable in organic solvents and in cell media containing FBS, but CFZ degraded in cell media without serum. CFZ lost therapeutic efficacy following pre-incubation in cell media, but CFZ-loaded PNAs maintained their efficacy for up to one hour. CFZ-loaded PNAs decreased proteasome activity in H23 lung cancer cells compared to free carfilzomib after 72 hours, suggesting that the sustained release of carfilzomib from PNAs can modulate proteasome activity and sustain treatment efficacy. Based on these

observations, PNAs may improve CFZ treatment efficacy by delivering active drug to solid tumors and increasing drug accumulation in cancer cells.

7.2 Future Directions

7.2.1 Increase the Tumor Penetration and Halo-Fluorochromism of PNAs for the Improved Detection of Metastatic Tumors

Halo-fluorochromic PNAs accumulated at the perimeter of liver metastatic tumors and detected the acidic interstitium of tumors. Although PNAs identified metastatic CRC tumors on the livers of mice, the GFP signals from metastatic tumors were not in perfect agreement with the fluorescence signals from halo-fluorochromic PNAs. Increasing the penetration of halo-fluorochromic PNAs into metastatic tumors would increase the accumulation of PNAs in the hypoxic and acidic regions of tumor tissue, which would increase the accuracy of liver MCRC detection. One method to achieve this goal is to decrease their diameter of nanoparticles entrapping halo-fluorochromic dyes, so that nanoparticles diffuse further into tumors (296). A second method is to increase the porosity of metastatic tumors such as by co-administration of tissue-penetrating peptides with PNAs (297, 298). In addition, increasing the halo-fluorochromism of dyes in PNAs can maximize the fluorescence signal of PNAs that are accumulating in the hypoxic region of metastatic tumors.

7.2.2 Predict the Treatment Efficacy of Drug-Loaded PNAs in Tumors from Solvato-Fluorochromic Drug Release Profiles

Solvato-fluorochromic PNAs indicated real-time drug release profiles in a non-invasive manner. Because fluorescence imaging can measure the fluorescence of organs, solvato-fluorochromic drug release profiles hold promise to predict treatment efficacy

based on measured drug delivery into tumors. In order to accomplish this, several characteristics of PNAs must be determined. First, the relationship between active drug concentrations in organs and drug release from PNAs must be evaluated. Next, the effects of tissue penetration on solvato-fluorochromic measurements of drug release in organs should be determined. Then, by treating animals with drug-loaded solvato-fluorochromic PNAs and measuring both fluorescence changes and drug concentrations in tumors over time, the relationship between solvato-fluorochromic drug release profiles, drug concentrations in tumors and treatment efficacy can be determined.

REFERENCES

1. Svenson S. Theranostics: are we there yet? Mol Pharm. 2013;10(3):848-856.

2. Choi KY, Liu G, Lee S, Chen X. Theranostic nanoplatforms for simultaneous cancer imaging and therapy: current approaches and future perspectives. Nanoscale. 2012;4(2):330-342.

3. Fernandez-Fernandez A, Manchanda R, McGoron AJ. Theranostic applications of nanomaterials in cancer: drug delivery, image-guided therapy, and multifunctional platforms. Appl Biochem Biotechnol. 2011;165(7-8):1628-1651.

4. Van Cutsem E, Verheul HM, Flamen P, Rougier P, Beets-Tan R, Glynne-Jones R, Seufferlein T. Imaging in Colorectal Cancer: Progress and Challenges for the Clinicians. Cancers (Basel). 2016;8(9).

5. Jo SD, Ku SH, Won YY, Kim SH, Kwon IC. Targeted Nanotheranostics for Future Personalized Medicine: Recent Progress in Cancer Therapy. Theranostics. 2016;6(9):1362-1377.

6. Liu Y, Feng L, Liu T, Zhang L, Yao Y, Yu D, Wang L, Zhang N. Multifunctional pH-sensitive polymeric nanoparticles for theranostics evaluated experimentally in cancer. Nanoscale. 2014;6(6):3231-3242.

7. Mura S, Couvreur P. Nanotheranostics for personalized medicine. Adv Drug Deliv Rev. 2012;64(13):1394-1416.

8. Kwok M, Wu SP, Mo C, Summers T, Roschewski M. Circulating Tumor DNA to Monitor Therapy for Aggressive B-Cell Lymphomas. Curr Treat Options Oncol. 2016;17(9):47.

9. Lin J, Chuang CC, Zuo L. Potential roles of microRNAs and ROS in colorectal cancer: diagnostic biomarkers and therapeutic targets. Oncotarget. 2017.

10. Das V, Kalita J, Pal M. Predictive and prognostic biomarkers in colorectal cancer: A systematic review of recent advances and challenges. Biomed Pharmacother. 2016;87:8-19.

11. Turner SA, Peterson JD, Pettus JR, de Abreu FB, Amos CI, Dragnev KH, Tsongalis GJ. The Pitfalls of Companion Diagnostics: Evaluation of Discordant EGFR Mutation Results from a Clinical Laboratory and a Central Laboratory. J Mol Diagn. 2016;18(3):331-335.

12. Zheng M, Zhao P, Luo Z, Gong P, Zheng C, Zhang P, Yue C, Gao D, Ma Y, Cai L. Robust ICG theranostic nanoparticles for folate targeted cancer imaging and highly effective photothermal therapy. ACS Appl Mater Inter. 2014;6(9):6709-6716.

13. Lanza GM, Moonen C, Baker JR, Chang E, Cheng Z, Grodzinski P, Ferrara K, Hynynen K, Kelloff G, Lee Y-EK, Patri AK, Sept D, Schnitzer JE, Wood BJ, Zhang M, Zheng G, Farahani K. Assessing the barriers to image-guided drug delivery. Wiley Interdisciplinary Reviews: Nanomedicine and Nanobiotechnology. 2014;6(1):1-14.

14. Lammers T, Kiessling F, Hennink WE, Storm G. Nanotheranostics and image-guided drug delivery: current concepts and future directions. Mol Pharm. 2010;7(6):1899-1912.

15. Gotta V, Widmer N, Decosterd LA, Chalandon Y, Heim D, Gregor M, Benz R, Leoncini-Franscini L, Baerlocher GM, Duchosal MA, Csajka C, Buclin T. Clinical usefulness of therapeutic concentration monitoring for imatinib dosage individualization: results from a randomized controlled trial. Cancer Chemother Pharmacol. 2014;74(6):1307-1319.

16. Ojha T, Rizzo L, Storm G, Kiessling F, Lammers T. Image-guided drug delivery: preclinical applications and clinical translation. Expert Opin Drug Deliv. 2015;12(8):1203-1207.

17. Blau R, Krivitsky A, Epshtein Y, Satchi-Fainaro R. Are nanotheranostics and nanodiagnostics-guided drug delivery stepping stones towards precision medicine? Drug Resist Updat. 2016;27:39-58.

18. Valastyan S, Weinberg RA. Tumor metastasis: molecular insights and evolving paradigms. Cell. 2011;147(2):275-292.

19. Bravo-Cordero JJ, Hodgson L, Condeelis J. Directed cell invasion and migration during metastasis. Curr Opin Cell Biol. 2012;24(2):277-283.

20. Junttila MR, de Sauvage FJ. Influence of tumour micro-environment heterogeneity on therapeutic response. Nature. 2013;501(7467):346-354.

21. Xing M, Kooby DA, El-Rayes BF, Kokabi N, Camacho JC, Kim HS. Locoregional therapies for metastatic colorectal carcinoma to the liver--an evidence-based review. J Surg Oncol. 2014;110(2):182-196.

22. Li D, Kang J, Golas BJ, Yeung VW, Madoff DC. Minimally invasive local therapies for liver cancer. Cancer Biol Med. 2014;11(4):217-236.

23. Haeno H, Gonen M, Davis Meghan B, Herman Joseph M, Iacobuzio-Donahue Christine A, Michor F. Computational Modeling of Pancreatic Cancer Reveals Kinetics of Metastasis Suggesting Optimum Treatment Strategies. Cell. 2012;148(1–2):362-375.

24. Kato Y, Ozawa S, Miyamoto C, Maehata Y, Suzuki A, Maeda T, Baba Y. Acidic extracellular microenvironment and cancer. Cancer Cell Int. 2013;13(1):89.

25. Barar J, Omidi Y. Dysregulated pH in Tumor Microenvironment Checkmates Cancer Therapy. Bioimpacts. 2013;3(4):149-162.

26. Mohammad AS, Adkins CE, Dolan EL, Terrell-Hall TB, Lockman PR. Abstract 2080: Demonstration of casual relationship between blood-tumor barrier permeability changes and chemotherapeutic uptake and effect in brain micrometastases of breast cancer. Cancer Res. 2016;76(14 Supplement):2080-2080.

27. Viganò L, Capussotti L, De Rosa G, De Saussure WO, Mentha G, Rubbia-Brandt L. Liver Resection for Colorectal Metastases after Chemotherapy: Impact of Chemotherapy-Related Liver Injuries, Pathological Tumor Response, and Micrometastases on Long-term Survival. Ann Surg. 2013;258(5):731-742.

28. Key J, Leary JF. Nanoparticles for multimodal in vivo imaging in nanomedicine. Int J Nanomedicine. 2014;9:711-726.

29. Hu H, Huang P, Weiss OJ, Yan X, Yue X, Zhang MG, Tang Y, Nie L, Ma Y, Niu G, Wu K, Chen X. PET and NIR optical imaging using self-illuminating (64)Cu-doped chelator-free gold nanoclusters. Biomaterials. 2014;35(37):9868-9876.

30. Jose J, Burgess K. Benzophenoxazine-based fluorescent dyes for labeling biomolecules. Tetrahedron. 2006;62(48):11021-11037.

31. Yao Z, Hu X, Huang B, Zhang L, Liu L, Zhao Y, Wu H-C. Halochromism of a Polythiophene Derivative Induced by Conformational Changes and Its Sensing Application of Carbon Dioxide. ACS Appl Mater Inter. 2013;5(12):5783-5787.

32. Marini A, Muñoz-Losa A, Biancardi A, Mennucci B. What is Solvatochromism? J Phys Chem B. 2010;114(51):17128-17135.

33. Nandi LG, Facin F, Marini VG, Zimmermann LM, Giusti LA, da Silva R, Caramori GF, Machado VG. Nitro-substituted 4-[(phenylmethylene)imino]phenolates: solvatochromism and their use as solvatochromic switches and as probes for the investigation of preferential solvation in solvent mixtures. J Org Chem. 2012;77(23):10668-10679.

34. Thipperudrappa J, Deepa HR, Raghavendra UP, Hanagodimath SM, Melavanki RM. Effect of solvents, solvent mixture and silver nanoparticles on photophysical properties of a ketocyanine dye. Luminescence. 2017;32(1):51-61.

35. Al-Ansari IA. Effects of Structure and Environment on the Spectroscopic Properties of (3-Amino-Substituted-Thieno[2,3-b] Pyridine-2-yl)Pyridine/Quinolin-2-yl)(Phenyl)Methanones: Experimental and Theoretical Study. J Fluoresc. 2016;26(3):821-834.

36. Li H, Wang C, She M, Zhu Y, Zhang J, Yang Z, Liu P, Wang Y, Li J. Two rhodamine lactam modulated lysosome-targetable fluorescence probes for sensitively and selectively monitoring subcellular organelle pH change. Anal Chim Acta. 2015;900:97-102.

37. Stockert JC, Abasolo MI, Blazquez-Castro A, Horobin RW, Revilla M, Lombardo DM. Selective labeling of lipid droplets in aldehyde fixed cell monolayers by lipophilic fluorochromes. Biotech Histochem. 2010;85(5):277-283.

38. Okuthe GE. DNA and RNA pattern of staining during oogenesis in zebrafish (Danio rerio): a confocal microscopy study. Acta Histochem. 2013;115(2):178-184.

39. Maeda H, Nakamura H, Fang J. The EPR effect for macromolecular drug delivery to solid tumors: Improvement of tumor uptake, lowering of systemic toxicity, and distinct tumor imaging in vivo. Adv Drug Del Rev. 2013;65(1):71-79.

40. Ponta A, Bae Y. PEG-poly(amino acid) block copolymer micelles for tunable drug release. Pharm Res. 2010;27(11):2330-2342.

41. Steichen SD, Caldorera-Moore M, Peppas NA. A review of current nanoparticle and targeting moieties for the delivery of cancer therapeutics. Eur J Pharm Sci. 2013;48(3):416-427.

42. Bobo D, Robinson KJ, Islam J, Thurecht KJ, Corrie SR. Nanoparticle-Based Medicines: A Review of FDA-Approved Materials and Clinical Trials to Date. Pharm Res. 2016;33(10):2373-2387.

43. Lytton-Jean AKR, Kauffman KJ, Kaczmarek JC, Langer R. Cancer Nanotherapeutics in Clinical Trials. In: Mirkin CA, Meade TJ, Petrosko SH, Stegh AH, editors. Nanotechnology-Based Precision Tools for the Detection and Treatment of Cancer. Cham: Springer International Publishing; 2015. p. 293-322.

44. Chen F, Nayak TR, Goel S, Valdovinos HF, Hong H, Theuer CP, Barnhart TE, Cai W. In Vivo Tumor Vasculature Targeted PET/NIRF Imaging with TRC105(Fab)-Conjugated, Dual-Labeled Mesoporous Silica Nanoparticles. Mol Pharm. 2014;11(11):4007-4014.

45. Ferber S, Baabur-Cohen H, Blau R, Epshtein Y, Kisin-Finfer E, Redy O, Shabat D, Satchi-Fainaro R. Polymeric nanotheranostics for real-time non-invasive optical imaging of breast cancer progression and drug release. Cancer Lett. 2014;352(1):81-89.

46. Cao P, Ponta A, Kim JA, Bae Y. Block copolymer crosslinked nanoassemblies co-entrapping acridine yellow and doxorubicin for cancer theranostics. British J Pharm Res. 2013;3(536-547).

47. Dan M, Scott DF, Hardy PA, Wydra RJ, Hilt JZ, Yokel RA, Bae Y. Block copolymer cross-linked nanoassemblies improve particle stability and biocompatibility of superparamagnetic iron oxide nanoparticles. Pharm Res. 2013;30(2):552-561.

48. Hoshyar N, Gray S, Han H, Bao G. The effect of nanoparticle size on in vivo pharmacokinetics and cellular interaction. Nanomedicine. 2016;11(6):673-692.

49. Merian J, Gravier J, Navarro F, Texier I. Fluorescent nanoprobes dedicated to in vivo imaging: from preclinical validations to clinical translation. Molecules. 2012;17(5):5564-5591.

50. Zeng C, Shang W, Wang K, Chi C, Jia X, Fang C, Yang D, Ye J, Fang C, Tian J. Intraoperative Identification of Liver Cancer Microfoci Using a Targeted Near-Infrared Fluorescent Probe for Imaging-Guided Surgery. Sci Rep. 2016;6:21959.

51. Hue JJ, Lee HJ, Jon S, Nam SY, Yun YW, Kim JS, Lee BJ. Distribution and accumulation of Cy5.5-labeled thermally cross-linked superparamagnetic iron oxide nanoparticles in the tissues of ICR mice. J Vet Sci. 2013;14(4):473-479.

52. Sayag D, Cabon Q, Texier I, Navarro FP, Boisgard R, Virieux-Watrelot D, Carozzo C, Ponce F. Phase-0/phase-I study of dye-loaded lipid nanoparticles for near-infrared fluorescence imaging in healthy dogs. Eur J Pharm Biopharm. 2016;100:85-93.

53. Wong CH, Choi LS, Yim SL, Lau KN, Chow HF, Hui SK, Sze KH. The effects of microenvironment polarity and dendritic branching of aliphatic hydrocarbon dendrons on the self-assembly of 2-ureido-4-pyrimidinones. Chem Asian J. 2010;5(10):2249-2257.

54. Chakravarty R, Hong H, Cai W. Image-Guided Drug Delivery with Single-Photon Emission Computed Tomography: A Review of Literature. Curr Drug Targets. 2015;16(6):592-609.

55. Justus CR, Dong L, Yang LV. Acidic tumor microenvironment and pH-sensing G protein-coupled receptors. Front Physiol. 2013;4:354.

56. Alfarouk KO, Muddathir AK, Shayoub MEA. Tumor Acidity as Evolutionary Spite. Cancers (Basel). 2011;3(1):408.

57. McIntyre A, Harris AL. The Role of pH Regulation in Cancer Progression. Recent Results Cancer Res. 2016;207:93-134.

58. Mahoney BP, Raghunand N, Baggett B, Gillies RJ. Tumor acidity, ion trapping and chemotherapeutics: I. Acid pH affects the distribution of chemotherapeutic agents in vitro. Biochem Pharmacol. 2003;66(7):1207-1218.

59. Raghunand N, Mahoney BP, Gillies RJ. Tumor acidity, ion trapping and chemotherapeutics: II. pH-dependent partition coefficients predict importance of ion trapping on pharmacokinetics of weakly basic chemotherapeutic agents. Biochem Pharmacol. 2003;66(7):1219-1229.

60. Wang Z, Yang J, Kirk C, Fang Y, Alsina M, Badros A, Papadopoulos K, Wong A, Woo T, Bomba D, Li J, Infante JR. Clinical pharmacokinetics, metabolism, and drug-drug interaction of carfilzomib. Drug Metab Dispos. 2013;41(1):230-237.

61. Wang J, Lu Z, Gao Y, Wientjes MG, Au JL. Improving delivery and efficacy of nanomedicines in solid tumors: role of tumor priming. Nanomedicine (Lond). 2011;6(9):1605-1620.

62. Lu D, Wientjes MG, Lu Z, Au JL. Tumor priming enhances delivery and efficacy of nanomedicines. J Pharmacol Exp Ther. 2007;322(1):80-88.

63. Hu C-MJ, Zhang L. Nanoparticle-based combination therapy toward overcoming drug resistance in cancer. Biochem Pharmacol. 2012;83(8):1104-1111.

64. Lee HJ, Bae Y. Brushed block copolymer micelles with pH-sensitive pendant groups for controlled drug delivery. Pharm Res. 2013;30(8):2077-2086.

65. Reichel D, Rychahou P, Bae Y. Polymer nanoassemblies with solvato- and halo-fluorochromism for drug release monitoring and metastasis imaging. Ther Deliv. 2015;6(10):1221-1237.

66. O'Connell CL, Nooney R, McDonagh C. Cyanine5-doped silica nanoparticles as ultra-bright immunospecific labels for model circulating tumour cells in flow cytometry and microscopy. Biosens Bioelectron. 2016;91:190-198.

67. Han J, Zhang C, Liu F, Liu B, Han M, Zou W, Yang L, Zhang Z. Upconversion nanoparticles for ratiometric fluorescence detection of nitrite. Analyst. 2014;139(12):3032-3038.

68. Kim H, Babu CR, Burgess DJ. Quantification of protonation in organic solvents using solution NMR spectroscopy: implication in salt formation. Int J Pharm. 2013;448(1):123-131.

69. Jose J, Ueno Y, Burgess K. Water-soluble Nile Blue derivatives: syntheses and photophysical properties. Chem Eur J. 2009;15(2):418-423.

70. Madsen J, Canton I, Warren NJ, Themistou E, Blanazs A, Ustbas B, Tian X, Pearson R, Battaglia G, Lewis AL, Armes SP. Nile Blue-Based Nanosized pH Sensors for Simultaneous Far-Red and Near-Infrared Live Bioimaging. J Am Chem Soc. 2013;135(39):14863-14870.

71. Cincotta L, Foley JW, Cincotta AH. Phototoxicity, redox behavior, and pharmacokinetics of benzophenoxazine analogues in EMT-6 murine sarcoma cells. Cancer Res. 1993;53(11):2571-2580.

72. Rheiner S, Bae Y. Increased poly(ethylene glycol) density decreases transfection efficacy of siRNA/poly(ethylene imine) complexes. AIMS Bioengineering. 2016;3(4):454-467.

73. Izunobi JU, Higginbotham CL. Polymer Molecular Weight Analysis by 1H NMR Spectroscopy. J Chem Educ. 2011;88(8):1098-1104.

74. Gavrilov M, Monteiro MJ. Derivation of the molecular weight distributions from size exclusion chromatography. Eur Polym J. 2015;65:191-196.

75. Qiu X, Zhou Z, Gobbi G, Redwine OD. Error Analysis for NMR Polymer Microstructure Measurement without Calibration Standards. Anal Chem. 2009;81(20):8585-8589.

76. Rheiner S, Rychahou P, Bae Y. Effects of the Lipophilic Core of Polymer Nanoassemblies on Intracellular Delivery and Transfection of siRNA. AIMS Biophysics. 2015;2(3):284-302.

77. Segets D, Marczak R, Schafer S, Paula C, Gnichwitz JF, Hirsch A, Peukert W. Experimental and theoretical studies of the colloidal stability of nanoparticles-a general interpretation based on stability maps. ACS Nano. 2011;5(6):4658-4669.

78. Kalia J, Raines RT. Advances in Bioconjugation. Curr Org Chem. 2010;14(2):138-147.

79. Boens N, Leen V, Dehaen W. Fluorescent indicators based on BODIPY. Chem Soc Rev. 2012;41(3):1130-1172.

80. Uchida Y, Maezawa Y, Uchida Y, Hiruta N, Shimoyama E. Molecular imaging of low-density lipoprotein in human coronary plaques by color fluorescent angioscopy and microscopy. PLoS One. 2012;7(11):e50678.

81. Thapa U, Ismail K. Urea effect on aggregation and adsorption of sodium dioctylsulfosuccinate in water. J Colloid Interface Sci. 2013;406:172-177.

82. Lee H. Molecular Dynamics Studies of PEGylated Single-Walled Carbon Nanotubes: The Effect of PEG Size and Grafting Density. The Journal of Physical Chemistry C. 2013;117(49):26334-26341.

83. Mariella R, Brown K. A novel SN1 displacement: The reaction of tertiary amines with acetic anhydride. Can J Chem. 1971;49(20):3348-3351.

84. Zhou J, Fang C, Chang T, Liu X, Shangguan D. A pH sensitive ratiometric fluorophore and its application for monitoring the intracellular and extracellular pHs simultaneously. J Mater Chem B. 2013;1(5):661-667.

85. Sanli S, Altun Y, Guven G. Solvent Effects on pKa Values of Some Anticancer Agents in Acetonitrile–Water Binary Mixtures. J Chem Eng Data. 2014;59(12):4015-4020.

86. Perrin DD, Dempsey B, Serjeant EP. pKa prediction for organic acids and bases: Springer; 1981.

87. Agency EM. Assessment Report: Kyprolis. 2015.

88. Cheng L, Yang K, Chen Q, Liu Z. Organic Stealth Nanoparticles for Highly Effective in Vivo Near-Infrared Photothermal Therapy of Cancer. ACS Nano. 2012;6(6):5605-5613.

89. Maeda H. Vascular permeability in cancer and infection as related to macromolecular drug delivery, with emphasis on the EPR effect for tumor-selective drug targeting. Proc Jpn Acad Ser B Phys Biol Sci. 2012;88(3):53-71.

90. Zou P, Chen H, Paholak HJ, Sun D. Noninvasive fluorescence resonance energy transfer imaging of in vivo premature drug release from polymeric nanoparticles. Mol Pharm. 2013;10(11):4185-4194.

91. Wang J, Gao PP, Yang XX, Wang TT, Wang J, Huang CZ. Real-time imaging of intracellular drug release from mesoporous silica nanoparticles based on fluorescence resonance energy transfer. J Mater Chem B. 2014;2(27):4379-4386.

92. Lai J, Shah BP, Garfunkel E, Lee K-B. Versatile Fluorescence Resonance Energy Transfer-Based Mesoporous Silica Nanoparticles for Real-Time Monitoring of Drug Release. ACS Nano. 2013;7(3):2741-2750.

93. Sarnat HB. Immunocytochemical markers of neuronal maturation in human diagnostic neuropathology. Cell Tissue Res. 2015;359(1):279-294.

94. Liu J, Zang L, Wang Y, Liu G. Preparation of acridine orange-doped silica nanoparticles for pH measurement. J Lumin. 2014;147(0):155-158.

95. Goetz M, Hoetker MS, Diken M, Galle PR, Kiesslich R. In vivo molecular imaging with cetuximab, an anti-EGFR antibody, for prediction of response in xenograft models of human colorectal cancer. Endoscopy. 2013;45(6):469-477.

96. Martinez V, Henary M. Nile Red and Nile Blue: Applications and Syntheses of Structural Analogues. Chemistry – A European Journal. 2016;22(39):13764-13782.

97. Hill TK, Abdulahad A, Kelkar SS, Marini FC, Long TE, Provenzale JM, Mohs AM. Indocyanine Green-Loaded Nanoparticles for Image-Guided Tumor Surgery. Bioconjugate Chem. 2015;26(2):294-303.

98. Yue C, Liu P, Zheng M, Zhao P, Wang Y, Ma Y, Cai L. IR-780 dye loaded tumor targeting theranostic nanoparticles for NIR imaging and photothermal therapy. Biomaterials. 2013;34(28):6853-6861.

99. Maeda H, Nakamura H, Fang J. The EPR effect for macromolecular drug delivery to solid tumors: Improvement of tumor uptake, lowering of systemic toxicity, and distinct tumor imaging in vivo. Adv Drug Del Rev. 2013;65(1):71-79.

100. Robinson PJ. The early detection of liver metastases. Cancer Imaging. 2002;2(2):1-3.

101. Spano D, Heck C, De Antonellis P, Christofori G, Zollo M. Molecular networks that regulate cancer metastasis. Semin Cancer Biol. 2012;22(3):234-249.

102. Patanaphan V, Salazar OM. Colorectal cancer: metastatic patterns and prognosis. South Med J. 1993;86(1):38-41.

103. Dhar V, Thomas RM, Ahmad SA. Repeat Hepatectomy for Colorectal Liver Metastases. In: Bentrem D, Benson AB, editors. Gastrointestinal Malignancies. Cham: Springer International Publishing; 2016. p. 203-220.

104. Lee SY, Oh SC. Advances of Targeted Therapy in Treatment of Unresectable Metastatic Colorectal Cancer. Biomed Res Int. 2016;2016:7590245.

105. Butler EB, Zhao Y, Munoz-Pinedo C, Lu J, Tan M. Stalling the engine of resistance: targeting cancer metabolism to overcome therapeutic resistance. Cancer Res. 2013;73(9):2709-2717.

106. Cercek A, Goodman KA, Hajj C, Weisberger E, Segal NH, Reidy-Lagunes DL, Stadler ZK, Wu AJ, Weiser MR, Paty PB, Guillem JG, Nash GM, Temple LK, Garcia-Aguilar J, Saltz LB. Neoadjuvant Chemotherapy First, Followed by Chemoradiation and Then Surgery, in the Management of Locally Advanced Rectal Cancer. J Natl Compr Canc Netw. 2014;12(4):513-519.

107. Matsuyama J, Doki Y, Yasuda T, Miyata H, Fujiwara Y, Takiguchi S, Yamasaki M, Makari Y, Matsuura N, Mano M, Monden M. The effect of neoadjuvant chemotherapy on lymph node micrometastases in squamous cell carcinomas of the thoracic esophagus. Surgery. 2007;141(5):570-580.

108. Kamiya M, Urano Y. Rapid and sensitive fluorescent imaging of tiny tumors in vivo and in clinical specimens. Curr Opin Chem Biol. 2016;33:9-15.

109. Maffione AM, Lopci E, Bluemel C, Giammarile F, Herrmann K, Rubello D. Diagnostic accuracy and impact on management of (18)F-FDG PET and PET/CT in colorectal liver metastasis: a meta-analysis and systematic review. Eur J Nucl Med Mol Imaging. 2015;42(1):152-163.

110. Weissleder R, Nahrendorf M. Advancing biomedical imaging. Proceedings of the National Academy of Sciences. 2015;112(47):14424-14428.

111. Barnes KD, Shafirstein G, Webber JS, Koonce NA, Harris Z, Griffin RJ. Hyperthermia-enhanced indocyanine green delivery for laser-induced thermal ablation of carcinomas. Int J Hyperthermia. 2013;29(5):474-479.

112. Wu L, Fang S, Shi S, Deng J, Liu B, Cai L. Hybrid polypeptide micelles loading indocyanine green for tumor imaging and photothermal effect study. Biomacromolecules. 2013;14(9):3027-3033.

113. Kraft JC, Ho RJ. Interactions of indocyanine green and lipid in enhancing near-infrared fluorescence properties: the basis for near-infrared imaging in vivo. Biochemistry. 2014;53(8):1275-1283.

114. Yang B, Han X, Ji B, Lu R. Competition Between Tumor and Mononuclear Phagocyte System Causing the Low Tumor Distribution of Nanoparticles and Strategies to Improve Tumor Accumulation. Curr Drug Deliv. 2016;13(8):1261-1274.

115. Mikhail AS, Eetezadi S, Ekdawi SN, Stewart J, Allen C. Image-based analysis of the size- and time-dependent penetration of polymeric micelles in multicellular tumor spheroids and tumor xenografts. Int J Pharm. 2014;464(1–2):168-177.

116. Yokoi K, Kojic M, Milosevic M, Tanei T, Ferrari M, Ziemys A. Capillary-Wall Collagen as a Biophysical Marker of Nanotherapeutic Permeability into the Tumor Microenvironment. Cancer Res. 2014;74(16):4239-4246.

117. Verkman AS. Diffusion in the extracellular space in brain and tumors. Phys Biol. 2013;10(4):045003.

118. . !!! INVALID CITATION !!! {Brown, 2016 #1360;Hoffman, 2015 #1659}.

119. Golovko D, Kedrin D, Yilmaz OH, Roper J. Colorectal cancer models for novel drug discovery. Expert Opin Drug Discov. 2015;10(11):1217-1229.

120. Ruggeri BA, Camp F, Miknyoczki S. Animal models of disease: pre-clinical animal models of cancer and their applications and utility in drug discovery. Biochem Pharmacol. 2014;87(1):150-161.

121. Hugen N, van de Velde CJH, de Wilt JHW, Nagtegaal ID. Metastatic pattern in colorectal cancer is strongly influenced by histological subtype. Ann Oncol. 2014;25(3):651-657.

122. Curtis LT, Rychahou P, Bae Y, Frieboes HB. A Computational/Experimental Assessment of Antitumor Activity of Polymer Nanoassemblies for pH-Controlled Drug Delivery to Primary and Metastatic Tumors. Pharm Res. 2016;33(10):2552-2564.

123. Curtis LT, England CG, Wu M, Lowengrub J, Frieboes HB. An interdisciplinary computational/experimental approach to evaluate drug-loaded gold nanoparticle tumor cytotoxicity. Nanomedicine. 2016;11(3):197-216.

124. Frieboes HB, Wu M, Lowengrub J, Decuzzi P, Cristini V. A computational model for predicting nanoparticle accumulation in tumor vasculature. PLoS One. 2013;8(2):e56876.

125. Xu X, Sabanayagam CR, Harrington DA, Farach-Carson MC, Jia X. A hydrogel-based tumor model for the evaluation of nanoparticle-based cancer therapeutics. Biomaterials. 2014;35(10):3319-3330.

126. Zhang X, Lin Y, Gillies RJ. Tumor pH and its measurement. J Nucl Med. 2010;51(8):1167-1170.

127. Chaudhari KR, Ukawala M, Manjappa AS, Kumar A, Mundada PK, Mishra AK, Mathur R, Monkkonen J, Murthy RS. Opsonization, biodistribution, cellular uptake and apoptosis study of PEGylated PBCA nanoparticle as potential drug delivery carrier. Pharm Res. 2012;29(1):53-68.

128. Zhang M, Liu Y-Q, Ye B-C. Colorimetric assay for sulfate using positively-charged gold nanoparticles and its application for real-time monitoring of redox process. Analyst. 2011;136(21):4558-4562.

129. Rausch K, Reuter A, Fischer K, Schmidt M. Evaluation of Nanoparticle Aggregation in Human Blood Serum. Biomacromolecules. 2010;11(11):2836-2839.

130. Chaudhari KR, Ukawala M, Manjappa AS, Kumar A, Mundada PK, Mishra AK, Mathur R, Mönkkönen J, Murthy RSR. Opsonization, Biodistribution, Cellular Uptake and Apoptosis Study of PEGylated PBCA Nanoparticle as Potential Drug Delivery Carrier. Pharm Res. 2012;29(1):53-68.

131. Opitz AW, Czymmek KJ, Wickstrom E, Wagner NJ. Uptake, efflux, and mass transfer coefficient of fluorescent PAMAM dendrimers into pancreatic cancer cells. Biochim Biophys Acta. 2013;1828(2):294-301.

132. Curtis LT, Wu M, Lowengrub J, Decuzzi P, Frieboes HB. Computational Modeling of Tumor Response to Drug Release from Vasculature-Bound Nanoparticles. PLoS One. 2015;10(12):e0144888.

133. van de Ven AL, Wu M, Lowengrub J, McDougall SR, Chaplain MA, Cristini V, Ferrari M, Frieboes HB. Integrated intravital microscopy and mathematical modeling to optimize nanotherapeutics delivery to tumors. AIP Adv. 2012;2(1):11208.

134. Curtis LT, Rychahou P, Bae Y, Frieboes HB. A computational/experimental assessment of antitumor activity of polymer nanoassemblies for ph-controlled drug delivery to primary and metastatic tumors. Pharm Res. 2016;33:2552–2564.

135. Wu M, Frieboes HB, Chaplain MA, McDougall SR, Cristini V, Lowengrub JS. The effect of interstitial pressure on therapeutic agent transport: coupling with the tumor blood and lymphatic vascular systems. J Theor Biol. 2014;355:194-207.

136. Wu M, Frieboes HB, McDougall SR, Chaplain MA, Cristini V, Lowengrub J. The effect of interstitial pressure on tumor growth: coupling with the blood and lymphatic vascular systems. J Theor Biol. 2013;320:131-151.

137. Macklin P, McDougall S, Anderson ARA, Chaplain MAJ, Cristini V, Lowengrub J. Multiscale modelling and nonlinear simulation of vascular tumour growth. Journal of Mathematical Biology. 2009;58(4-5):765-798.

138. McDougall SR, Anderson ARA, Chaplain MAJ. Mathematical modelling of dynamic adaptive tumour-induced angiogenesis: Clinical implications and

therapeutic targeting strategies. Journal of Theoretical Biology. 2006;241(3):564-589.

139. Macklin P, McDougall S, Anderson AR, Chaplain MA, Cristini V, Lowengrub J. Multiscale modelling and nonlinear simulation of vascular tumour growth. J Math Biol. 2009;58(4-5):765-798.

140. Curtis LT, England CG, Wu M, Lowengrub J, Frieboes HB. An interdisciplinary computational/experimental approach to evaluate drug-loaded gold nanoparticle tumor cytotoxicity. Nanomedicine (Lond). 2016;11(3):197-216.

141. Wu M, Frieboes HB, McDougall SR, Chaplain MA, Cristini V, Lowengrub J. The effect of interstitial pressure on tumor growth: coupling with the blood and lymphatic vascular systems. J Theor Biol. 2013;320:131-151.

142. Ponta A, Bae Y. Tumor-preferential sustained drug release enhances antitumor activity of block copolymer micelles. J Drug Target. 2014;22(7):619-628.

143. Nugent LJ, Jain RK. Extravascular diffusion in normal and neoplastic tissues. Cancer Res. 1984;44(1):238-244.

144. Kekelidze M, D'Errico L, Pansini M, Tyndall A, Hohmann J. Colorectal cancer: current imaging methods and future perspectives for the diagnosis, staging and therapeutic response evaluation. World J Gastroenterol. 2013;19(46):8502-8514.

145. Terranova N, Girard P, Klinkhardt U, Munafo A. Resistance Development: A Major Piece in the Jigsaw Puzzle of Tumor Size Modeling. CPT Pharmacometrics Syst Pharmacol. 2015;4(6):320-323.

146. Etrych T, Lucas H, Janouskova O, Chytil P, Mueller T, Mader K. Fluorescence optical imaging in anticancer drug delivery. J Control Release. 2016;226:168-181.

147. Shao D, Lu MM, Zhao YW, Zhang F, Tan YF, Zheng X, Pan Y, Xiao XA, Wang Z, Dong WF, Li J, Chen L. The shape effect of magnetic mesoporous silica nanoparticles on endocytosis, biocompatibility and biodistribution. Acta Biomater. 2017;49:531-540.

148. Kumar R, Roy I, Ohulchanskky TY, Vathy LA, Bergey EJ, Sajjad M, Prasad PN. In vivo biodistribution and clearance studies using multimodal organically modified silica nanoparticles. ACS Nano. 2010;4(2):699-708.

149. Sindhwani S, Syed AM, Wilhelm S, Glancy DR, Chen YY, Dobosz M, Chan WCW. Three-Dimensional Optical Mapping of Nanoparticle Distribution in Intact Tissues. ACS Nano. 2016;10(5):5468-5478.

150. Shrinivas P, Kasapis S, Tongdang T. Morphology and mechanical properties of bicontinuous gels of agarose and gelatin and the effect of added lipid phase. Langmuir. 2009;25(15):8763-8773.

151. Tufto I, Lyng H, Rofstad EK. Interstitial fluid pressure, perfusion rate and oxygen tension in human melanoma xenografts. Br J Cancer Suppl. 1996;27.

152. Watson KD, Lai CY, Qin S, Kruse DE, Lin YC, Seo JW, Cardiff RD, Mahakian LM, Beegle J, Ingham ES, Curry FR, Reed RK, Ferrara KW. Ultrasound increases nanoparticle delivery by reducing intratumoral pressure and increasing transport in epithelial and epithelial-mesenchymal transition tumors. Cancer Res. 2012;72(6):1485-1493.

153. Durymanov MO, Rosenkranz AA, Sobolev AS. Current Approaches for Improving Intratumoral Accumulation and Distribution of Nanomedicines. Theranostics. 2015;5(9):1007-1020.

154. Podduturi VP, Magaña IB, O'Neal DP, Derosa PA. Simulation of transport and extravasation of nanoparticles in tumors which exhibit enhanced permeability and retention effect. Comput Methods Programs Biomed;112(1):58-68.

155. Tan J, Shah S, Thomas A, Ou-Yang HD, Liu Y. The influence of size, shape and vessel geometry on nanoparticle distribution. Microfluid Nanofluid. 2013;14(1-2):77-87.

156. Schultz SG, Solomon AK. Determination of the Effective Hydrodynamic Radii of Small Molecules by Viscometry. The Journal of General Physiology. 1961;44(6):1189-1199.

157. Krishna R. Diffusion in porous crystalline materials. Chem Soc Rev. 2012;41(8):3099-3118.

158. Beck-Broichsitter M, Nicolas J, Couvreur P. Design attributes of long-circulating polymeric drug delivery vehicles. Eur J Pharm Biopharm. 2015;97(Pt B):304-317.

159. Gao H, He Q. The interaction of nanoparticles with plasma proteins and the consequent influence on nanoparticles behavior. Expert Opin Drug Deliv. 2014;11(3):409-420.

160. Park JE, Chun S-E, Reichel D, Min JS, Lee S-C, Han S, Ryoo G, Oh Y, Park S-H, Ryu H-M, Kim KB, Lee H-Y, Bae SK, Bae Y, Lee W. Polymer micelle formulation for the proteasome inhibitor drug carfilzomib: Anticancer efficacy and pharmacokinetic studies in mice. PLoS One. 2017;12(3):e0173247.

161. Del Monte U. Does the cell number 10(9) still really fit one gram of tumor tissue? Cell Cycle. 2009;8(3):505-506.

162. Vestvik IK, Egeland TAM, Gaustad J-V, Mathiesen B, Rofstad EK. Assessment of microvascular density, extracellular volume fraction, and radiobiological hypoxia in human melanoma xenografts by dynamic contrast-enhanced MRI. J Magn Reson Imaging. 2007;26(4):1033-1042.

163. Keij JF, Bell-Prince C, Steinkamp JA. Staining of mitochondrial membranes with 10-nonyl acridine orange, MitoFluor Green, and MitoTracker Green is affected by mitochondrial membrane potential altering drugs. Cytometry. 2000;39(3):203-210.

164. Weigel A, Schild D, Zeug A. Resolution in the ApoTome and the confocal laser scanning microscope: comparison. J Biomed Opt. 2009;14(1):014022.

165. Tangrea MA, Mukherjee S, Gao B, Markey SP, Du Q, Armani M, Kreitman MS, Rosenberg AM, Wallis BS, Eberle FC, Duncan FC, Hanson JC, Chuaqui RF, Rodriguez-Canales J, Emmert-Buck MR. Effect of Immunohistochemistry on Molecular Analysis of Tissue Samples: Implications for Microdissection Technologies. J Histochem Cytochem. 2011;59(6):591-600.

166. Dickerson M, Howerton B, Bae Y, Glazer E. Light-sensitive ruthenium complex-loaded cross-linked polymeric nanoassemblies for the treatment of cancer. J Mater Chem B Mater Biol Med. 2016;4:394-408.

167. Lee HJ, Bae Y. Pharmaceutical differences between block copolymer self-assembled and cross-linked nanoassemblies as carriers for tunable drug release. Pharm Res. 2013;30(2):478-488.

168. Cao P, Ponta A, Kim JA, Bae Y. Block copolymer crosslinked nanoassemblies co-entrapping acridine yellow and doxorubicin for cancer theranostics. British J Pharm Res. 2013;3:536-547.

169. Lee HJ, Ponta A, Bae Y. Polymer nanoassemblies for cancer treatment and imaging. Ther Deliv. 2010;1(6):803-817.

170. Scott D, Bae Y. Block copolymer crosslinked nanoassemblies co-entrapping hydrophobic drugs and lipophilic polymer additives. J Pharm Drug Deliv Res. 2013;2(1000116):1-5.

171. Ponta A, Bae Y. PEG-poly(amino acid) block copolymer micelles for tunable drug release. Pharm Res. 2010;27(11):2330-2342.

172. Bae Y. Drug delivery systems using polymer nanoassemblies for cancer treatment. Ther Delivery. 2010;1:361-363.

173. Howard MD, Ponta A, Eckman AM, Jay M, Bae Y. Polymer micelles with hydrazone-ester dual linkers for tunable release of dexamethasone. Pharm Res. 2011;28:2435-2446.

174. Eckman AM, Tsakalozou E, Kang NY, Ponta A, Bae Y. Drug release patterns and cytotoxicity of PEG-poly(aspartate) block copolymer micelles in cancer cells. Pharm Res. 2012;29(7):1755-1767.

175. Dickerson M, Winquist N, Bae Y. Photo-inducible crosslinked nanoassemblies for pH-controlled drug release. Pharm Res. 2014;31(5):1254-1263.

176. Ao L, Reichel D, Hu D, Jeong H-Y, Kim KB, Bae Y, Lee W. Polymer micelle formulations of proteasome inhibitor carfilzomib for improved metabolic stability and anti-cancer efficacy in human multiple myeloma and lung cancer cell lines. J Pharmacol Exp Ther. 2015;355:168-173.

177. Lee HJ, Bae Y. The effect of core crosslinking degree on drug release patterns of pH-sensitive block copolymer crosslinked nanoassemblies. Nano Bull. 2013;2:1302101-1302109.

178. Akter S, Clem BF, Lee HJ, Chesney J, Bae Y. Block copolymer micelles for controlled delivery of glycolytic enzyme inhibitors. Pharm Res. 2012;29(3):847-855.

179. Scott D, Rohr J, Bae Y. Nanoparticulate formulations of mithramycin analogs for enhanced cytotoxicity. Int J Nanomed. 2011;6:2757-2767.

180. Ponta A, Akter S, Bae Y. Degradable cross-linked nanoassemblies as drug carriers for heat shock protein 90 inhibitor 17-N-allylamino-17-demethoxygeldanamycin. Pharmaceuticals. 2011;4:1281-1292.

181. Lee HJ, Bae Y. Cross-linked nanoassemblies from poly(ethylene glycol)-poly(aspartate) block copolymers as stable supramolecular templates for particulate drug delivery. Biomacromolecules. 2011;12:2686-2696.

182. Alani AWG, Bae Y, Rao DA, Kwon GS. Polymeric micelles for the pH-dependent controlled, continuous low dose release of paclitaxel. Biomaterials. 2010;31(7):1765-1772.

183. Bae Y, Nishiyama N, Fukushima S, Koyama H, Matsumura Y, Kataoka K. Preparation and biological characterization of polymeric micelle drug carriers with intracellular pH-triggered drug release property: Tumor permeability, controlled subcellular drug distribution, and enhanced in vivo antitumor efficacy. Bioconjugate Chem. 2005;16(1):122-130.

184. Ponta A, Fugit KD, Anderson BD, Bae Y. Release, partitioning, and conjugation stability of doxorubicin in polymer micelles determined by mechanistic modeling. Pharm Res. 2015;32(5):1752-1763.

185. Fugit KD, Xiang TX, Choi du H, Kangarlou S, Csuhai E, Bummer PM, Anderson BD. Mechanistic model and analysis of doxorubicin release from liposomal formulations. J Control Release. 2015;217:82-91.

186. Wu H, Zhu L, Torchilin VP. pH-sensitive poly(histidine)-PEG/DSPE-PEG co-polymer micelles for cytosolic drug delivery. Biomaterials. 2013;34(4):1213-1222.

187. Yadav S, Gupta S. Development and in vitro characterization of docetaxel-loaded ligand appended solid fat nanoemulsions for potential use in breast cancer therapy. Artif Cells Nano Biotechnol. 2015;43(2):93-102.

188. Li J, Guo X, Liu Z, Okeke CI, Li N, Zhao H, Aggrey MO, Pan W, Wu T. Preparation and evaluation of charged solid lipid nanoparticles of tetrandrine for ocular drug delivery system: pharmacokinetics, cytotoxicity and cellular uptake studies. Drug Dev Ind Pharm. 2014;40(7):980-987.

189. Dickerson M, Winquist N, Bae Y. Photo-inducible cross-linked nanoassemblies for controlled drug delivery. Pharm Res. 2013;31:1254-1263.

190. Dickerson M, Bae Y. Block copolymer nanoassemblies for photodynamic therapy and diagnosis. Ther Deliv. 2013;4(11):1431-1441.

191. Jin G-W, Bae Y. Reductant-dependent none-partial-complete degradation of block copolymer disulfide crosslinked nanoassemblies. J App Pharm Sci. 2013;3:1-6.

192. Bera A, Chandel AKS, Kumar CU, Jewrajka SK. Degradable/cytocompatible and pH responsive amphiphilic conetwork gels based on agarose-graft copolymers and polycaprolactone. J Mat Chem B. 2015;3(43):8548-8557.

193. de Andrade DF, Zuglianello C, Pohlmann AR, Guterres SS, Beck RCR. Assessing the in vitro drug release from lipid-core nanocapsules: a new strategy combining dialysis sac and a continuous-flow system. AAPS PharmSciTech. 2015;16(6):1409-1417.

194. Fuchs K, Bize PE, Denys A, Borchard G, Jordan O. Sunitinib-eluting beads for chemoembolization: Methods for in vitro evaluation of drug release. Int J Pharm. 2015;482(1):68-74.

195. Salmela L, Washington C. A continuous flow method for estimation of drug release rates from emulsion formulations. International journal of pharmaceutics. 2014;472(1):276-281.

196. Wasik S, Arabski M, Drulis-Kawa Z, Gubernator J. Laser interferometry analysis of ciprofloxacin and ampicillin diffusion from liposomal solutions to water phase. Eur Biophy J. 2013;42(7):549-558.

197. Li Z, Paulson AT, Gill TA. Encapsulation of bioactive salmon protein hydrolysates with chitosan-coated liposomes. J Func Foods. 2015;19:733-743.

198. Gullotti E, Yeo Y. Beyond the imaging: limitations of cellular uptake study in the evaluation of nanoparticles. J Control Release. 2012;164(2):170-176.

199. Zhou Y, He C, Chen K, Ni J, Cai Y, Guo X, Wu XY. A New Method for Evaluating Actual Drug Release Kinetics of Nanoparticles inside Dialysis Devices via Numerical Deconvolution. J Control Release. 2016;243:11-20.

200. Xie L, Beyer S, Vogel V, Wacker MG, Mantele W. Assessing the drug release from nanoparticles: Overcoming the shortcomings of dialysis by using novel optical techniques and a mathematical model. Int J Pharm. 2015;488(1):108-119.

201. Reichel D, Rychahou P, Bae Y. Polymer nanoassemblies with solvato- and halo-fluorochromic properties for real-time monitoring of drug release and pH-enhanced ex vivo imaging of metastatic tumors. Ther Delivery. 2015;6:1221-1237.

202. Cheng Y, Xu T. The effect of dendrimers on the pharmacodynamic and pharmacokinetic behaviors of non-covalently or covalently attached drugs. Eur J Med Chem. 2008;43(11):2291-2297.

203. Jaimes-Aguirre L, Gibbens-Bandala BV, Morales-Avila E, Ocampo-Garcia BE, Seyedeh-Fatemeh M, Amirhosein A. Polymer-Based Drug Delivery Systems, Development and Pre-Clinical Status. Curr Pharm Des. 2016;22(19):2886-2903.

204. Chu KS, Hasan W, Rawal S, Walsh MD, Enlow EM, Luft JC, Bridges AS, Kuijer JL, Napier ME, Zamboni WC, DeSimone JM. Plasma, tumor and tissue pharmacokinetics of Docetaxel delivered via nanoparticles of different sizes and shapes in mice bearing SKOV-3 human ovarian carcinoma xenograft. Nanomedicine. 2013;9(5):686-693.

205. Stylianopoulos T, Jain RK. Design considerations for nanotherapeutics in oncology. Nanomedicine. 2015;11(8):1893-1907.

206. Diou O, Greco S, Beltran T, Lairez D, Authelin JR, Bazile D. A method to Quantify the Affinity of Cabazitaxel for PLA-PEG Nanoparticles and Investigate the Influence of the Nano-Assembly Structure on the Drug/Particle Association. Pharm Res. 2015;32(10):3188-3200.

207. Modi S, Anderson BD. Determination of Drug Release Kinetics from Nanoparticles: Overcoming Pitfalls of the Dynamic Dialysis Method. Mol Pharm. 2013;10(8):3076-3089.

208. Han HS, Choi KY, Ko H, Jeon J, Saravanakumar G, Suh YD, Lee DS, Park JH. Bioreducible core-crosslinked hyaluronic acid micelle for targeted cancer therapy. J Controlled Release. 2015;200:158-166.

209. Talelli M, Barz M, Rijcken CJF, Kiessling F, Hennink WE, Lammers T. Core-crosslinked polymeric micelles: Principles, preparation, biomedical applications and clinical translation. Nano Today. 2015;10(1):93-117.

210. Souza S. A Review of In Vitro Drug Release Test Methods for Nano-Sized Dosage Forms. Advances in Pharmaceutics. 2014;2014:12.

211. Modi S, Anderson BD. Determination of Drug Release Kinetics from Nanoparticles: Overcoming Pitfalls of the Dynamic Dialysis Method. Mol Pharm. 2013;10(8):3076-3089.

212. Puskás I, Varga E, Tuza K, Szemán J, Fenyvesi É, Sohajda T, Szente L. Sulfobutylether-cyclodextrins: structure, degree of substitution and functional performance. In. Cyclodextrins: Synthesis, Chemical Applications and Role in Drug Delivery: Nova Science Publishers, Hauppauge, NY; 2015. p. 293-320.

213. Cao L, Bornscheuer UT, Schmid RD. Lipase-catalyzed solid-phase synthesis of sugar esters. Influence of immobilization on productivity and stability of the enzyme. J Mol Cat B Enzymatic. 1999;6(3):279-285.

214. Roda A, Minutello A, Angellotti MA, Fini A. Bile acid structure-activity relationship: evaluation of bile acid lipophilicity using 1-octanol/water partition coefficient and reverse phase HPLC. J Lipid Res. 1990;31(8):1433-1443.

215. Hopfner T, Bluma A, Rudolph G, Lindner P, Scheper T. A review of non-invasive optical-based image analysis systems for continuous bioprocess monitoring. Bioprocess Biosyst Eng. 2010;33(2):247-256.

216. Beutel S, Henkel S. In situ sensor techniques in modern bioprocess monitoring. Appl Microbiol Biotechnol. 2011;91(6):1493-1505.

217. Cho EJ, Holback H, Liu KC, Abouelmagd SA, Park J, Yeo Y. Nanoparticle Characterization: State of the Art, Challenges, and Emerging Technologies. Mol Pharm. 2013;10(6):2093-2110.

218. Duan R, Li C, Liu S, Liu Z, Li Y, Zhu J, Hu X. A selective fluorescence quenching method for the determination of trace hypochlorite in water samples with nile blue A. J Taiwan Inst Chem Eng. 2015;50:43-48.

219. Frick AA, Busetti F, Cross A, Lewis SW. Aqueous Nile blue: a simple, versatile and safe reagent for the detection of latent fingermarks. Chem Comm. 2014;50(25):3341-3343.

220. Fugit KD, Anderson BD. Dynamic, nonsink method for the simultaneous determination of drug permeability and binding coefficients in liposomes. Mol Pharm. 2014;11(4):1314-1325.

221. Zambito Y, Pedreschi E, Di Colo G. Pharmaceutical Nanotechnology. Int J Pharm. 2012;434(1-2):28-34.

222. Reichel D, Bae Y. Comparison of Dialysis- and Solvatofluorochromism-Based Methods to Determine Drug Release Rates from Polymer Nanoassemblies. Pharm Res. 2016.

223. Lee JH, Yeo Y. Controlled drug release from pharmaceutical nanocarriers. Chem Eng Sci. 2015;125:75-84.

224. Yin W, Kimbrough CW, Gomez-Gutierrez JG, Burns CT, Chuong P, Grizzle WE, McNally LR. Tumor specific liposomes improve detection of pancreatic adenocarcinoma in vivo using optoacoustic tomography. J Nanobiotechnology. 2015;13:90.

225. Tucker-Schwartz JM, Beavers KR, Sit WW, Shah AT, Duvall CL, Skala MC. In vivo imaging of nanoparticle delivery and tumor microvasculature with multimodal optical coherence tomography. Biomed Opt Express. 2014;5(6):1731-1743.

226. Amjadi I, Rabiee M, Hosseini MS. Anticancer Activity of Nanoparticles Based on PLGA and its Co-polymer: In-vitro Evaluation. Iran J Pharm Res. 2013;12(4):623-634.

227. Cha C, Jeong JH, Kong H. Poly(ethylene glycol)-poly(lactic-co-glycolic acid) core-shell microspheres with enhanced controllability of drug encapsulation and release rate. J Biomater Sci Polym Ed. 2015;26(13):828-840.

228. Duncan TV. Release of engineered nanomaterials from polymer nanocomposites: the effect of matrix degradation. ACS Appl Mater Interfaces. 2015;7(1):20-39.

229. Duncan TV, Pillai K. Release of engineered nanomaterials from polymer nanocomposites: diffusion, dissolution, and desorption. ACS Appl Mater Interfaces. 2015;7(1):2-19.

230. Dinerman AA, Cappello J, El-Sayed M, Hoag SW, Ghandehari H. Influence of solute charge and hydrophobicity on partitioning and diffusion in a genetically engineered silk-elastin-like protein polymer hydrogel. Macromol Biosci. 2010;10(10):1235-1247.

231. Suksiriworapong J, Phoca K, Ngamsom S, Sripha K, Moongkarndi P, Junyaprasert VB. Comparison of poly(epsilon-caprolactone) chain lengths of poly(epsilon-caprolactone)-co-d-alpha-tocopheryl-poly(ethylene glycol) 1000 succinate nanoparticles for enhancement of quercetin delivery to SKBR3 breast cancer cells. Eur J Pharm Biopharm. 2016;101:15-24.

232. Arifin DY, Lee LY, Wang C-H. Mathematical modeling and simulation of drug release from microspheres: Implications to drug delivery systems. Adv Drug Del Rev. 2006;58(12–13):1274-1325.

233. Sutton D, Wang S, Nasongkla N, Gao J, Dormidontova EE. Doxorubicin and β-Lapachone Release and Interaction with Micellar Core Materials: Experiment and Modeling. Exp Biol Med. 2007;232(8):1090-1099.

234. Kim K-M, Kim H-M, Choi M-H, Lee JK, Jeong J, Lee M-H, Kim YS, Paek S-M, Oh J-M. Colloidal Properties of Surface Coated Colloidal Silica Nanoparticles in Aqueous and Physiological Solutions. Science of Advanced Materials. 2014;6(7):1573-1581.

235. Stockert JC, Blazquez A, Galaz S, Juarranz A. A mechanism for the fluorogenic reaction of amino groups with fluorescamine and MDPF. Acta Histochem. 2008;110(4):333-340.

236. Brewer J, Roberts C, Stimson W, Alexander J. Accurate determination of adjuvant-associated protein or peptide by ninhydrin assay. Vaccine. 1995;13(15):1441-1444.

237. Starcher B. A Ninhydrin-Based Assay to Quantitate the Total Protein Content of Tissue Samples. Anal Biochem. 2001;292(1):125-129.

238. Bae Y. Drug delivery systems using polymer nanoassemblies for cancer treatment. Ther Deliv. 2010;1(3):361-363.

239. Dickerson M, Howerton B, Bae Y, Glazer E. Light-Sensitive Ruthenium Complex-Loaded Cross-linked Polymeric Nanoassemblies for the Treatment of Cancer. J Mater Chem B Mater Biol Med. 2016;4(3):394-408.

240. Lee HJ, Bae Y. Cross-linked nanoassemblies from poly(ethylene glycol)-poly(aspartate) block copolymers as stable supramolecular templates for particulate drug delivery. Biomacromolecules. 2011;12(7):2686-2696.

241. Owen SC, Chan DPY, Shoichet MS. Polymeric micelle stability. Nano Today. 2012;7(1):53-65.

242. Attia AB, Yang C, Tan JP, Gao S, Williams DF, Hedrick JL, Yang YY. The effect of kinetic stability on biodistribution and anti-tumor efficacy of drug-loaded biodegradable polymeric micelles. Biomaterials. 2013;34(12):3132-3140.

243. Yang C, Attia AB, Tan JP, Ke X, Gao S, Hedrick JL, Yang YY. The role of non-covalent interactions in anticancer drug loading and kinetic stability of polymeric micelles. Biomaterials. 2012;33(10):2971-2979.

244. Li Z, Tan BH. Towards the development of polycaprolactone based amphiphilic block copolymers: molecular design, self-assembly and biomedical applications. Materials Science and Engineering: C. 2014;45:620-634.

245. Pitto-Barry A, Barry NP. Pluronic® block-copolymers in medicine: from chemical and biological versatility to rationalisation and clinical advances. Polymer Chemistry. 2014;5(10):3291-3297.

246. Yoon HY, Koo H, Choi KY, Chan Kwon I, Choi K, Park JH, Kim K. Photo-crosslinked hyaluronic acid nanoparticles with improved stability for in vivo tumor-targeted drug delivery. Biomaterials. 2013;34(21):5273-5280.

247. Duan X, He C, Kron SJ, Lin W. Nanoparticle formulations of cisplatin for cancer therapy. Wiley Interdiscip Rev Nanomed Nanobiotechnol. 2016.

248. Woodman JL, Suh MS, Zhang J, Kondaveeti Y, Burgess DJ, White BA, Prestwich GD, Kuhn LT. Carboxymethyl Hyaluronan-Stabilized Nanoparticles for Anticancer Drug Delivery. Int J Cell Biol. 2015;2015:249573.

249. Wang Y, Li P, Kong L. Chitosan-modified PLGA nanoparticles with versatile surface for improved drug delivery. AAPS PharmSciTech. 2013;14(2):585-592.

250. Rabanel J-M, Hildgen P, Banquy X. Assessment of PEG on polymeric particles surface, a key step in drug carrier translation. J Controlled Release. 2014;185:71-87.

251. Nauka PC, Lee J, Maynard HD. Enhancing Conjugation Yield of Brush Polymer-Protein Conjugates by Increasing Linker Length at the Polymer End-Group. Polymer Chemistry. 2016;7(13):2352-2357.

252. Pinter B, Fievez T, Bickelhaupt FM, Geerlings P, De Proft F. On the origin of the steric effect. Phys Chem Chem Phys. 2012;14(28):9846-9854.

253. Richard I, Thibault M, De Crescenzo G, Buschmann MD, Lavertu M. Ionization behavior of chitosan and chitosan-DNA polyplexes indicate that chitosan has a similar capability to induce a proton-sponge effect as PEI. Biomacromolecules. 2013;14(6):1732-1740.

254. Curtis KA, Miller D, Millard P, Basu S, Horkay F, Chandran PL. Unusual Salt and pH Induced Changes in Polyethylenimine Solutions. PLoS One. 2016;11(9):e0158147.

255. Ao L, Reichel DA, Hu D, Jeong H, Kim KB, Bae Y, Lee W. Polymer Micelle Formulations of Proteasome Inhibitor Carfilzomib for Improved Metabolic Stability and Anti-Cancer Efficacy in Human Multiple Myeloma and Lung Cancer Cell Lines. J Pharmacol Exp Ther. 2015.

256. Jager M, Schubert S, Ochrimenko S, Fischer D, Schubert US. Branched and linear poly(ethylene imine)-based conjugates: synthetic modification, characterization, and application. Chem Soc Rev. 2012;41(13):4755-4767.

257. England CG, Miller MC, Kuttan A, Trent JO, Frieboes HB. Release kinetics of paclitaxel and cisplatin from two and three layered gold nanoparticles. Eur J Pharm Biopharm. 2015;92:120-129.

258. Ritger PL, Peppas NA. A simple equation for description of solute release II. Fickian and anomalous release from swellable devices. J Controlled Release. 1987;5(1):37-42.

259. Dash S, Murthy PN, Nath L, Chowdhury P. Kinetic modeling on drug release from controlled drug delivery systems. Acta Pol Pharm. 2010;67(3):217-223.

260. Rehage G, Ernst O, Fuhrmann J. Fickian and non-Fickian diffusion in high polymer systems. Discuss Faraday Soc. 1970;49(0):208-221.

261. Fu Y, Kao WJ. Drug release kinetics and transport mechanisms of non-degradable and degradable polymeric delivery systems. Expert Opinion on Drug Delivery. 2010;7(4):429-444.

262. Reichel D, Lee MJ, Lee W, Kim KB, Bae Y. Tethered Polymer Nanoassemblies for Sustained Carfilzomib Release and Prolonged Suppression of Proteasome Activity. Ther Delivery. 2016;(Accepted).

263. Ciechanover A. Intracellular protein degradation: from a vague idea through the lysosome and the ubiquitin-proteasome system and onto human diseases and drug targeting. Bioorg Med Chem. 2013;21(12):3400-3410.

264. Orlowski RZ, Kuhn DJ. Proteasome Inhibitors in Cancer Therapy: Lessons from the First Decade. Clin Cancer Res. 2008;14(6):1649-1657.

265. Baker AF, Hanke NT, Sands BJ, Carbajal L, Anderl JL, Garland LL. Carfilzomib demonstrates broad anti-tumor activity in pre-clinical non-small cell and small cell lung cancer models. J Exp Clin Cancer Res. 2014;33(1):1-12.

266. Gu JJ, Hernandez-Ilizaliturri FJ, Kaufman GP, Czuczman NM, Mavis C, Skitzki JJ, Czuczman MS. The novel proteasome inhibitor carfilzomib induces cell cycle

arrest, apoptosis and potentiates the anti-tumour activity of chemotherapy in rituximab-resistant lymphoma. Br J Haematol. 2013;162(5):657-669.

267. Buac D, Shen M, Schmitt S, Kona FR, Deshmukh R, Zhang Z, Neslund-Dudas C, Mitra B, Dou QP. From bortezomib to other inhibitors of the proteasome and beyond. Curr Pharm Des. 2013;19(22):4025-4038.

268. Kouroukis TC, Baldassarre FG, Haynes AE, Imrie K, Reece DE, Cheung MC. Bortezomib in multiple myeloma: systematic review and clinical considerations. 2014. 2014;21(4):31.

269. Redic K. Carfilzomib: a novel agent for multiple myeloma. J Pharm Pharmacol. 2013;65(8):1095-1106.

270. Shirley M. Ixazomib: First Global Approval. Drugs. 2016;76(3):405-411.

271. Nooka AK, Kastritis E, Dimopoulos MA, Lonial S. Treatment options for relapsed and refractory multiple myeloma. Blood. 2015;125(20):3085-3099.

272. Mansour MA, Aljoufi MA, Al-Hosaini K, Al-Rikabi AC, Nagi MN. Possible role of selective, irreversible, proteasome inhibitor (carfilzomib) in the treatment of rat hepatocellular carcinoma. Chem Biol Interact. 2014;215:17-24.

273. Baker AF, Hanke NT, Sands BJ, Carbajal L, Anderl JL, Garland LL. Carfilzomib demonstrates broad anti-tumor activity in pre-clinical non-small cell and small cell lung cancer models. J Exp Clin Cancer Res. 2014;33(1):111.

274. Papadopoulos KP, Burris HA, 3rd, Gordon M, Lee P, Sausville EA, Rosen PJ, Patnaik A, Cutler RE, Jr., Wang Z, Lee S, Jones SF, Infante JR. A phase I/II study of carfilzomib 2-10-min infusion in patients with advanced solid tumors. Cancer Chemother Pharmacol. 2013;72(4):861-868.

275. Papadopoulos KP, Burris HA, Gordon M, Lee P, Sausville EA, Rosen PJ, Patnaik A, Cutler RE, Wang Z, Lee S, Jones SF, Infante JR. A phase I/II study of carfilzomib 2–10-min infusion in patients with advanced solid tumors. Cancer Chemother Pharmacol. 2013;72(4):861-868.

276. Sebestyen Z, Szepesi K, Szabo B. [Pharmaceutical applications of sulfobuthylether-beta-cyclodextrin]. Acta Pharm Hung. 2013;83(2):57-67.

277. Chu KS, Schorzman AN, Finniss MC, Bowerman CJ, Peng L, Luft JC, Madden AJ, Wang AZ, Zamboni WC, DeSimone JM. Nanoparticle drug loading as a design parameter to improve docetaxel pharmacokinetics and efficacy. Biomaterials. 2013;34(33):8424-8429.

278. Luke DR, Wood ND, Tomaszewski KE, Damle B. Pharmacokinetics of sulfobutylether-beta-cyclodextrin (SBECD) in subjects on hemodialysis. Nephrol Dial Transplant. 2012;27(3):1207-1212.

279. Kim HS, Lee JY, Lim SH, Sun JM, Lee SH, Ahn JS, Park K, Moon SH, Ahn MJ. A Prospective Phase II Study of Cisplatin and Cremophor EL-Free Paclitaxel (Genexol-PM) in Patients with Unresectable Thymic Epithelial Tumors. J Thorac Oncol. 2015;10(12):1800-1806.

280. Ahn HK, Jung M, Sym SJ, Shin DB, Kang SM, Kyung SY, Park JW, Jeong SH, Cho EK. A phase II trial of Cremorphor EL-free paclitaxel (Genexol-PM) and gemcitabine in patients with advanced non-small cell lung cancer. Cancer Chemother Pharmacol. 2014;74(2):277-282.

281. Bobo D, Robinson KJ, Islam J, Thurecht KJ, Corrie SR. Nanoparticle-Based Medicines: A Review of FDA-Approved Materials and Clinical Trials to Date. Pharm Res. 2016.

282. Prabhu RH, Patravale VB, Joshi MD. Polymeric nanoparticles for targeted treatment in oncology: current insights. Int J Nanomedicine. 2015;10:1001-1018.

283. Mishima Y, Santo L, Eda H, Cirstea D, Nemani N, Yee AJ, O'Donnell E, Selig MK, Quayle SN, Arastu-Kapur S, Kirk C, Boise LH, Jones SS, Raje N. Ricolinostat (ACY-1215) induced inhibition of aggresome formation accelerates carfilzomib-induced multiple myeloma cell death. Br J Haematol. 2015;169(3):423-434.

284. Nguyen HQ, Kimoto E, Callegari E, Obach RS. Mechanistic Modeling to Predict Midazolam Metabolite Exposure from In Vitro Data. Drug Metab Dispos. 2016;44(5):781-791.

285. Liu R, Schyman P, Wallqvist A. Critically Assessing the Predictive Power of QSAR Models for Human Liver Microsomal Stability. J Chem Inf Model. 2015;55(8):1566-1575.

286. Perryman AL, Stratton TP, Ekins S, Freundlich JS. Predicting Mouse Liver Microsomal Stability with "Pruned" Machine Learning Models and Public Data. Pharm Res. 2016;33(2):433-449.

287. Fonsi M. Extrahepatic metabolism may complicate the IVIVC in rats. Drug Metab Lett. 2014;8(1):51-66.

288. Nishimuta H, Houston JB, Galetin A. Hepatic, intestinal, renal, and plasma hydrolysis of prodrugs in human, cynomolgus monkey, dog, and rat: implications for in vitro-in vivo extrapolation of clearance of prodrugs. Drug Metab Dispos. 2014;42(9):1522-1531.

289. Sestak V, Roh J, Klepalova L, Kovarikova P. A UHPLC-UV-QTOF study on the stability of carfilzomib, a novel proteasome inhibitor. J Pharm Biomed Anal. 2016;124:365-373.

290. Phizackerley KM, Jumaa M, Lopalco A, Wolfe BH, Ablan CD, Stella VJ. Mechanism of Degradation of an α-Keto-Epoxide, a Model for the Warhead for Various Proteasome Inhibitor Anticancer Agents. J Pharm Sci;106(4):1051-1061.

291. Sun C, Roboti P, Puumalainen MR, Fryknas M, Wang X, D'Arcy P, Hult M, High S, Linder S, Swanton E. Elevation of proteasomal substrate levels sensitizes cells to apoptosis induced by inhibition of proteasomal deubiquitinases. PLoS One. 2014;9(10):e108839.

292. Mukherjee B, Das S, Chakraborty S, Satapathy BS, Das PJ, Mondal L, Hossain CM, Dey NS, Chaudhury A. Potentials of polymeric nanoparticle as drug carrier for cancer therapy: with a special reference to pharmacokinetic parameters. Curr Drug Metab. 2014;15(6):565-580.

293. Hoshyar N, Gray S, Han H, Bao G. The effect of nanoparticle size on in vivo pharmacokinetics and cellular interaction. Nanomedicine (Lond). 2016;11(6):673-692.

294. Li Y, Lin J, Huang Y, Li Y, Yang X, Wu H, Wu S, Xie L, Dai L, Hou Z. Self-Targeted, Shape-Assisted, and Controlled-Release Self-Delivery Nanodrug for Synergistic Targeting/Anticancer Effect of Cytoplasm and Nucleus of Cancer Cells. ACS Appl Mater Interfaces. 2015;7(46):25553-25559.

295. Liu H, Xu H, Jiang Y, Hao S, Gong F, Mu H, Liu K. Preparation, characterization, in vivo pharmacokinetics, and biodistribution of polymeric micellar dimethoxycurcumin for tumor targeting. Int J Nanomedicine. 2015;10:6395-6410.

296. Wong C, Stylianopoulos T, Cui J, Martin J, Chauhan VP, Jiang W, Popović Z, Jain RK, Bawendi MG, Fukumura D. Multistage nanoparticle delivery system for deep penetration into tumor tissue. Proceedings of the National Academy of Sciences. 2011;108(6):2426-2431.

297. Jain RK, Stylianopoulos T. Delivering nanomedicine to solid tumors. Nat Rev Clin Oncol. 2010;7(11):653-664.

298. Sugahara KN, Teesalu T, Karmali PP, Kotamraju VR, Agemy L, Girard OM, Hanahan D, Mattrey RF, Ruoslahti E. Tissue-Penetrating Delivery of Compounds and Nanoparticles into Tumors. Cancer Cell. 2009;16(6):510-520.

VITA

Derek Alexander Reichel

EDUCATION

2007-2012 B.S. Chemical Engineering, College of Engineering, The Ohio State University (*summa cum laude*, honors in research, graduate with distinction)

HONORS AND AWARDS

2016-2017 Graduate School Allocated Year Fellowship; UK College of Pharmacy

2016 Graduate School Travel Award; UK College of Pharmacy

2015 Monthly Publication Highlight, UK College of Pharmacy

2014 Graduate School Travel Award; UK College of Pharmacy

2012-2015 Daniel R. Reedy Quality Achievement Fellowship; University of Kentucky

2012 Outstanding Undergraduate Award for Research; OSU Chemical Engineering

2011-2012 Undergraduate Research Scholarship; OSU College of Engineering

PUBLICATIONS

Peer-Reviewed Journals

9. Submitted: Davis, S.; Reichel, D.; Bae, Y.; Pennypacker, K.; Enhanced Stability of Leukemia Inhibitory Factor loaded in Nanoparticles Targeted to Ischemic Stroke and Other Inflammatory Diseases, *Pharm. Res*.

8. Submitted: Rychahou, P.; Bae, Y.; Reichel, D.; Zaytseva, Y.; Lee, E. Y.; Napier, D.; Weiss, H. L.; Evers, B. M.; Targeting Colorectal Cancer Lung Metastasis with Lung-Selective Drug Delivery, *Proc. Natl. Acad. Sci. U.S.A.*

7. Submitted: Reichel, D.; Curtis, L.T.; Ehlman, E.; Evers, B. M.; Rychahou, P.; Frieboes, H. B.; Bae, Y.; Halofluorochromic Polymer Nanoassemblies for Early and Accurate Detection of Liver Metastatic Colorectal Cancer Tumors, *Pharm. Res.*

6. Rheiner, S.; Reichel, D.; Rychahou, P.; Izumi, T.; Yang, H.-S.; Bae, Y.; Polymer Nanoassemblies with Hydrophobic Pendant Groups in the Core Induce False Positive

siRNA Transfection in Luciferase Reporter Assays, *Int. J. Pharm*. **2017**, *528*, 536-546 (DOI 10.1016/j.ijpharm.2017.06.056)

5. Park, J. E.; Chun, S.-E.; Reichel, D.; Min, J. S.; Lee, S.-C.; Han, S.; Ryoo, G.; Oh, Y.; Park, S.-H.; Ryu, H.-M.; Kim, K. B.; Lee, H.-Y.; Bae, S. K.; Bae, Y.; Lee, W.; Polymer Micelle Formulation for the Proteasome Inhibitor Drug Carfilzomib: Anticancer Efficacy and Pharmacokinetic Studies in Mice, *PLoS ONE*. **2017**, *12*, 1-12 (DOI 10.1371/journal.pone.0173247)

4. Reichel, D.; Bae, Y.; Comparison of Dialysis- and Solvatofluorochromism-based Methods to Determine Drug Release Rates from Polymer Nanoassemblies, *Pharm. Res.* **2017**, *34*, 394-407. (DOI 10.1007/s11095-016-2070-6)

3. Reichel, D.; Lee, M. J.; Lee, W.; Kim, K. B.; Bae, Y.; Tethered Polymer Nanoassemblies for Sustained Carfilzomib Release and Prolonged Suppression of Proteasome Activity, *Ther. Deliv.* **2016**, *7*, 665-681. (DOI 10.4155/tde-2016-0041)

2. Ao, L.; Reichel, D.; Hu, D.; Jeong, H. Y.; Kim, K. B.; Bae, Y.; Lee, W.; Polymer Micelle Formulations of Proteasome Inhibitor Carfilzomib for Improved Metabolic Stability and Anti-Cancer Efficacy in Human Multiple Myeloma and Lung Cancer Cell Lines, *J. Pharmacol. Exp. Ther.* **2015**, *355*, 168-173. (DOI 10.1124/jpet.115.226993)

1. Reichel, D.; Rychahou, P.; Bae, Y. Polymer Nanoassemblies with Solvato- and Halo-fluorochromism for Drug Release Monitoring and Metastasis Imaging, *Ther. Deliv.* **2015**, *6*, 1221-1237. (DOI 10.4155/tde.15.59)

Conference Proceedings

4. Rychahou, P.; Bae, Y.; Reichel, D.; Zaytseva, Y.; Lee, E. Y.; Weiss, H. L.; Evers, B. M.; Targeting Colorectal Cancer Lung Metastasis Microenvironment with PI3K Inhibitors and Chemotherapy (American Association for Cancer Research, Washington, DC), *Cancer Res*., **2017**, 77, 201. (DOI 10.1158/1538-7445.AM2017-201)

3. Park, J. E.; Chun, S.-E.; Reichel, D.; Park, J.; Min, J. S.; Ryoo, G.; Oh, Y.; Bae, S. K.; Yeo, Y.; Bae, Y.; Lee, W.; Novel Polymer Micelle and Nanocrystal Formulations for the Proteasome Inhibitor Drug Carfilzomib: Pharmacokinetic and Pharmacodynamic Studies in Human Lung and Breast Cancer Models (Experimental Biology, Chicago, IL), *FASEB J.*, **2017**, 31, 822.

2. Park, J. E.; Ao, L.; Chun, S.-E.; Reichel, D.; Hu, D.; Han, S.; Ryoo, G.; Oh, Y.; Park, S.-H.; Min, J. S.; Ryu, H.-M.; Bae, S. K.; Lee, H.-Y.; Kim, K. B.; Jeong, H. Y.; Bae, Y.; Lee, W. Polymer Micelle Formulation of Proteasome Inhibitor Carfilzomib as a Potential Strategy to Improve Metabolic Stability and Anti-Cancer Efficacy in Human

Multiple Myeloma and Lung Cancer (Japanese Society for the Study of Xenobiotics, Matsumoto, Japan), *Drug Metab. Pharmacokinet.*, **2017**, 32, 1, S46. (DOI 10.1016/j.dmpk.2016.10.195)

1. Ao, L.; Reichel, D.; Hu, D.; Jeong, H.-Y.; Kim, K. B.; Bae, Y.; Lee, W.; Nanoformulations of Carfilzomib for Improved Metabolic Stability and Anti-Cancer Efficacy (Experimental Biology, Boston, MA), *FASEB J.*, **2015**, *29*, 620.

PRESENTATIONS

Oral Presentations

7. *Early Detection of Liver Metastatic Colorectal Cancer by using Polymer Tethered Nanoassemblies*, Pharmaceutics Graduate Student Research Meeting, June 2016, Kansas City, MO

6. *Polymer Tethered Nanoassemblies for Cancer Detection and Therapeutics*, University of Kentucky, May 2016, Lexington, KY

5. *Polymer Tethered Nanoassemblies for Improving Cancer Detection and Treatment*, National Science Foundation EPSCoR Membrane Pillar and University of Kentucky Center for Membrane Sciences, March 2016, Lexington, KY

4. *Solvatochromic Polymer Tethered Nanoassemblies for Liver Metastasis Detection*, University of Kentucky, February 2015, Lexington, KY

3. *Environment-Sensitive Tethered Nanoassemblies for Cancer Theranostics*, Pharmaceutics Graduate Student Research Meeting, June 2014, Chicago, IL

2. *Tethered Nanoassemblies for Cancer Theranostics*, University of Kentucky, April 2014, Lexington, KY

1. *Crosslinked Nanoassemblies for Cancer Theranostics*, University of Kentucky, April 2013, Lexington, KY

Poster Presentations

20. Rychahou, P.; Bae, Y.; Reichel, D.; Zaytseva, Y.; Lee, E. Y.; Weiss, H. L.; Evers, B. M.; *Targeting Colorectal Cancer Lung Metastasis Microenvironment with PI3K Inhibitors and Chemotherapy*, American Association for Cancer Research, April 2017, Washington, DC

19. Park, J.; Chun, S.; Reichel, D.; Park, J.; Min, J.; Ryoo, G.; Oh, Y.; Bae, S.; Yeo, Y.; Bae, Y.; Lee, W.; *Novel Polymer Micelle and Nanocrystal Formulations for the Proteasome Inhibitor Carfilzomib: Pharmacokinetic and Pharmacodynamic Studies*

in Human Lung and Breast Cancer Models, Experimental Biology, April 2017, Chicago, IL

18. Park, J. E.; Ao, L.; Chun, S.-E.; Reichel, D.; Hu, D.; Han, S.; Ryoo, G.; Oh, Y.; Park, S.-H.; Min, J. S.; Ryu, H.-M.; Bae, S. K.; Lee, H.-Y.; Kim, K. B.; Jeong, H. Y.; Bae, Y.; Lee, W.; *Polymer Micelle Formulation of Proteasome Inhibitor Carfilzomib as a Potential Strategy to Improve Metabolic Stability and Anti-Cancer Efficacy in Human Multiple Myeloma and Lung Cancer*, Japanese Society for the Study of Xenobiotics, October 2016, Matsumoto, Japan

17. Reichel, D.; Rychahou, P.; Bae, Y.; *Early Detection of Liver Metastatic Colorectal Cancer by Using Polymer Tethered Nanoassemblies*, Markey Cancer Center Research Day, May 2016, Lexington, KY

16. Reichel, D.; Bae, Y.; *Ionic and Hydrophobic Core Modifications of Polymer Tethered Nanoassemblies to Control Entrapment and Release of Carfilzomib*, Rho Chi Research Day, March 2016, Lexington, KY

15. Reichel, D.; Bae, Y.; *Effects of Ionic and Hydrophobic Core Modifications on Drug Release from Polymer Tethered Nanoassemblies*, Drug Discovery and Development Symposium, November 2015, Lexington, KY

14. Reichel, D.; Bae, Y.; *Controlling Drug Release Properties and Preventing Burst Release from Polymer Tethered Nanoassemblies Using Core Environment Modifications*, Nanobiotechnology Center Symposium, October 2015, Lexington, KY

13. Reichel, D.; Rychahou, P.; Bae, Y.; *Polymer Nanoassemblies for Real-time Drug Release Monitoring and Ex Vivo Imaging for Theranostics of Metastatic Tumors*, Pharmaceutics Graduate Student Research Meeting, June 2015

12. Ao, L.; Reichel, D.; Hu, D.; Jeong, H.-Y.; Kim, K. B.; Bae, Y.; Lee, W.; *Polymer Micelle Formulations of Proteasome Inhibitor Carfilzomib for Improved Metabolic Stability and Anti-Cancer Efficacy*, Markey Cancer Center Research Day, May 2015, Lexington, KY

11. Reichel, D.; Rychahou, P.; Bae, Y.; *Polymer Nanoassemblies for Real-time Drug Release Monitoring and Ex Vivo Imaging for Theranostics of Metastatic Tumors*, Markey Cancer Center Research Day, May 2015, Lexington, KY

10. Ao, L.; Reichel, D.; Hu, D.; Jeong, H.-Y.; Kim, K. B.; Bae, Y.; Lee, W.; *Nanoformulations of Carfilzomib for Improved Metabolic Stability and Anti-Cancer Efficacy*, Experimental Biology, March 2015, Boston, MA

9. Reichel, D.; Bae, Y.; *Polymeric Theranostic Tethered Nanoassemblies for Drug Release and Tissue pH Monitoring*, 6th Annual Biomaterials Day, September 2014, Lexington, KY

8. Reichel, D.; Bae, Y.; *Polymeric Theranostic Tethered Nanoassemblies for Drug Release and Tissue pH Monitoring*, Symposium on Drug Discovery and Development, September 2014, Lexington, KY

7. Piroli, M.; Reichel, D.; Pack, D.; Bae, Y.; *Controlling Drug Release from Theranostic Polymer Tethered Nanoassemblies*, Research Experience for Undergraduates, August 2014, Lexington, KY

6. Reichel, D.; Bae, Y.; *Nile Blue Tethered Nanoassemblies for Cancer Theranostics*, Markey Cancer Center Research Day, May 2014, Lexington, KY

5. Plasko, G.; Reichel, D.; Geddes, J.; Bae, Y.; *Crosslinked Nanoassemblies Entrapping Fluorescent Probes for Drug Release Monitoring*, Research Experience for Undergraduates, July 2013, Lexington, KY

4. Reichel, D.; Bae, Y.; *Crosslinked Nanoassemblies for Cancer Theranostics*, Pharmaceutics Graduate Student Research Meeting, June 2013, Lexington, KY

3. Reichel,D.; Bae, Y.; *Crosslinked Nanoassemblies for Cancer Theranostics*, Markey Cancer Center Research Day, April 2013, Lexington, KY

2. Reichel,D.; Glick, L.; Chen, A.; Baretto, J.; Wood, D.; *A Comparison of Estrogenic Properties of Small Molecules across Several Species Using Biosensors*, AIChE, October 2012, Pittsburgh, PA

1. Reichel, D.; Glick, L.; Chen, A.; Saunders, B.; Miskioglu, E.; Wood, D.; *High-Throughput Screening System for the Determination of Estrogenic Properties of ICCVAM-Recommended Compounds*, AIChE, October 2012, Pittsburgh, PA